12-2022

Core-Collapse Supernova Simulations With Spectral Two-Moment Neutrino Transport

Ran Chu
rchu@vols.utk.edu

To the Graduate Council:

I am submitting herewith a dissertation written by Ran Chu entitled "Core-Collapse Supernova Simulations With Spectral Two-Moment Neutrino Transport." I have examined the final electronic copy of this dissertation for form and content and recommend that it be accepted in partial fulfillment of the requirements for the degree of Doctor of Philosophy, with a major in Physics.

Anthony Mezzacappa, Major Professor

We have read this dissertation and recommend its acceptance:

Eirik Endeve, Otis Messer, Cory Hauck, William R. Hix, Thomas Papenbrock

Accepted for the Council:

Dixie L. Thompson

Vice Provost and Dean of the Graduate School

(Original signatures are on file with official student records.)

Core-Collapse Supernova Simulations With Spectral Two-Moment Neutrino Transport

A Dissertation Presented for the

Doctor of Philosophy

Degree

The University of Tennessee, Knoxville

Ran Chu

December 2022

Dedication

This dissertation is dedicated to Deliang Chu, Ping Jiang, and myself.

谨以此论文献给我的父亲、母亲、与年少时的自己。

A dream comes true.

纪念这段梦想成真的旅程。

Acknowledgements

First and foremost, I want to express my gratitude to Anthony Mezzacappa, my primary advisor. He gave me this incredible opportunity to work with an incredible team on the most advanced supercomputer in the world to study computational astrophysics. He encouraged, trained, and improved me. In many ways, he has taught me how to be a professional scientist. This endeavor would be impossible without his help and support.

Eirik Endeve deserves my thanks no less. He patiently guided me from the beginning and taught me to work independently. His insightful feedback pushed me to sharpen my thinking and brought my work to a higher level. He has treated me with a level of respect that I think is rare for any student to receive.

For their assistance in my research, I thank the entire astrophysics group at the University of Tennessee in Knoxville physics department and ORNL. I appreciate each of their contributions to our project meetings and attempts to move the program ahead. Bronson Messer, Raph Hix, Eric Lentz, and Austin Harris deserve special thanks.

I would like to express my gratitude to the entire UT Physics Department, particularly Chrisanne Romeo. They offered me advice and assistance during my stay at UT, as well as support during difficult times. I remember every hug Chrisanne gave me, which delighted me at the darkest moment.

Last but not the least, I would like to shout-out to my family members and friends. Thank you for your accompaniment and patience, for understanding my struggles, for guarding my back, and for answering my call whenever I need you.

Every wind, every rain, every sand, every flower, every star, and every instant mean something to me. I am grateful to the Universe for this once-in-a-lifetime opportunity.

Quote

"Who by the riverside first saw the moon arise? When did the moon first see a man by riverside?"
"江畔何人初见月？江月何年初照人"

– Zhang Ruoxu, Chinese poet of the early Tang dynasty, 720AD
张若虚，中国唐朝诗人，720年

Abstract

The primary focus of this dissertation is to develop a next-generation, state-of-the-art neutrino kinetics capability that will be used in the context of the next-generation, state-of-the-art core-collapse supernova (CCSN) simulation frameworks `thornado` and Flash-X. `thornado` is a **t**oolkit for **h**igh-**or**der **n**eutrino-r**ad**iation hydr**o**dynamics, which is a collection of modules that can be incorporated into a simulation code/framework, such as Flash-X, together with a nuclear equation of state (EOS) library, such as the `WeakLib` EOS tables.

The first part of this work extends the `WeakLib` code to compute neutrino interaction rates from Bruenn (1985) and produce corresponding opacity tables. The processes of emission, absorption, scattering of neutrinos from nucleons and nuclei, neutrino–electron scattering, and neutrino pair production and annihilation are included.

The second part of this dissertation builds the special-relativity-corrected ($\mathcal{O}(v/c)$) neutrino radiation module in `thornado`, based on the spectral two-moment method. This part of the work involved studying the accuracy, efficiency, and robustness of the numerical solver. We propose a special kind of implicit-explicit scheme, PDARSs, based on efficiency, diffusion accuracy, and physics-preserving (positivity-preserving and realizability-preserving) requirements. Emission, absorption, scattering of neutrinos from nucleons and nuclei, neutrino–electron scattering, and neutrino pair production and annihilation are included as neutrino–matter couplings.

The third part of this work builds interfaces between Flash-X and `thornado`, Flash-X and `WeakLib`, and `thornado` and `WeakLib` for simulations with the Flash-X hydrodynamics module, `WeakLib` EOS module, and `thornado` neutrino kinetics module. This part of the work includes data mapping between finite-volume grids and finite-element grids, time-step balancing between hydrodynamics time steps and radiation transport time steps, and GPU enhancement.

The fourth part of this work makes a detailed comparison of the results of a spherically symmetric simulation performed by Flash-X+`thornado` with the result of the CHIMERA code, which is a sophisticated, mature, and evolving code with spectral flux-limited diffusion (one-moment) neutrino kinetics and improved input physics (Bruenn et al., 2020). This part of the work demonstrates the ability of Flash-X+`thornado` to perform CCSN simulations and quantifies the potential differences between the two codes caused by the different neutrino kinetics treatments, as well as other differences.

Supported by all of the above work, spherically symmetric CCSN simulations with spectral two-moment neutrino kinetics were performed for three low-mass progenitors of 9-, 10-, and 11-Solar-mass ($M_\odot$) from Sukhbold et al. (2016).

Table of Contents

List of Tables

List of Figures

List of Algorithms

Chapter 1

Introduction

"Who by the riverside first saw the moon arise? When did the moon first see a man by riverside?"

— Zhang Ruoxu (张若虚), 720AD

What are those bright objects in the sky? For how long have they been around? What is their connection to us? These questions have been pondered in humans' brains and hearts since there was language. They evoke human emotion and stimulate learning. Supernovae are among the most brilliant phenomena in the universe, as gorgeous and mysterious as the Mona Lisa, full of poetry and scientific elegance. Why and how do they die, give birth to new objects, and shape the Universe? We are on a mission to learn everything there is to know about them. This is a field that bridges theories and observations, challenges, and examines the cutting edge of human knowledge, particularly in fundamental science.

1.1 Core-Collapse Supernova

Core-collapse supernovae (CCSNe) are the dramatic explosions that end the life of a massive star whose mass is at least 8 $M_\odot$, giving birth to neutron stars and black holes. The iron cores in such massive stars are surrounded by burning shells of silicon,

oxygen, carbon, and so on, supported by electron degeneracy pressure. The Si shell burning continues to grow the iron core until the iron core exceeds a Chandrasekhar mass (~ 1.2 $M_\odot$). Once an iron core attains this critical mass, electron degeneracy pressure is unable to balance the gravity, and unstable gravitational collapse ensues. The collapse of the iron core accelerates rapidly, and its density and temperature increases until the central density exceeds the density of nuclear matter, $\rho_{\rm nuc} \approx 2 \times 10^{14}$ g cm^{-3} (given by nuclear saturation density 0.16 fm^{-3}). Its mass, which is in order of solar mass, is 100 km or less in radius. These conditions are not Newtonian and definitely require a general relativistic model. The strong nuclear force becomes important at such density, halting the collapse of the inner core and launching a strong shock wave into the still collapsing outer core. At first, the shock propagates rapidly through the outer core. Meanwhile, neutrino cools matter behind the shock. The photodissociation of matter causes the shock to stall at ∼150 km from the center of the star, and neutrino losses. The whole process that begins with a Chandrasekhar-mass core and ends with a protoneutron star (PNS) takes only a fraction of a second. CCSNe have been observed across the electromagnetic spectrum and in neutrinos by Hirata et al. (1987). When the explosion wave, generated in the stellar center, reaches the surface of the star, the optical supernova outburst begins. The extreme conditions in the stellar center make CCSNe one of the few detectable sources of neutrinos outside the solar system. Observation of CCSNe is also now being devoted to the observation of the gravitational wave signals of CCSNe.

CCSNe are interesting for many reasons. They are responsible for the elements heavier than oxygen up to germanium (Ge). They play important roles in many astrophysical phenomena, such as the chemical evolution of galaxies (Arnett and Arnett, 1996; Woosley et al., 2002), star formation (Krumholz, 2014), neutron star and black hole formation (Özel et al., 2010, 2012; Foucart et al., 2015, 2016). These explosions occur at energies and densities relevant to addressing fundamental questions in nuclear, particle, and gravitational physics. All these together make CCSNe one of the most important problems in modern astrophysics.

With the development of new technology and bigger telescopes, we find several hundred CCSNe every year, based on the sne website [*]. We know that progenitors of CCSNe have at least 8 times, but no more than 40 to 50 times the mass of the Sun. We also know that heavy elements, gravitational waves (suspected), and neutrinos are produced during the explosion. In the past decade, numerous studies have been performed regarding CCSN neutrinos (for examples: Scholberg 2012; Kuroda et al. 2017; Khaitan 2018; O'Connor and Couch 2018; Müller 2019; Burrows et al. 2019; Hansen et al. 2019) and gravitational wave emission (for examples: Ott et al. 2011, 2018; Abdikamalov et al. 2014; Yakunin et al. 2015; Kuroda et al. 2016, 2017; Powell et al. 2017; O'Connor and Couch 2018; Radice et al. 2019; Mezzacappa et al. 2020a).

However, we do not yet know definitively what determines whether a massive star will explode (Burrows and Vartanyan, 2021). This is because CCSNe are the epitome of a "multi-physics" problem. Aspects of stellar structure and evolution, nuclear and neutrino physics, fluid dynamics, radiation-hydrodynamics, kinetic theory, and general relativity are combined in it. According to modern CCSN theory (Mezzacappa et al., 2020a; Burrows and Vartanyan, 2021), neutrino heating powers the shock wave through the absorption of electron-neutrino and electron-antineutrinos emitted from the neutrinosphere,

Observational probes have given clues to the explosion mechanism. The kinetic energy of the supernova explosion observed is $\sim 10^{51}$ ergs. $\sim 10^{53}$ ergs of energy in neutrinos and antineutrinos are released from the newly formed PNS after core bounce. It is roughly confirmed by SN1987A neutrinos observation that $\sim 99\%$ of the gravitational binding energy released during collapse is carried away by neutrinos. Neutrino energy deposition is now widely believed (for reviews, see Janka et al. 2016; Müller 2016, 2020; Mezzacappa et al. 2020a; Burrows and Vartanyan 2021) to be the major driver of CCSN explosions, except in peculiar cases where rapid rotation is present and magnetohydrodynamic effects may dominate (Heger et al., 2005; Mösta et al., 2014, 2015; Coleman et al., 2021).

[*](sne), https://sne.space

1.1.1 Simulation of CCSNe

Direct and immediate information about the supernova "engine" can only be gathered from observation. These observations include neutrinos emitted from the forming neutron star, and gravitational waves emitted when the collapse does not proceed perfectly symmetrically. Numerical simulations are a more active way to study the explosion mechanism. It provides unique insight into CCSNe deep layer mechanism, refines theories in weak physics, and shapes our understanding of CCSNe.

However, numerical simulations present a true challenge, as they require comprehensive physics, including general relativity, microphysics (which includes nuclear and particle physics), transport kinetics, hydrodynamics, and electromagnetic mechanisms; accurate and stable numerical solvers; and powerful supercomputers.

Starting from the 1960s with the seminal work of Colgate and White (1966), in which they proposed that core-collapse supernova could be neutrino driven, many brave and determined researchers have been devoting their lives to CCSNe simulations. Since then, significant progress has been made, especially the development of simulation codes to study the explosion mechanism. It is believed the delayed neutrino-heating mechanism is emerging as the key driver of supernova explosions, but there are many issues to address (Burrows and Vartanyan, 2021). Emphasizing neutrino-driven mechanism aspects, some well-known codes include Prometheus-Vertex (Rampp and Janka, 2002; Buras et al., 2006; Müller et al., 2010) and CoCoNut-Vertex (Dimmelmeier et al., 2002, 2005; Müller et al., 2010; Müller and Janka, 2015) of the MPA-QUB-Monash collaboration, the Aenus-Alcar code (Obergaulinger, 2008; Just et al., 2015), the fGR1 code (Kuroda et al., 2012, 2016), the Chimera code (Bruenn, 1985; Bruenn et al., 2013; Lentz et al., 2015; Bruenn et al., 2016, 2020) of the Oak Ridge-UT-Florida Atlantic-NC State collaboration, the Fornax code (Skinner et al., 2019) of the Princeton group, and the latest Flash-X code (O'Connor and Couch, 2018; Harris et al., 2021; Dubey et al., 2022) (evolved from previous Flash code Fryxell et al. 2000; Dubey et al. 2009). Here

we describe the key features of these codes, with a focus on their neutrino transport methods first. The aspects that can be improved will be discussed at the end.

PROMETHEUS-VERTEX and COCONUT-VERTEX shared the neutrino transport scheme VERTEX. VERTEX employs a three-flavor, fully energy-dependent, two-moment variable Eddington factor neutrino transport scheme (Rampp and Janka, 2002; Buras et al., 2006) with "ray-by-ray plus" approximation (assume the neutrino flux direction point along the radial ray). The microphysics in VERTEX includes a number of additional neutrino interactions compared to the "standard" set in Bruenn (1985). (See Burrows and Sawyer 1998; Hannestad and Raffelt 1998; Buras et al. 2003; Langanke et al. 2003; Itoh et al. 2004; Marek et al. 2005; Langanke 2008 for the extension of the standard opacities.) VERTEX is coupled to different hydrodynamic modules, PROMETHEUS (Fryxell et al., 1989), a finite-volume Newtonian hydrodynamics code, and COCONUT (Dimmelmeier et al., 2002, 2005; Müller et al., 2010), a relativistic hydrodynamics code that employs a high-resolution shock-capturing finite volume method.

The AENUS-ALCAR code is developed to model multi-energy-group neutrino transport for supernovae and neutron-star mergers. Its hydrodynamics module, which is provided by AENUS (Obergaulinger, 2008), employs a Godunov-type finite-volume scheme in spherical polar coordinates with piecewise-parabolic method (Colella and Woodward, 1984), and the HLLC and HLLE Riemann solvers to solve the equations of Newtonian hydrodynamics. It uses an effective general relativistic gravitational potential. It solves fully multidimensional two-moment neutrino transport to $O(v/c)$ with algebraic closure (Minerbo, 1978). Its neutrino interactions include opacities in Bruenn (1985); Rampp and Janka (2002).

The `fGR1` code is a 3D-GR radiation hydrodynamics code with magnetohydrodynamics (Kuroda and Umeda, 2010). It employs general orthogonal coordinates with adaptive-mesh refinement in multi-dimensions, uses the Arnowitt-Deser-Misner (ADM) 3+1 formalism, the Baumgarte-Shapiro-Shibata-Nakamura (BSSN) formalism for gravity (Shibata and Nakamura, 1995; Baumgarte and Shapiro, 1998), and

utilizes the HLLE Riemann solver and a standard high-resolution-shock-capturing scheme. It employs full GR radiation-hydrodynamics. It solves the multi-group two-moment transport equations with analytical closure (Levermore, 1984; Shibata et al., 2011). Its neutrino interactions are based on Bruenn (1985); Hannestad and Raffelt (1998); Rampp and Janka (2002), which include inelastic neutrino–electron scattering, thermal neutrino production via pair annihilation, and nucleon–nucleon bremsstrahlung.

The CHIMERA code is a CCSNe simulation code, which contains modules for the equations of state, multidimensional compressible hydrodynamics, various neutrino interactions, neutrino transport, and nuclear reactions. Its hydrodynamics is based on a dimensionally-split, Lagrangian-plus-remap version of the piecewise parabolic method (Colella and Woodward, 1984) with a sliding radial grid algorithm in a spherical coordinate system. The gravity in CHIMERA approximates the GR monopole component. Neutrino transport in CHIMERA is built from the original formulation in Bruenn (1985), developed to a modified version, and solves with the "ray-by-ray" approximation and flux limited diffusion. The neutrino weak interactions in the Chimera code include absorption-emission, scattering and pair-production opacities in Bruenn (1985); Mezzacappa and Bruenn (1993c); Bruenn and Mezzacappa (1997); Horowitz (1997); Hannestad and Raffelt (1998); Reddy et al. (1998); Hix et al. (2003); Langanke et al. (2003); Buras et al. (2006). `XNet` is a thermonuclear reaction network code developed by Hix and Thielemann (1999). `XNet` solves the nuclear composition when material is not under nuclear statistical equilibrium (NSE) appropriate conditions.

The FORNAX code employs general orthogonal coordinates in multi-dimensions. It uses the comoving-frame and solves multi-group two-moment transport equations to $O(v/c)$ with the algebraic closure of Vaytet et al. (2011), and high-order reconstruction (Skinner et al., 2019). Three neutrino species are followed using the implicit-explicit (IMEX) scheme. Its neutrino-matter interactions are described

in Burrows et al. (2006), which includes absorption in Horowitz (2002), ion-ion-correlations, weak screening, form-factor corrections for neutrino-nucleus scattering, inelastic neutrino–electron scattering (Thompson et al., 2003; Reddy et al., 1999), nucleon-nucleon bremsstrahlung and electron–positron annihilation (Thompson et al., 2000), and correction in the neutrino-nucleon scattering rate in Horowitz et al. (2017). It also includes weak magnetism and recoil corrections to neutrino-nucleon scattering. Its hydrodynamics is based on a directionally unsplit Godunov-type finite-volume method with static mesh, implements the local Lax-Friedrichs, HLLE, and HLLC Riemann solvers, and approximates general relativistic gravity for the monopole gravitational term.

Flash-X* (Dubey et al., 2022) is a new incarnation of the code derived from FLASH† (Dubey et al., 2009; Fryxell et al., 2000) as part of the US Department of Energy's Exascale Computing Project (ECP) project `ExaStar`, providing a multiphysics software system used by multiple science communities, the primary software instrument for `ExaStar`. Flash-X has a redesigned architecture that provides performance portability across various platforms, both with and without accelerators. It leverages adaptive mesh refinement (AMR) via either Paramesh (MacNeice et al., 2000) and AMReX (Zhang et al., 2019). As an example of the capability of Flash-X: it is capable of nearly ideal weak-scaling to 10,000 MPI ranks on the Summit computer at the Oak Ridge Leadership Computing Facility (OLCF) (Harris et al., 2021). Most notable among the newer and higher-fidelity physics solvers in Flash-X are `Spark` (Couch et al., 2021) for magnetohydrodynamics, `XNet`‡ (Hix and Thielemann, 1999) for nuclear burning, `thornado`§ (Chu et al., 2019a; Laiu et al., 2021; Endeve et al., 2022a; Laiu et al., 2022; Endeve et al., 2022b) for neutrino radiation transport,

*https://github.com/Flash-X/Flash-X
†flash.uchicago.edu/site/index.shtml
‡https://github.com/starkiller-astro/xnet
§https://github.com/endeve/thornado

and `WeakLib`[¶] (Pochik et al. 2021; Landfield December 2018, and this dissertation) for tabulated microphysics.

Each code has room for improvement and optimization. Considering the CCSNe explosion in nature, an ideal code runs three-dimensional, general-relativistic, full-dimensional radiation-magneto-hydrodynamics with every microphysics and nuclear reaction. Based on this background, VERTEX has sophisticated microphysics and can have improvement in two-moment neutrino transport; AENUS-ALCAR can have improvement in relativity; `fGR1` has powerful 3D-GR radiation-magneto-hydrodynamics and sophisticated microphysics, and can have improvement in radiation analytical closure; CHIMERA has sophisticated microphysics and nuclear reactions, and can have improvement in neutrino transport; FORNAX has sophisticated microphysics and can have an improvement in neutrino transport; Flash-X, after upgrading and developing, will have the ability to make 3D-GR radiation-magneto-hydrodynamics simulations with sophisticated microphysics and nuclear reaction.

Due to the numerical and physical complexity, these enhancements cannot be made in a short period. Take neutrino transport for example. The computational challenge has two parts (Mezzacappa et al., 2020a). First, the kinetic equations, which govern the evolution of neutrino distributions, need to be mapped onto appropriate discrete representations. The discrete representations need to be stable, accurate, and respect physical laws. These include, but are not limited to, lepton number and energy conservation, and the Fermi-Dirac nature of neutrino as fermion. Second, the resultant nonlinear algebraic equations need to be solved by efficient, supercomputer-architecture-aware methods. Mezzacappa et al. (2020a) presents a review of the latest efforts to meet this challenge. The primary focus of this dissertation is to develop a next-generation, state-of-the-art neutrino kinetic capability that will be used in CCSN simulation frameworks `thornado` and Flash-X in the sense of the above challenge.

[¶] https://github.com/starkiller-astro/weaklib

1.2 Motivation

Although significant progress has been made, general relativistic three-dimensional models with Boltzmann neutrino transport, weak interaction physics that meets industry standards, and equations of state that meet industry standards have not yet been produced. A list of the lessons that guide us to improve models of neutrino transport include: (Mezzacappa et al., 2020a)

1. All three flavors of neutrinos and their antineutrino partners are required.
2. A quantum kinetics description of neutrino transport is required.
3. Simulations must be general relativistic.
4. Simulations must include all the neutrino weak interactions, and the description of the interactions must be state of the art.
5. Lepton number and energy need to be conserved.
6. The discretization of the Boltzmann equations must accommodate both small- and large-energy scattering.
7. Realistic EOS for the nuclear, leptonic, and photonic components must be accommodated by numerical methods.
8. Neutrino transport must be solved in moments approaches until Boltzmann approaches become feasible.
9. The closures must respect the Fermi-Dirac statistics of neutrinos.

It is a natural and required starting point to use a classical Boltzmann description when developing a quantum kinetics treatment of neutrino transport. Likewise, for general relativistic and all neutrino weak interactions requirements, a special relativistic CCSN model with standard basic neutrino weak interactions (Bruenn, 1985) is the natural and required starting point for the development. All neutrino

flavors, the moment approaches, lepton number and energy conservation, small- and large-energy scattering, the proper closure that respects the Fermi-Dirac statistics of neutrinos, and the proper numerical methods are targeted in this project: Among the moment approaches, we choose the two-moment approach because it is the higher order moment approach, compared with the flux-limited approach, and yet not as expensive as the discretized full-dimensional Boltzmann solver approach. The discontinuous Galerkin (DG) method (Reed and Hill, 1973; Cockburn and Shu, 2001; Hesthaven and Warburton, 2008), as one type of finite-element method, is preferred when model CCSN explosions. First, the DG method can be used to develop structure-preserving methods for physical-constraint-preserving. Second, the DG method is easy to leverage in higher order needs. Third, it practices the correct behavior in the diffusion limit without modification. In addition, the DG method can be combined with other (such as finite-volume) methods (Klöckner et al., 2009; Teukolsky, 2016; Adams, 2001; Guermond and Kanschat, 2010). The DG method has received attention from the astrophysics community recently, and was used in the latest codes (Radice and Rezzolla, 2011; Radice et al., 2013; Endeve et al., 2015; Schaal et al., 2015; Wu and Tang, 2016; Teukolsky, 2016). (More reviews for the DG method can be found in Cockburn and Shu 2001; Hesthaven and Warburton 2008; Bassi et al. 2013; Shu 2016.)

The implicit-explicit method is targeted as a time integration method for efficiency, with implicit update for the collision update and explicit update for the advection term. It avoids a distributed implicit solve, which can be expensive and more difficult to scale. For weak physics, we use tabulated EOS and neutrino interaction rates, so that upgrading weak physics can be made in parallel with the other developments, and is easy to implement.

To sum up, we aim to build a neutrino transport code for a next-generation, state-of-the-art CCSN simulation capability and use it to investigate the dynamics of CCSN. The new capabilities of the code include: a. implementing the discontinuous Galerkin method in spectral two-moment neutrino kinetics in the context of CCSN;

b. applying an accurate, efficient, physics-preserving implicit-explicit time update method; c. computational/parallel efficient boosted by GPU; d. easy to incorporate into other simulation codes/frameworks; e. can be modularly updated in future development.

This dissertation is organized as follows to address our efforts towards this goal. Initial work on developing a DG method for spectral two-moment neutrino kinetics is presented in Chapter 3 for $\mathcal{O}(1)$ and simplified neutrino-matter interactions scenario (which are published in Chu et al. 2019a; Chu et al. 2019b), and Chapter 4 for an $\mathcal{O}(v/c)$ model. The work for developing an accurate, efficient, physis-preserving time update method is presented in Chapter 3 for our implicit-explicit scheme, and Chapter 5 for the nonlinear solver (Laiu et al., 2020, 2021). In parallel with the neutrino kinetics numerical method and code development, we developed `WeakLib` for weak physics. The work for `WeakLib` development is presented in Chapter 5, with the development of interfaces between `WeakLib`, `thornado`, and Flash-X. `WeakLib` and `thornado` module structure, which is rooted in operator splitting, enable modularly update/development. In addition, effective implementations with graphics processing units (GPUs) of the weak physics and kinetic update are produced as code optimization on the Summit supercomputer at the Oak Ridge Leadership Computing Facility (OLCF) (Harris et al., 2021). We examined the capability and efficiency of the code by running spherical symmetric (1D) CCSN simulations on Summit. We leveraged the existing infrastructure of Flash-X for hydrodynamics and gravity, via the `Spark` module (Couch et al., 2021). The simulation results are presented in Chapter 6 for a detailed comparison between CHIMERA and Flash-X+`thornado` using a 9 $M_\odot$ progenitor in spherical symmetry, and Chapter 7 for simulations with a set of low mass progenitors in spherical symmetry. In this dissertation, we consider only Newtonian simulations. All our codes are released to the public and serve the Flash-X users and astrophysics community. In Chapter 8 we give conclusions and a list of future improvements.

Chapter 2

Neutrino Radiation Hydrodynamics: Formalism

In neutrino-driven core-collapse supernova models, neutrino radiation hydrodynamics involves the movement of matter, the transport of neutrinos, and their interactions. The subject of neutrino radiation hydrodynamics, including the moment method, moment realizability, and the closure approach, is presented in this chapter. The numerical approach for solving the moment equations, including the discretization, the time integrator, and numerical limiters, will be discussed in Chapters 3 and 4. The framework in Flash-X + `thornado` that solves the neutrino radiation hydrodynamics will be presented in Chapter 5. Throughout, we use a system of natural units, i.e., the speed of light c and the Planck constant h are $h = c = 1$.

2.1 3+1 Formulation of General Relativity

We begin with the fundamental element of general relativity's "3+1" formulation (Cardall and Mezzacappa, 2003; Cardall et al., 2013; Mezzacappa et al., 2020a). In this formulation, space and time are separated by foliating spacetime in a series of spacelike hypersurfaces, Σ_t, each corresponding to a constant coordinate time t.

A unit timelike normal four-vector $\boldsymbol{n}$, satisfying $n_\mu n^\mu = -1$ (using Einstein's summation convention), exists at each point of the hypersurface Σ_t. Here $\boldsymbol{n}$ corresponds to the four-velocity of the observer at rest with respect to the hypersurface. The four-vector $\boldsymbol{\beta}$ describes how the spatial coordinates move within each hypersurface. It is also known as the "shift" vector. With α being the "lapse" function, αdt gives the proper time between two hypersurfaces, Σ_t and Σ_{t+dt}. In this foliation of spacetime, the spacetime metric can be read off from

$$ds^2 = g_{\mu\nu} dx^\mu dx^\nu = (-\alpha^2 + \beta_i \beta^i) dt^2 + 2\beta_i dt\, dx^i + \gamma_{ij} dx^i dx^j, \tag{2.1}$$

as

$$g_{\mu\nu} = \begin{pmatrix} -\alpha^2 + \beta_i \beta^i & \beta_i \\ \beta_i & \gamma_{ij} \end{pmatrix}, \tag{2.2}$$

where $\gamma_{i\,j}$ is the metric on the hypersurface Σ_t. The determinant of $g_{\mu\nu}$ is g, and $\sqrt{-g} = \alpha\sqrt{\gamma}$, where $\sqrt{\gamma}$ is the determinant of the spatial metric γ_{ij}. The timelike normal four-vector

$$n^\mu = \frac{1}{\alpha}(1, -\beta^i) \quad \text{with} \quad n_\mu = (-\alpha, 0), \tag{2.3}$$

and

$$\gamma^\alpha_\mu = \delta^\alpha_\mu + n^\alpha\, n_\mu, \tag{2.4}$$

provide timelike and spacelike projections, respectively.

In this chapter, we will elaborate on how we formulate the radiation-hydrodynamics equations in a form suitable for numerical solutions using the 3+1 slicing of spacetime.

2.2 Hydrodynamics Equations

We will begin the discussion with the equations of general relativistic hydrodynamics with radiation coupling, which governs the evolution of matter and neutrino in CCSN explosions, and end with the Newtonian limit of these equations.

2.2.1 General Relativistic Hydrodynamics Equations

In CCSN models, the stellar fluid is modeled as a perfect fluid. Without including effects due to electromagnetic fields, the evolution equations are (see, e.g. Rezzolla and Zanotti (2013) for details)

$$\nabla_\nu J^\nu_{\rm B} = 0, \tag{2.5}$$

$$\nabla_\nu J^\nu_e = -m_{\rm B} Q_L \left(f_{\nu_e}, f_{\bar{\nu}_e}, \ldots\right), \tag{2.6}$$

$$\nabla_\nu T^{\mu\nu}_{\rm fluid} = -G^\mu \left(f_{\nu_e}, f_{\bar{\nu}_e}, \ldots\right). \tag{2.7}$$

Equation (2.5) is the mass conservation equation, where $J^\nu_{\rm B}$ is the baryon rest-mass current density given by

$$J^\nu_{\rm B} = \rho u^\nu, \tag{2.8}$$

where $\rho = M_{\rm B} n_{\rm B}$ gives the baryon rest mass density, with $M_{\rm B}$ being the average baryon rest mass, and $n_{\rm B}$ being the baryon density, and u^ν being the fluid four-velocity. In a nuclear fluid, $\rho = \sum_B M_{\rm B} n_{\rm B}$ sums over all baryon type B with rest mass $M_{\rm B}$ and density $n_{\rm B}$, and mass $M_{\rm B}$ is not conserved.

Equation (2.6) expresses the local conservation of electron lepton number, where the electron density current J^ν_e is given by

$$J^\nu_e = \rho Y_e u^\nu, \tag{2.9}$$

with Y_e being the electron fraction. The source term on the right-hand side of Equation (2.6), $-m_{\rm B}Q_L$, represents the lepton exchange between the fluid and the neutrinos.

Equation (2.7) expresses the conservation of four-momentum (energy and momentum conservation), where the fluid energy-momentum tensor $T^{\mu\nu}_{\rm fluid}$ is given by

$$T^{\mu\nu}_{\rm fluid} = \rho h u^\mu u^\nu + p g^{\mu\nu}, \tag{2.10}$$

with $h = 1 + \dfrac{e+p}{\rho}$ being the specific enthalpy, e being the internal energy density, and p being the pressure. The source term on the right-hand side of Equation (2.7), $-G^\mu$, is the four-momentum exchange between the fluid and the neutrinos.

Equations (2.5)–(2.7) are an open system. To close the system, an EOS is needed, which gives the pressure p, i.e., $p = p(\rho, e, Y_e)$ or $p = p(\rho, T, Y_e)$. The source terms, $-G^\mu$ and $-m_{\rm B}Q_L$, depend on the neutrino distribution functions and the thermodynamic properties of the stellar fluid. We will discuss these later.

2.2.2 General Relativistic 3+1 Hydrodynamics Equations

We begin with the 3+1 slicing of spacetime form of the hydrodynamics equations. The fluid four-velocity can be expressed as

$$u^\mu = W(n^\mu + v^\mu), \tag{2.11}$$

where $W = -n_\mu u^\mu$ is the Lorentz factor, $v^\mu = (\gamma^\mu_\nu\, u^\nu)/W$ is the fluid three-velocity, u_μ provide timelike projection, and γ^μ_ν provide spacelike projection. There is a corresponding spacelike hypersurface to which u^μ is the unit timelike normal. And the timelike basis elements defined by u^μ give an orthonormal frame of reference in which the inertial observer instantaneously comoving with the fluid. This observer is the generalized Lagrangian observer. Then, we can rewrite the general relativistic hydrodynamics equations given by Equation (2.5) - (2.7).

The mass conservation equation, Equation (2.5), is now expressed as

$$\frac{1}{\alpha\sqrt{\gamma}}\left[\partial_t(\sqrt{\gamma}D)+\partial_i\left(\sqrt{\gamma}D\left[\alpha v^i-\beta^i\right]\right)\right]=0, \tag{2.12}$$

where $D=W\rho$, and v^i is the fluid three-velocity.

The lepton number conservation equation, Equation (2.6), becomes

$$\frac{1}{\alpha\sqrt{\gamma}}\left[\partial_t\left(\sqrt{\gamma}DY_e\right)+\partial_i\left(\sqrt{\gamma}DY_e\left[\alpha v^i-\beta^i\right]\right)\right]=-m_{\mathrm{B}}Q_L. \tag{2.13}$$

The normal and tangential projections of Equation (2.7) relative to Σ_t give the energy and momentum conservation equations, which are

$$\begin{aligned}&\frac{1}{\alpha\sqrt{\gamma}}\left[\partial_t\left(\sqrt{\gamma}\tau_{\text{fluid}}\right)+\partial_i\left(\sqrt{\gamma}\left[\alpha\left(S^i-Dv^i\right)-\tau_{\text{fluid}}\beta^i\right]\right)\right]\\&=\frac{1}{\alpha}\left[\alpha S^{ik}K_{ik}-S^i\partial_i\alpha\right]+n_\mu G^\mu,\end{aligned} \tag{2.14}$$

for the energy, where $\tau_{\text{fluid}}=E-D$, $E=\rho\,h\,W^2-p$, $S^i=\rho hW^2v^i$, and $S^{i\,k}=\rho hW^2v^iv^k+p\,\gamma^{i\,k}$, and $K_{i\,k}$ are the components of the extrinsic curvature, and

$$\begin{aligned}&\frac{1}{\alpha\sqrt{\gamma}}\left[\partial_t\left(\sqrt{\gamma}S_j\right)+\partial_i\left(\sqrt{\gamma}\left[\alpha S^i_j-\beta^iS_j\right]\right)\right]\\&\quad=\frac{1}{\alpha}\left[S_i\partial_j\beta^i+\frac{1}{2}\alpha S^{ik}\partial_j\gamma_{ik}-E\partial_j\alpha\right]-\gamma_{j\mu}G^\mu,\end{aligned} \tag{2.15}$$

for the momentum.

2.2.3 Newtonian Hydrodynamics Equations

If a CCSN model includes the full PNS with a realistic nuclear EOS and approximate general relativistic gravity, it can simulate the onset of PNS collapse to a black hole, if it collapses to a black hole. In such a model, Newtonian hydrodynamic is a reasonable approximation. It makes Newtonian hydrodynamic a good starting point for a CCSN simulation code development. As a starting step, we restrict ourselves

in this dissertation work to the Newtonian limit and the basic Euler equations, and neglect physics such as magnetic fields or nuclear burning. First, expand W to $\mathcal{O}(v^2)$ such that

$$W = \frac{1}{\sqrt{1-v^2}} = 1 + \frac{v^2}{2} + \mathcal{O}(v^4), \tag{2.16}$$

and in Newtonian approximation $v \to 0$, $W = 1$. Newtonian limit also assumes a weak gravitational field, and the field is near static. These lead to

$$\beta_i = 0, \quad \alpha = 1. \tag{2.17}$$

Consequently, $D = \rho$ and Equations (2.12)-(2.15) can be rewritten as

$$\frac{\partial \rho}{\partial t} + \frac{1}{\sqrt{\gamma}}\partial_i(\sqrt{\gamma}\rho v^i) = 0, \tag{2.18}$$

$$\frac{\partial(\rho Y_e)}{\partial t} + \frac{1}{\sqrt{\gamma}}\partial_i\left(\sqrt{\gamma}\rho Y_e v^i\right) = -m_{\rm B} Q_L, \tag{2.19}$$

$$\frac{\partial e_t}{\partial t} + \frac{1}{\sqrt{\gamma}}\,\partial_i\big(\,\sqrt{\gamma}\,[\,e_t + p\,]\,v^i\,\big) = -\rho\, v^i\,\partial_i\Phi - Q_{\rm E}, \tag{2.20}$$

$$\frac{\partial(\rho\, v_j)}{\partial t} + \frac{1}{\sqrt{\gamma}}\,\partial_i\big(\,\sqrt{\gamma}\,\Pi^i{}_j\,\big) = \frac{1}{2}\,\Pi^{ik}\,\partial_j\gamma_{ik} - \rho\,\partial_j\Phi - Q_{{\rm M}j}, \tag{2.21}$$

where $e_t = e + \rho v^i v_i/2$ is the total fluid energy density, Φ is the gravitational potential, which in Newtonian gravity is related to the mass density ρ by the Poisson equation,

$$\frac{1}{\sqrt{\gamma}}\partial_i\left(\sqrt{\gamma}\,\gamma^{ij}\partial_j\Phi\right) = 4\pi G\rho, \tag{2.22}$$

$-\rho\,\partial_j\Phi$ and $-\rho\,v^i\,\partial_i\Phi$ are gravity sources, $\Pi^i{}_j = \rho\,v^i\,v_j + p\,\delta^i{}_j$ the fluid stress tensor, and $\frac{1}{2}\,\Pi^{ik}\,\partial_j\gamma_{ik}$ are geometry sources. The other source terms $(Q_L, Q^i_{\rm M}, Q_{\rm E})$ modeling lepton and four-momentum exchange introduced by neutrino-matter interaction will be discussed in detail in Section 2.4.3.

In this dissertation work, the Flash-X `Spark` (Couch et al., 2021) hydrodynamics code solves the Newtonian hydrodynamics equations. A description of the numerical solver is presented in Section 5.3.

2.3 Neutrino Kinetics

Now we move on to the neutrino kinetic equation, which is coupled with the hydrodynamics. Modelers must choose momentum coordinates. A typical choice is the inertial frame of reference that is instantaneously comoving with the fluid (Mihalas and Mihalas, 1984). In this frame, neutrino–matter interactions are most naturally and easily described. While the description of neutrino–matter interactions is simplified, additional terms that correspond to relativistic angular aberration and Doppler shift are introduced. Special care must be taken to address the additional terms and conservation.

2.3.1 General Relativistic Boltzmann Equation

When the neutrino mean free paths exceed the scale of the PNS, a kinetic description of the neutrinos is required. Because the neutrinos are not well described as a component of the fluid by then. Such a description would supply the neutrino distribution functions f for each species of neutrinos at each phase-space point:

$$dn = f d\boldsymbol{x} d\boldsymbol{p}. \tag{2.23}$$

Here dn is the number of neutrinos (at time t) at space point $\boldsymbol{x}$ in a differential volume element $d\boldsymbol{x}$, with momentum $\boldsymbol{p}$ in a momentum interval $d\boldsymbol{p}$, and the

distribution function f gives the density of such identical neutrinos per phase-space volume (Pomraning, 2005).

The Boltzmann equation gives the equation for the distribution function. Following Cardall and Mezzacappa (2003), it is derived using the Liouville operator L such that

$$L[f] = \mathcal{C}[f], \tag{2.24}$$

which describes the equation of the flow defined by the neutrino trajectories in phase space. The Liouville operator is given by

$$L = p^{\hat{\mu}}\, \mathcal{L}^{\mu}{}_{\hat{\mu}}\, \frac{\partial}{\partial x^{\mu}} - \Gamma^{\hat{\imath}}{}_{\hat{\nu}\hat{\rho}}\, p^{\hat{\nu}}\, p^{\hat{\rho}}\, \frac{\partial}{\partial p^{\hat{\imath}}}, \tag{2.25}$$

where $p^{\hat{\mu}}$ is the neutrino four-momentum components measured by a fluid-comoving observer, p^{μ} is the neutrino four-momentum components in the coordinate basis, $p^{\mu} = \mathcal{L}^{\mu}{}_{\hat{\mu}}\, p^{\hat{\mu}}$, $\mathcal{L}^{\mu}{}_{\hat{\mu}}$ is the inverse transformation of $\mathcal{L}^{\hat{\mu}}{}_{\mu}$. $\mathcal{L}^{\hat{\mu}}{}_{\mu}$ is a composite transformation. It first takes from the coordinate basis to the orthonormal frame of the Eulerian observer at rest with respect to the laboratory, then from the Eulerian frame to the comoving frame via a Lorentz transformation.

The Ricci rotation coefficients, $\Gamma^{\hat{\imath}}{}_{\hat{\nu}\hat{\rho}}$, are defined as (Cardall et al., 2013)

$$\Gamma^{\hat{\rho}}{}_{\hat{\nu}\hat{\mu}} = \mathcal{L}^{\hat{\rho}}{}_{\nu} \mathcal{L}^{\mu}{}_{\hat{\mu}} \nabla_{\mu} \mathcal{L}^{\nu}{}_{\hat{\nu}}. \tag{2.26}$$

The right-hand side $\mathcal{C}[f]$ denotes the collision term. It describes the neutrino-matter interactions and depends on the distribution function f. Because of the comoving momentum coordinates we chose, the collision term $\mathcal{C}[f]$ is relative simple. We will present a detailed discussion of the collision term in section 2.4.

A manifestly number conservative reformulation of the Boltzmann equation was given by Cardall and Mezzacappa (2003). It reads

$$\begin{aligned}
&\frac{1}{\sqrt{-g}}\frac{\partial}{\partial x^{\mu}}\left(\sqrt{-g}\mathcal{L}^{\mu}{}_{\hat{\mu}}p^{\hat{\mu}}f\right) \\
&\quad - E(\mathbf{p})\left\|\det\left[\frac{\partial \mathbf{p}}{\partial \mathbf{u}}\right]\right\|^{-1}\frac{\partial}{\partial u^{\hat{\imath}}}\left(\frac{1}{E(\mathbf{p})}\left\|\det\left[\frac{\partial \mathbf{p}}{\partial \mathbf{u}}\right]\right\|\Gamma^{\hat{\jmath}}{}_{\hat{\nu}\hat{\rho}}p^{\hat{\nu}}p^{\hat{\rho}}\frac{\partial u^{\hat{\imath}}}{\partial p^{\hat{\jmath}}}f\right) \\
&= \mathcal{C}[f],
\end{aligned} \tag{2.27}$$

where $E = \|\mathbf{p}\|/c$, and $\mu^{\hat{\imath}}$ is the basis in the comoving frame of the fluid four-velocity. Similarly, a four-momentum conservative formulation reads

$$\begin{aligned}
&\frac{1}{\sqrt{-g}}\frac{\partial}{\partial x^{\nu}}\left(\sqrt{-g}T^{\mu\nu}\right) \\
&- E(\mathbf{p})\left\|\det\left[\frac{\partial \mathbf{p}}{\partial \mathbf{u}}\right]\right\|^{-1}\frac{\partial}{\partial u^{\hat{\imath}}}\left(\frac{1}{E(\mathbf{p})}\left\|\det\left[\frac{\partial \mathbf{p}}{\partial \mathbf{u}}\right]\right\|\Gamma^{\hat{\jmath}}{}_{\hat{\nu}\hat{\rho}}p^{\hat{\rho}}\frac{\partial u^{\hat{\imath}}}{\partial p^{\hat{\jmath}}}\mathcal{L}^{\hat{\nu}}{}_{\nu}T^{\mu\nu}\right) \\
&= -\Gamma^{\mu}{}_{\nu\rho}T^{\nu\rho} + \mathcal{L}^{\mu}{}_{\hat{\mu}}p^{\hat{\mu}}\mathcal{C}[f],
\end{aligned} \tag{2.28}$$

where

$$T^{\mu\nu} \equiv \mathcal{L}^{\mu}{}_{\hat{\mu}}\mathcal{L}^{\nu}{}_{\hat{\nu}}p^{\hat{\mu}}p^{\hat{\nu}}f, \tag{2.29}$$

is the specific neutrino stress-energy tensor.

2.3.2 General Relativistic Moment Equations

Because solving the Boltzmann equation with sufficient phase-space resolution is expensive, most supernova models solve approximate equations for angular moments of the distribution function. In this moments approach, a finite number of angular moments are evolved, and the hierarchy of moment equations is closed by a closure procedure that relates higher-order moments to the evolved lower-order moments.

The first few angular moments, or spectral moments, of the distribution function f are

$$\mathcal{N}^{\mu} = \frac{1}{4\pi} \int_{\mathbb{S}^2} f \, p^{\mu} \, \frac{d\boldsymbol{\omega}}{\varepsilon}, \tag{2.30}$$

$$\mathcal{T}^{\mu\nu}_{\mathrm{Rad}} = \frac{1}{4\pi} \int_{\mathbb{S}^2} f \, p^{\mu} \, p^{\nu} \, \frac{d\boldsymbol{\omega}}{\varepsilon}, \tag{2.31}$$

$$\mathcal{Q}^{\mu\nu\rho}_{\mathrm{Rad}} = \frac{1}{4\pi} \int_{\mathbb{S}^2} f \, p^{\mu} \, p^{\nu} \, p^{\rho} \, \frac{d\boldsymbol{\omega}}{\varepsilon}, \tag{2.32}$$

where

$$d\boldsymbol{\omega} = \sin\vartheta d\vartheta d\varphi, \tag{2.33}$$

denotes the integral over the sphere of momentum space:

$$\mathbb{S}^2 = \{\omega \in (\vartheta, \varphi) \mid \vartheta \in [0, \pi], \varphi \in [0, 2\pi)\}, \tag{2.34}$$

where ϑ and φ are momentum-space angular coordinates. The four-current density is

$$N^{\mu} = 4\pi \int_0^{\infty} \mathcal{N}^{\mu} \varepsilon^2 d\varepsilon, \tag{2.35}$$

with ε the particle energy measured by an observer comoving with the fluid. The stress-energy tensor is

$$T^{\mu\nu} = 4\pi \int_0^{\infty} \mathcal{T}^{\mu\nu}_{\mathrm{Rad}} \varepsilon^2 d\varepsilon, \tag{2.36}$$

and

$$Q^{\mu\nu\rho} = 4\pi \int_0^{\infty} \mathcal{Q}^{\mu\nu\rho}_{\mathrm{Rad}} \varepsilon^2 d\varepsilon, \tag{2.37}$$

is the rank three tensor, which is also referred to as the tensor of fluxes, or heat flux tensor.

If the moment system is truncated at the zeroth moment equation, it results in the flux-limited diffusion (FLD) method. FLD for neutrino transport was first proposed by Wilson et al. (1975) and implemented by Bruenn et al. (1978). Similarly, if the system is truncated at the first moment equation, the approximate method is the so-called two-moment method, first proposed by Anderson and Spiegel (1972), and later studied by Thorne (1981) and Cernohorsky and Van Weert (1992). There are also higher-order moment methods, such as described in Yueh and Buchler (1977). `thornado` (Endeve et al., 2022a; Endeve et al., 2022b) currently employs the two-moment method and is used in this dissertation work.

Two-Moment Model

In the two-moment model, the evolved variables are the spectral neutrino number density, energy density, and three-momentum density in a coupled manner. The evolution equation for the spectral neutrino number density can be obtained by integrating Equation (2.27) over $\mathbb{S}^2$ and multiplying by a factor $\frac{1}{4\pi\varepsilon}$:

$$\nabla_\nu \mathcal{N}^\nu - \frac{1}{\varepsilon^2}\frac{\partial}{\partial\varepsilon}\left(\varepsilon^2 \mathcal{T}^{\mu\nu}\nabla_\mu u_\nu\right) = \frac{1}{4\pi}\int_{\mathbb{S}^2} \mathcal{C}[f]\frac{d\boldsymbol{\omega}}{\varepsilon}. \tag{2.38}$$

Integrating over energy leads to the balance equation, whose right-hand side leads to lepton exchange sources and sinks due to neutrino–matter interactions.

In a similar manner, the evolution equation for the neutrino four-momentum density can be obtained by integrating Equation (2.28) over $\mathbb{S}^2$ and multiplying by a factor $\frac{1}{4\pi\varepsilon}$:

$$\nabla_\nu \mathcal{T}^{\mu\nu} - \frac{1}{\varepsilon^2}\frac{\partial}{\partial\varepsilon}\left(\varepsilon^2 \mathcal{Q}^{\mu\nu\rho}\nabla_\nu u_\rho\right) = \frac{1}{4\pi}\int_{\mathbb{S}^2} \mathcal{C}[f]p^\mu\frac{d\boldsymbol{\omega}}{\varepsilon}. \tag{2.39}$$

Integrating over energy gives rise to the balance equation whose right-hand side describes the four-momentum exchange with the fluid. We will present a more detailed discussion about the source terms in Section 2.4.3.

2.3.3 General Relativistic 3+1 Moment Equations

In the 3+1 approach, Eulerian decompositions are natural to use. It also simplifies terms appearing in the moment equations. Moreover, Eulerian number density, energy density, and three-momentum density should be conserved. These make Eulerian decomposition preferred when deriving evolution equations for modeling neutrino transport.

Before giving the Eulerian evolution equations, we define primitive angular moments of the distribution function as

$$\left\{ \mathcal{D}, \mathcal{I}^{\mu}, \mathcal{K}^{\mu\nu}, \mathcal{L}^{\mu\nu\rho} \right\}(\varepsilon, \boldsymbol{x}, t) = \frac{1}{4\pi} \int_{\mathbb{S}^2} f(\boldsymbol{\omega}, \varepsilon, \boldsymbol{x}, t) \left\{ 1, \ell^{\mu}, \ell^{\mu}\ell^{\nu}, \ell^{\mu}\ell^{\nu}\ell^{\rho} \right\} d\boldsymbol{\omega}, \tag{2.40}$$

where $\boldsymbol{x}$ are the spatial coordinates,

$$\ell_{\mu} p^{\mu} = \varepsilon(\ell_{\mu} u^{\mu} + \ell_{\mu}\ell^{\mu}) = \varepsilon, \tag{2.41}$$

with $\ell_{\mu}\ell^{\mu} = 1$, $p^{\mu} = \varepsilon(u^{\mu} + \ell^{\mu})$. The zeroth and first moments $\mathcal{D}$ and $\mathcal{I}^{\mu}$ are the spectral number density and number flux density, respectively, measured by a Lagrangian (comoving) observer. The second and third moments $\mathcal{K}^{\mu\nu}$ and $\mathcal{L}^{\mu\nu\rho}$ are rank-two and rank-three tensors of fluxes.

Eulerian Decompositions

First, the Eulerian energy density, momentum density, and stress $\{\mathcal{E}, \mathcal{F}^{\mu}, \mathcal{S}^{\mu\nu}\}$ can be expressed in terms of the corresponding Lagrangian quantities $\left\{\mathcal{J}, \mathcal{H}^{\mu}, \hat{\mathcal{K}}^{\mu\nu}\right\}$

as (Cardall et al., 2013)

$$\mathcal{E} = W^2\mathcal{J} + 2Wv_\mu\mathcal{H}^\mu + v_\mu v_\nu\hat{\mathcal{K}}^{\mu\nu}, \tag{2.42}$$

$$\mathcal{F}^\mu = Wv^\mu\left(W\mathcal{J} + v_\nu\mathcal{H}^\nu\right) + \left[\delta^\mu{}_\rho - n^\mu v_\rho\right]\left(W\mathcal{H}^\rho + v_\nu\hat{\mathcal{K}}^{\nu\rho}\right), \tag{2.43}$$

$$\begin{aligned}\mathcal{S}^{\mu\nu} = {} & W^2\mathcal{J}v^\mu v^\nu + Wv^\nu\left[\delta^\mu{}_\rho - n^\mu v_\rho\right]\mathcal{H}^\rho + Wv^\mu\left[\delta^\nu{}_\sigma - n^\nu v_\sigma\right]\mathcal{H}^\sigma \\ & + \left[\delta^\mu{}_\rho - n^\mu v_\rho\right]\left[\delta^\nu{}_\sigma - n^\nu v_\sigma\right]\hat{\mathcal{K}}^{\rho\sigma},\end{aligned} \tag{2.44}$$

where $\left\{\mathcal{J}, \mathcal{H}^\mu, \hat{\mathcal{K}}^{ij}\right\}$ are expressed by primitive angular moments as

$$\left\{\,\mathcal{J}, \mathcal{H}^i, \hat{\mathcal{K}}^{ij}\,\right\} = \varepsilon\left\{\,\mathcal{D}, \mathcal{I}^i, \mathcal{K}^{ij}\,\right\}. \tag{2.45}$$

The Eulerian decomposition of the stress-energy tensor is

$$\mathcal{T}^{\mu\nu} = \mathcal{E}n^\mu n^\nu + \mathcal{F}^\mu n^\nu + n^\mu\mathcal{F}^\nu + \mathcal{S}^{\mu\nu}. \tag{2.46}$$

Then the Eulerian two-moment evolution equations can be obtained by projecting Equation (2.39) onto the four-velocity of the Eulerian observer, such that contracting $-n_\mu$ with Equation (2.39) and noting that

$$-n_\mu\mathcal{T}^{\mu\nu} = \mathcal{E}n^\nu + \mathcal{F}^\nu \tag{2.47}$$

gives

$$\begin{aligned}&\frac{1}{\alpha\sqrt{\gamma}}\left[\partial_t(\sqrt{\gamma}\mathcal{E}) + \partial_i\left(\sqrt{\gamma}\left[\alpha\mathcal{F}^i - \beta^i\mathcal{E}\right]\right)\right] - \frac{1}{\varepsilon^2}\frac{\partial}{\partial\varepsilon}\left(\varepsilon^2\left(-n_\mu\right)\mathcal{Q}^{\mu\nu\rho}\nabla_\nu u_\rho\right) \\ &= \frac{1}{\alpha}\left[\alpha\mathcal{S}^{ij}\mathrm{K}_{ij} - \mathcal{F}^i\partial_i\alpha\right] + \frac{W}{4\pi}\int_{\mathbb{S}^2}\mathcal{C}(f)d\boldsymbol{\omega} + \frac{v^j}{4\pi}\int_{\mathbb{S}^2}\mathcal{C}(f)\ell_j d\boldsymbol{\omega},\end{aligned} \tag{2.48}$$

and contracting $\gamma_{\mu\nu}$ with Equation (2.39), and noting that

$$\gamma_{j\mu}\mathcal{T}^{\mu\nu} = \mathcal{F}_j n^\nu + \mathcal{S}_j^\nu, \tag{2.49}$$

gives

$$\frac{1}{\alpha\sqrt{\gamma}}\left[\partial_t\left(\sqrt{\gamma}\mathcal{F}_j\right)+\partial_i\left(\sqrt{\gamma}\left[\alpha\mathcal{S}^i{}_j-\beta^i\mathcal{F}_j\right]\right)\right]-\frac{1}{\varepsilon^2}\frac{\partial}{\partial\varepsilon}\left(\varepsilon^2\gamma_{j\mu}\mathcal{Q}^{\mu\nu\rho}\nabla_\nu u_\rho\right)$$
$$=\frac{1}{\alpha}\left[\mathcal{F}_i\partial_j\beta^i+\frac{1}{2}\alpha\mathcal{S}^{ik}\partial_j\gamma_{ik}-\mathcal{E}\partial_j\alpha\right]+\frac{1}{4\pi}\int_{\mathbb{S}^2}\mathcal{C}(f)\ell_j d\boldsymbol{\omega}+\frac{Wv_j}{4\pi}\int_{\mathbb{S}^2}\mathcal{C}(f)d\boldsymbol{\omega}. \tag{2.50}$$

In `thornado`, equations for number density and number flux density are solved (Endeve et al., 2022b). These can be obtained from Equation (2.38) or by contraction of Equation (2.39) with $-u_\mu/\varepsilon$:

$$\frac{1}{\alpha\sqrt{\gamma}}\left[\partial_t\left(\sqrt{\gamma}\left[W\mathcal{D}+v^i\mathcal{I}_i\right]\right)+\partial_i\left(\sqrt{\gamma}\left[\alpha\mathcal{I}^i+\left(\alpha v^i-\beta^i\right)W\mathcal{D}\right]\right)\right]$$
$$-\frac{1}{\varepsilon^2}\frac{\partial}{\partial\varepsilon}\left(\varepsilon^2\mathcal{T}^{\mu\nu}\nabla_\mu u_\nu\right)=\frac{1}{4\pi}\int_{\mathbb{S}^2}\mathcal{C}(f)\frac{d\omega}{\varepsilon}, \tag{2.51}$$

and contraction of Equation (2.39) with $-h_{j\mu}/\varepsilon$:

$$\frac{1}{\alpha\sqrt{\gamma}}\left[\partial_t\left(\sqrt{\gamma}\left[W\mathcal{I}_j+v^i\widehat{\mathcal{K}_{ij}}\right]\right)+\partial_i\left(\sqrt{\gamma}\left[\alpha\widehat{\mathcal{K}^i}_j+\left(\alpha v^i-\beta^i\right)W\mathcal{I}_j\right]\right)\right]$$
$$-\frac{1}{\varepsilon^2}\frac{\partial}{\partial\varepsilon}\left(\varepsilon^2 h_{j\mu}\widehat{\mathcal{Q}}^{\mu\nu\rho}\nabla_\nu u_\rho\right)=\frac{1}{2}\widehat{\mathcal{T}}^{\mu\nu}\partial_j g_{\mu\nu}+\frac{1}{\varepsilon}\widehat{\mathcal{Q}}^{\mu\nu}_j\nabla_\nu u_\mu-\mathcal{N}^\nu\partial_\nu u_j$$
$$+\frac{1}{4\pi}\int_{\mathbb{S}^2}\mathcal{C}(f)\ell_j\frac{d\omega}{\varepsilon}, \tag{2.52}$$

correspondingly.

2.3.4 $\mathcal{O}(v/c)$ Moment Equations

In flat space ($\alpha=1,\beta^i=0$) and dropping terms that depend on v^2 and higher, Equation (2.51) for the Eulerian number density becomes (Mezzacappa et al., 2020a;

Endeve et al., 2022b)

$$\partial_t \left(\mathcal{D} + v^i \mathcal{I}_i\right) + \frac{1}{\sqrt{\gamma}} \partial_i \left(\sqrt{\gamma} \left[\mathcal{I}^i + v^i \mathcal{D}\right]\right) - \frac{1}{\varepsilon^2} \frac{\partial}{\partial \varepsilon} \left(\varepsilon^3 \left[\mathcal{I}_i \partial_t v^i + \mathcal{K}^i{}_j \nabla_i v^j\right]\right)$$
$$= \frac{1}{4\pi} \int_{\mathbb{S}^2} \mathcal{C}(f) \frac{d\boldsymbol{\omega}}{\varepsilon}, \tag{2.53}$$

and Equation (2.52) for the number flux becomes

$$\partial_t \left(\mathcal{I}_j + v^i \mathcal{K}_{ij}\right) + \frac{1}{\sqrt{\gamma}} \partial_i \left(\sqrt{\gamma} \left[\mathcal{K}^i_j + v^i \mathcal{I}_j\right]\right) - \frac{1}{\varepsilon^2} \frac{\partial}{\partial \varepsilon} \left(\varepsilon^3 \left[\mathcal{K}_{jk} \partial_t v^k + \mathcal{L}^i_{kj} \nabla_i v^k\right]\right)$$
$$- \frac{1}{2} \left(\mathcal{K}^{ik} + \mathcal{I}^i v^k + v^i \mathcal{I}^k\right) \partial_j \gamma_{ik} - \left(\mathcal{K}_{jk} \partial_t v^k + \mathcal{L}^i_{kj} \nabla_i v^k\right) + \left(\mathcal{D} \partial_t v_j + \mathcal{I}^i \partial_i v_j\right)$$
$$= \frac{1}{4\pi} \int_{\mathbb{S}^2} \mathcal{C}(f) \ell_j \frac{d\boldsymbol{\omega}}{\varepsilon}. \tag{2.54}$$

In $\mathcal{O}(v/c)$ limit, all general relativistic effects in the moment equations are neglected, and special relativistic effects are kept to $\mathcal{O}(v/c)$ limit. In this limit, blue and red shift of neutrino energies are left out, and special relativistic Doppler shift of neutrino energies to $\mathcal{O}(v/c)$ are included. In CCSN simulation, $\mathcal{O}(v/c)$ limit is acceptable for low-mass progenitors, and is a common starting point. Some CCSN simulation codes in this limit include Fornax, Aenus-Alcar, Prometheus-Vertex, CoCoNut-Vertex, and others.

2.3.5 $\mathcal{O}(1)$ Moment Equations

We can further simplify the moment equations by taking $v = 0$ to arrive at the $\mathcal{O}(1)$ limit. In this limit, the evolution equations for the Eulerian number density and number flux, Equation (2.53) and (2.54) become

$$\partial_t \mathcal{D} + \frac{1}{\sqrt{\gamma}} \partial_i \left(\sqrt{\gamma} \mathcal{I}^i\right) = \frac{1}{4\pi} \int_{\mathbb{S}^2} \mathcal{C}(f) \frac{d\boldsymbol{\omega}}{\varepsilon}, \tag{2.55}$$

$$\partial_t \mathcal{I}_j + \frac{1}{\sqrt{\gamma}} \partial_i \left(\sqrt{\gamma} \mathcal{K}^i_j\right) - \frac{1}{2} \mathcal{K}^{ik} \partial_j \gamma_{ik} = \frac{1}{4\pi} \int_{\mathbb{S}^2} \mathcal{C}(f) \ell_j \frac{d\boldsymbol{\omega}}{\varepsilon}. \tag{2.56}$$

In $\mathcal{O}(1)$ limit, all relativistic effects in the moment equations are neglected. These effects include Doppler shift of neutrino energies, blue and red shift of neutrino energies, angular aberration of neutrino propagation and others. We know that the CCSN environment is a general relativistic environment, and $\mathcal{O}(1)$ (Newtonian) limit is not a good approximation Bruenn et al. (2001): using $\mathcal{O}(1)$ limit in CCSN simulation leads to dramatic differences in the PNS generated after bounce, the dynamics, and neutrino radiation Bruenn et al. (2001); neutrino luminosities and root mean square energies is lower in $\mathcal{O}(1)$ limit than in the general relativistic case.

2.4 Neutrino Interactions

What makes neutrinos important to CCSN are the weak interactions between the neutrinos and the matter. It has been well addressed that the impacts of neutrino interactions on CCSN simulation include: (1), the impact of the addition of new weak interaction channels (Bruenn, 1985; Hannestad and Raffelt, 1998; Buras et al., 2003; Lentz et al., 2012); (2), the impact of improved treatments (Burrows and Sawyer, 1998; Reddy et al., 1998; Müller et al., 2012; Langanke et al., 2003; Hix et al., 2003; Bollig et al., 2017; Burrows et al., 2018; Just et al., 2018; Kotake et al., 2018); (3), the impact of uncertainties in the interaction rates (Melson et al., 2015b). A more comprehensive review for neutrino interactions in CCSN simulation can be found in Mezzacappa et al. (2020a). Fortunately, we can have the main processes represented by a standard collision term and start with the industry standard Bruenn 1985 opacity set.

This section focuses on the collision term $\mathcal{C}(f)$. We start with the collision term in the Boltzmann equation, then move on to the corresponding terms in the moment equations, and end with how the collision terms couple the transport equations with the hydrodynamics equations.

2.4.1 Collision Term in the Boltzmann Equation

The collision term in Boltzmann equation can be written as the sum of four terms that correspond to the main interactions – emission and absorption, scattering, and pair production. In this dissertation, we focus on the neutrino interactions given in Bruenn (1985) and write:

$$\mathcal{C}(f_s) = \mathcal{C}_{\text{EA}}(f_s) + \mathcal{C}_{\text{Iso}}(f_s) + \mathcal{C}_{\text{NES}}(f_s) + \mathcal{C}_{\text{Pair}}(f_s, \bar{f}_s), \tag{2.57}$$

where lower index s denotes neutrino species, $\bar{f}_s$ is the distribution function for antiparticle of neutrino s, $\mathcal{C}_{\text{EA}}(f_s)$ corresponds to neutrino emission and absorption, $\mathcal{C}_{\text{Iso}}(f_s)$ corresponds to iso-energetic scattering on nucleons and nuclei, $\mathcal{C}_{\text{NES}}(f_s)$ corresponds to neutrino-electron scattering, and $\mathcal{C}_{\text{Pair}}(f_s, \bar{f}_s)$ corresponds to pair production and annihilation. These four collision terms represent four categories of neutrino–matter interactions classified by mathematics form, and not necessary to be bounded to the physics.

Emission and Absorption

The collision term for neutrino emission and absorption, $\mathcal{C}_{\text{EA}}(f)$, can be written as

$$\mathcal{C}_{\text{EA}}(f) = (1 - f)\,\eta - \chi f, \tag{2.58}$$

where η and χ are the emissivity and absorption opacity. η and χ depend on the neutrino energy ε, and are assumed to be isotropic in the momentum-space angle. $(1 - f)$ is the blocking factor. It is included to account for the Fermi-Dirac statistics of neutrinos, which are fermions; i.e. the Pauli exclusion principle. Equation (2.58) can be rewritten as

$$\mathcal{C}_{\text{EA}}(f) = \tilde{\chi}(f_0 - f), \tag{2.59}$$

with

$$\tilde{\chi} = (\eta + \chi), \tag{2.60}$$

which is the so-called stimulated absorption opacity, and

$$f_0 = \frac{\eta}{\tilde{\chi}},$$

is the equilibrium distribution.

Scattering

A general scattering term has the following form:

$$\begin{aligned}\mathcal{C}_{\text{Scat}}(f) = \Bigg\{ \big[1 - f\big] \int_{\mathbb{R}+} \int_{\mathbb{S}^2} \mathcal{R}^{\text{In}}_{\text{Scatt}}\big(\varepsilon, \varepsilon', \hat{\boldsymbol{n}}(\boldsymbol{\omega}) \cdot \hat{\boldsymbol{n}}(\boldsymbol{\omega}')\big) f(\varepsilon', \boldsymbol{\omega}')\, \varepsilon'^{\,2}\, d\boldsymbol{\omega}'\, d\varepsilon' \\ - f(\varepsilon, \boldsymbol{\omega}) \int_{\mathbb{R}+} \int_{\mathbb{S}^2} \mathcal{R}^{\text{Out}}_{\text{Scatt}}\big(\varepsilon, \varepsilon', \hat{\boldsymbol{n}}(\boldsymbol{\omega}) \cdot \hat{\boldsymbol{n}}(\boldsymbol{\omega}')\big) \big[1 - f(\varepsilon', \boldsymbol{\omega}')\big]\, \varepsilon'^{\,2}\, d\boldsymbol{\omega}'\, d\varepsilon' \Bigg\},\end{aligned} \tag{2.61}$$

with $\boldsymbol{\omega} = (\theta_p, \phi_p)$ is a point on the unit sphere given by the solid angle of neutrino momentum, i.e., $\boldsymbol{p} = (\varepsilon, \theta_p, \phi_p)$, and $\hat{\boldsymbol{n}}(\boldsymbol{\omega})$ the unit vector along $\boldsymbol{\omega}$, $\boldsymbol{n}(\boldsymbol{\omega}) \cdot \hat{\boldsymbol{n}}(\boldsymbol{\omega}')$ the cosine of the angle between the incident and emergent neutrino with energy ε and ε', respectively. And $\mathcal{R}^{\text{In/Out}}_{\text{Scatt}}$ are the scattering kernels, which also depend on the fluid thermal state. Note also the blocking factors in Equation (2.61), $(1 - f)$, which suppress scattering to high-occupancy regions of momentum-space. Both $\mathcal{C}_{\text{Iso}}$ and $\mathcal{C}_{\text{NES}}$ are examples of scattering kernels; i.e., $\mathcal{C}_{\text{Iso}}, \mathcal{C}_{\text{NES}} \in \mathcal{C}_{\text{Scat}}$.

For iso-energetic scattering, the scattering out energy and in energy are the same, i.e., $\varepsilon = \varepsilon'$, and

$$\mathcal{R}^{\text{In}}_{\text{Scatt}}\big(\varepsilon, \varepsilon', \hat{\boldsymbol{n}}(\boldsymbol{\omega}) \cdot \hat{\boldsymbol{n}}(\boldsymbol{\omega}')\big) = \mathcal{R}^{\text{Out}}_{\text{Scatt}}\big(\varepsilon, \varepsilon', \hat{\boldsymbol{n}}(\boldsymbol{\omega}) \cdot \hat{\boldsymbol{n}}(\boldsymbol{\omega}')\big). \tag{2.62}$$

Defining

$$\mathcal{R}^0_{\text{Iso}}(\varepsilon, \hat{\boldsymbol{n}}(\boldsymbol{\omega}) \cdot \hat{\boldsymbol{n}}(\boldsymbol{\omega}')) \equiv \delta(\varepsilon - \varepsilon')\, \mathcal{R}_{\text{Iso}}(\varepsilon, \varepsilon', \hat{\boldsymbol{n}}(\boldsymbol{\omega}) \cdot \hat{\boldsymbol{n}}(\boldsymbol{\omega}')), \tag{2.63}$$

$\mathcal{C}_{\text{Iso}}(f)$ can be written as

$$\mathcal{C}_{\text{Iso}}(f) = \varepsilon^2 \int_{\mathbb{S}^2} \mathcal{R}^0_{\text{Iso}}(\varepsilon, \hat{\boldsymbol{n}}(\boldsymbol{\omega}) \cdot \hat{\boldsymbol{n}}(\boldsymbol{\omega}'))\, [f(\varepsilon, \boldsymbol{\omega}') - f(\varepsilon, \boldsymbol{\omega})]\, d\boldsymbol{\omega}'. \tag{2.64}$$

Pair Production

The collision term for neutrino pair processes, $\mathcal{C}_{\text{Pair}}(f, \bar{f})$, is written as

$$\begin{aligned}\mathcal{C}_{\text{Pair}}(f, \bar{f}) = \Bigg[(1-f) \int_{\mathbb{R}^+} \int_{\mathbb{S}^2} \mathcal{R}^p_{\text{Pair}}(\hat{\boldsymbol{n}}(\boldsymbol{\omega}) \cdot \hat{\boldsymbol{n}}(\boldsymbol{\omega}'), \varepsilon, \varepsilon') \left(1 - \bar{f}(\boldsymbol{\omega}', \varepsilon')\right) d\boldsymbol{\omega}' dV_{\varepsilon'} \\ - f \int_{\mathbb{R}^+} \int_{\mathbb{S}^2} \mathcal{R}^a_{\text{Pair}}(\hat{\boldsymbol{n}}(\boldsymbol{\omega}) \cdot \hat{\boldsymbol{n}}(\boldsymbol{\omega}'), \varepsilon, \varepsilon')\, \bar{f}(\boldsymbol{\omega}', \varepsilon')\, d\boldsymbol{\omega}' dV_{\varepsilon'} \Bigg],\end{aligned} \tag{2.65}$$

where $\mathcal{R}^p_{\text{Pair}}$ and $\mathcal{R}^a_{\text{Pair}}$ are the neutrino-antineutrino pair production and annihilation kernels, respectively. The block factors in the production term are $(1-f)$ and $(1-\bar{f})$.

All the above — $\tilde{\chi}$, $\mathcal{R}^{\text{In/Out}}_{\text{Scatt}}$, and $\mathcal{R}^{p/a}_{\text{Pair}}$ — depend on the thermal state of the stellar fluid (e.g., ρ, T, and Y_e for NSE).

2.4.2 Collision Term in the Moment Equations

The collision terms in the moment equations (Equations (2.51) and (2.52)) require $\frac{1}{4\pi}\int_{\mathbb{S}^2} \mathcal{C}(f)\, \frac{d\boldsymbol{\omega}}{\varepsilon}$ and $\frac{1}{4\pi}\int_{\mathbb{S}^2} \mathcal{C}(f)\ell_i\, \frac{d\boldsymbol{\omega}}{\varepsilon}$. For example, the collision terms on the right-hand sides of $\mathcal{O}(v/c)$ moment equations, Equation (2.53) and (2.54), are

$$\frac{1}{4\pi}\int_{\mathbb{S}^2} \mathcal{C}(f)\frac{d\boldsymbol{\omega}}{\varepsilon}, \quad \text{and} \quad \frac{1}{4\pi}\int_{\mathbb{S}^2} \mathcal{C}(f)\ell_j\frac{d\boldsymbol{\omega}}{\varepsilon}, \tag{2.66}$$

respectively.

Legendre Expansion Using a Legendre expansion, any scattering/production/annihilation kernel can be written as

$$\mathcal{R}(\varepsilon, \varepsilon', \alpha) \simeq C_0 \Phi_0(\varepsilon, \varepsilon') + C_1 \Phi_1(\varepsilon, \varepsilon')\, \alpha, \tag{2.67}$$

with $\alpha = \hat{\boldsymbol{n}}(\boldsymbol{\omega}) \cdot \hat{\boldsymbol{n}}(\boldsymbol{\omega}')$. For $C_0 = 1$ and $C_1 = 1$, we have

$$\frac{1}{2} \int_{-1}^{1} \mathcal{R}(\varepsilon, \varepsilon', \alpha)\, d\alpha = \Phi_0(\varepsilon, \varepsilon'), \tag{2.68}$$

$$\frac{3}{2} \int_{-1}^{1} \mathcal{R}(\varepsilon, \varepsilon', \alpha) \alpha\, d\alpha = \Phi_1(\varepsilon, \varepsilon'), \tag{2.69}$$

$$\mathcal{R}(\varepsilon, \varepsilon', \alpha) = \Phi_0(\varepsilon, \varepsilon') + \Phi_1(\varepsilon, \varepsilon')\, \alpha. \tag{2.70}$$

Emission and Absorption

With Equation (2.59) and (2.60), the collision terms for neutrino emission and absorption in the moment equations are

$$\frac{1}{4\pi} \int_{\mathbb{S}^2} \mathcal{C}_{\text{EA}}(f) d\boldsymbol{\omega} = \tilde{\chi}(\mathcal{D}_0 - \mathcal{D}), \tag{2.71}$$

$$\frac{1}{4\pi} \int_{\mathbb{S}^2} \mathcal{C}_{\text{EA}}(f) \ell_i d\boldsymbol{\omega} = -\tilde{\chi} \mathcal{I}_i, \tag{2.72}$$

where $\mathcal{D}_0 = \frac{1}{4\pi} \int_{\mathbb{S}^2} f_0 d\boldsymbol{\omega}$ and $\frac{1}{4\pi} \int_{\mathbb{S}^2} f_0 \ell_i d\boldsymbol{\omega} = 0$ for the equilibrium distribution f_0.

Scattering

Using the Legendre expansion, Equation (2.70), in the scattering term $\mathcal{C}_{\text{Scat}}$, Equation (2.61), we have

$$\begin{aligned}
&\frac{1}{4\pi}\int_{\mathbb{S}^2}\mathcal{C}_{\text{Scat}}(f)\,d\boldsymbol{\omega}\\
&\quad=\big[1-\mathcal{D}(\varepsilon)\big]\int_{\mathbb{R}+}\Phi_0^{\text{In}}(\varepsilon,\varepsilon')\mathcal{D}(\varepsilon')dV_{\varepsilon'}-\mathcal{D}(\varepsilon)\int_{\mathbb{R}+}\Phi_0^{\text{Out}}(\varepsilon,\varepsilon')\left[1-\mathcal{D}(\varepsilon')\right]dV_{\varepsilon'}\\
&\qquad+\mathcal{I}_i(\varepsilon)\int_{\mathbb{R}+}\left[\Phi_1^{\text{Out}}(\varepsilon,\varepsilon')-\Phi_1^{\text{In}}(\varepsilon,\varepsilon')\right]\mathcal{I}^i(\varepsilon')\,dV_{\varepsilon'},
\end{aligned}\tag{2.73}$$

and

$$\begin{aligned}
&\frac{1}{4\pi}\int_{\mathbb{S}^2}\mathcal{C}_{\text{Scat}}(f)\,\ell_i\,d\boldsymbol{\omega}\\
&\quad=-\mathcal{I}_i(\varepsilon)\int_{\mathbb{R}+}\Phi_0^{\text{In}}(\varepsilon,\varepsilon')\,\mathcal{D}(\varepsilon')\,dV_{\varepsilon'}-\mathcal{I}_i(\varepsilon)\int_{\mathbb{R}+}\Phi_0^{\text{Out}}(\varepsilon,\varepsilon')\left[1-\mathcal{D}(\varepsilon')\right]dV_{\varepsilon'}\\
&\qquad+\frac{1}{3}\int_{\mathbb{R}+}\Phi_1^{\text{In}}(\varepsilon,\varepsilon')\,\mathcal{I}_i(\varepsilon')\,dV_{\varepsilon'}+\mathcal{K}_{ij}(\varepsilon)\int_{\mathbb{R}+}\left[\Phi_1^{\text{Out}}(\varepsilon,\varepsilon')-\Phi_1^{\text{In}}(\varepsilon,\varepsilon')\right]\mathcal{I}^j(\varepsilon')\,dV_{\varepsilon'}.
\end{aligned}\tag{2.74}$$

Isoenergetic Scattering For isoenergetic scattering,

$$\frac{1}{4\pi}\int_{\mathbb{S}^2}\mathcal{C}_{\text{Iso}}(f)d\boldsymbol{\omega}=0,\tag{2.75}$$

$$\frac{1}{4\pi}\int_{\mathbb{S}^2}\mathcal{C}_{\text{Iso}}(f)\ell_i d\boldsymbol{\omega}=-\mathcal{I}_i(\varepsilon)\int_{\mathbb{R}+}\Phi_{\text{Iso}\,0}^{\text{Out}}(\varepsilon,\varepsilon')\,dV_{\varepsilon'}+\frac{1}{3}\int_{\mathbb{R}+}\Phi_{\text{Iso}\,1}^{\text{In}}(\varepsilon,\varepsilon')\,\mathcal{I}_i(\varepsilon')\,dV_{\varepsilon'}.\tag{2.76}$$

Pair Production

Combining Equation (2.65) and Equation (2.70), the pair-production collision terms become

$$\begin{aligned}\frac{1}{4\pi}\int_{\mathbb{S}^2}\mathcal{C}_{\text{Pair}}(f)d\boldsymbol{\omega} =&\big[1-\mathcal{D}(\varepsilon)\big]\int_{\mathbb{R}+}\Phi_0^{\text{P}}(\varepsilon,\varepsilon')\left[1-\bar{\mathcal{D}}(\varepsilon')\right]dV_{\varepsilon'}\\&+\mathcal{I}_j(\varepsilon)\int_{\mathbb{R}+}\Phi_1^{\text{P}}(\varepsilon,\varepsilon')\,\bar{\mathcal{I}}^j(\varepsilon')\,dV_{\varepsilon'}\\&-\mathcal{D}(\varepsilon)\int_{\mathbb{R}+}\Phi_0^{\text{A}}(\varepsilon,\varepsilon')\,\bar{\mathcal{D}}(\varepsilon')\,dV_{\varepsilon'}-\mathcal{I}_j(\varepsilon)\int_{\mathbb{R}+}\Phi_1^{\text{A}}(\varepsilon,\varepsilon')\,\bar{\mathcal{I}}^j(\varepsilon')\,dV_{\varepsilon'},\end{aligned}\tag{2.77}$$

$$\begin{aligned}\frac{1}{4\pi}\int_{\mathbb{S}^2}\mathcal{C}_{\text{Pair}}(f)\ell_i d\boldsymbol{\omega} =&-\mathcal{I}_i(\varepsilon)\int_{\mathbb{R}+}\Phi_0^{\text{P}}(\varepsilon,\varepsilon')\left[1-\bar{\mathcal{D}}(\varepsilon')\right]dV_{\varepsilon'}\\&-\left[\frac{1}{3}\delta_{ij}-\mathcal{K}_{ij}(\varepsilon)\right]\int_{\mathbb{R}+}\Phi_1^{\text{P}}(\varepsilon,\varepsilon')\,\bar{\mathcal{I}}^j(\varepsilon')\,dV_{\varepsilon'}\\&-\mathcal{I}_i(\varepsilon)\int_{\mathbb{R}+}\Phi_0^{\text{A}}(\varepsilon,\varepsilon')\,\bar{\mathcal{D}}(\varepsilon')\,dV_{\varepsilon'}-\mathcal{K}_{ij}(\varepsilon)\int_{\mathbb{R}+}\Phi_1^{\text{A}}(\varepsilon,\varepsilon')\,\bar{\mathcal{I}}^j(\varepsilon')\,dV_{\varepsilon'}.\end{aligned}\tag{2.78}$$

2.4.3 Neutrino – Matter Coupling

Next, using conservation principles for lepton number, momentum, and energy, we can give explicit expressions of the source terms on the right-hand side of the hydrodynamic equations (Equations (2.19), (2.20) and (2.21)) in terms of the collision term. These terms are critical when developing a physics-preserving numerical approach for a hydrodynamics and radiation coupled system. We enforce these conservation laws in the algorithm for modeling neutrino-matter coupling in `thornado`.

Lepton Exchange

We consider electron neutrinos (ν_e) and antineutrinos ($\bar{\nu}_e$) as agents for lepton exchange. The Eulerian number density and number flux density are given by the integral of the spectral number density and spectral number flux over the neutrino

energy. Define the lepton number density and number flux as

$$\mathcal{N}_s = \mathcal{D}_s + \mathcal{I}_s v^i, \tag{2.79}$$

$$\left\{N_\nu, F_N^i\right\} = 4\pi \sum_{s=\nu_e,\bar{\nu}_e} g_s \int_{\mathbb{R}^+} \left\{\mathcal{N}_s, \mathcal{I}_s^i + \mathcal{D}_s v^i\right\} \varepsilon^2 d\varepsilon, \tag{2.80}$$

with g_s the corresponding lepton number; i.e. $g_s = 1$ for ν_e, and $g_s = -1$ for $\bar{\nu}_e$, where the index s indicates the neutrino species. With the hydrodynamics equation (Equation (2.19)), the radiation equations (Equations (2.53) and (2.54)), and $n_e = \frac{\rho Y_e}{M_B}$, to preserve total lepton number, we must have

$$\partial_t \left(n_\mathrm{e} + N_\nu\right) + \frac{1}{\sqrt{\gamma}} \partial_i \left(\sqrt{\gamma}\left[n_\mathrm{e} v^i + F_N^i\right]\right) = 0, \tag{2.81}$$

and

$$Q_L = \sum_{s=\nu_e,\bar{\nu}_e} g_s \int_{\mathbb{R}^+} \frac{1}{\varepsilon} \int_{\mathbb{S}^2} \mathcal{C}(f_s) d\boldsymbol{\omega} \varepsilon^2 d\varepsilon. \tag{2.82}$$

Energy and Momentum Exchange

Next, we consider energy and momentum conservation. The total neutrino energy density E, total momentum density F_E^i, and total stress tensor S^{ij} are defined as

$$\left\{E, F_E^i, S^{ij}\right\} = 4\pi \sum_{s=1}^{N_s} \int_{\mathbb{R}^+} \left\{\mathcal{E}_s, \mathcal{F}_s^i, \mathcal{S}_s^{ij}\right\} \varepsilon^2 d\varepsilon, \tag{2.83}$$

with N_s the total number of neutrino species included. With the hydrodynamics energy conservation equation (Equation (2.20)) and the radiation number density equation (Equation (2.53)), to preserve total energy, we must have

$$\partial_t \left(e_t + E\right) + \frac{1}{\sqrt{\gamma}} \partial_i \left(\sqrt{\gamma}\left[\left(e_t + p\right) v^i + {F_E}^i\right]\right) = -\rho v^i \partial_i \Phi, \tag{2.84}$$

and

$$Q_{\mathrm{E}} = 4\pi \sum_{s=1}^{N_s} \int_{\mathbb{R}^+} \left[\frac{1}{4\pi} \int_{\mathbb{S}^2} \mathcal{C}(f_s) d\boldsymbol{\omega} + \frac{v^j}{4\pi} \int_{\mathbb{S}^2} \mathcal{C}(f_s) \ell_j d\boldsymbol{\omega} \right] \varepsilon^2 d\varepsilon. \tag{2.85}$$

With the hydrodynamics momentum conservation equation (Equation (2.21)) and the radiation number flux equation (Equation (2.54)), to preserve total momentum, we must have

$$\partial_t \big(\rho v_j + F_{Ej} \big) + \frac{1}{\sqrt{\gamma}} \partial_i \big(\sqrt{\gamma} \, [\, \Pi^i{}_j + S^i{}_j \,] \big) = \frac{1}{2} \left(\Pi^{ik} + S^{ik} \right) \partial_j \gamma_{ik} - \rho \partial_j \Phi, \tag{2.86}$$

and

$$Q^i_{\mathrm{M}} = 4\pi \sum_{s=1}^{N_s} \int_{\mathbb{R}^+} \left[\frac{1}{4\pi} \int_{\mathbb{S}^2} \mathcal{C}(f_s) \ell^i \, d\boldsymbol{\omega} + \frac{v^i}{4\pi} \int_{\mathbb{S}^2} \mathcal{C}(f_s) d\boldsymbol{\omega} \right] \varepsilon^2 d\varepsilon. \tag{2.87}$$

2.5 Moment Realizability and Closure Problem

As we mentioned in Section 2.3.2, the two-moment models discussed above are not closed until a closure procedure is employed. This section focuses on the requirements of the closure procedure and algebraic closures. Many discussions in this section have been published in Chu et al. (2019a).

2.5.1 Moment Realizability

To be physically meaningful, the distribution function must satisfy the following inequality: $f \geq 0$. For neutrinos, which are fermions and obey the Pauli exclusion principle, $f \in [0, 1]$. These limits lead to restrictions on the admissible values for the moments of f.

We define

$$\mathfrak{R} := \left\{ f \mid 0 \leq f \leq 1 \text{ and } 0 < \frac{1}{4\pi} \int_{\mathbb{S}^2} f \, d\omega < 1 \right\}. \tag{2.88}$$

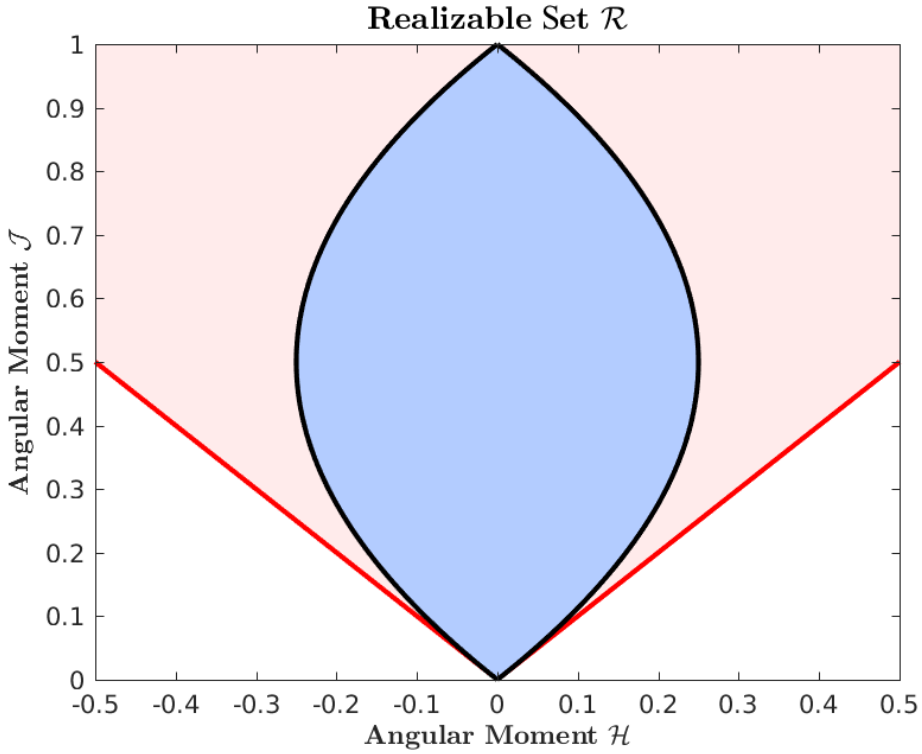

Figure 2.5.1: Illustration of the realizable set $\mathcal{R}$ (light blue region) defined in Equation (2.89). The black lines define the boundary $\partial\mathcal{R}$, while the red lines indicate the boundary of the realizable set $\mathcal{R}^+$ (light red region) defined in Equation (2.91). Published in Chu et al. (2019a).

The moments $\boldsymbol{\mathcal{M}} = \left(\mathcal{J}, \boldsymbol{\mathcal{H}}\right)^T$ are realizable if they can be obtained from a distribution function $f(\omega) \in \mathfrak{R}$. The set of all realizable moments, $\mathcal{R}$, is

$$\mathcal{R} := \left\{ \boldsymbol{\mathcal{M}} = \left(\mathcal{J}, \boldsymbol{\mathcal{H}}\right)^T \mid \mathcal{J} \in (0,1) \text{ and } \gamma(\boldsymbol{\mathcal{M}}) \geq 0 \right\}, \tag{2.89}$$

where we have defined the concave function

$$\gamma(\boldsymbol{\mathcal{M}}) \equiv (1 - \mathcal{J})\mathcal{J} - |\boldsymbol{\mathcal{H}}|. \tag{2.90}$$

The inequality, $\gamma(\boldsymbol{\mathcal{M}}) \geq 0$, is valid when the distribution function is a step/Heaviside function. A detailed proof of this condition can be found in Banach and Larecki (2017) as Theorem 7.1, also Larecki and Banach (2011); Banach and Larecki (2013).

The realizable set $\mathcal{R}$ is convex, since any point in $\mathcal{R}$ can be represented by two points in $\mathcal{R}$ using a convex combination. Figure 2.5.1 illustrates the geometry of the convex set $\mathcal{R}$ in the $(\mathcal{H}, \mathcal{J})$-plane (light blue region). The boundary $\partial\mathcal{R}$ (black curves) is given by $\gamma(\boldsymbol{\mathcal{M}}) = 0$. The realizable domain of positive distribution functions, $\mathcal{R}^+$ (no upper bound on f), is a convex cone defined by

$$\mathcal{R}^+ := \left\{ \boldsymbol{\mathcal{M}} = \left(\mathcal{J}, \boldsymbol{\mathcal{H}}\right)^T \mid \mathcal{J} > 0 \text{ and } \gamma^+(\boldsymbol{\mathcal{M}}) \geq 0 \right\}, \tag{2.91}$$

$$\gamma^+(\boldsymbol{\mathcal{M}}) \equiv \mathcal{J} - |\boldsymbol{\mathcal{H}}|. \tag{2.92}$$

$\mathcal{R}^+$ is partially shown as the light red region above the red lines, which mark the boundary of $\mathcal{R}^+$ (denoted $\partial\mathcal{R}^+$). The realizable set $\mathcal{R}$ is a bounded subset of $\mathcal{R}^+$.

When solving the moment equations numerically, ensuring that moments stay in the realizable set is essential, and the efforts needed to ensure this are non-trivial. Explicitly, the angular moments, $\mathcal{J}$ and $\boldsymbol{\mathcal{H}}$, satisfy the following bounds (Levermore, 1984; Larecki and Banach, 2011; Kershaw, 1976; Shohat and Tamarkin, 1943):

$$\mathcal{J} \in [0,1], \quad (1 - \mathcal{J})\mathcal{J} - |\boldsymbol{\mathcal{H}}| \geq 0. \tag{2.93}$$

If an algebraic closure method is used, the bounds also apply on the closure. Take the Eddington factor closure method for an example. The Eddington factor χ is defined by the Eddington tensor $\boldsymbol{k}$ (Levermore, 1984)

$$\boldsymbol{k} = \boldsymbol{\mathcal{K}}/\mathcal{J}, \tag{2.94}$$

assuming the radiation field is symmetric about a preferred direction $\widehat{\boldsymbol{h}} = \boldsymbol{\mathcal{H}}/|\boldsymbol{\mathcal{H}}|$, such that

$$\boldsymbol{k} = \frac{1}{2}\big[\,(1-\chi)\,\boldsymbol{I} + (3\,\chi - 1)\,\widehat{\boldsymbol{h}} \otimes \widehat{\boldsymbol{h}}\,\big], \tag{2.95}$$

and the bounds on the Eddington factor χ are

$$\chi_{\min} = \max\left(1 - \frac{2}{3\mathcal{J}}, h^2\right) \leq \chi \leq \min\left(1, \frac{1}{3\mathcal{J}} - \frac{\mathcal{J}}{1-\mathcal{J}}h^2\right) = \chi_{\max}, \tag{2.96}$$

where flux factor h is defined as

$$h = |\boldsymbol{\mathcal{H}}|/\mathcal{J}. \tag{2.97}$$

We call moments satisfying inequality (2.93) realizable moments. Additional discussion about the realizable set can be found in Chu et al. (2019a). If the moments become nonrealizable, nonphysical solutions occur. For example, $\mathcal{J} > 1$ changes the sign of the blocking factor $(1 - \mathcal{J})$ in the collision terms, which indicates a source (or sink) becomes a sink (or source). When the constraints are violated, nonphysical and unpredictable results are produced and render the results vulnerable.

One may want to fix the problem by mapping the non-realizable moments back to the realizable domain before computing the closure function, though the mapping should be manipulated to preserve the particle number and four-momentum simultaneously. In Section 3.3, we will discuss our efforts to design a numerical method to maintain realizable moments, and, in Section 3.6, exactly how we map the non-realizable moments back to the realizable domain.

2.5.2 Closure Problem

The moment model given by Equation (2.38) and (2.39) is not closed because of the appearance of higher-order moments. Taking the $\mathcal{O}(v/c)$ two-moment model as an example, because of the existence of $\mathcal{K}^{ij}$ and $\mathcal{L}^{ijk}$ in Equation (2.53) and (2.54), which are not the evolution variables $\mathcal{D}$ or $\mathcal{I}^i$ but rather high-order moments, the equation system is open. The algebraic closure method is a type of approach for closing the equation system. In the algebraic closure method, these high-order moments are expressed in terms of the evolved moments, in closed form, to make the system of equations solvable. Algebraic moment closures are computationally efficient, as they provide an algebraic approximation formula. And the accuracy of an algebraic moment closure is determined directly by how well its algebraic approximation is. Algebraic moment closures are used in applications where transport plays an important role, but where limited computational resources preclude the use of higher fidelity models. For the purpose of this dissertation, we limit ourselves to a so-called Eddington algebraic closure method and employ a family of algebraic Eddington factor (AEF) closures in `thornado`. The expression of the Eddington factor χ and the Eddington tensor $\boldsymbol{k}$ are given in Equations (2.94)-(2.95).

The two-moment model is then closed once the Eddington factor χ is determined from $\mathcal{J}$ and $\boldsymbol{\mathcal{H}}$. The two-moment closure procedure should satisfy the isotropic limit:

$$\chi(\mathcal{J}, h \to 0) = \frac{1}{3}, \tag{2.98}$$

which can be derived assuming an isotropic distribution function. Algebraic moment closures for the two-moment model are computationally efficient, as they provide the Eddington factor in closed form expressions. Examples of their use include simulation of neutrino transport in core-collapse supernovae (Roberts et al., 2016) and compact binary mergers (Foucart et al., 2015). Algebraic moment closures in the context of these applications have also been discussed elsewhere (see Janka et al. 1992; Pons et al. 2000; Smit et al. 2000; Just et al. 2015; Murchikova et al. 2017). We will see

how the closure affects the two-moment model in our numerical tests in Section 5.6.2. In the following, we focus on properties of the algebraic closures that are critical to the development of numerical methods for the two-moment model of fermion transport.

For the algebraic closures we consider, the Eddington factor in Equation (2.95) can be written in the following form (Cernohorsky and Bludman, 1994)

$$\chi(\mathcal{J}, h) = \frac{1}{3} + \frac{2\,(1-\mathcal{J})\,(1-2\mathcal{J})}{3}\,\Theta\Big(\frac{h}{1-\mathcal{J}}\Big), \tag{2.99}$$

where the *closure function* $\Theta(x)$ depends on the specifics of the closure procedure. We consider two basic closure procedures: the maximum entropy (ME) closure and the Kershaw (K) closure. In the low occupancy limit ($\mathcal{J} \ll 1$), the Eddington factor in Equation (2.99) depends solely on h; i.e.,

$$\chi(\mathcal{J}, h) \to \chi_0(h) = \frac{1}{3} + \frac{2}{3}\,\Theta\big(h\big). \tag{2.100}$$

This form of χ yields a moment closure suitable for particle systems obeying Maxwell-Boltzmann statistics.

Maximum Entropy (ME) Closure

The ME closure constructs an approximation of the angular distribution as a function of $\mathcal{J}$ and $\boldsymbol{\mathcal{H}}$ (Cernohorsky and Bludman, 1994; Larecki and Banach, 2011). It assumes the general form (Cernohorsky and Bludman, 1994)

$$f_{\text{ME}}(\omega; a, \boldsymbol{b}) = \frac{1}{e^{a+\boldsymbol{b}\cdot\boldsymbol{\ell}(\omega)}+1}, \tag{2.101}$$

obeying Fermi-Dirac statistics, and finds a distribution f_{ME} that maximizes the entropy functional

$$S[f_{\text{ME}}] = \int_{\mathbb{S}^2} \big[\,(1-f_{\text{ME}})\log(1-f_{\text{ME}}) + f_{\text{ME}}\log f_{\text{ME}}\,\big]\,d\omega \tag{2.102}$$

while also subject to the constraints

$$\frac{1}{4\pi}\int_{\mathbb{S}^2} f_{\text{ME}}(\omega)\,d\omega = \mathcal{J} \quad \text{and} \quad \frac{1}{4\pi}\int_{\mathbb{S}^2} f_{\text{ME}}(\omega)\,\boldsymbol{\ell}(\omega)\,d\omega = \boldsymbol{\mathcal{H}}. \tag{2.103}$$

The solution of this problem gives the Lagrange multipliers a and $\boldsymbol{b}$, then the distribution $f_{\text{ME}}(\omega; a, \boldsymbol{b})$, which can be used to compute higher-order moment(s). The ME distribution function satisfies $0 < f_{\text{ME}} < 1$ intuitively. For the maximum entropy problem to be solvable, we must have $\boldsymbol{\mathcal{M}} \in \mathcal{R}$ (Larecki and Banach, 2011).

To arrive at an algebraic form of the ME closure, more constraints need to be given. Cernohorsky and Bludman postulate the closure function Θ is independent of $\mathcal{J}$ but a function of the flux saturation, defined as

$$x \equiv h/(1-\mathcal{J}). \tag{2.104}$$

With it, the closure function Θ can be written explicitly in terms of the inverse Langevin function. Cernohorsky and Bludman (1994) give a polynomial fit (accurate to 2%) for Θ:

$$\Theta_{\text{ME}}^{\text{CB}}(x) = \frac{1}{5}\left(3 - x + 3\,x^2\right)x^2, \tag{2.105}$$

which we will refer to as the CB closure in the following context and figures. More recently, Larecki and Banach (2011) have shown that the explicit expression given in Equation (2.105) is not exact and provide another approximate expression (BL closure)

$$\Theta_{\text{ME}}^{\text{BL}}(x) = \frac{1}{8}\left(9\,x^2 - 5 + \sqrt{33\,x^4 - 42\,x^2 + 25}\right), \tag{2.106}$$

which is accurate to within 0.35%. On the interval $x \in [0, 1]$, the curves given by Equations (2.105) and (2.106) lie practically on top of each other. The closure functions given by Equations (2.105) and (2.106), together with the Eddington factor in Equation (2.99) and the pressure tensor in Equation (2.95), constitute the

algebraic maximum entropy closures for fermionic particle systems considered in this dissertation.

Minerbo Closure In addition, we note that using the closure function given by Equation (2.105) with the low occupancy Eddington factor in Equation (2.100) results in the algebraic maximum entropy closure attributed to Minerbo (Minerbo, 1978) (MI closure):

$$\Theta^{\mathrm{MI}}(h) = \frac{1}{5}h^2\left(3 - h + 3h^2\right), \tag{2.107}$$

and

$$\chi^{\mathrm{CB}}_{\mathrm{ME}}(\mathcal{J}, h) \to \chi^{\mathrm{MI}}(h) = \frac{1}{3} + \frac{2}{3}\Theta^{\mathrm{MI}}(h). \tag{2.108}$$

Minerbo closure is currently used in simulations of neutrino (fermion) transport in the aforementioned nuclear astrophysics applications. In a recent comparison of algebraic closures for the two-moment model applied to neutrino transport around the PNS, Murchikova et al. (2017) obtained nearly identical results when using the closures of CB and Minerbo. Moreover, Minerbo closure is less vulnerable to non-realizable moments, which makes it stand out in situations where realizability cannot be guaranteed. As will be discussed later, we use Minerbo closure as our primary closure for our $\mathcal{O}(v/c)$ supernova simulations.

Kershaw (K) Closure

Another algebraic closure that we consider is a Kershaw-type closure (Kershaw, 1976), developed for fermion particle systems in Banach and Larecki (2017). The basic principle of the Kershaw closure for the two-moment model is derived from the fact

that the realizable set generated by the triplet of scalar moments

$$\{\mathcal{J}, \mathcal{H}, \mathcal{K}\} = \frac{1}{2}\int_{-1}^{1} f(\mu)\, \mu^{\{0,1,2\}}\, d\mu, \tag{2.109}$$

is convex when the distribution function satisfies $f(\mu) \in [0,1]$, $\forall \mu \in [-1,1]$. The moments in Equation (2.109) are a set of unique moments obtained from the moments in Equation (2.40) under the assumption that the distribution function is axisymmetric about a preferred direction, and μ is the cosine of the angle between this preferred direction and the particle propagation direction given by $\boldsymbol{\ell}$.

For a bounded distribution $f(\mu) \in [0,1]$, it is possible to show (e.g., see Banach and Larecki (2017)) that the second moment satisfies

$$\mathcal{K} \in [\mathcal{K}_{\text{L}}(\mathcal{J}, h), \mathcal{K}_{\text{U}}(\mathcal{J}, h)]\,, \tag{2.110}$$

where $\mathcal{K}_{\text{L}} = \mathcal{J}\left(\frac{1}{3}\mathcal{J}^2 + h^2\right)$ and $\mathcal{K}_{\text{U}} = \mathcal{K}_{\text{L}} + \mathcal{J}\,(1-\mathcal{J})\,(1-x^2)$. By convexity of the realizable set generated by the moments in Equation (2.109), the convex combination

$$\mathcal{K}(\beta, \mathcal{J}, h) = \beta\, \mathcal{K}_{\text{L}}(\mathcal{J}, h) + (1-\beta)\, \mathcal{K}_{\text{U}}(\mathcal{J}, h), \tag{2.111}$$

with $\beta \in [0,1]$, is realizable whenever $(\mathcal{J}, \mathcal{H})^T \in \mathcal{R}$. The Kershaw closure for the two-moment model is then obtained with the additional requirement that it be correct in the limit of isotropic distribution functions; i.e., that $\mathcal{K}(\beta, \mathcal{J}, 0) = \mathcal{J}/3$. One choice for β, which leads to a strictly hyperbolic and causal two-moment model (and a particularly simple closure function), is $\beta = (2-\mathcal{J})/3$ (Banach and Larecki, 2017). This gives $\mathcal{K}_{\text{K}}(\mathcal{J}, h) = \chi_{\text{K}}(\mathcal{J}, h)\, \mathcal{J}$, where

$$\chi_{\text{K}}(\mathcal{J}, h) = \frac{1}{3} + \frac{2\,(1-\mathcal{J})\,(1-2\mathcal{J})}{3}\, \Theta_{\text{K}}\Big(\frac{h}{1-\mathcal{J}}\Big), \tag{2.112}$$

and

$$\Theta_{\text{K}}(x) = x^2. \tag{2.113}$$

Realizability of Algebraic Moment Closures

It is not immediately obvious that all the algebraic moment closures discussed above are suitable for designing realizability-preserving methods for the two-moment model of fermion transport. The Kershaw closure is consistent with a bounded distribution, $f_{\mathrm{K}} \in (0,1)$, and should be well suited, but the algebraic ME closures are based on approximations to the closure function. We need to consider if these approximate closures remain consistent with the assumed bounds on the underlying distribution function. To this end, we rely on results in Levermore (1984); Larecki and Banach (2011) (see also Kershaw (1976); Shohat and Tamarkin (1943)), which state that realizability of the moment triplet $\{\mathcal{J}, \boldsymbol{\mathcal{H}}, \boldsymbol{\mathcal{K}}\}$ (with $\boldsymbol{\mathcal{K}}$ given by Equation (2.95)) is equivalent to the requirement for the Eddington factor given by Equation (2.96), i.e.,

$$\chi_{\min} = \max\left(1 - \frac{2}{3\mathcal{J}}, h^2\right) < \chi < \min\left(1, \frac{1}{3\mathcal{J}} - \frac{\mathcal{J}}{1-\mathcal{J}}h^2\right) = \chi_{\max}. \tag{2.114}$$

Fortunately, these bounds are satisfied by the algebraic closures based on Fermi-Dirac statistics. (Note that for $\mathcal{J} \ll 1$, the bounds in Equation (2.96) limit to the bounds for positive distributions given by Levermore (1984); i.e., $h^2 < \chi < 1$.)

We can see from Equation (2.96) that the bounds on the Eddington factor χ have dependences on both the occupancy $\mathcal{J}$ and the flux factor h (Equation (2.97)). To better understand the bounds, we plot the Eddington factor χ versus the flux factor h for the various algebraic closures in Figure 2.5.2 for different values of $\mathcal{J} \in (0,1)$: 0.01 (upper left panel), 0.4 (upper right panel), 0.6 (lower left panel), and 0.99 (lower right panel). The lower and upper bounds on the Eddington factor for realizable closures ($\chi_{\min}$ and $\chi_{\max}$, respectively) are also plotted. We note that for all closures, the Eddington factor $\chi \to 1/3$ as $h \to 0^+$.

When $\mathcal{J} = 0.01$, the maximum entropy closures (CB, BL, and Minerbo) are practically indistinguishable, while the Eddington factor of the Kershaw closure is larger than the other closures over most of the domain. When $\mathcal{J} = 0.4$, the Eddington factor for the closures based on Fermi-Dirac statistics (CB, BL, and Kershaw) remain

close together, while the Eddington factor for the Minerbo closure is larger than the other closures for $h \gtrsim 0.2$. The Eddington factor for all closures remains between $\chi_{\min}$ and $\chi_{\max}$ when $\mathcal{J} = 0.01$ and $\mathcal{J} = 0.4$.

When $\mathcal{J} = 0.6$, the Eddington factor for the closures based on Fermi-Dirac statistics remain close together and within the bounds in Equation (2.96). The dependence of the Eddington factor on h for the Minerbo closure differs from the other closures (i.e., increases versus decreases with increasing h), and exceeds $\chi_{\max}$ for $h \gtrsim 0.34$. When $\mathcal{J} = 0.99$, the Eddington factor of the CB and BL closures (indistinguishable) and the Kershaw closure remain within the bounds given in Equation (2.96). The Eddington factor of the Minerbo closure is nearly flat, and exceeds $\chi_{\max}$ for $h \gtrsim 0.006$.

We have also checked numerically that for all the algebraic closures based on Fermi-Dirac statistics (CB, BL, and Kershaw), the bounds on the Eddington factor in Equation (2.96) holds for all $\boldsymbol{\mathcal{M}} \in \mathcal{R}$. In this sense, these closures are preferred for the development of realizability-preserving numerical methods for the two-moment model of fermion transport.

In Figure 2.5.3, we further illustrate properties of the algebraic closures by plotting $\boldsymbol{\mathcal{M}}_{ab}$, a normalized sum of two moment sets defined by two distribution states. We define

$$\boldsymbol{\mathcal{M}}_{ab} \equiv \Phi^{+}(\boldsymbol{\mathcal{M}}_a, \boldsymbol{\mathcal{K}}_a) + \Phi^{-}(\boldsymbol{\mathcal{M}}_b, \boldsymbol{\mathcal{K}}_b), \tag{2.115}$$

$$\Phi^{\pm}(\boldsymbol{\mathcal{M}}, \boldsymbol{\mathcal{K}}) = \frac{1}{2}(\boldsymbol{\mathcal{M}} \pm \widehat{\boldsymbol{e}} \cdot \boldsymbol{\mathcal{F}}), \tag{2.116}$$

$$\widehat{\boldsymbol{e}} \cdot \boldsymbol{\mathcal{F}} = \left(\widehat{\boldsymbol{e}} \cdot \boldsymbol{\mathcal{H}}, \widehat{\boldsymbol{e}} \cdot \boldsymbol{\mathcal{K}}\right)^{T}, \tag{2.117}$$

where $\widehat{\boldsymbol{e}} \in \mathbb{R}^3$ is an arbitrary unit vector, for the maximum entropy closures of CB and Minerbo. As we will see later, this sum is related to the numerical flux term in our numerical approach. In both panels, we plot $\boldsymbol{\mathcal{M}}_{ab}$ constructed from randomly selected pairs $\boldsymbol{\mathcal{M}}_a, \boldsymbol{\mathcal{M}}_b \in \mathcal{R}$ (each blue dot represents one realization of $\boldsymbol{\mathcal{M}}_{ab}$). Results for

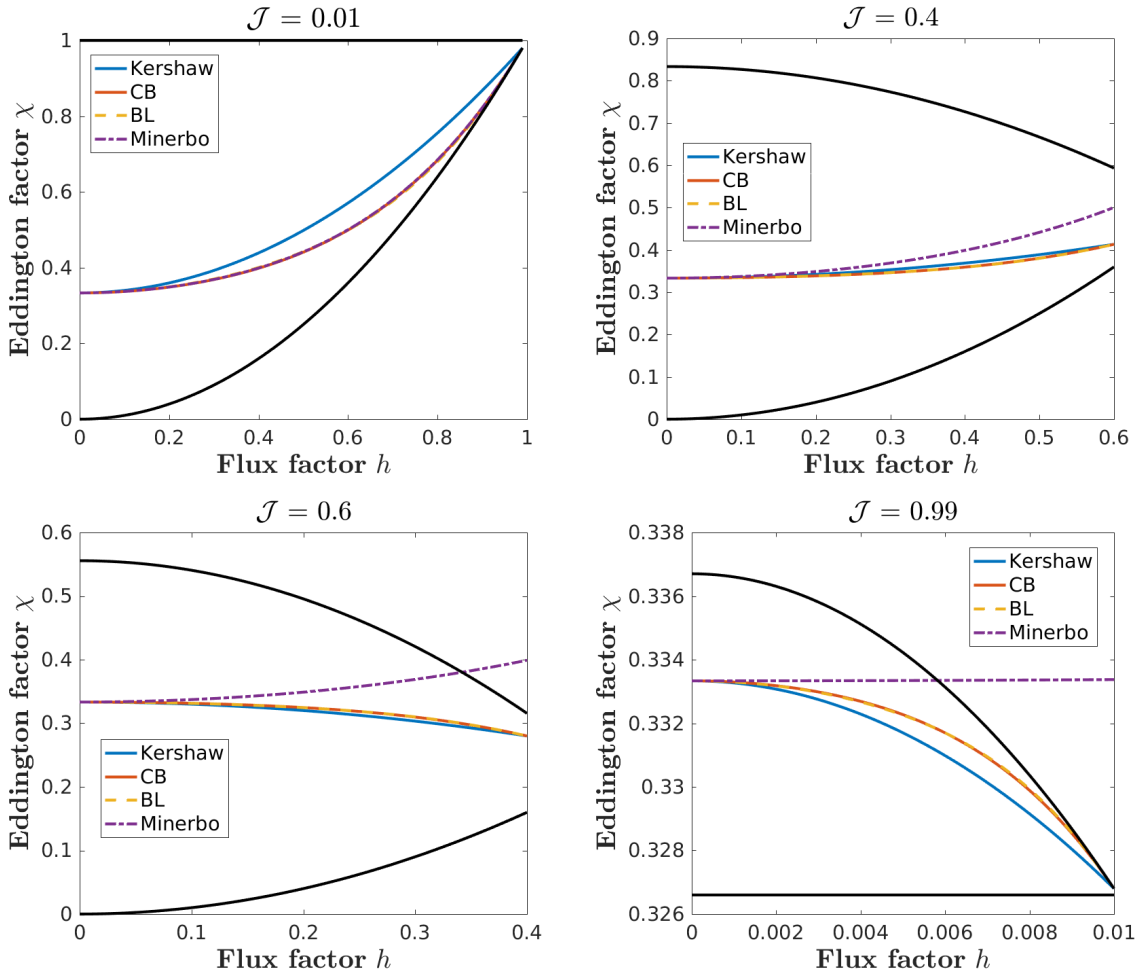

Figure 2.5.2: Plot of the Eddington factor, χ, versus the flux factor, h, for different values of $\mathcal{J}$ and for various algebraic closures: $\mathcal{J} = 0.01$ (upper left panel), $\mathcal{J} = 0.4$ (upper right panel), $\mathcal{J} = 0.6$ (lower left panel), and $\mathcal{J} = 0.99$ (lower right panel). In each panel, we plot the Eddington factors of Kershaw (solid blue lines), Cernohorsky & Bludman (CB, solid red lines), Banach & Larecki (BL, dashed orange lines), and Minerbo (dash-dot purple lines). We also plot $\chi_{\min}$ and $\chi_{\max}$ defined in Equation (2.96) (lower and upper solid black lines, respectively). Published in Chu et al. (2019a).

the maximum entropy closure of CB are plotted in the left panel, while results for the Minerbo closure are plotted in the right panel. As expected for the closure, consistent with moments of Fermi-Dirac distributions (CB), we find $\boldsymbol{\mathcal{M}}_{ab} \in \mathcal{R}$. For the Minerbo closure, which is consistent with positive distributions, $\boldsymbol{\mathcal{M}}_{ab}$ is not confined to $\mathcal{R}$.

Extending the Closure

In the $\mathcal{O}(v/c)$ moment equations Equations (2.53) and (2.54) the rank-three moment is also included. So we need to extend the closure to rank-three moment to close the equation system. We extend the closure without assuming the radiation field is symmetric about a preferred direction, such that

$$\mathcal{K}^{ij} = k^{ij}\mathcal{D}, \tag{2.118}$$

and the Eddington tensor is

$$k^{ij} \equiv \frac{1}{2}\left[\,(1-\chi)\,\gamma^{ij} + (3\,\chi - 1)\,\hat{n}^i\,\hat{n}^j\,\right], \tag{2.119}$$

where $\hat{n}^i = \mathcal{I}^i/\mathcal{I}$ and $\mathcal{I} = \sqrt{\gamma_{ij}\mathcal{I}^i\mathcal{I}^j}$. The Eddington tensor in Equation (2.119) satisfies the trace condition $\gamma_{ij}k^{ij} = 1$. The rank-three moment is related to the number density by

$$\mathcal{L}^{ijk} = \mathsf{q}^{ijk}\,\mathcal{D}, \tag{2.120}$$

where the heat flux tensor is approximated as (Just et al., 2015)

$$\mathsf{q}^{ijk} = \frac{1}{2}\left[\,(h-\zeta)\left(\hat{n}^i\,\gamma^{jk} + \hat{n}^j\,\gamma^{ik} + \hat{n}^k\,\gamma^{ij}\right) + (5\zeta - 3h)\,\hat{n}^i\,\hat{n}^j\,\hat{n}^k\,\right], \tag{2.121}$$

where h is the flux factor (Equation (2.97)), and the heat flux factor is

$$\zeta = \hat{n}_i\,\hat{n}_j\,\hat{n}_k\,\mathsf{q}^{ijk} = \langle f(\hat{n}_i\ell^i)^3\rangle_{\mathbb{S}^2}/\langle f\rangle_{\mathbb{S}^2}. \tag{2.122}$$

The rank-three tensor in Equation (2.121) satisfies the trace condition

$$\gamma_{ij}\,\mathsf{q}^{ijk} = h\,\hat{n}^k. \tag{2.123}$$

Following Richers (2020), the pressure and third moment of maximum entropy Fermi-Dirac (MEFD) closure in terms of the flux saturation $x = f/f_{\max}$ can be written as

$$\begin{aligned} p(e,x) &= \left[p_{\max}(e) - p_{\text{diff}}\,(e,1)\right]\zeta_p(e,x) + p_{\text{diff}}\,(e,x), \\ l(e,x) &= \left[l_{\max}(e) - l_{\text{diff}}\,(e,1)\right]\zeta_l(e,x) + l_{\text{diff}}\,(e,x), \end{aligned} \tag{2.124}$$

where the diffusive solution is

$$\begin{aligned} p_{\text{diff}}(e,x) &= 1/3, \\ l_{\text{diff}}(e,x) &= 3x f_{\max}(e)/5, \end{aligned} \tag{2.125}$$

and the maximum packing solution is

$$f_{\max}(e) = 1 - e, \tag{2.126}$$

$$p_{\max}(e) = \frac{2(1-e)(1-2e)}{3} + \frac{1}{3}, \tag{2.127}$$

$$l_{\max}(e) = (1-e)\left(1 - 2e + 2e^2\right). \tag{2.128}$$

Following (Cernohorsky and Bludman, 1994; Richers, 2020), $\zeta_l(e,x)$ can be approximated using the lowest-order polynomial that satisfies the values and derivatives of the functions in the high-packing and isotropic limits, along with the requirement that $0 \leq \zeta_l(e,x) \leq 1$:

$$\begin{aligned} \zeta_p(e,x) &\approx x^2\left(3 - x + 3x^2\right)/5, \\ \zeta_l(e,x) &\approx x^6. \end{aligned} \tag{2.129}$$

Substitude Equation (2.125), (2.128), (2.129) to Equation (2.124) to obtain the explicit expression for CB closure:

$$\begin{aligned} p(e,x) &= \frac{2(1-e)(1-2e)(3-x+3x^2)x^2}{15} + \frac{1}{3}, \\ l(e,x) &= (1-e)\left\{[(1-2e+2e^2) - \frac{3}{5}]x^6 + \frac{3x}{5}\right\}. \end{aligned} \tag{2.130}$$

Vaytet et al. (2011) gives

$$q_{\mathrm{M1}}(h) = 3\varphi_1(h)h + \varphi_2(h)h^3 \tag{2.131}$$

where

$$\begin{aligned} \varphi_1(h) =& \frac{(h-2+a)(h+2-a)}{4h(a-2)^5}\left[12\ln\left(\frac{h-2+a}{h+2-a}\right)\left(h^4+2ah^2-7h^2-4a+8\right)\right. \\ & \left. +48h^3-9ah^3-80h+40ah\right], \end{aligned} \tag{2.132}$$

$$\begin{aligned} \varphi_2(h) =& \frac{1}{h^3(a-2)^5}\left[60\ln(\frac{h-2+a}{h+2-a})\left(-h^6+15h^4-3ah^4\right.\right. \\ & \left. +15ah^2-42h^2-16a+32\right) \\ & \left. +54ah^5-465h^5-674ah^3+2140h^3+1056ah-2112h\right], \end{aligned} \tag{2.133}$$

and $a = \sqrt{4-3h^2}$. And Minerbo closure gives (Just et al., 2015)

$$q_{\mathrm{MI}}(h) = h\left(45+10h-12h^2-12h^3+38h^4-12h^5+18h^6\right)/75. \tag{2.134}$$

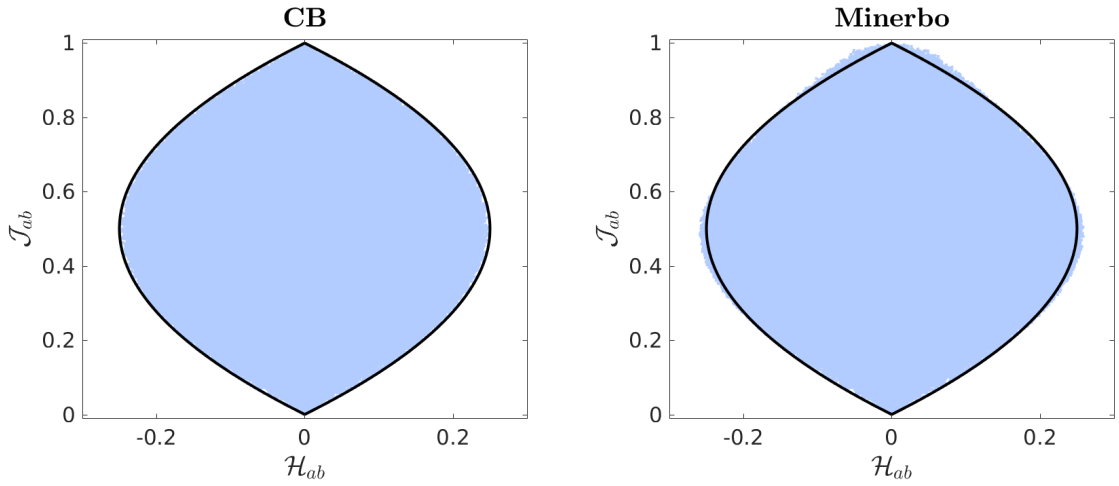

Figure 2.5.3: Illustration of $\boldsymbol{\mathcal{M}}_{ab}$, as defined in Equation (2.117), computed with algebraic maximum entropy closures of Cernohorsky & Bludman (left) and Minerbo (right). In each panel, $\boldsymbol{\mathcal{M}}_{ab}$ was computed using the respective closure, using 10^6 random pairs ($\boldsymbol{\mathcal{M}}_a, \boldsymbol{\mathcal{M}}_b \in \mathcal{R}$), and plotted as a light-blue point. The solid black lines mark the boundary of $\mathcal{R}$: $\gamma(\boldsymbol{\mathcal{M}}) = 0$. Published in Chu et al. (2019a).

Chapter 3

Realizability-Preserving DG-IMEX Method for an $\mathcal{O}(1)$ Two-Moment Model

In this chapter, we design numerical methods to solve a two-moment model that governs the transport of particles obeying Fermi-Dirac statistics. As the first step in building a neutrino transport model for CCSNe modeling, we assume the transport has emission, absorption, and iso-energetic scattering in the neutrino-matter collision term and is in the Newtonian limit. The numerical method is based on the discontinuous Galerkin method for spatial discretization and implicit-explicit methods for time integration. It is designed to preserve certain physical constraints of the underlying model by considering the spatial and temporal discretization together with the closure procedure for the two-moment model. The results from this chapter have been published in Chu et al. (2019a); Chu et al. (2019b).

3.1 Introduction

In this chapter, we present the numerical methods we have developed to solve the $\mathcal{O}(1)$ two-moment model based on the discontinuous Galerkin method for spatial and neutrino energy discretization, and on implicit-explicit (IMEX) methods for time integration. Our method is specifically designed to preserve bounds on the moments introduced by Pauli's exclusion principle, as discussed in Section 2.5.1. For an initial investigation, we limit ourselves to Cartesian geometry and a simplified collision term. Our simplified analysis will highlight the role of the moment closure in the design of robust two-moment methods for neutrino transport. It will lay the foundations for a framework that may help develop robust methods for models with improved physical fidelity.

Multiple groups have developed numerical methods for solving equations for two-moment kinetics in core-collapse supernovae (Müller et al., 2010; O'Connor and Couch, 2015; Just et al., 2015; Kuroda et al., 2016; Roberts et al., 2016; Skinner et al., 2019).

3.2 Model

In Cartesian coordinates ($\gamma = 1$) and with a simplified collision term, i.e. $\mathcal{C} = \mathcal{C}_{\text{EA}} + \mathcal{C}_{\text{Iso}}$, the moment equations Equation (2.55) and (2.56) become

$$\partial_t \mathcal{D} + \partial_i \mathcal{I}^i = \tilde{\chi}(\mathcal{D}_0 - \mathcal{D}), \tag{3.1}$$

$$\partial_t \mathcal{I}_j + \partial_i \mathcal{K}^i_{\ j} = -\tilde{\chi}\,\mathcal{I}_i - 4\pi\,\varepsilon^2\,\mathcal{I}_i(\varepsilon)\left[\Phi_{\text{Iso}\,0}(\varepsilon) - \frac{1}{3}\Phi_{\text{Iso}\,1}(\varepsilon)\right], \tag{3.2}$$

where the i-th component of the number flux given by the equilibrium distribution f_0 is zero, $\tilde{\chi}$ is defined in Equation (2.60), and $\Phi_{\text{Iso}\,0/1}$ is given in Equation (2.76).

We can define the "primitive" moments

$$\boldsymbol{\mathcal{M}} = (\mathcal{D}, \mathcal{I}^i)^T, \tag{3.3}$$

$$\boldsymbol{\mathcal{F}} = (\mathcal{I}^i, \mathcal{K}^{ij})^T, \tag{3.4}$$

and rewrite Equations (3.1)–(3.2) as

$$\partial_t \boldsymbol{\mathcal{M}} + \nabla \cdot \boldsymbol{\mathcal{F}} = \frac{1}{\tau} \boldsymbol{\mathcal{C}}(\boldsymbol{\mathcal{M}}), \tag{3.5}$$

with τ being the ratio of the particle mean-free path to some characteristic length scale, and

$$\boldsymbol{\mathcal{C}}(\boldsymbol{\mathcal{M}}) = \boldsymbol{\eta} - \boldsymbol{\mathcal{D}} \boldsymbol{\mathcal{M}}, \tag{3.6}$$

where $\boldsymbol{\eta} = (\xi f_0, \mathbf{0})^T$, $\boldsymbol{\mathcal{D}} = \mathrm{diag}(\xi, \boldsymbol{I})$, $\xi = \sigma_A / \sigma_T$ is the ratio of the absorption opacity σ_A to the total opacity $\sigma_T = \sigma_A + \sigma_S$, $\sigma_S = 4\pi\varepsilon^2 \left[\Phi_{\mathrm{Iso}\,0} - \frac{1}{3}\Phi_{\mathrm{Iso}\,1}\right]$ is the scattering opacity, and $\boldsymbol{I}$ is the identity matrix. Expressed explicitly, $\dfrac{1}{\tau} = \tilde{\chi} + (1/\lambda)_{\mathrm{Iso}} = \sigma_T$, $\dfrac{\xi}{\tau} = \tilde{\chi} = \sigma_A$, where $(1/\lambda)_{\mathrm{Iso}}$ is inverse mean free path due to isoenergetic scattering. In this chapter, we assume $\sigma_A \geq 0$. The inequality may not be guaranteed with the linear correction, as in Chapter 4, but it is valid in this chapter.

3.3 Realizability-Preserving DG-IMEX Method

When solving the moment equations, we need to prevent non-physical states from developing. Failure to maintain these bounds can lead to an ill-posed closure problem and loss of hyperbolicity for the moment equations. We will show how to develop a realizability-preserving discontinuous Galerkin (DG) (Cockburn and Shu, 2001) implicit-explicit (IMEX) schemes for the two-moment model in this chapter.

There are three main ingredients for the realizability-preserving DG-IMEX method:

1. a time step restriction to ensure the cell average is realizable for a forward Euler step (requires point-wise realizability in each element and a realizability-preserving closure method; the backward Euler step preserves realizability of the cell average without a time step restriction); (Section 3.5.5 and Section 2.5.2)

2. a convex-invariant time-stepping method; (Section 3.5.2 and Section 3.5.4)

3. a realizability-enforcing limiter to recover point-wise realizability within the element (requires realizable cell averages). (Section 3.6.1)

3.4 Phase-Space Discretization

To discretize the moment equations (Equation (3.5)) in phase space, we implement the high-order discontinuous Galerkin (DG) method (Cockburn and Shu, 2001). (See Hesthaven and Warburton (2008) for an overview of the DG method.) The DG method combines elements from both spectral and finite-volume methods. One of its major advantages is that it achieves high-order accuracy on a compact stencil: since values in $k+1$ cells are needed to reconstruct a polynomial of degree k, data only communicate with their nearest neighbors, regardless of the formal order of accuracy. This locality in memory access leads to a high computation to-communication ratio and favors parallel computation (Klöckner et al., 2009). In addition, the DG method recovers the correct asymptotic behavior in the diffusion limit, without modification (Larsen et al., 1987; Adams, 2001; Guermond and Kanschat, 2010). Reed and Hill introduced the DG method in 1973 (Reed and Hill, 1973). It has only recently received attention from the computational astrophysics community, mainly to solve the Euler equations for ideal hydrodynamics (Radice and Rezzolla, 2011; Schaal et al., 2015; Wu and Tang, 2016), the Einstein's field equations (Teukolsky, 2016) and the neutrino transport problem (Radice et al., 2013; Endeve et al., 2015;

Chu et al., 2019a; Pochik et al., 2021; Laiu et al., 2021; Endeve et al., 2022a; Endeve et al., 2022b).

We apply the nodal DG discretization to Equation (3.5) in space $\boldsymbol{x} \in \mathbb{R}^3$ and energy $\varepsilon \in \mathbb{R}^+$. We first divide the computational domain $D = D_{\boldsymbol{x}} \times D_\varepsilon \subset \mathbb{R}^3 \times \mathbb{R}^+$ into a disjoint union $\mathbb{K}$ of open elements $\boldsymbol{K}$, where each element takes the form

$$\boldsymbol{K} = \{\, (\boldsymbol{x}, \varepsilon) \colon x^i \in K^i := (x^i_{\mathrm{L}}, x^i_{\mathrm{H}}),\ i = 1, 2, 3,\ \varepsilon \in K^\varepsilon := (\varepsilon_{\mathrm{L}}, \varepsilon_{\mathrm{H}}) \,\} \tag{3.7}$$

with $\Delta x^i = x^i_{\mathrm{H}} - x^i_{\mathrm{L}}$ and $\Delta\varepsilon = \varepsilon_{\mathrm{H}} - \varepsilon_{\mathrm{L}}$ denoting the side lengths of $\boldsymbol{K}$. For $i = 1, 2, 3$, the spatial surface elements in direction x^i are denoted as $\tilde{\boldsymbol{K}}^i = \times_{j \neq i} K^j$, while $\tilde{\boldsymbol{x}}^i := \{x^j \in \boldsymbol{x} \colon j \neq i\}$ on $\tilde{\boldsymbol{K}}^i$, and the proper volume of the element $V_{\boldsymbol{K}}$ is

$$V_{\boldsymbol{K}} = \int_{\boldsymbol{K}} dV, \quad \text{where} \quad dV = d\boldsymbol{x}\, dV_\varepsilon = d\boldsymbol{x}\, \varepsilon^2 d\varepsilon\,. \tag{3.8}$$

We let the approximation space for the DG method, $\mathbb{V}^{N_{\boldsymbol{x}}, N_\varepsilon}$, be constructed from the tensor product of one-dimensional polynomials of maximal degrees $N_{\boldsymbol{x}}$ and N_ε in space and energy, respectively. Note that functions in $\mathbb{V}^{N_{\boldsymbol{x}}, N_\varepsilon}$ can be discontinuous across element interfaces. The semi-discrete DG problem is to find $\boldsymbol{\mathcal{M}}_{\mathrm{h}} \in \mathbb{V}^{N_{\boldsymbol{x}}, N_\varepsilon}$ (which approximates $\boldsymbol{\mathcal{M}}$ in Equation (3.5)) such that

$$\begin{aligned} &\partial_t \int_{\boldsymbol{K}} \boldsymbol{\mathcal{M}}_{\mathrm{h}}\, \phi\, dV + \sum_{i=1}^{3} \int_{K^\varepsilon} \int_{\tilde{\boldsymbol{K}}^i} \left(\widehat{\boldsymbol{\mathcal{F}}}^i(\boldsymbol{\mathcal{M}}_{\mathrm{h}})\, \phi \big|_{x^i_{\mathrm{H}}} - \widehat{\boldsymbol{\mathcal{F}}}^i(\boldsymbol{\mathcal{M}}_{\mathrm{h}})\, \phi \big|_{x^i_{\mathrm{L}}} \right) d\tilde{\boldsymbol{x}}^i\, dV_\varepsilon \\ &\quad - \sum_{i=1}^{3} \int_{\boldsymbol{K}} \left(\boldsymbol{\mathcal{F}}^i(\boldsymbol{\mathcal{M}}_{\mathrm{h}})\, \frac{\partial \phi}{\partial x^i} \right) dV = \frac{1}{\tau} \int_{\boldsymbol{K}} \boldsymbol{\mathcal{C}}(\boldsymbol{\mathcal{M}}_{\mathrm{h}})\, \phi\, dV \end{aligned} \tag{3.9}$$

holds for all function basis $\phi \in \mathbb{V}^{N_{\boldsymbol{x}}, N_\varepsilon}$ and all $\boldsymbol{K} \in \mathbb{K}$. Here the numerical flux approximating the flux on the spatial surface element $\tilde{\boldsymbol{K}}^i$ is denoted as $\widehat{\boldsymbol{\mathcal{F}}}^i(\boldsymbol{\mathcal{M}}_{\mathrm{h}})$. In

this work, we consider the Lax-Friedrichs (LF) flux

$$\begin{aligned}\widehat{\boldsymbol{\mathcal{F}}}^i(\boldsymbol{\mathcal{M}}_{\mathrm{h}})|_{x^i} &= \boldsymbol{f}^{\mathrm{LF},i}(\boldsymbol{\mathcal{M}}_{\mathrm{h}}|_{x^{i,-}}, \boldsymbol{\mathcal{M}}_{\mathrm{h}}|_{x^{i,+}}) \\ &:= \frac{1}{2}\left(\boldsymbol{\mathcal{F}}^i(\boldsymbol{\mathcal{M}}_{\mathrm{h}}|_{x^{i,-}}) + \boldsymbol{\mathcal{F}}^i(\boldsymbol{\mathcal{M}}_{\mathrm{h}}|_{x^{i,+}}) - \alpha^i\left(\boldsymbol{\mathcal{M}}_{\mathrm{h}}|_{x^{i,+}} - \boldsymbol{\mathcal{M}}_{\mathrm{h}}|_{x^{i,-}}\right)\right), \quad (3.10)\end{aligned}$$

where $\boldsymbol{\mathcal{M}}_{\mathrm{h}}|_{x^{i,\pm}} = \lim_{\delta\to 0}\boldsymbol{\mathcal{M}}_{\mathrm{h}}|_{x^i\pm\delta}$ are the evaluations of $\boldsymbol{\mathcal{M}}_{\mathrm{h}}$ at the immediate right/left of x^i, which thus are functions of $(\tilde{\boldsymbol{x}}^i, \varepsilon, t)$. The parameter $\alpha^i = ||\mathrm{eig}\big(\partial\boldsymbol{\mathcal{F}}^i/\partial\boldsymbol{\mathcal{M}}\big)||_\infty$ is the largest eigenvalue of the flux Jacobian. For massless neutrinos, which propagate at the speed of light, we can take $\alpha^i = 1$ (speed of light) (i.e., the global LF flux).

3.5 Time Integration

Using the DG method, the moment equations are discretized in space and energy. The moment equations becomes a ordinary differential equations (ODEs), which is still continuous in temporal and needs to be integrated:

$$\dot{\boldsymbol{u}} = \boldsymbol{\mathcal{T}}(\boldsymbol{u}) + \frac{1}{\tau}\boldsymbol{\mathcal{Q}}(\boldsymbol{u}), \quad (3.11)$$

where $\boldsymbol{u} = \{\boldsymbol{u}_{\boldsymbol{K}}\}_{\boldsymbol{K}\in\mathbb{K}}$ are the degrees of freedom evolved with the DG method. For example, for a test space spanned by $\{\phi_i(\boldsymbol{x})\}_{i=1}^N \in \mathbb{V}^k$, we let

$$\boldsymbol{u}_{\boldsymbol{K}} = \frac{1}{|\boldsymbol{K}|}\Big(\int_{\boldsymbol{K}}\boldsymbol{\mathcal{M}}_h\,\phi_1\,d\boldsymbol{x}, \int_{\boldsymbol{K}}\boldsymbol{\mathcal{M}}_h\,\phi_2\,d\boldsymbol{x}, \ldots, \int_{\boldsymbol{K}}\boldsymbol{\mathcal{M}}_h\,\phi_N\,d\boldsymbol{x}\Big)^T. \quad (3.12)$$

Thus, for $\phi_1 = 1$, the first components of $\boldsymbol{u}_{\boldsymbol{K}}$ are the cell-averaged moments. In Equation (3.11), $\boldsymbol{\mathcal{T}}$ is the transport operator, corresponding to the second and third term on the left-hand side of Equation (3.9), and $\boldsymbol{\mathcal{Q}}$ is the collision operator, corresponding to the right-hand side of Equation (3.9). Equation (3.11) is to be integrated forward in time with an ODE integrator.

In CCSN simulation, the duration of the CCSN explosion ($\sim \mathcal{O}(1)$ second) is long compared to the time scales of neutrino interactions with the background (they can be $\sim \mathcal{O}(10^{-10})$ second). To model the system fully explicitly, $\sim \mathcal{O}(10^{10})$ time steps would be needed, while solving the system fully implicitly would require inverting for each time step global band-structured matrices whose sizes depend on the phase-space discretization, which would be expensive. Considering the fact that the fluid and the neutrinos have comparable propagation speeds for the relativistic setting of a CCSN explosion, implicit-explicit (IMEX) method can be used to alleviate the challenge in computation. IMEX methods treat the local stiff collision term implicitly and the non-stiff convection terms explicitly. The cost of inverting matrices declines, and the time step for stability is determined by the non-stiff term only. Therefore, IMEX methods require far fewer time steps compared with a fully explicit method, and the computation for each step is less expensive compared with a fully implicit method. In addition, the splitting has some advantages when solving kinetic equations since the collisional interactions may couple across momentum space, but are local in position space, and are easier to parallelize then a fully implicit approach. Hence, IMEX methods are the approach we will use to obtain numerical approximations to the solution of the ODEs.

3.5.1 Standard IMEX Schemes

Treating the transport operator explicitly and the collision operator implicitly, a standard s-stage IMEX scheme takes the following form (Pareschi and Russo, 2005):

$$\boldsymbol{u}^{(i)} = \boldsymbol{u}^n + \Delta t \sum_{j=1}^{i-1} \tilde{a}_{ij}\, \boldsymbol{\mathcal{T}}(\boldsymbol{u}^{(j)}) + \Delta t \sum_{j=1}^{i} a_{ij}\, \boldsymbol{\mathcal{Q}}(\boldsymbol{u}^{(j)}), \quad i = 1, \ldots, s, \tag{3.13}$$

$$\boldsymbol{u}^{n+1} = \boldsymbol{u}^n + \Delta t \sum_{i=1}^{s} \tilde{w}_i\, \boldsymbol{\mathcal{T}}(\boldsymbol{u}^{(i)}) + \Delta t \sum_{i=1}^{s} w_i\, \boldsymbol{\mathcal{Q}}(\boldsymbol{u}^{(i)}), \tag{3.14}$$

where $(\tilde{a}_{ij})$ and (a_{ij}), coefficients of the i-th stage, are elements of matrices $\tilde{A}$ and A, respectively. The matrices $\tilde{A}$ and A are lower triangular. ($\tilde{A}$ is strictly lower triangular so that the transport part is explicit.) The vectors $\tilde{\boldsymbol{w}} = (\tilde{w}_1, \ldots, \tilde{w}_s)^T$ and $\boldsymbol{w} = (w_1, \ldots, w_s)^T$ are the weights in the assembly step in Equation (3.14). These coefficients and weights must satisfy certain order conditions for consistency, accuracy, and other properties.

For second-order temporal accuracy, the following conditions are required:

$$\sum_{i=1}^{s} \tilde{w}_i = \sum_{i=1}^{s} w_i = 1, \tag{3.15}$$

$$\sum_{i=1}^{s} \tilde{w}_i \, \tilde{c}_i = \sum_{i=1}^{s} \tilde{w}_i \, c_i = \sum_{i=1}^{s} w_i \, \tilde{c}_i = \sum_{i=1}^{s} w_i \, c_i = \frac{1}{2}, \tag{3.16}$$

where $\tilde{c}_i = \sum_{j=1}^{s} \tilde{a}_{ij}$ and $c_i = \sum_{j=1}^{s} a_{ij}$.

The IMEX scheme is called globally stiffly accurate (GSA) if the coefficients satisfy (Dimarco and Pareschi, 2013):

$$a_{si} = w_i \quad \text{and} \quad \tilde{a}_{si} = \tilde{w}_i, \quad \text{for} \quad i = 1, \ldots, s. \tag{3.17}$$

It results in $\boldsymbol{u}^{n+1} = \boldsymbol{u}^{(s)}$, which is simplifying because the assembly step in Equation (3.14) is not necessary.

IMEX schemes are further classified by the structure of the implicit matrix A. If A is invertible, the IMEX scheme is of type A (Pareschi and Russo, 2005). If $a_{i1} = 0$ for $i = 1, \ldots, s$, $w_1 = 0$, and the submatrix consisting of the last $s - 1$ rows and columns is invertible, the IMEX scheme is of type ARS (Ascher et al., 1997; Pareschi and Russo, 2005).

3.5.2 Convex-Invariant IMEX Schemes

Since the set of realizable moments is convex, as we have discussed in Section 2.5.1, convex-invariant schemes, which map the initial values into this set, can be used to

design realizability-preserving methods for the two-moment model. To construct a convex-invariant scheme, the coefficients and weights, a_{ij}, $\tilde{a}_{ij}$, $\tilde{w}_i$, and w_i, should enable each $\boldsymbol{u}^{(i)}$ in Equation (3.13) to be expressed as a convex combination of realizable states.

To this end, we rewrite the stage values in Equation (3.13) as

$$\boldsymbol{u}^{(i)} = \sum_{j=0}^{i-1} c_{ij}\Big[\,\boldsymbol{u}^{(j)} + \hat{c}_{ij}\,\Delta t\,\boldsymbol{\mathcal{T}}(\boldsymbol{u}^{(j)})\,\Big] + a_{ii}\,\Delta t\,\boldsymbol{\mathcal{Q}}(\boldsymbol{u}^{(i)}), \quad i = 1,\ldots,s, \tag{3.18}$$

following Hu et al. (2018), where c_{ij} and $\hat{c}_{ij} \equiv \tilde{c}_{ij}/c_{ij}$ are defined in terms of a_{ij} and $\tilde{a}_{ij}$. For IMEX schemes of type ARS, c_{ij} and $\tilde{c}_{ij}$ are given by (Hu et al., 2018)

$$\begin{aligned} c_{i0} &= 1 - \sum_{j=2}^{i-1}\sum_{l=j}^{i-1} a_{il}b_{lj}, & c_{ij} &= \sum_{l=j}^{i-1} a_{il}b_{lj}, \\ \tilde{c}_{i0} &= \tilde{a}_{i1} + \sum_{j=2}^{i-1} a_{ij}\tilde{b}_{j1}, & \tilde{c}_{ij} &= \tilde{a}_{ij} + \sum_{l=j+1}^{i-1} a_{il}\tilde{b}_{lj}, \end{aligned} \tag{3.19}$$

with

$$b_{ii} = \frac{1}{a_{ii}}, \quad b_{ij} = -\frac{1}{a_{ii}}\sum_{l=j}^{i-1} a_{il}b_{lj}, \quad \tilde{b}_{ij} = -\frac{1}{a_{ii}}\Big(\tilde{a}_{ij} + \sum_{l=j+1}^{i-1} a_{il}\tilde{b}_{lj}\Big). \tag{3.20}$$

And we must set $c_{i1} = \tilde{c}_{i1} = 0$ in Equation (3.19) to have $\sum_{j=0}^{i-1} c_{ij} = 1$. For the IMEX scheme to be GSA, $\boldsymbol{u}^{n+1} = \boldsymbol{u}^{(s)}$.

If $c_{ij}, \tilde{c}_{ij} \geq 0$ and $a_{ii} > 0$, each stage in Equation (3.18) is a convex combination of explicit Euler steps with time step $\hat{c}_{ij}\Delta t$, followed by an implicit Euler step. Each of the explicit Euler steps has a time step condition that ensures its realizability given by $\max(\hat{c}_{ij}\,\Delta t) \leq \Delta t_{\text{Ex}}$, where Δt_{Ex} is the time step that ensures the explicit update with the transport operator is admissible. This is the CFL condition of the scheme. We will elaborate on the condition for Δt_{Ex} in Section 3.5.5.

3.5.3 Diffusion-Accurate IMEX Schemes

Accuracy in the diffusion limit is another important property to consider when an IMEX scheme is applied to the two-moment model. Note, beginning from this section to the end of this chapter, we use $\{\mathcal{J}, \boldsymbol{\mathcal{H}}\}$ to denote the number density and number flux, instead of $\{\mathcal{D}, \boldsymbol{\mathcal{I}}\}$, to be consistent with our publication (Chu et al., 2019a). In the diffusion limit, the distribution function is nearly isotropic, so $\boldsymbol{\mathcal{K}} \approx \frac{1}{3}\mathcal{J}\,\boldsymbol{I}$ and $\boldsymbol{\mathcal{H}} \approx -\frac{1}{3}\tau\,\nabla\mathcal{J}$, and the two-moment model is approximately governed by (e.g., Jin and Levermore (1996))

$$\partial_t \mathcal{J} + \nabla\cdot\boldsymbol{\mathcal{H}} = 0 \quad \text{and} \quad \boldsymbol{\mathcal{H}} = -\tau\,\nabla\cdot\boldsymbol{\mathcal{K}}. \tag{3.21}$$

To interpret the diffusion limit in the context of IMEX schemes, we first write the stages of the IMEX scheme as

$$\vec{\mathcal{J}} = \mathcal{J}^n\,\vec{\boldsymbol{e}} - \Delta t\,\tilde{A}\,\nabla\cdot\vec{\boldsymbol{\mathcal{H}}}, \tag{3.22}$$

$$\vec{\boldsymbol{\mathcal{H}}} = \boldsymbol{\mathcal{H}}^n\,\vec{\boldsymbol{e}} - \Delta t\,\Big(\frac{1}{3}\tilde{A}\,\nabla\vec{\mathcal{J}} + \frac{1}{\tau}\,A\,\vec{\boldsymbol{\mathcal{H}}}\Big), \tag{3.23}$$

where $\vec{\mathcal{J}}$ and $\vec{\boldsymbol{\mathcal{H}}}$ can be the cell averages evolved with the DG method, $\vec{\boldsymbol{e}}$ is a vector of length of $\vec{\mathcal{J}}$ containing all ones, the divergence operator acts individually on the components of $\vec{\boldsymbol{\mathcal{H}}}$, and matrices $\tilde{A}$ and A gives the coefficients of the IMEX i-th stage. In the context of IMEX schemes, the diffusion limit (cf. the second equation in (3.21)) implies that the relationship $A\,\vec{\boldsymbol{\mathcal{H}}} = -\frac{1}{3}\tau\,\tilde{A}\,\nabla\vec{\mathcal{J}}$ should hold. Define the pseudoinverse of the implicit coefficient matrix for IMEX schemes of type ARS as

$$A^{-1} = \begin{pmatrix} 0 & 0 \\ 0 & \hat{A}^{-1} \end{pmatrix}.$$

Then, for the stages $i = 1, \ldots, s$,

$$\boldsymbol{\mathcal{H}}^{(i)} = -\frac{1}{3}\,\tau\,\vec{\boldsymbol{e}}_i^T A^{-1}\tilde{A}\,\vec{\boldsymbol{e}}\,\nabla\mathcal{J}^n + \mathcal{O}(\Delta t\,\tau^2), \tag{3.24}$$

where $\vec{\boldsymbol{e}}_i$ is the ith column of the $s \times s$ identity matrix and we have introduced the expansion $\vec{\mathcal{J}} = \mathcal{J}^n \vec{\boldsymbol{e}} + \mathcal{O}(\Delta t\, \tau)$. For $\boldsymbol{\mathcal{H}}^{(i)}$ to be accurate in the diffusion limit, we require that

$$\boldsymbol{e}_i^T A^{-1} \tilde{A}\, \boldsymbol{e} = 1, \quad i = 2, \ldots, s. \tag{3.25}$$

This proof is also given in Chu et al. (2019a). Equation (3.25) implies:

$$c_i = \tilde{c}_i, \quad i = 1, \ldots, s. \tag{3.26}$$

In Chu et al. (2019a) we have proven that only IMEX schemes of type ARS can be both diffusion-accurate and convex-invariant. See Appendix C in Chu et al. (2019a) for the proof.

3.5.4 PD-ARS IMEX schemes

Ideally, the scheme should be high-order accurate, convex-invariant, and work well in the asymptotic diffusion limit (characterized by frequent collisions and long time scales). Assuming an algebraic closure, which is based on Fermi-Dirac statistics, is used (i.e., the Eddington factor satisfies Equation (2.96)), we desire to construct an IMEX scheme satisfying all the requirements.

Unfortunately, coefficients satisfying the order conditions in Equations (3.15)-(3.16) and the conditions for convex-invariance do not exist for the standard IMEX scheme in Equations (3.13)-(3.14), unless a small time step is invoked that makes the scheme essentially explicit. To circumvent this problem, correction steps can be introduced after the assembly step in Equation (3.14) (e.g., see Chertock et al. (2015) and Hu et al. (2018)). However, the correction steps can impose time step constraints for realizability or accuracy in the diffusion limit, which ruin the efficiency gains expected from the IMEX scheme. Because of this, we sacrifice overall high-order accuracy, and aim for IMEX schemes that are high-order accurate in the streaming limit, diffusion accurate, and convex-invariant. Combining these requirements we

seek GSA IMEX schemes of type ARS with coefficients satisfying the following constraints (Chu et al., 2019b):

1. Consistency of the implicit coefficients:

$$\sum_{i=1}^{s} w_i = 1. \tag{3.27}$$

2. High-order accuracy in the streaming limit:

   For second-order accuracy:

$$\sum_{i=1}^{s} \tilde{w}_i = 1 \quad \text{and} \quad \sum_{i=1}^{s} \tilde{w}_i \, \tilde{c}_i = \frac{1}{2}. \tag{3.28}$$

   For third-order accuracy:

$$\sum_{i=1}^{s} \tilde{w}_i = 1, \quad \sum_{i=1}^{s} \tilde{w}_i \, \tilde{c}_i = \frac{1}{2}, \quad \sum_{i=1}^{s} \tilde{w}_i \, \tilde{c}_i^{\,2} = \frac{1}{3} \quad \text{and} \quad \sum_{i=1}^{s} \tilde{w}_i \, \tilde{a_{ij}} \tilde{c}_j = \frac{1}{6}. \tag{3.29}$$

3. Diffusion accuracy:

$$c_i = \tilde{c}_i, \quad i = 1, \ldots, s. \tag{3.30}$$

4. Convex-invariance:

$$\begin{aligned} &a_{ii} > 0, \quad c_{i0}, \tilde{c}_{i0} \geq 0, \quad \text{for} \quad i = 2, \ldots, s, \\ &\text{and} \quad c_{ij}, \tilde{c}_{ij} \geq 0, \quad \text{for} \quad i = 3, \ldots, s, \quad \text{and} \quad j = 2, \ldots, i-1, \end{aligned} \tag{3.31}$$

   with $\sum_{j=0}^{i-1} c_{ij} = 1$, for $i = 1, \ldots, s$, and

$$c_{\text{Sch}} := \min_{\substack{i=2,\ldots,s \\ j=0,2,\ldots,i-1}} \frac{1}{\hat{c}_{ij}}, \tag{3.32}$$

   with $c_{\text{Sch}} > 0$. Note $c_{\text{Sch}} \leq 1$. And the greater the c_{Sch}, the larger the time step can be.

5. Having less than five stages ($s \leq 4$). This is introduced for efficiency considerations to limit the number of implicit solves.

6. Are globally stiffly accurate: $a_{si} = w_i$ and $\tilde{a}_{si} = \tilde{w}_i, \quad i = 1, \ldots, s$.

Fortunately, these IMEX schemes are easy to find. We call the IMEX schemes satisfying the above conditions PD-ARS (see also Definition 3 in Chu et al. (2019a)), and we provide two optimal PD-ARS schemes below: PD-ARS2 and PD-ARS3, each limiting to the optimal second-order and third-order SSPRK schemes from Shu and Osher (1988), respectively.

PD-ARS2

The optimal 3-stage PD-ARS, denoted PD-ARS2, in the standard double Butcher tableau form, with explicit tableau ($\tilde{A}$) on the left and implicit tableau (A) on the right, is given by

$$\begin{array}{c|c} \tilde{c} & \tilde{A} \\ \hline & \tilde{w} \end{array} = \begin{array}{c|ccc} 0 & 0 & 0 & 0 \\ 1 & 1 & 0 & 0 \\ 1 & 1/2 & 1/2 & 0 \\ \hline & 1/2 & 1/2 & 0 \end{array} \qquad \begin{array}{c|c} c & A \\ \hline & w \end{array} = \begin{array}{c|ccc} 0 & 0 & 0 & 0 \\ 1 & 0 & 1 & 0 \\ 1 & 0 & 1/2 & 1/2 \\ \hline & 0 & 1/2 & 1/2 \end{array} \tag{3.33}$$

Note that its explicit tableau is SSPRK2. For this scheme, only two implicit solves are needed per time step, and $c_{\text{Sch}} = 1$, which implies that the time step restriction for preserving moment realizability is only due to the explicit part.

PD-ARS3

The optimal 4-stage PD-ARS, denoted as PD-ARS3, is given in its standard double Butcher tableau form (explicit tableau on the left and implicit tableau on the right)

by

$$\begin{array}{c|c} \tilde{c} & \tilde{A} \\ \hline & \tilde{w}^T \end{array} = \begin{array}{c|ccc} 1 & 1 & & \\ 1/2 & 1/4 & 1/4 & \\ 1 & 1/6 & 1/6 & 2/3 \\ \hline & 1/6 & 1/6 & 2/3 \end{array} \qquad \begin{array}{c|c} c & A \\ \hline & w^T \end{array} = \begin{array}{c|ccc} 0 & 0 & 0 & 0 \\ 1 & 0 & 1 & 0 \\ 1/2 & 0 & 1/4 & 1/4 \\ 1 & 0 & 1/6 & 1/6 & 2/3 \\ \hline & 0 & 1/6 & 1/6 & 2/3 \end{array} \tag{3.34}$$

Its explicit tableau is SSPRK3. This scheme requires three implicit solves per time step, and $c_{\text{Sch}} = 1$. Since PD-ARS3 is not more accurate than PD-ARS2 in collision-dominated regions (see our results in Chu et al. (2019b)), it may not offer any practical advantage over PD-ARS2.

3.5.5 Time Step Restriction

As mentioned in Section 3.5.2, a time step condition needs to be satisfied to ensure the realizability for each of the explicit Euler steps; namely $\max(\hat{c}_{ij}\,\Delta t) \leq \Delta t_{\text{Ex}}$, where Δt_{Ex} is the time step that ensures the explicit update with the transport operator is realizability preserving. Using c_{Sch} as defined in Equation (3.32), it can be written as

$$\Delta t \leq c_{\text{Sch}} \Delta t_{\text{Ex}}, \tag{3.35}$$

where c_{Sch} is a definite number given by the IMEX scheme, and Δt_{Ex} depends on the spatial discretization and numerical flux. To be precise, Δt_{Ex} is the time step condition that ensures the realizability of the explicit update $\boldsymbol{u}^{(j)} + \hat{c}_{ij}\,\Delta t\,\boldsymbol{\mathcal{T}}(\boldsymbol{u}^{(j)})$ for the cell average over space for each energy node. It can be proved (see Chu et al. (2019a) Lemma 7, with Lemma 5 and Lemma 6) that with DG discretization, the cell average (Equation (3.12) with $\phi_1 = 1$) is

$$\boldsymbol{u}_{\boldsymbol{K}} = \left|K^k\right| \sum_{q=1}^{N} \hat{w}_q \boldsymbol{u}_h\left(\hat{x}_q^k\right), \tag{3.36}$$

and the cell average of $\boldsymbol{\mathcal{T}}(\boldsymbol{u})$, which is the divergence operator in Equation (3.5), using the LF flux (Equation (3.10)) is

$$\left\langle \nabla \cdot \mathcal{F}\left(\boldsymbol{u}_h^{(j)}\right)\right\rangle_{\boldsymbol{K}} = \frac{1}{|\boldsymbol{K}|}\sum_{k=1}^{d}\int_{\tilde{\boldsymbol{K}}^k}\left(\widehat{\mathcal{F}}^k\left(\boldsymbol{u}_h^{(j)}\right)\Big|_{x_{\mathrm{H}}^k} - \widehat{\mathcal{F}}^k\left(\boldsymbol{u}_h^{(j)}\right)\Big|_{\chi_{\mathrm{L}}^k}\right) d\tilde{\boldsymbol{x}}^k, \tag{3.37}$$

and the time step Δt to ensure the realizability of the explicit update should satisfy

$$\lambda_{ij}^k \equiv \hat{c}_{ij}\Delta t/\left(\beta_k \hat{w}_N \left|K^k\right|\right) \leq 1. \tag{3.38}$$

Explicitly, (given by Remark 5 and proved in Chu et al. (2019a)) for the DG-IMEX scheme to be realizability-preserving, it is sufficient to set the time step such that

$$\Delta t \leq c_{\mathrm{Scn}} \min_k \left(\beta_k \hat{w}_N \left|K^k\right|\right), \tag{3.39}$$

where $\sum_{k=1}^{k}\beta_k = 1$, β_k is a set of strictly positive constants, $\hat{w}_N \in (0,1]$ is the weight of the N-th quadrature point within the element, $|K^k|$ is element volume.

3.6 Limiters

As we discussed in the previous section, it is clear that key to the realizability-preserving scheme is to express the updated cell-averages of the moments as convex combinations of elements in $\mathcal{R}$. Realizability of the cell-average of the updated moments is then guaranteed by convexity arguments. Sufficient conditions include: (i) the polynomial representation of the moments are realizable in a finite set of quadrature points in each element $\boldsymbol{K}$, and (ii) the timestep Δt is restricted by a CFL-like condition, which is somewhat stricter than that required for stability. Since the realizability-preserving scheme only guarantees the realizability of the cell-averages,

polynomial limiting is needed after each timestep (and after each stage in the Runge-Kutta method) to enforce realizability in the quadrature points. The discussion about these limiters is presented in this section.

3.6.1 Realizability-enforcing Limiter

First, we use the limiter in Liu and Osher (1996) to enforce the bounds on the zeroth moment $\mathcal{J}$. If $\mathcal{J} < 0$ for any of the quadrature points, we replace $\mathcal{J}_{\text{h}} \to \widetilde{\mathcal{J}}_{\text{h}}$, where the new polynomial representation is given by

$$\widetilde{\mathcal{J}}_h(\boldsymbol{x}) = \vartheta_1 \mathcal{J}_h(\boldsymbol{x}) + (1 - \vartheta_1)\, \mathcal{J}_{\mathbf{K}}, \tag{3.40}$$

where the limiter parameter $\vartheta_1 \in [0, 1]$ is given by

$$\vartheta_1 \equiv \min\left\{ \left| \frac{1 - \mathcal{J}_{\mathbf{K}}}{M_S - \mathcal{J}_{\mathbf{K}}} \right|, \left| \frac{\mathcal{J}_{\mathbf{K}}}{m_S - \mathcal{J}_{\mathbf{K}}} \right|, 1 \right\}, \tag{3.41}$$

with

$$M_S = \max_{\boldsymbol{x} \in S} \mathcal{J}_h(\boldsymbol{x}) \quad \text{and} \quad m_S = \min_{\boldsymbol{x} \in S} \mathcal{J}_h(\boldsymbol{x}). \tag{3.42}$$

Next, we ensure the realizability of the moments by following Zhang and Shu (2010). Denote $\widetilde{\boldsymbol{\mathcal{M}}}_{\text{h}} = (\widetilde{\mathcal{J}}_{\text{h}}, \boldsymbol{\mathcal{H}}_{\text{h}})^{\text{T}}$. If $\widetilde{\boldsymbol{\mathcal{M}}}_{\text{h}}$ lies outside $\mathcal{R}$ (defined by Equation (2.89)) for any quadrature point, i.e., $\gamma(\widetilde{\boldsymbol{\mathcal{M}}}_{\text{h}}) < 0$ (γ is concave function, defined by Equation (2.90)), there exists an intersection point of the straight line connecting $\boldsymbol{\mathcal{M}}_{\boldsymbol{K}} \in \mathcal{R}$ and $\widetilde{\boldsymbol{\mathcal{M}}}_{\text{h}}$ evaluated in the troubled quadrature point (denoted $\widetilde{\boldsymbol{\mathcal{M}}}_q$), with the surface of $\mathcal{R}$. Any point on this line is given by the convex combination

$$\boldsymbol{s}_q(\psi) = (1 - \psi)\, \boldsymbol{\mathcal{M}}_{\boldsymbol{K}} + \psi\, \widetilde{\boldsymbol{\mathcal{M}}}_q, \tag{3.43}$$

where $\psi \in [0, 1]$, and the intersection point is obtained by solving the equation $\gamma(\boldsymbol{s}_q(\psi)) = 0$ for ψ, using the bisection algorithm. We then replace the polynomial

representation $\widetilde{\boldsymbol{\mathcal{M}}}_{\mathrm{h}} \rightarrow \widehat{\boldsymbol{\mathcal{M}}}_{\mathrm{h}}$, where

$$\widehat{\boldsymbol{\mathcal{M}}}_{\mathrm{h}} = \theta_2 \, \widetilde{\boldsymbol{\mathcal{M}}}_{\mathrm{h}} + (1 - \theta_2) \, \boldsymbol{\mathcal{M}}_{\mathrm{h}}, \tag{3.44}$$

and θ_2 is the smallest ψ obtained in the element by considering all the troubled quadrature points, such that

$$\theta_2 \equiv \min_q \psi_q \tag{3.45}$$

This limiter is conservative in the sense that it preserves the cell-average, i.e., $\widehat{\boldsymbol{\mathcal{M}}}_{\boldsymbol{K}} = \widetilde{\boldsymbol{\mathcal{M}}}_{\boldsymbol{K}} = \boldsymbol{\mathcal{M}}_{\boldsymbol{K}}$. The proof is described in our published article (Chu et al., 2019a). The basic key to the realizability-preserving scheme is to express the updated cell-averages of the moments as positive combinations of elements in $\mathcal{R}$. Realizability of the cell-average of the updated moments is then guaranteed by convexity arguments. Sufficient conditions include: (i) the polynomial representation of the moments are realizable in a finite set of quadrature points in each element $\boldsymbol{K}$, and (ii) the timestep Δt is restricted by a CFL-like condition, which is somewhat stricter than that required for stability.

3.7 Numerical Tests

In this section, we present numerical results to verify the accuracy and realizability-preserving property of the DG-IMEX methods developed in this chapter. These tests include numerical accuracy, stability, and realizability tests. The first set of tests (Section 3.7.1) is desiged to compare the time integration schemes in various regimes. The test in Section 3.7.2 is designed to demonstrate the convex-invariance of PD-ARS schemes. These results are also published in Chu et al. (2019a) and Chu et al. (2019b).

3.7.1 Smooth Sine Wave Tests

Problems with known smooth solutions are made to examine the accuracy of the time integration scheme, PDARSs (discussed in Section 3.5.4), in various regimes. (A version of this problem is discussed in Chu et al. (2019a) for PD-ARS2 and Chu et al. (2019b) for PD-ARS3.)

These tests are designed to compare the accuracy of these PD-ARS schemes in streaming, absorption, and scattering-dominated regimes. They are all one-dimensional. For all tests in this section, we use third order accurate spatial discretization (i.e., polynomials of degree $k = 2$) and we employ the maximum entropy closure in the low occupancy limit (i.e., the Minerbo closure). We compare results obtained using IMEX schemes proposed here (PD-ARS) with IMEX schemes from Hu et al. (2018) (PA2), McClarren et al. (2008) (PC2), Pareschi and Russo (2005) (SSP2332), and Cavaglieri and Bewley (2015) (RKCB2). In the streaming test, we also include results obtained with second-order and third-order accurate explicit strong stability-preserving Runge-Kutta methods Gottlieb et al. (2001) (SSPRK2 and SSPRK3, respectively). The time step is set to $\Delta t = 0.1 \times \Delta x$.

To compare the numerical results to analytic solutions, the averaged absolute error or the averaged relative error are computed in the L^1-error norm.

Streaming Sine Wave

The sine wave streaming test is designed to test accuracy in the free-steaming regime; i.e. $\sigma_A = \sigma_S = 0$ for ξ in Equation (3.6). A periodic domain of unit length is used, and the initial condition is

$$\mathcal{J}_0 = \boldsymbol{\mathcal{H}}_0 = 0.5 + 0.49 \times \sin\big(2\pi\, x\big). \tag{3.46}$$

We evolve the test until the sine wave has completed 10 crossings of the domain. Figure 3.7.1 plots the absolute error for the number density versus the number of elements N. We see that the errors obtained with SSPRK3 and PD-ARS3 are smallest

and decrease as N^{-3}, as expected for a scheme combining third-order accurate time stepping with third-order accurate spatial discretization. For all of the other schemes, using second-order accurate explicit time stepping, the error decreases as N^{-2}. Among the second-order schemes, SSP2332 has the smallest error. In the streaming limit, the PD-ARS schemes reduce to SSPRK schemes — PD-ARS2 to SSPRK2 and PD-ARS3 to SSPRK3, respectively. Therefore, the absolute errors of PD-ARS schemes and SSPRK schemes are indistinguishable.

Damping Sine Wave

The next test, adapted from Skinner and Ostriker (2013), is designed for absorption-dominated regimes, with $\sigma_S = 0$ and $f_0 = 0$, which results in exponential damping of the wave amplitude. A periodic domain $D = \{x : x \in [0, 1]\}$ and initial condition

$$\mathcal{J}_0 = \boldsymbol{\mathcal{H}}_0 = 0.5 + 0.49 \times \sin\big(2\pi\, x\big), \tag{3.47}$$

are used. The amplitude of the analytical solution decreases as $e^{-\sigma_A t}$. For $\sigma_A = 0.1$, 1 and 10 we evolve the test until the initial condition has been damped by a factor e^{-10}. Figure 3.7.2 shows convergence results of the test in the relative error. Results for $\sigma_A = 0.1$, 1, and 10 are plotted with red, green, and blue lines, respectively. SSP2332 is the most accurate among these schemes for $\sigma_A = 1$ and 10. For $\sigma_A = 0.1$, PD-ARS2 is the most accurate scheme for $N = 8$ and $N = 16$. We have seen the same behavior for the scheme proposed by McClarren et al. (2008) (PC2 in Chu et al. (2019a)). Since $N = 8$ and $N = 16$ are special cases, we do not recommend PD-ARS2 over SSP2332 for the damping problem. Only SSP2332, a second-order accurate scheme, displays a second-order convergence rate. The PD-ARS schemes are first-order accurate.

Diffusion Sine Wave

The final test with known smooth solutions, adopted from Radice et al. (2013), is the sine wave diffusion test; i.e. $\sigma_A = 0$ and $f_0 = 0$. A periodic domain $D = \{x : x \in$

$[-3, 3]\}$ with initial conditions

$$\mathcal{J}_0 = 0.5 + 0.49 \times \sin\big(\frac{\pi\, x}{3}\big), \tag{3.48}$$

$$\mathcal{H}_0 = -\frac{1}{3\sigma_S}\frac{\partial \mathcal{J}_0}{\partial x}, \tag{3.49}$$

are used. The reference diffusion solution is given by

$$\mathcal{J} = \mathcal{J}_0 \times \exp\big(-\frac{\pi^2 t}{27\sigma_S}\big), \tag{3.50}$$

$$\mathcal{H} = (3\,\sigma_S)^{-1}\partial_x \mathcal{J}. \tag{3.51}$$

We evolve with $\sigma_S = 10^2$, 10^3, and 10^4, and adjust the end time so that $t_{\text{end}}/\sigma_S = 1$, at which time the amplitude of the sine wave has been reduced by a factor $e^{-\pi^2/27} \approx 0.694$ for all values of σ_S. Figure 3.7.3 shows the absolute error, obtained using different values of σ_S, for various IMEX schemes at $t = t_{\text{end}}$, versus N. Results for $\sigma_S = 10^2$, 10^3, and 10^4 are plotted with red, green, and blue lines, respectively. SSP2332 and PD-ARS schemes display third-order accuracy for the number density, $\mathcal{J}$, and second-order accuracy for $\mathcal{H}_x$, and their errors are difficult to distinguish. For $\sigma = 10^2$, the errors in the number density $\mathcal{J}$ do not drop below 10^{-6} due to differences between the two-moment model and the diffusion equation used to obtain the analytic solution. For larger values of the scattering opacity, $\sigma = 10^3$ or 10^4, the two-moment model agrees better with the diffusion model, and we observe convergence over the entire range of N. PD-ARS2 behaves as well as SSP2332 in the diffusion region but requires 33% less implicit solves per time step.

Summary Here are the behaviors we observed:

- In the streaming regime, PD-ARS schemes converge as expected and give as accurate results as the explicit strong-stability-preserving Runge-Kutta methods in Gottlieb et al. (2001).

- In the absorption-dominated regime, PD-ARS schemes converge with a first-order convergence rate.

- In the scattering-dominated regime, using a third-order DG method for spatial discretization, PD-ARS schemes display third-order accuracy for the number density, $\mathcal{J}$, and second-order accuracy for $\mathcal{H}$. In our particular problem, PD-ARS scheme works as well as Pareschi and Russo (2005) (SSP2332), but PD-ARS2 requires 33% less calculation. A convergent result was observed with increasing scattering opacity.

3.7.2 Neutrino Stationary-State Test

In this test, we consider a more "realistic" test: two-dimensional multigroup neutrino transport with emission, absorption, and isoenergetic scattering through a stationary background. This test is designed to test the realizability-preserving properties of the PD-ARS schemes. In the left panel in Figure 3.7.4, we plot the thermal state of the background, which mimics the conditions in a collapsed stellar core (Messer, 2000):

$$\text{Mass Density:} \quad \rho = 4 \times 10^{14} \times \frac{7.5}{(7.5 + (r/5\ \text{km})^4)}\ \text{g cm}^{-3}, \tag{3.52a}$$

$$\text{Temperature:} \quad T = 1.5 \times 10^{11} \times \frac{1}{1 + (r/50\ \text{km})^2}\ \text{K}, \tag{3.52b}$$

$$\text{Electron Fraction:} \quad Y_e = 0.25 \times \left(1 + \frac{1}{1 + (r/50\ \text{km})^{-12}}\right), \tag{3.52c}$$

where the radius $r = \sqrt{(x^1)^2 + (x^2)^2}$ is in kilometers. In the right panel in Figure 3.7.4 we plot the neutrino opacities, computed by interpolating in a pre-calculated opacity table based on Bruenn (1985) (Bruenn 1985) and Steiner et al. (2010) (SFHo) EOS. This test is computed using Cartesian coordinates on a two-dimensional domain $D = \{\boldsymbol{x} \in \mathbb{R}^2 : x^1 \in [0, 200]\ \text{km}, x^2 \in [0, 200]\ \text{km}\}$, using a grid of 128 elements in each direction, 10 energy groups covering 0-300 MeV, reflecting inner boundaries, and outflow outer boundaries. Because we use Cartesian coordinates

in two spatial dimensions, this problem has cylindrical geometry, and results in an artificial stratification of the radiation quantities compared to a three-dimensional model or a spherical symmetry model. We initialize the neutrino number density to $\mathcal{J} = 10^{-99}$ per phase space volume, the number flux density to $\boldsymbol{\mathcal{H}} = 0$, and evolve until a thermally and dynamically approximate steady state is reached ($t = 5$ ms). The background is kept fixed during the entire run. For this test, we employed both CB and Minerbo closures. We attempted to run this test with our PD-ARS schemes, SSP2332 from Pareschi and Russo (2005), IMEXRKCB2 proposed by Cavaglieri and Bewley (2015), and the IMEX PC2 scheme proposed by McClarren et al. (2008). Only the PD-ARS schemes produce realizable moments and can evolve to a steady state with either CB or Minerbo closure. SSP2332 and IMEX PC2 failed after a few time steps with either CB or Minerbo closure because of the development of unrealizable moments. Even though IMEXRKCB2 with Minerbo closure can run through and reach a steady state in this test, its results are different from that of PD-ARS schemes with CB closure, and there is no guarantee of stability. To be precise, IMEXRKCB2 with Minerbo closure ends at a same stationary state as PD-ARS schemes with Minerbo closure. But IMEXRKCB2 with Minerbo closure has different dynamics with PD-ARS schemes with Minerbo closure. The maximum relative difference in number density during the evolution is 5% at the outer region and in the first 1 ms. The difference in the final stationary state is depended on the closure method other than the time integrator.

Results obtained with the IMEX PD-ARS schemes are plotted in Figure 3.7.5 for various times: $t = 0.01$ ms (top panels), 0.35 ms (middle panels), and 5.0 ms (bottom panels). In the left column, we plot the solution in the $|\boldsymbol{\mathcal{H}}|\mathcal{J}$-plane. In the middle column, we show scatter plots of the number density $\mathcal{J}$ versus radius for select neutrino energies: 5 MeV (red lines), 16 MeV (magenta lines), and 93 MeV (blue lines). In the right column, we plot the flux factor $|\boldsymbol{\mathcal{H}}|/\mathcal{J}$ versus radius for the same neutrino energies as in the middle column. In the left panels, each solution point in the domain is marked as a red dot in the $|\boldsymbol{\mathcal{H}}|\mathcal{J}$-plane, and the realizable domain is

shown as the light blue region. The figures show that all the states in the simulation with the PD-ARS schemes are realizable. In the middle and right column, we can see how the neutrinos are generated near the core, stream out, and eventually reach an equilibrium distribution over the phase space. The oscillations in the flux factor seen in the right columns are associated with steep gradients in the radiation field, as the initial transient propagates through the computational domain. Note that we do not apply any limiters to prevent oscillations in the numerical solution, and these will likely go away when we implement slope limiters; e.g., as described in Cockburn and Shu (1998). The fact that we can still evolve the solution to a steady state speaks to the robustness of the scheme.

3.8 Outlook

We developed a realizability-preserving DG-IMEX scheme for a two-moment model of fermion transport in Cartesian coordinates, a linear collision operator, and a fixed material background in this chapter. The scheme employs algebraic closures based on Fermi-Dirac statistics. It combines a time step restriction, a realizability-enforcing limiter, and a convex-invariant time integrator to maintain point-wise realizability of the moments. Two PD-ARS schemes are proposed. In the streaming limit, the one with SSPRK2 has second-order accuracy, while the other with SSPRK3 has third-order accuracy, and both have the strong-stability preserving property. Their accuracy was demonstrated on problems with known smooth solutions in streaming, absorption-dominated, and scattering-dominated regimes. The neutrino transport test with emission, absorption, and isoenergetic scattering through a stationary background was designed to test the convex-invariance of our PD-ARS schemes. The neutrino stationary state test shows that a method combining an algebraic closure based on Fermi-Dirac statistics and convex-invariant time integration is promising for robust CCSN simulation. The realizability of the fermionic two-moment model

depends sensitively on the closure procedure. This is one of the most important findings of this chapter.

Curvilinear coordinates, scattering with energy exchange, and relativistic effects were not included by now. To solve more realistic problems of scientific interest, it will be necessary to include all the additional physical effects. Nevertheless, adding these considerations is not simply repeating the derivative with changes in the IMEX equations. It not only increases the complexity to the model, but also can lead to unsolvable questions. In addition, simply interpreting the requirements from physics to the evolved variables are not trivial, such as interpreting the requirement on the primitive moments to the requirement on the evolved comoving variables. Our efforts to this end will be presented in the next chapter.

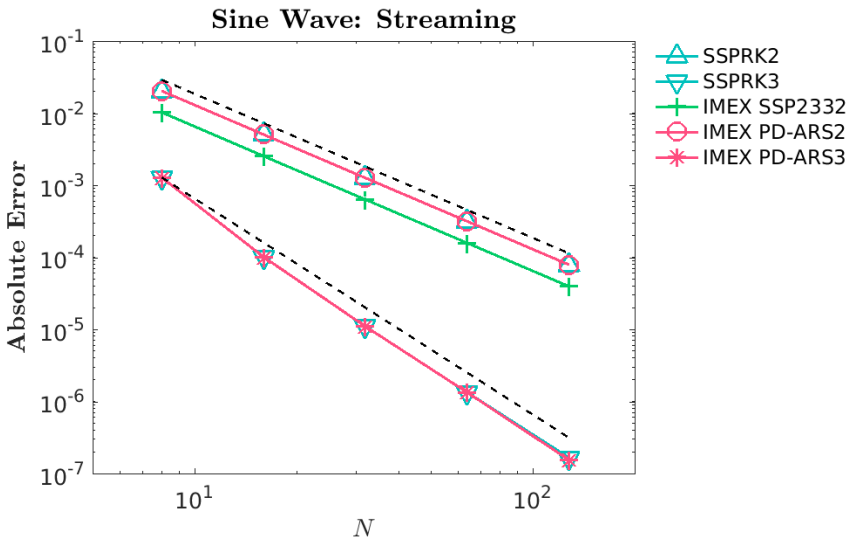

Figure 3.7.1: Absolute error versus number of elements, N, for the streaming sine wave test. Results employing various time stepping schemes are compared: SSPRK2 (cyan triangles pointing up), SSPRK3 (cyan triangles pointing down), SSP2332 (green crosses), PD-ARS2 (light red circles) and PD-ARS3 (light red asterisks). Black dashed reference lines are proportional to N^{-2} (top) and N^{-3} (bottom), respectively. Published in Chu et al. (2019b).

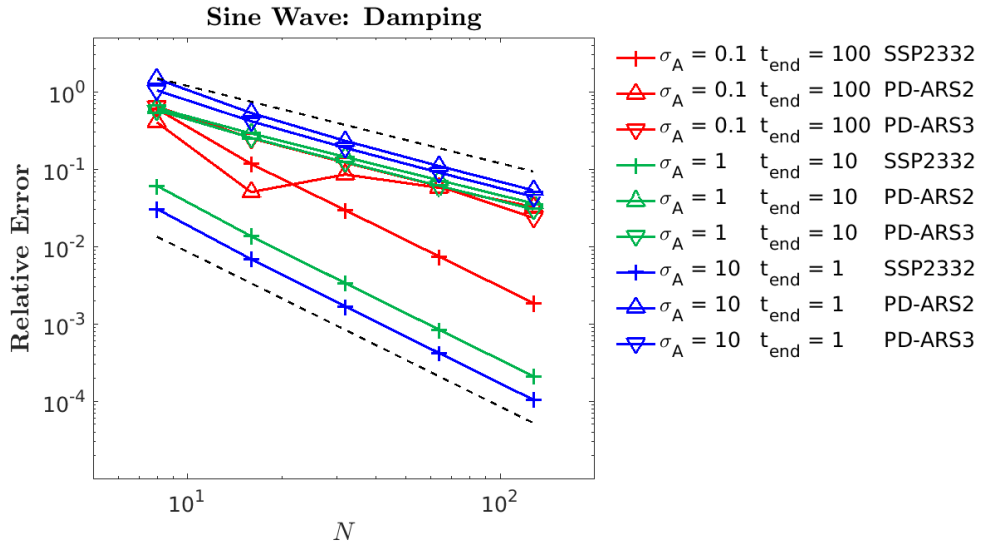

Figure 3.7.2: Relative error versus number of elements, N, for the damping sine wave test. Results for different values of the absorption opacity, σ_A, employing various IMEX time stepping schemes, are compared. Errors for $\sigma_A = 0.1$, 1, and 10 are plotted with red, green, and blue lines, respectively. The IMEX schemes employed are SSP2332 (+), PD-ARS2 (triangles pointing up) and PD-ARS3 (triangles pointing down). Black dashed reference lines are proportional to N^{-1} (top) and N^{-2} (bottom), respectively. Published in Chu et al. (2019b).

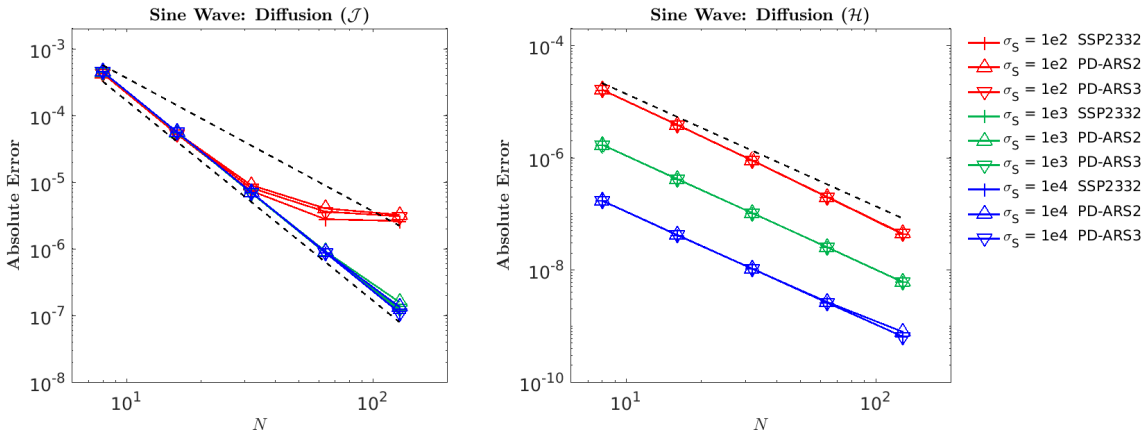

Figure 3.7.3: Absolute error for the number density $\mathcal{J}$ (left) and the number flux $\mathcal{H}_x$ (right) versus number of elements for the sine wave diffusion test. Results with different values of the scattering opacity, σ_S, employing different IMEX schemes, are compared. Errors with $\sigma_S = 10^2$, 10^3, and 10^4 are plotted with red, green, and blue lines, respectively. The IMEX schemes employed are: SSP2332 (+), PD-ARS2 (triangles pointing up), and PD-ARS3 (triangles pointing down). Black dashed lines in the left plot are reference lines proportional to N^{-2} (top) and N^{-3} (bottom), respectively. The black dashed line in the right plot is a reference line proportional to N^{-2} . Published in Chu et al. (2019b).

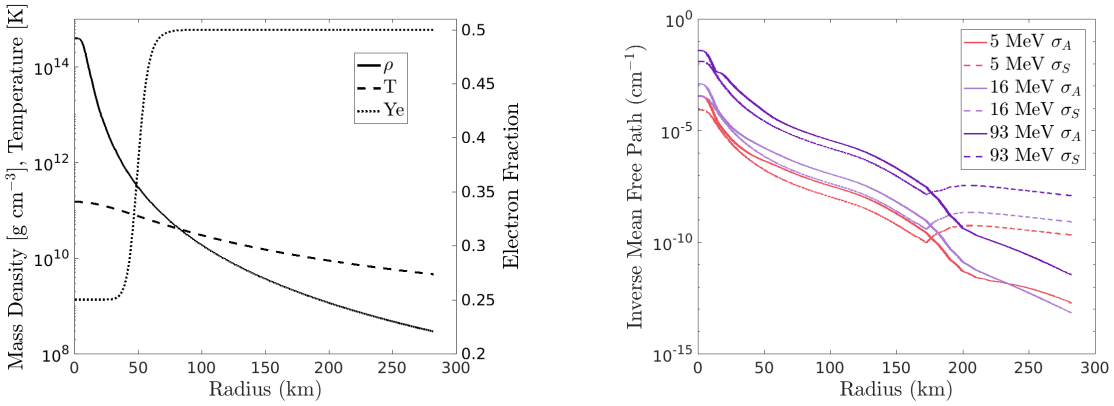

Figure 3.7.4: Left panel: thermal state of the background versus radius in the neutrino stationary-state test: mass density (solid line), temperature (dashed line), and electron fraction (dotted line). Right panel: corresponding opacities for select neutrino energies: absorptivity (σ_A) and scattering opacity (σ_S). Published in Chu et al. (2019b).

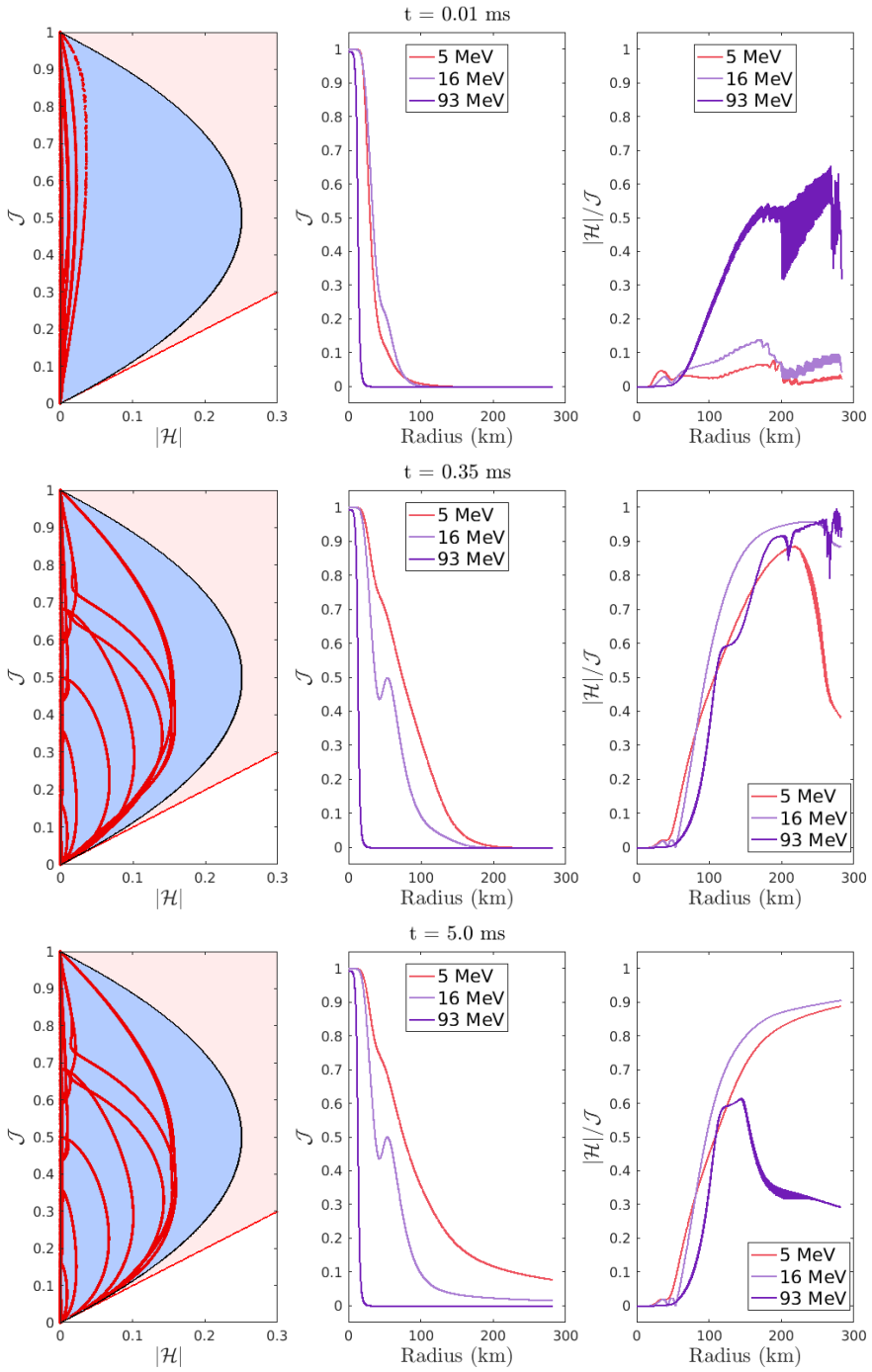

Figure 3.7.5: Results from the neutrino stationary-state test: Moments relative to the realizable domain (left column, the light blue domain is for $f \in [0, 1]$, with the black-solid-line as its boundary, while the light red domain is for $f \geq 0$, with the thin red solid line as its boundary). The number density $\mathcal{J}$ versus radius (middle column), and the flux factor $|\boldsymbol{\mathcal{H}}|/\mathcal{J}$ versus radius (right column). $t = 0.01$ ms, 0.35 ms, and 5.0 ms. For the plots in the left column, each $\boldsymbol{\mathcal{M}} = (\mathcal{J}, \boldsymbol{\mathcal{H}})^T$ state is marked by a red dot, which are all inside the light blue region (the realizable domain for fermions). The results of PD-ARS2 and PD-ARS3 are indistinguishable in these plots. Published in Chu et al. (2019b).

Chapter 4

DG-IMEX Method for the $\mathcal{O}(v/c)$ Two-Moment Model

As we have discussed in Section 1.1, due to fluid motion and spacetime curvature, CCSNe simulations must include special and general relativistic effects, such as Doppler and red or blue shifts of the neutrino energy spectra. The simulations must also include all important neutrino weak interactions. In this chapter, we extend the numerical method in Chapter 3, which is for $\mathcal{O}(1)$ two-moment model with a simplified collision term for neutrino weak interactions, and develop a numerical method that solves the $\mathcal{O}(v/c)$ two-moment model with a more comprehensive collision term. In exact terms, we aim to design and implement numerical methods for $\mathcal{O}(v/c)$ two-moment model, which is conservative for lepton number and energy, robust in the sense that moments remain realizable, able to capture asymptotic limits (e.g., diffusion limit), efficient integration of collision terms, integrated into Flash-X for CCSN simulations, high physical fidelity in microphysics sector by using tabulate modern opacity set in `WeakLib` efficient use of GPUs, and can be extend to form with general relativity. The numerical implementation with the nonlinear solver for the collision term will be presented in Chapter 5, and we focus on the method design in this chapter.

4.1 Introduction

Comparing with Chapter 3, the model in this chapter improves physical fidelity in both the collision term and the inclusion of relativistic effects. It is also formulated for curvilinear spatial coordinates. The discretization method and IMEX time integration scheme are inherited from the $\mathcal{O}(1)$ work, while the metric dependency and limiters are newly designed. The coupled fluid-radiation field update and the implicit solver will be discussed in the next chapter.

4.2 Model

Our model in the $\mathcal{O}(v/c)$ limit is based on the general relativistic moment formalism (Shibata et al., 2011; Cardall et al., 2013), using laboratory-frame coordinate basis coordinates ($\boldsymbol{x}$ and t), and comoving-frame spherical-polar momentum-space coordinates (ε, ϑ, and φ).

In curvilinear coordinates and with all collision terms in Bruenn (1985) (see Section 2.4.2 for collision terms in the moment equations), the moment equations for the number density and number flux, which are given by Equation (2.53) and Equation (2.54), with species index s can be written as

$$\partial_t\big(\mathcal{D}_s + v^i\,\mathcal{I}_{si}\big) + \frac{1}{\sqrt{\gamma}}\partial_i\big(\sqrt{\gamma}\,\big[\mathcal{I}_s{}^i + \mathcal{D}_s\,v^i\big]\big) - \frac{1}{\varepsilon^2}\partial_\varepsilon\big(\varepsilon^3\,\big[\mathcal{I}_{si}\,\partial_t v^i + \mathcal{K}_s{}^i_k\,\nabla_i v^k\big]\big) = \frac{1}{4\pi}\int_{\mathbb{S}^2}\mathcal{C}_s(f)\frac{d\boldsymbol{\omega}}{\varepsilon}, \tag{4.1}$$

and

$$\partial_t\big(\mathcal{I}_{sj} + v^i\,\mathcal{K}_{sij}\big) + \frac{1}{\sqrt{\gamma}}\partial_i\big(\sqrt{\gamma}\,\big[\mathcal{K}_s{}^i_j + \mathcal{I}_{sj}\,v^i\big]\big) - \frac{1}{\varepsilon^2}\partial_\varepsilon\big(\varepsilon^3\,\big[\mathcal{K}_{sjk}\,\partial_t v^k + \mathcal{L}_s{}^i_{kj}\,\nabla_i v^k\big]\big) = \frac{1}{2}\big(\mathcal{K}_s{}^{ik} + \mathcal{I}_s{}^i\,v^k + v^i\,\mathcal{I}_s{}^k\big)\,\partial_j\gamma_{ik} + \big(\mathcal{K}_{sjk}\,\partial_t v^k + \mathcal{L}_s{}^i_{kj}\,\nabla_i v^k\big) - \big(\mathcal{D}_s\,\partial_t v_j + \mathcal{I}_s{}^i\,\partial_i v_j\big) + \frac{1}{4\pi}\int_{\mathbb{S}^2}\mathcal{C}_s(f)\ell_j\frac{d\boldsymbol{\omega}}{\varepsilon}, \tag{4.2}$$

respectively. The high order moments, $\mathcal{K}_{sjk}$ and $\mathcal{L}_s{}^i{}_{kj}$, in the above equations are computed using the closure method, as we discussed in Section 2.5.2.

Equation (4.1) and (4.2) can be written in a compact form, i.e.,

$$\partial_t \boldsymbol{\mathcal{U}} + \frac{1}{\sqrt{\gamma}}\partial_i(\sqrt{\gamma}\,\boldsymbol{\mathcal{F}}^i(\boldsymbol{\mathcal{U}},\boldsymbol{v})) + \frac{1}{\varepsilon^2}\partial_\varepsilon(\varepsilon^2\,\boldsymbol{\mathcal{F}}^\varepsilon(\boldsymbol{\mathcal{U}},\boldsymbol{v})) = \boldsymbol{\mathcal{S}}(\boldsymbol{\mathcal{U}},\boldsymbol{v}) + \boldsymbol{\mathcal{C}}(\boldsymbol{\mathcal{U}},\boldsymbol{u}), \tag{4.3}$$

where the solution vector $\boldsymbol{\mathcal{U}}$, and position and energy space fluxes, $\boldsymbol{\mathcal{F}}^i$ and $\boldsymbol{\mathcal{F}}^\varepsilon$, include all N_s neutrino species; i.e., $\boldsymbol{\mathcal{U}} = \{\boldsymbol{\mathcal{U}}_s\}_{s=1}^{N_s}$, $\boldsymbol{\mathcal{F}}^i = \{\boldsymbol{\mathcal{F}}_s{}^i\}_{s=1}^{N_s}$, and $\boldsymbol{\mathcal{F}}^\varepsilon = \{\boldsymbol{\mathcal{F}}_s{}^\varepsilon\}_{s=1}^{N_s}$, where

$$\boldsymbol{\mathcal{U}}_s = \begin{bmatrix} \mathcal{D}_s + v^i\,\mathcal{I}_{si} \\ \mathcal{I}_{sj} + v^i\,\mathcal{K}_{sij} \end{bmatrix}, \quad \boldsymbol{\mathcal{F}}_s{}^i = \begin{bmatrix} \mathcal{I}_s{}^i + \mathcal{D}_s\,v^i \\ \mathcal{K}_s{}^i{}_j + \mathcal{I}_{sj}\,v^i \end{bmatrix}, \quad \text{and} \quad \boldsymbol{\mathcal{F}}_s{}^\varepsilon = -\varepsilon \begin{bmatrix} \mathcal{K}_s{}^i{}_k \\ \mathcal{L}_s{}^i{}_{kj} \end{bmatrix} \nabla_i v^k. \tag{4.4}$$

Note, the $\partial_t v$ terms in $\boldsymbol{\mathcal{F}}_s{}^\varepsilon$ are dropped. Similarly, the sources on the right-hand side of Eq. (4.3) are $\boldsymbol{\mathcal{S}} = \{\boldsymbol{\mathcal{S}}_s\}_{s=1}^{N_s}$ and $\boldsymbol{\mathcal{C}} = \{\boldsymbol{\mathcal{C}}_s\}_{s=1}^{N_s}$, where

$$\boldsymbol{\mathcal{S}}_s = \begin{bmatrix} 0 \\ \frac{1}{2}\left(\mathcal{K}_s{}^{ik} + \mathcal{I}_s{}^i\,v^k + v^i\,\mathcal{I}_s{}^k\right)\partial_j\gamma_{ik} + \left(\mathcal{L}_s{}^i{}_{kj}\,\nabla_i v^k - \mathcal{I}_s{}^i\,\partial_i v_j\right) \end{bmatrix}, \tag{4.5}$$

$\boldsymbol{\mathcal{S}}_s$ also drops the $\partial_t v$ terms, and

$$\boldsymbol{\mathcal{C}}_s = \begin{bmatrix} \frac{1}{4\pi}\int_{\mathbb{S}^2}\mathcal{C}_s(f)\frac{d\boldsymbol{\omega}}{\varepsilon} \\ \frac{1}{4\pi}\int_{\mathbb{S}^2}\mathcal{C}_s(f)\ell_j\frac{d\boldsymbol{\omega}}{\varepsilon} \end{bmatrix}, \tag{4.6}$$

$\boldsymbol{\mathcal{C}}_s$ depends on fluid thermal state, for example, $\boldsymbol{u} = (\rho, T, Y_e)^{\mathrm{T}}$.

Because of the pair process in the collision term, the moments for neutrinos and their antineutrinos are coupled. Therefore, for a model with electron neutrinos and electron antineutrinos, the solution vector $\boldsymbol{\mathcal{U}}$ is

$$\boldsymbol{\mathcal{U}} = (\mathcal{D} + v^i\,\mathcal{I}_i, \mathcal{I}_j + v^i\,\mathcal{K}_{ij}, \bar{\mathcal{D}} + v^i\bar{\mathcal{I}}_i\,, \bar{\mathcal{I}}_i + v^i\,\bar{\mathcal{K}}_{ij})^{\mathrm{T}}, \tag{4.7}$$

with $(\mathcal{D}, \mathcal{I}_i)^{\mathrm{T}} = \boldsymbol{\mathcal{M}}$ for electron neutrinos and $(\bar{\mathcal{D}}, \bar{\mathcal{I}}_i)^{\mathrm{T}} = \bar{\boldsymbol{\mathcal{M}}}$ for electron antineutrinos. Neutrino–matter interactions allow matter and neutrinos to exchange lepton number, momentum, and energy. Furthermore, the relativistic effects (Doppler and red/blue shifts of the neutrino energy spectra) are fluid-field dependent. As a result, a fluid–radiation coupled system is formed.

4.3 Phase-Space Discretization

The phase-space discretization is essentially the same as that described in Chapter 3, but extended to include curvilinear spatial coordinates and special relativistic effects to $\mathcal{O}(v/c)$. The moment equations is discretized in energy-position space using the DG method. We use $V_{\boldsymbol{K}}$ to denote the proper volume of the element, which is

$$V_{\boldsymbol{K}} = \int_{\boldsymbol{K}} dV, \quad \text{where} \quad dV = \sqrt{\gamma}\, d\boldsymbol{x}\, dV_{\varepsilon} = \sqrt{\gamma}\, d\boldsymbol{x}\, \varepsilon^2 d\varepsilon\,. \tag{4.8}$$

The semi-discrete DG problem is to find $\boldsymbol{\mathcal{U}}_{\mathrm{h}} \in \mathbb{V}^{N_{\boldsymbol{x}}, N_{\varepsilon}}$ that approximates $\boldsymbol{\mathcal{U}}$ such that

$$\begin{aligned}
&\partial_t \int_{\boldsymbol{K}} \boldsymbol{\mathcal{U}}_{\mathrm{h}}\, \phi\, dV \\
&+ \sum_{i=1}^{3} \int_{K^{\varepsilon}} \int_{\tilde{\boldsymbol{K}}^i} \left(\sqrt{\gamma}\, \widehat{\boldsymbol{\mathcal{F}}}^i(\boldsymbol{\mathcal{U}}_{\mathrm{h}}, \boldsymbol{v}_{\mathrm{h}})\, \phi\big|_{x^i_{\mathrm{H}}} - \sqrt{\gamma}\, \widehat{\boldsymbol{\mathcal{F}}}^i(\boldsymbol{\mathcal{U}}_{\mathrm{h}}, \boldsymbol{v}_{\mathrm{h}})\, \phi\big|_{x^i_{\mathrm{L}}} \right) d\tilde{\boldsymbol{x}}^i\, dV_{\varepsilon} \\
&\quad - \sum_{i=1}^{3} \int_{\boldsymbol{K}} \left(\boldsymbol{\mathcal{F}}^i(\boldsymbol{\mathcal{U}}_{\mathrm{h}}, \boldsymbol{v}_{\mathrm{h}})\, \frac{\partial \phi}{\partial x^i} \right) dV \\
&+ \int_{\boldsymbol{K}} \left(\varepsilon^2 \widehat{\boldsymbol{\mathcal{F}}^{\varepsilon}}(\boldsymbol{\mathcal{U}}_{\mathrm{h}}, \boldsymbol{v}_{\mathrm{h}})\, \phi\big|_{\varepsilon_{\mathrm{H}}} - \varepsilon^2 \widehat{\boldsymbol{\mathcal{F}}^{\varepsilon}}(\boldsymbol{\mathcal{U}}_{\mathrm{h}}, \boldsymbol{v}_{\mathrm{h}})\, \phi\big|_{\varepsilon_{\mathrm{L}}} \right) dV - \int_{\boldsymbol{K}} \boldsymbol{\mathcal{F}}^{\varepsilon}(\boldsymbol{\mathcal{U}}_{\mathrm{h}}, \boldsymbol{v}_{\mathrm{h}})\, \frac{\partial \phi}{\partial \varepsilon}\, dV \\
&= \int_{\boldsymbol{K}} \boldsymbol{\mathcal{S}}(\boldsymbol{\mathcal{U}}_{\mathrm{h}}, \boldsymbol{v}_{\mathrm{h}})\, \phi\, dV + \int_{\boldsymbol{K}} \boldsymbol{\mathcal{C}}(\boldsymbol{\mathcal{U}}_{\mathrm{h}}, \boldsymbol{u}_{\mathrm{h}})\, \phi\, dV,
\end{aligned} \tag{4.9}$$

holds for all $\phi \in \mathbb{V}^{N_{\boldsymbol{x}}, N_{\varepsilon}}$ and all $\boldsymbol{K} \in \mathbb{K}$. Similar to in Chapter 3 for the $\mathcal{O}(1)$ model, $\widehat{\boldsymbol{\mathcal{F}}^i}$ (numerical flux in spatial) and $\widehat{\boldsymbol{\mathcal{F}}^{\varepsilon}}$ (numerical flux in energy) are numerical fluxes which approximate $\boldsymbol{\mathcal{F}}^i$ and $\boldsymbol{\mathcal{F}}^{\varepsilon}$, respectively, on the surface of element $V_{\boldsymbol{K}}$. For the

spatial divergence in Eq. (4.9), with notation

$$x^{i,\pm} \equiv \lim_{\delta \to 0^+} x^i \pm \delta, \tag{4.10}$$

the numerical flux in the i-th spatial dimension, i.e.,

$$\widehat{\boldsymbol{\mathcal{F}}^i}(\boldsymbol{\mathcal{U}}_h, \boldsymbol{v}_h; x^i, \tilde{\boldsymbol{z}}^i) = \boldsymbol{f}^i(\boldsymbol{\mathcal{U}}_h(x^{i,-}, \tilde{\boldsymbol{z}}^i), \boldsymbol{\mathcal{U}}_h(x^{i,+}, \tilde{\boldsymbol{z}}^i), \hat{\boldsymbol{v}}(x^i, \tilde{\boldsymbol{x}}^i)), \tag{4.11}$$

is evaluated using a Lax–Friedrichs-type flux function $\boldsymbol{f}^i$ (Endeve et al., 2022b), i.e.,

$$\boldsymbol{f}^i(\boldsymbol{\mathcal{U}}_a, \boldsymbol{\mathcal{U}}_b, \hat{\boldsymbol{v}}) = \frac{1}{2}\Big\{ \boldsymbol{\mathcal{F}}^i(\boldsymbol{\mathcal{U}}_a, \hat{\boldsymbol{v}}) + \boldsymbol{\mathcal{F}}^i(\boldsymbol{\mathcal{U}}_b, \hat{\boldsymbol{v}}) - \alpha^i \left[\boldsymbol{\mathcal{U}}(\boldsymbol{\mathcal{M}}_b, \hat{\boldsymbol{v}}^i) - \boldsymbol{\mathcal{U}}(\boldsymbol{\mathcal{M}}_a, \hat{\boldsymbol{v}}^i) \right] \Big\}, \tag{4.12}$$

where α^i is the largest absolute eigenvalue of the flux Jacobian $\partial \boldsymbol{\mathcal{F}}^i / \partial \boldsymbol{\mathcal{U}}$. The components of the fluid three-velocity at element interfaces, $\hat{\boldsymbol{v}}$, are set to the average of the left and right state

$$\hat{\boldsymbol{v}}(x^i, \tilde{\boldsymbol{x}}^i) := \frac{1}{2}\big(\boldsymbol{v}(x^{i,-}, \tilde{\boldsymbol{x}}^i) + \boldsymbol{v}(x^{i,+}, \tilde{\boldsymbol{x}}^i) \big). \tag{4.13}$$

Similarly, for the energy divergence in Eq. (4.9), the numerical fluxes on energy element interfaces are evaluated as

$$\widehat{\boldsymbol{\mathcal{F}}^\varepsilon}(\boldsymbol{\mathcal{U}}_h, \boldsymbol{v}_h; \varepsilon, \boldsymbol{x}) = \boldsymbol{f}^\varepsilon(\boldsymbol{\mathcal{U}}_h(\varepsilon^-, \boldsymbol{x}), \boldsymbol{\mathcal{U}}_h(\varepsilon^+, \boldsymbol{x}), \boldsymbol{v}_h(\boldsymbol{x})), \tag{4.14}$$

where the flux function is given by the Lax–Friedrichs-type expression $\boldsymbol{f}^\varepsilon$ (Endeve et al., 2022b), i.e.,

$$\boldsymbol{f}^\varepsilon(\boldsymbol{\mathcal{U}}_a, \boldsymbol{\mathcal{U}}_b, \boldsymbol{v}) = \frac{1}{2}\Big\{ \boldsymbol{\mathcal{F}}^\varepsilon(\boldsymbol{\mathcal{U}}_a, \boldsymbol{v}) + \boldsymbol{\mathcal{F}}^\varepsilon(\boldsymbol{\mathcal{U}}_b, \boldsymbol{v}) - \alpha^\varepsilon \left[\boldsymbol{\mathcal{M}}_b - \boldsymbol{\mathcal{M}}_a \right], \Big\} \tag{4.15}$$

where $\boldsymbol{\mathcal{M}}_{a/b}$ are obtained by solving $\boldsymbol{\mathcal{U}}_{a/b} = \boldsymbol{\mathcal{U}}(\boldsymbol{\mathcal{M}}_{a/b}, \boldsymbol{v})$. In Eq. (4.15), α^ε is an estimate on the largest eigenvalue of the flux Jacobian $\partial \boldsymbol{\mathcal{F}}^\varepsilon / \partial \boldsymbol{\mathcal{U}}$.

4.4 Time Discretization

We use the PD-ARS2 IMEX scheme presented in Section 3.5.4 for the development of IMEX methods for time integration, where fluid flows and neutrino phase-space advection are integrated with explicit methods, while the neutrino-matter coupling problem is integrated with implicit methods. In the context of IMEX methods, we can split the fluid-radiation coupled problem into three subproblems: hydrodynamics with self-gravity (solved by Flash-X), neutrino phase-space advection, and neutrino-mattering coupling. In this dissertation, we will discuss methods for solving the phase-space advection problem in this Section, while the neutrino-matter coupling problem will be discussed in Section 5.5.

We proved in Chapter 3 (also Chu et al. (2019a); Chu et al. (2019b)) that realizability (with respect to $\mathcal{R}$) of the cell-averaged primitive moments $\boldsymbol{\mathcal{M}}^{n+1}$ requires a closure based on Fermi-Dirac statistics, a Courant-Friedrichs-Lewy (CFL) condition Δt, a convex-invariant time-stepping method, and a realizability-enforcing limiter to recover point-wise realizability within the element with simplified collision term, Cartesian coordinates, and $\mathcal{O}(1)$ moment equations. Unfortunately, the full collision term in Section 2.4, curvilinear coordinates, and $\mathcal{O}(v/c)$ correction render it hard to find sufficient conditions for the realizability of $\boldsymbol{\mathcal{M}}^{n+1}$. How to preserve moment realizability in this context is still an open question, but progress towards this end, in the context of Cartesian coordinates, simplified collisions, and positive distributions (i.e., with respect to $\mathcal{R}^+$ in Equation (2.91)) is currently being made (Laiu et al., 2022).

In addition, extra requirements are needed to define the positivity limiters.

4.4.1 Positivity Limiters

We need a limiter to preserve realizability. We leverage the realizability-enforcing limiter in Section 3.6.1 and make adjustments for the positivity limiter.

In $\mathcal{O}(v/c)$ two-moment model, the evolved radiation variables are the conservative moments, which we denoted as

$$\boldsymbol{\mathcal{U}} = \begin{bmatrix} \mathcal{D} + v^i \mathcal{I}_i \\ \mathcal{I}_j + v^i \mathcal{K}_{ij} \end{bmatrix} \equiv \begin{bmatrix} \mathcal{N} \\ \mathcal{G}_j \end{bmatrix}. \tag{4.16}$$

Note that we have the following relationship, i.e.,

$$\mathcal{N} = \frac{1}{4\pi} \int_{\mathbb{S}^2} (1 + v^i \ell_i) f \, d\omega \equiv \frac{1}{4\pi} \int_{\mathbb{S}} g \, d\omega, \tag{4.17}$$

$$\mathcal{G}_j = \frac{1}{4\pi} \int_{\mathbb{S}^2} (1 + v^i \ell_i) \ell_j f \, d\omega \equiv \frac{1}{4\pi} \int_{\mathbb{S}} g \ell_j \, d\omega, \tag{4.18}$$

with

$$g \equiv (1 + v^i \ell_i) f > 0. \tag{4.19}$$

Therefore, the positivity requirements on the solution vector are

$$\mathcal{N} > 0, \quad |\mathcal{G}| < \mathcal{N}, \tag{4.20}$$

similar as the requirements on the primitive moments. We implement a positivity limiter on $\boldsymbol{\mathcal{U}}$ to ensure the above inequalities.

4.5 Numerical Tests

This section presents a suite of test problems that are designed to analyze the capabilities of the $\mathcal{O}(v/c)$ two-moment neutrino transport method discussed above. The test to verfy the framework of Flash-X + `thornado` will be presented in Chapter 5.

4.5.1 Shadow Casting Test

A advantages of a two-moment scheme over a flux-limited diffusion method (one-moment scheme) is the ability of an opaque object to generate a shadow. And this two-dimensional idealized test problem is designed to emphasis this advantages. This test has also been done before in various other radiative transport codes (Skinner and Ostriker, 2013; Just et al., 2015; O'Connor and Couch, 2018).

A purely absorbing region ($\mathbb{V}_A$) is exposed to near free-streaming radiation emanating from a source region ($\mathbb{V}_S$). And we performed the test both in 2D cylindrical coordinates and in 2D Cartesian coordinates. An illustration can be found in Figure 4.5.1a.

Shadow Casting Test in 2D Cartesian Coordinates

In Cartesian coordinates, we follow the 2D shadow test proposed in Just et al. (2015). The physical domain is $\boldsymbol{x} \equiv (x, y) \in [0, 15] \times [-5, 5]$ and resolved by $N_x \times N_y = 300 \times 200$ linear DG elements. The purely absorbing region $\mathbb{V}_A$ is a circular region centered at $\boldsymbol{x}_A = (11, 0)$ with radius $r_A = 2$. The source region $\mathbb{V}_S$ is a circular region centered at $\boldsymbol{x}_S = (3, 0)$ with radius $r_S = 3/2$. The absorption opacity σ_A and equilibrium energy density E^{eq} are defined as follows:

$$\sigma_A(\boldsymbol{x}) = \begin{cases} 10 \exp\left\{-\left(4\left|\boldsymbol{x} - \boldsymbol{x}_S\right| / r_S\right)^2\right\}, & \boldsymbol{x} \in \mathbb{V}_S, \\ 10, & \boldsymbol{x} \in \mathbb{V}_A, \\ 0, & \text{elsewhere}, \end{cases} \tag{4.21}$$

$$E^{\text{eq}}(\boldsymbol{x}) = \begin{cases} 10^{-1}, & \boldsymbol{x} \in \mathbb{V}_S, \\ 0, & \text{elsewhere}, \end{cases} \tag{4.22}$$

and illustrated in Figure 4.5.1a.

The model is initialized with a homogeneous distribution of negligibly small energy densities and zero flux densities. Figure 4.5.1b shows the isotropic luminosity L emitted by the source which in the two-dimensional geometry is given by $L = 2\pi\, r_c|\boldsymbol{\mathcal{H}}|$ with $r_c \equiv |\boldsymbol{x}-\boldsymbol{x}_S|$. A clear obscured region behind the absorbing region emerges. The luminosity behind the absorbing region changes continuously within a fan of opening angle $\approx 0^\circ - 30^\circ$. It is because the radiation is emitted from a spatially extended circle source, causing the flux-factor to be less than 1. In addition, the absorbing region has a finite σ_A value and is not perfectly absorbing. As Figure 4.5.1b shows, our code performs well in this test.

Shadow Casting Test in 2D Cylindrical Coordinates

In Cylindrical coordinates, we follow the 2D shadow test presented in O'Connor and Couch (2018), which apart from a geometric factor of r, the setups are identical. The physical domain is $\boldsymbol{x} \equiv (r, z) \in [0, 12] \times [-5, 5]$ and resolved by $N_r \times N_z = 240 \times 200$ DG elements with $k = 1$, which gives the same resolution as in Cartesian version. Correspondently, the purely absorbing region $\mathbb{V}_A$ is a circular region centered at $\boldsymbol{x}_A = (8, 0)$ with radius $r_A = 2$, and the radiation region $\mathbb{V}_S$ is a circular region centered at $\boldsymbol{x}_S = (0, 0)$ with radius $r_S = 3/2$. Figure 4.5.2 shows the neutrino energy density multiplied by r_c^2 with $r_c \equiv |\boldsymbol{x} - \boldsymbol{x}_S|$. Like in the Cartesion version of this test, a clear obscured region behind the absorbing region emerges. The neutrino energy density behind the absorbing region changes continuously within a fan of opening angle $\approx 20^\circ - 30^\circ$. It is because the radiation is emitted from a spatially extended circle source, causing the flux-factor to be less than 1. Like the previous test, the absorbing region is not perfectly absorbing. Figure 4.5.2 shows that our code performs better in cylindrical coordinates than in Cartesian coordinates in this test, and well in both coordinates.

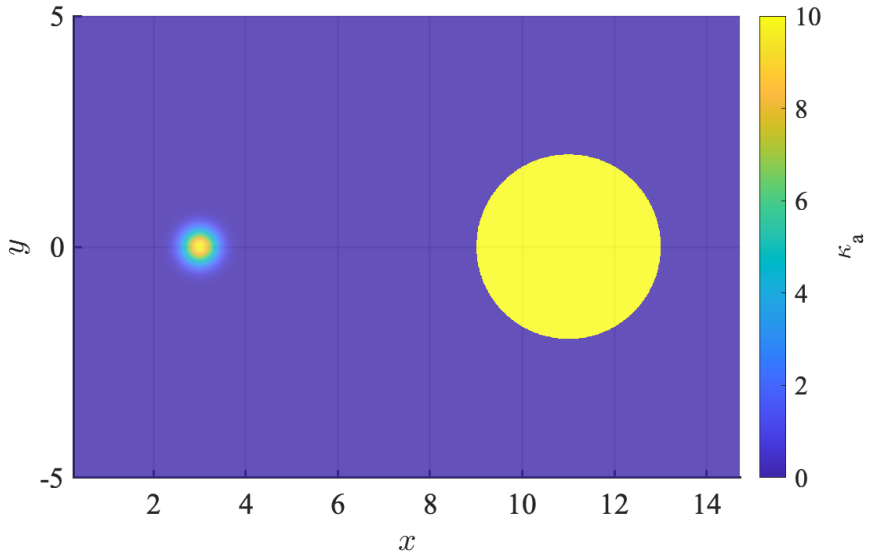

(a) Opacity setting for the shadow casting test in Cartesian coordinates. The background color denotes the opacity rates σ_A. The source region is a circular region centered at (3,0) with radius 3/2. The purely absorbing region is a circular region centered at (11,0) with radius 2.

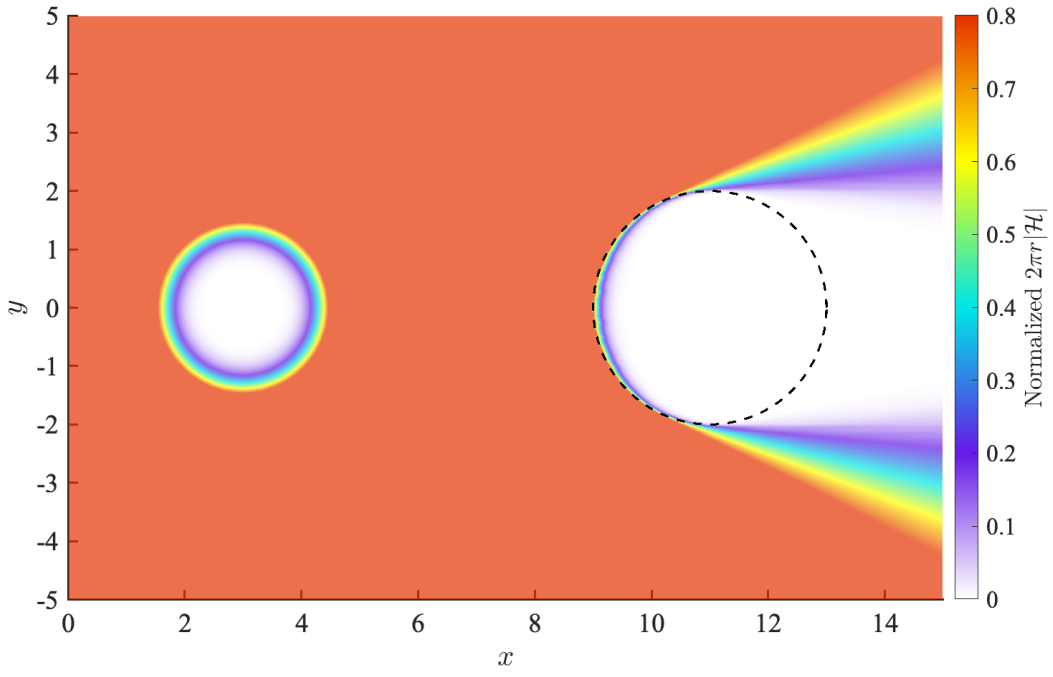

(b) Isotropic luminosity for the shadow casting test in Cartesian coordinates. The luminosity behind the absorbing region, centered at (11,0) with radius 2, changes continuously within a fan of opening angle $\approx 0° - 30°$

Figure 4.5.1: Shadow Casting Test in Cartesian coordinates.

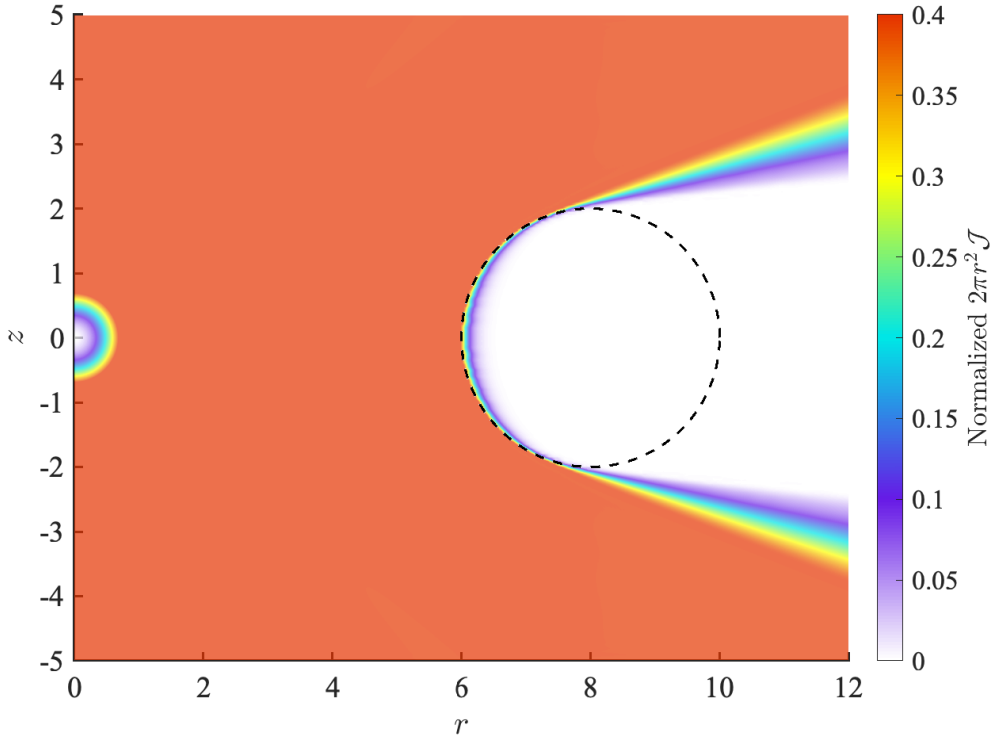

Figure 4.5.2: Neutrino energy density multiplied by r_c^2 for the shadow casting test in cylindrical coordinates. The neutrino energy density behind the absorbing region, centered at (8,0) with radius 2, changes continuously within a fan of opening angle $\approx 20^\circ - 30^\circ$

4.5.2 Streaming Doppler Shift

The numerical test we use to test the observer corrections – Doppler shift effect in neutrino energy spectra – is the streaming Doppler shift problem. This test was also used in Just et al. (2015); Vaytet et al. (2011). The Cartesian domain covers $x \in [0, 1000]$ and is resolved by 96 equidistant linear DG elements (192 points in total). The energy space is discretized between $\varepsilon \in [0, 30]$ using 16 equidistant linear DG elements (32 points in total). Three velocity field settings, $\beta_{\max} \in \{0.05, 0.1, 0.3\}$ where $\beta = \dfrac{v}{c}$, are used. We inject a beam of radiation at $x = 0$ by imposing a fixed inner boundary:

$$D = \frac{1}{e^{\frac{\varepsilon}{3}-3}+1}, \quad I = 0.999 \times D. \tag{4.23}$$

Since $\dfrac{D}{|\boldsymbol{\mathcal{I}}|} \sim 1$, the radiation field is strongly forward peaked, and $(D, \boldsymbol{\mathcal{I}})^{\mathrm{T}}$ is very close to the boundary of the realizable set $\mathcal{R}$. A outflow outer boundary ($x = 1000$) is used. Figure 4.5.3a shows the velocity field which has a shape of smoothed step-functions and is travered by the radiation field. Within regions where $\beta > 0$, the redshifted spectrum of the comoving-frame energy density is given by

$$E_\beta = \frac{s^3}{e^{\frac{s\varepsilon}{3}-3}+1}, \qquad \text{where } s \equiv \sqrt{\frac{1+\beta}{1-\beta}}, \tag{4.24}$$

with $0 \leq \beta \leq 1$. The differences between the spectra in the frames, $\beta = 0$ and $\beta_{\max}$, for both our numerical result (cross marker) and the analytic solution (solid line) are shown in Figure 4.5.3b. The Doppler shift is well captured for the agreement, especially for low β. For high velocities, $\beta_{\max} = 0.3$, the $\mathcal{O}(v/c)$ approximation leads to errors of about 10% with respect to the analytic solution.

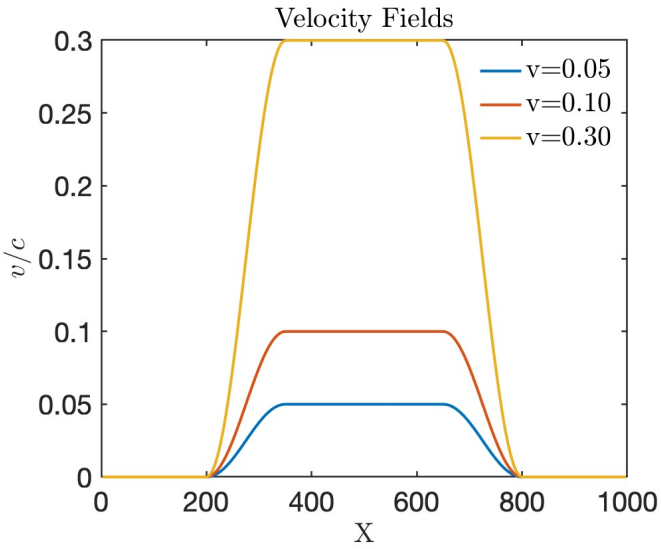

(a) Settings for the Doppler shift test. Three settings, $v = 0.05c$, $v = 0.10c$, and $v = 0.30c$, for fluid velocity field, are plotted. The fluid field has a "step" like velocity field with zero velocity at boundaries $x = 0$ and $x = 1000$, and the maximum velocity at middle. The settings are specified by the maximum velocities.

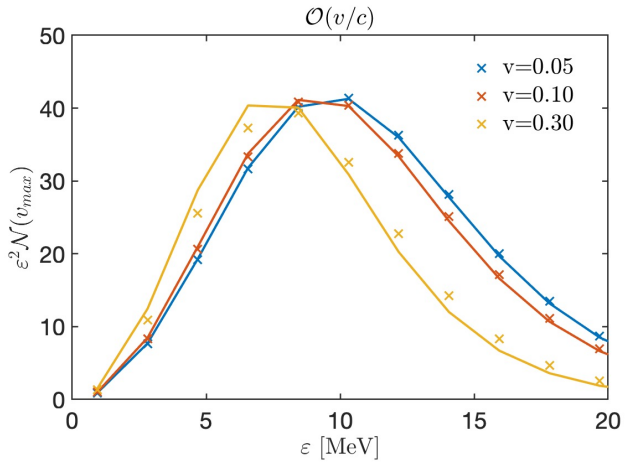

(b) Doppler shift test result in spectra measured at the maximum velocity field region. The analytic solutions are plotted in lines, and cross marks the numerical solutions. Color indicates the different settings.

Figure 4.5.3: Plots for the Doppler shift test with the settings in Figure 4.5.3a and results in Figure fig: doppler shift spectra.

Chapter 5

Neutrino Radiation Hydrodynamics: Numerical Implementation

After presenting the neutrino radiation hydrodynamics formalism in Chapter 2, this chapter describes the numerical implementation; i.e., the code implementation and numerical tests performed while developing Flash-X + `thornado`. The contents are ordered as follows: in Section 5.1 we present the model; in Section 5.2 we present details on the development of EOS and opacity tabulation and interpolation in `WeakLib`; in Section 5.4 we describe the code interfaces (i.e., between `WeakLib` and Flash-X and between Flash-X and `thornado`); in Section 5.5 we discuss the nonlinear solver for neutrino–matter coupling in `thornado`; and the results of our numerical tests are layed out in Section 5.6. The discussion presented in this chapter is based on an implementation of the latest $\mathcal{O}(v/c)$ transport module in `thornado` (presented in Chapter 4).

5.1 Model

Continuing the discussion in Section 2.3.4 and Section 4.2, the coupled neutrino radiation hydrodynamics equations can be written in compact form:

$$\partial_t \boldsymbol{u} + \frac{1}{\sqrt{\gamma}} \partial_i (\sqrt{\gamma}\, \boldsymbol{F}^i(\boldsymbol{u})) = \boldsymbol{S}(\boldsymbol{u}, \Phi) + \boldsymbol{C}(\boldsymbol{u}, \boldsymbol{\mathcal{U}}), \tag{5.1}$$

$$\partial_t \boldsymbol{\mathcal{U}} + \frac{1}{\sqrt{\gamma}} \partial_i (\sqrt{\gamma}\, \boldsymbol{\mathcal{F}}^i(\boldsymbol{\mathcal{U}}, \boldsymbol{v})) + \frac{1}{\varepsilon^2} \partial_\varepsilon (\varepsilon^2\, \boldsymbol{\mathcal{F}}^\varepsilon(\boldsymbol{\mathcal{U}}, \boldsymbol{v})) = \boldsymbol{\mathcal{S}}(\boldsymbol{\mathcal{U}}, \boldsymbol{v}) + \boldsymbol{\mathcal{C}}(\boldsymbol{\mathcal{U}}, \boldsymbol{u}), \tag{5.2}$$

where the solution vector $\boldsymbol{u}$, flux vectors $\boldsymbol{F}^i$, the sources due to curvilinear coordinates $\boldsymbol{S}$, gravity, and neutrino–matter interactions $\boldsymbol{C}$ are

$$\boldsymbol{u} = \begin{bmatrix} \rho \\ \rho v_j \\ E_\mathrm{f} \\ \rho Y_e \end{bmatrix}, \quad \boldsymbol{F}^i = \begin{bmatrix} \rho v^i \\ \Pi^i{}_j \\ (E_\mathrm{f} + p) v^i \\ \rho Y_e v^i \end{bmatrix}, \quad \boldsymbol{S} = \begin{bmatrix} 0 \\ \frac{1}{2}, \Pi^{ik}\, \partial_j \gamma_{ik} \\ -v_j\, G^j_\mathrm{M} \\ 0 \end{bmatrix}, \tag{5.3a}$$

$$\text{and} \quad \boldsymbol{C} = - \begin{bmatrix} 0 \\ G^j_\mathrm{M} \\ G_\mathrm{E} \\ m_\mathrm{B}\, Q_\mathrm{L} \end{bmatrix}, \tag{5.3b}$$

respectively, and $\boldsymbol{\mathcal{U}} = \{\boldsymbol{\mathcal{U}}_s\}_{s=1}^{N_s}$, $\boldsymbol{\mathcal{F}}^i = \{\boldsymbol{\mathcal{F}}_s{}^i\}_{s=1}^{N_s}$, and $\boldsymbol{\mathcal{F}}^\varepsilon = \{\boldsymbol{\mathcal{F}}_s{}^\varepsilon\}_{s=1}^{N_s}$, with

$$\boldsymbol{\mathcal{U}}_s = \begin{bmatrix} \mathcal{D}_s + v^i\, \mathcal{I}_{si} \\ \mathcal{I}_{sj} + v^i\, \mathcal{K}_{sij} \end{bmatrix}, \quad \boldsymbol{\mathcal{F}}_s{}^i = \begin{bmatrix} \mathcal{I}_s{}^i + \mathcal{D}_s\, v^i \\ \mathcal{K}_s{}^i_j + \mathcal{I}_{sj}\, v^i \end{bmatrix}, \tag{5.4a}$$

$$\text{and} \quad \boldsymbol{\mathcal{F}}_s{}^\varepsilon = -\varepsilon \begin{bmatrix} \mathcal{K}_s{}^i_k \\ \mathcal{L}_s{}^i_{kj} \end{bmatrix} \nabla_i v^k, \tag{5.4b}$$

where s denotes the neutrino species. Equation (5.1) is the compact form of the equations for hydrodynamics and electron fraction, Equations (2.18)-(2.21). Equation (5.2) is the compact form of the equations for the $\mathcal{O}(v/c)$ neutrino transport equations in the two-moment approximation. These equations are coupled through $\boldsymbol{C}(\boldsymbol{u},\boldsymbol{\mathcal{U}})$ and $\boldsymbol{\mathcal{F}}^{\varepsilon}(\boldsymbol{\mathcal{U}},\boldsymbol{v})$. A pseudo code, Alorithm 1, explains how Flash-X + `thornado` solves this coupled neutrino radiation hydrodynamics equation system. First, the fluid equations, Equation (5.1), are closed with a photonic, leptonic, and nuclear EOS, which is provided in tabular form by `WeakLib`. Second, the thermodynamic quantities and electron fraction, such as mass density, temperature, pressure and specific internal energy, are updated by Flash-X. Third, the updated thermodynamic quantities and electron fraction are provided to `thornado` for the radiation (neutrino) update through an interface. Fourth, the coupled fluid–radiation field are updated by `thornado`. Fifth, the interface maps the thermodynamic quantities and electron fraction back to Flash-X, and be ready for the next update. In the update order, we will discuss `WeakLib`, the Flash-X hydrodynamics, the code interfaces, `thornado` $\mathcal{O}(v/c)$ transport, and then provide the results of numerical tests. And because we implemented the PDARS2 (and PDARS3) IMEX schemes (developed in Chapter 3), second-order (and third-order) accuracy in streaming limit, and diffusion accuracy are expected.

Algorithm 1 An algorithm for Flash-X + `thornado` update.

1: Flash-X `spark` $\leftarrow$ `WeakLib` EOS
2: $\boldsymbol{u}^{*}_{FV} \leftarrow \boldsymbol{u}^{n}_{FV}$ by Flash-X `spark`
3: $\boldsymbol{u}^{*}_{DG} \leftarrow \boldsymbol{u}^{*}_{FV}$ by interface
4: $(\boldsymbol{u}^{n+1}_{DG},\boldsymbol{\mathcal{U}}^{n+1}_{DG}) \leftarrow (\boldsymbol{u}^{*}_{DG},\boldsymbol{\mathcal{U}}^{n}_{DG})$ by `thornado` with `WeakLib` opacities
5: $\boldsymbol{u}^{n+1}_{FV} \leftarrow \boldsymbol{u}^{n+1}_{DG}$ by interface

5.2 WeakLib

The microphysics, including the equation of state and neutrino–matter interaction rates, is provided in tabulated form by WeakLib, which is publicly accessible: https://github.com/starkiller-astro/weaklib. WeakLib is a library under development at the University of Tennessee and Oak Ridge National Laboratory to provide pre-processed equation of state and neutrino opacity tables for use in neutrino transport simulations. The WeakLib tables are intended to be usable in a straightforward manner by Flash-X, thornado, CHIMERA, and other neutrino radiation hydrodynamics codes. Using the WeakLib tables, opacity rates are interpolated from pre-processed opacity rates on a grid of values of density, electron fraction, and temperature, and the neutrino energy. WeakLib includes a framework to implement opacity tables in astrophysics simulation codes, as well as a strategy to test the tables independently of the code using them, by defining simple test cases to allow troubleshooting (Landfield, December 2018). WeakLib uses pre-tabulated EOS data from the Compstar Online Supernova Equations of State prepository (CompOSE).* It can be used as an external library, and its routines/modules can be called directly. One of the goals of this dissertation is to enable WeakLib to provide the neutrino interaction base set given by Bruenn (1985) (Bruenn 1985), which includes emission and absorption on nucleons and nuclei, isoenergetic scattering on nucleons and nuclei, neutrino–electron scattering, and neutrino pair production. See Table 5.1 for a summary. WeakLib also aims to provide more modern weak interaction tables. This work is currently under development and beyond the scope of this dissertation work.

5.2.1 Code Structure

The hierarchy of the WeakLib framework is shown in Figure 5.4.3. The Distributions stem is meant to be distributed to users of WeakLib to incorporate in their simulation codes. It contains the modules for application, such as an IO module, an interpolation

*https://compose.obspm.fr/

module, code for building an external library, and unit tests. The `UnitTests` contains unit tests for the EOS table and each opacity table, which can also be used as example usage demonstrations for users. The `TableCreator` stem contains the codes for creating the EOS and opacity tables. The creator for building Bruenn 1985 opacity tables, `Bruenn85`, is separated from the `FullWeakPhysics` creator, which contains more comprehensive and state-of-the-art weak physics, e.g., Nucleon-Nucleon Bremsstrahlung (Hannestad and Raffelt, 1998) and muonization (Fischer et al., 2020).

5.2.2 Table Structures

EOS Tables

A `WeakLib` EOS table has three main datasets: `ThermoState`, `DependentVariables`, and `Metadata`. `ThermoState` stores the information of the three independent variables; i.e. the number of grid points in each dimension, and the value and range in density, temperature, and electron fraction. `DependentVariables` includes the dependent variables, including pressure in dynes per cm^2, entropy per baryon in k_b, internal energy density in erg per gram, electron chemical potential in MeV, proton chemical potential in MeV, neutron chemical potential in MeV, proton mass fraction, neutron mass fraction, alpha mass fraction, heavy mass fraction, heavy charge number, heavy binding energy in MeV, thermal energy in MeV, and Γ_1 which is the first adiabatic index. `Metadata` stores the table ID tag, lepton EOS link, source link, table link, code version, and other information relevant to the table creation.

Opacity Tables

`WeakLib` has three main opacity table types (as defined in `wlOpacityFieldsModule.f90`).

Type 1; emission and absorption type: with one neutrino energy (ε) dependency and three thermal state dependencies (ρ, T, Y_e) (1+3=4 dimensional). Neutrino emission and absorption on nucleons and nuclei are of this type.

Type 2; elastic scattering type: with one energy dependency (ε), one Legendre moment order dependency (l), and three thermal state dependencies (ρ, T, Y_e)(1+1+3=5 dimensional). Coherent scattering of neutrinos on nucleons and nuclei is of this type.

Type 3; inelastic scattering type: with two energy dependencies ($\varepsilon, \varepsilon'$), one Legendre moment order dependency (l), and two thermal state dependencies (T, η) (2+1+2=5 dimensional), where

$$\eta \equiv \frac{\mu_e}{k_B T}. \tag{5.5}$$

Neutrino–electron scattering and pair processes are of this type.

Based on the application scenario, `WeakLib` writes opacities into separate files based on the table type: 1, one table for neutrino emission and absorption on nucleons and nuclei; 2, one table for neutrino scattering on nucleons and nuclei; 3, one table for neutrino–electron scattering; 4, and one table for pair processes. Each opacity table contains four datasets: `Metadata`, `ThermoState`, `EnergyGrid`, and its corresponding opacity dataset. Each opacity table can be used independently with its basis EOS table. The table reader has handlers for each of the four opacities, and makes it easy to turn on or off a particular opacity. We will expand the discussion of how each type is tabulated and how to use them in Section 5.2.4.

All `WeakLib` tables are provided in HDF5 format and are publicly available on https://code.ornl.gov/astro/weaklib-tables.

5.2.3 Tabulated Equation of State

This part of the work in `WeakLib` was done by Ryan Landfield, and more details, including the tabulated variables and the interpolation accuracy, can be found in Landfield (December 2018). The works presented in this dissertation use the LS220 EOS (Lattimer and Swesty, 1991) or the SFHo EOS (Steiner et al., 2010).

5.2.4 Tabulated Neutrino Interactions and the Interpolation Methods

All the neutrino opacities from Bruenn (1985) were implemented in `WeakLib` by the author. Due to the wide range of rates, it is most practical to tabulate and interpolate all the rates using the log10 base. This is how the positive rates are tabulated, and an offset is added to the whole dataset if its minimum value is non-positive.

The opacity table uses the same thermal grids as the EOS table. The energy grid is logarithmically spaced between $[0.1, 300]$ MeV, with 40 points. The η (defined in Equation (5.5)) grid is logarithmically spaned between $[10^{-3}, 2.5 \times 10^{3}]$, with 60 points. This grid for η is selected so that the majority of the range in η given by the EOS is covered without loss of accuracy.

We implemented several multidimensional linear interpolation methods in `WeakLib`, including 2D, 3D, 4D, 1D3D, 2D2D, and 2D2D-aligned interpolation. In these notations, 'D' denotes the dimension of the array, 'aligned' is with the assumption that the first two interpolation dimensions are aligned with the energy grid used to discrete the transport equations. For example, 4D is a tetra-linear interpolation method for $(\varepsilon_i, \rho_i, T_i, Y_{ei})$ 4-tuples — 4-dimensional arrays for i points. The output is a one-dimensional array with i points. 1D3D is a 1+3 linear interpolation method for $(\varepsilon_i, \rho_j, T_j, Y_{ej})$. It interpolates for ε_i on each (ρ_j, T_j, Y_{ej}). The output is a two-dimensional array with size (i,j). 2D2D is a 2+2 linear interpolation method for $(\varepsilon_i, \varepsilon'_j, T_k, \eta_k)$. It interpolates for each ε_i and ε'_j at (T_k, η_k). The output is a three-dimensional array of size (i,j,k). It can be considered as a collection of bilinear interpolations. We will give examples of how to use the interpolation methods with specific opacity tables.

Neutrino Absorption on Nucleons and Nuclei (AbEm)

The neutrino stimulated absorptivity on nucleons and nuclei, which is $\tilde{\chi}$ in Equation (2.60), is expressed as $\left[j(\varepsilon) + 1/\lambda^{(a)}(\varepsilon)\right]$ in Bruenn (1985). Given by Equations

(C13) + (C15) + (C19) + (C20) + (C27) + (C29) in Bruenn (1985), $\tilde{\chi}(\varepsilon, \rho, T, Y_e)$ is tabulated in a four-dimensional `WeakLib` AbEm table in units of cm^{-1}. To interpolate on an AbEm opacity with a given energy array (ε_j) for (ρ_i, T_i, Y_{ei}) state(s), one can call 1D3D interpolation routine. See Section 5.2.5 for the verification result.

Neutrino Isoenergetic Scattering on Nucleons and Nuclei (Iso)

The 0-th and 1-st order Legendre coefficients of the neutrino isoenergetic scattering kernel on nucleons and nuclei, $\mathrm{R}_{\mathrm{Iso}\,0}$ and $\mathrm{R}_{\mathrm{Iso}\,1}$, which are given by

$$\mathrm{R}_{\mathrm{Iso}\,0} = \frac{1}{c(2\pi\hbar c)^3}\Phi_{\mathrm{Iso}\,0}(\varepsilon) = \frac{1}{2c(2\pi\hbar c)^3} \times (\mathrm{C38}) + \frac{1}{2c(2\pi\hbar c)^3} \times (\mathrm{C44}), \tag{5.6}$$

$$\mathrm{R}_{\mathrm{Iso}\,1} = \frac{1}{c(2\pi\hbar c)^3}\Phi_{\mathrm{Iso}\,1}(\varepsilon) = \frac{3}{2c(2\pi\hbar c)^3} \times (\mathrm{C39}) + \frac{3}{2c(2\pi\hbar c)^3} \times (\mathrm{C45}), \tag{5.7}$$

where (C38), (C39), (C44), (C45) are Equations in Bruenn (1985), are tabulated in a five-dimensional `WeakLib` Iso table in units of $\mathrm{MeV}^{-2}\mathrm{cm}^{-1}$, i.e. $\mathrm{R}_{\mathrm{Iso}\,0} = \mathrm{R}_{\mathrm{Iso}}(\varepsilon, 1, \rho, T, Y_e)$, $\mathrm{R}_{\mathrm{Iso}\,1} = \mathrm{R}_{\mathrm{Iso}}(\varepsilon, 2, \rho, T, Y_e)$.

Therefore, the inverse free mean path $(1/\lambda)_{\mathrm{Iso}}$ is given by $-B^{(1)}_{\mathrm{IS}}$ in Equation (A41) in Bruenn (1985), such that

$$(1/\lambda)_{\mathrm{Iso}} = \frac{4\pi\varepsilon^2}{c(2\pi\hbar c)^3}\left[\frac{1}{3}\Phi_{\mathrm{Iso}\,1}(\varepsilon) - \Phi_{\mathrm{Iso}\,0}(\varepsilon)\right] = 4\pi\,\varepsilon^2\left[\frac{\mathrm{R}_{\mathrm{Iso}\,1}}{3} - \mathrm{R}_{\mathrm{Iso}\,0}\right]. \tag{5.8}$$

To interpolate on the Iso opacity with a given ε_j array for state(s) (ρ_i, T_i, Y_{ei}) for the inverse free path, one can call 1D3D interpolation routine for each Legendre coefficient component, $\mathrm{R}_{\mathrm{Iso}\,0,1}$. See Section 5.2.5 for the verification results.

Neutrino-Electron Scattering (NES)

The coefficients for the integral of the functions H^I_l and H^{II}_l ($l = 0, 1$ indicates the first two Legendre coefficients of the neutrino–electron scattering kernel) over electron energy E_e in Equation (C50) in Bruenn (1985), see also Equation (43)

in Mezzacappa and Bruenn (1993c), with all coefficients $\frac{1}{2c(2\pi\hbar c)^3}$, $\frac{3}{2c(2\pi\hbar c)^3}$, and $F_e\left(E_e\right)\left[1-F_e\left(E_e+\varepsilon-\varepsilon'\right)\right]$, are tabulated in the `WeakLib` NES table. Expressed explicitly, they are

$$\mathrm{H}_l^I = \frac{1}{2}\frac{1}{c(2\pi\hbar c)^3}\frac{G^2}{\pi\varepsilon^2\varepsilon'^2}\int dE_e F_e\left(E_e\right)\left[1-F_e\left(E_e+\varepsilon-\varepsilon'\right)\right]H_l^{\mathrm{I}}\left(\varepsilon,\varepsilon',E_e\right), \tag{5.9}$$

$$\mathrm{H}_l^{II} = \frac{3}{2}\frac{1}{c(2\pi\hbar c)^3}\frac{G^2}{\pi\varepsilon^2\varepsilon'^2}\int dE_e F_e\left(E_e\right)\left[1-F_e\left(E_e+\varepsilon-\varepsilon'\right)\right]H_l^{\mathrm{II}}\left(\varepsilon,\varepsilon',E_e\right). \tag{5.10}$$

NES tables are five-dimensional, with $\mathrm{H}_0^I = \mathrm{H}_0^I(\varepsilon',\varepsilon,1,T,\eta)$, $\mathrm{H}_0^{II} = \mathrm{H}_0^{II}(\varepsilon',\varepsilon,2,T,\eta)$, $\mathrm{H}_1^I = \mathrm{H}_1^I(\varepsilon',\varepsilon,3,T,\eta)$, and $\mathrm{H}_1^{II} = \mathrm{H}_1^{II}(\varepsilon',\varepsilon,4,T,\eta)$, where $\eta = \mu_e/k_BT$. Using the same definition as in Equation (A38) in Bruenn (1985), $-B_{\mathrm{NES}}^{(1)}$, for the inverse mean free path and taking zero as the final occupancy ($f_{\mathrm{final}} = 0$), we have

$$\begin{aligned}(1/\lambda)_{\mathrm{NES}} &= \frac{4\pi}{c(2\pi\hbar c)^3}\int_0^\infty \Phi_{0,\mathrm{NES}}^{\mathrm{out}}\left(\varepsilon,\varepsilon'\right)\varepsilon'^2 d\varepsilon' \\ &\approxeq 4\pi\int_{\text{table min}}^{\text{table max}}\left[(C_V+C_A)^2\mathrm{H}_l^I\left(\varepsilon,\varepsilon'\right)+(C_V-C_A)^2\mathrm{H}_l^{II}\left(\varepsilon,\varepsilon'\right)\right]\varepsilon'^2 d\varepsilon'.\end{aligned} \tag{5.11}$$

To compute this rate by interpolating on the NES table using a same energy array for scatter-in and scatter-out energy, (i.e. ε_k, ε'_j with $\varepsilon_j = \varepsilon'_j$), and state(s) (ρ_i, T_i, Y_{ei}), one needs to interpolate for η_i first. It can be done by calling `LogInterpolateSingleVariable` with (ρ_i, T_i, Y_{ei}) for $\mu_{e,i}$, then compute η_i by $\mu_{e,i}/k_bT_i$. Next, interpolate for $(\mathrm{H}_l^{\mathrm{I/II}})_{kji}$ with $(\varepsilon_k, \varepsilon'_j, T_i, \eta_i)$ using 2D2D interpolation routine, and assemble $\Phi_{l,\mathrm{NES}}^{\mathrm{In/Out}}$ using the corresponding coefficients $(C_V+C_A)^2$ and $(C_V-C_A)^2$. See Section 5.2.5 for the verification tests.

Neutrino Pair Production (Pair)

In a similar manner, the coefficients for the integrals of the functions J_l^I and J_l^{II}, with $l = 0, 1$ of the first two Legendre coefficients of the pair process kernel with coefficients $\frac{1}{2c(2\pi\hbar c)^3}$, $\frac{3}{2c(2\pi\hbar c)^3}$, and $\left[1-F_e\left(E_e\right)\right]\left[1-F_{e^+}\left(\varepsilon+\varepsilon'-E_e\right)\right]$

(annihilation coefficient) are tabulated in the `WeakLib` Pair table; i.e.,

$$\mathrm{J}_l^I = \frac{1}{2}\frac{1}{c(2\pi\hbar c)^3}\frac{G^2}{\pi}\int_0^{\varepsilon+\varepsilon^+} dE_e\left[1-F_e\left(E_e\right)\right]\left[1-F_{e^+}\left(\varepsilon+\varepsilon'-E_e\right)\right]J_l^{\mathrm{I}}\left(\varepsilon,\varepsilon',E_e\right), \tag{5.12}$$

$$\mathrm{J}_l^{II} = \frac{3}{2}\frac{1}{c(2\pi\hbar c)^3}\frac{G^2}{\pi}\int_0^{\varepsilon+\varepsilon^+} dE_e\left[1-F_e\left(E_e\right)\right]\left[1-F_{e^+}\left(\varepsilon+\varepsilon'-E_e\right)\right]J_l^{\mathrm{II}}\left(\varepsilon,\varepsilon',E_e\right). \tag{5.13}$$

Using the same definition as in Equation (A47) in Bruenn (1985) for the inverse mean free path and taking the final occupancy to zero, we have

$$\begin{aligned}(1/\lambda)_{\mathrm{TP}} &= \frac{4\pi}{c(2\pi\hbar c)^3}\int_0^{\infty}\Phi^p_{0,\mathrm{Pair}}\left(\varepsilon,\varepsilon'\right)\varepsilon'^2 d\varepsilon' \\ &\approxeq 4\pi\int_{\text{table min}}^{\text{table max}}\left[(C_V+C_A)^2\mathrm{J}_l^I\left(\varepsilon,\varepsilon'\right)+(C_V-C_A)^2\mathrm{J}_l^{II}\left(\varepsilon,\varepsilon'\right)\right]e^{-(\varepsilon+\varepsilon')/k_BT}\varepsilon'^2 d\varepsilon'.\end{aligned} \tag{5.14}$$

Similar as interpolating for NES, one needs to interpolate for η_i before interpolating on the Pair table for state(s) (ρ_i, T_i, Y_{ei}). Then, interpolate for $(\mathrm{J}_l^{\mathrm{I/II}})_{kji}$ with $(\varepsilon_k, \varepsilon'_j, T_i, \eta_i)$ using 2D2D interpolation routine, and assemble $\Phi_{l,\mathrm{Pair}}$ using the corresponding coefficients $(C_V + C_A)^2$ and $(C_V - C_A)^2$. See Section 5.2.5 for the verification tests.

5.2.5 Opacity Rates Tests

To verify the opacities and interpolation routines provided by `WeakLib`, we compared `WeakLib`'s opacities with those provided by others. First, we performed a comparison at select thermal states adopted from Bruenn (1985). Then, we compared the opacity rate given by `WeakLib` and `Agile-Boltztran`. The second comparison uses a post-bounce snapshot from a real supernova simulation.

Thermal states from Bruenn (1985) Two thermal states from Bruenn (1985) are adopted for the comparison, as shown in Figures 5.2.1 and 5.2.2, where the inverse

mean free path for each of the four opacity types given in Section 5.2.4. We used the SFHo EOS for this comparison. Despite the potential differences caused by using different EOSs, the plots show fairly good agreement with results plotted in Bruenn (1985).

Post-bounce snapshot The profile used for this test is a 100 ms post-bounce snapshot of a 25 $M_\odot$ progenitor (Woosley and Heger, 2007) supernova simulation obtained using CHIMERA with the Lattimer-Swesty equation of state (Lattimer and Swesty, 1991) LS220 (provided by Stephen Bruenn, private communication). It is presented in Figure 5.2.3. The same profile is used for the stationary state test, which is described in Section 5.6.3. In Figure 5.2.4 and 5.2.5, we plot the comparison for each opacity channel for radii spanning 0 km to 300 km, and neutrino energies spanning 0.1 MeV to 300 MeV, using the same energy grid for two codes. The final distribution function used in defining NES and Pair inverse mean free paths is the stationary distribution function given by `Agile-Boltztran`. We see that `WeakLib` has fairly good agreement with `Agile-Boltztran` for electron neutrino/antineutrino isoenergetic scattering opacities. For emission, absorption, neutrino–electron scattering, and neutrino pair production process, we see a good agreement inside PNS ($r<150$ km). Outside PNS, differences in emission and absorption inverse mean free path for high energy groups are observed.

5.3 Hydrodynamics Solver: Flash-X `Spark`

The compressible hydrodynamics solver used in this dissertation is provided by `Spark` (Couch et al., 2021; Dubey et al., 2022). `Spark` uses a finite-volume discretization, high-order spatial reconstruction, strong stability preserving Runge-Kutta time integration, leveraging adaptive mesh refinement via both Paramesh and AMReX. It can be used in 1-, 2-, or 3-dimensional simulations. Details regarding `Spark`'s parallel performance for both CPUs and accelerators can be found in Couch

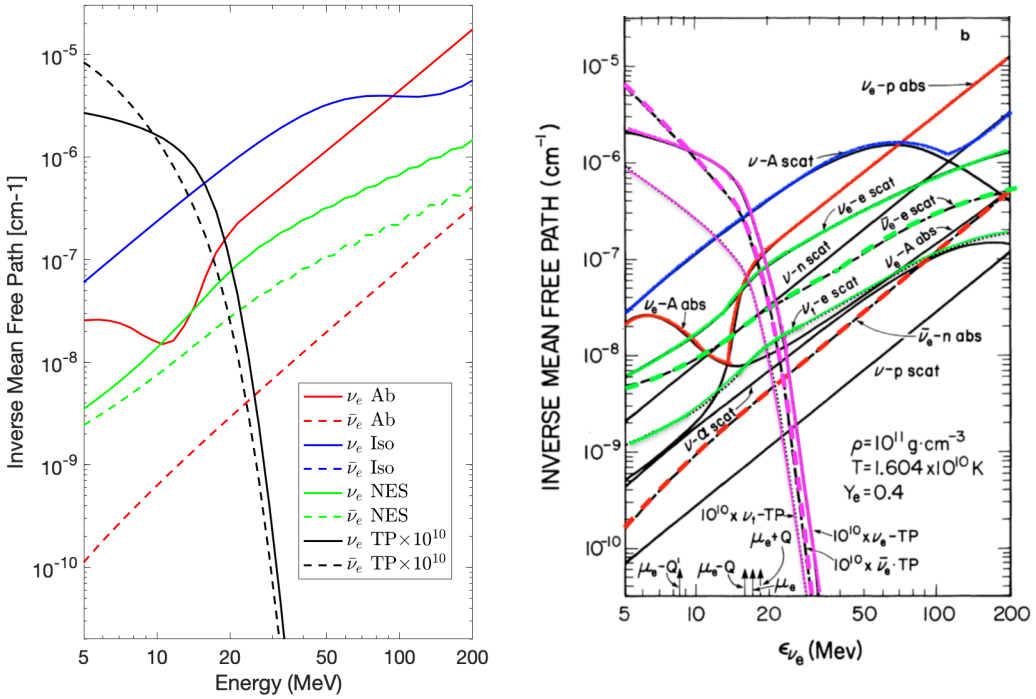

(a) $\rho = 10^{11}$ g cm^{-3}, $T = 1.604 \times 10^{10}$ K, $Y_e = 0.4$ (b) For same thermal state from Bruenn (1985)

Figure 5.2.1: Neutrino opacities for a thermal state adopted from Bruenn (1985) Fig. 36 ($\rho = 10^{11}$ g cm^{-3}, $T = 1.604 \times 10^{10}$ K, $Y_e = 0.4$)): solid lines are for neutrinos and dashed lines are for antineutrinos. The neutrino–electron scattering and pair creation and annihilation opacities were computed with the neutrino and antineutrino number densities set to zero, as Bruenn did in Bruenn (1985). The EOS used for `WeakLib` plot in Figure 5.2.1a is SFHo. Figure 5.2.1b is adapted from Bruenn (1985) Fig. 36 with manually colored for comparison. The color on the left and right matches besides magenta on the right for the pair process, while black on the left. Note that the right figure has more detailed categories, which can be combined in the left figure.

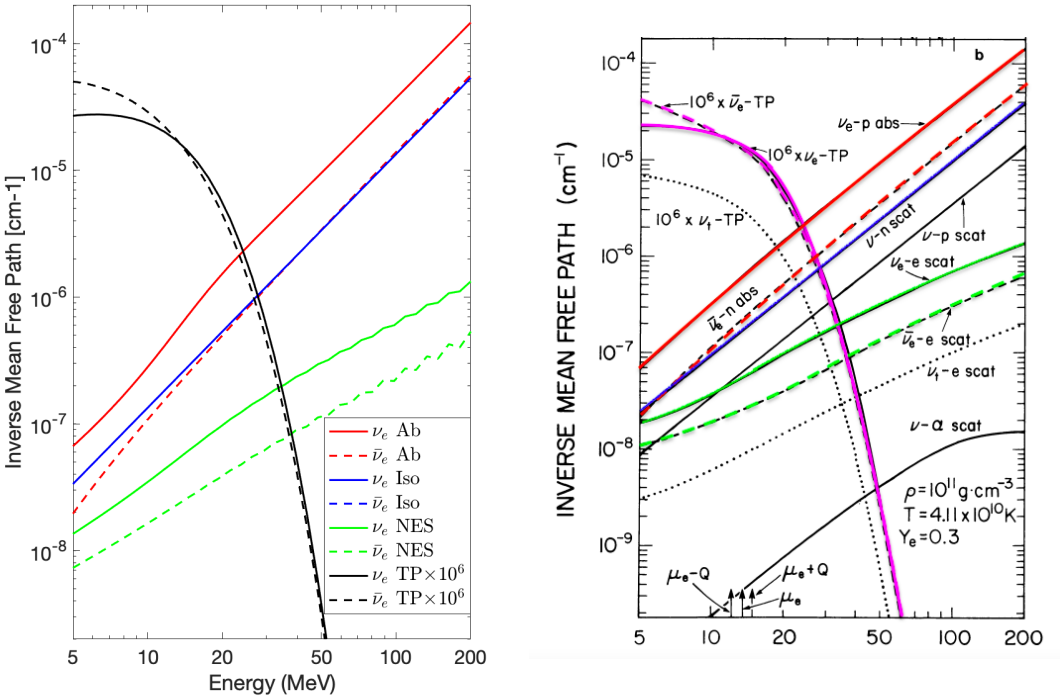

(a) $\rho = 10^{11}$ g cm^{-3}, $T = 4.11 \times 10^{11}$ K, $Y_e = 0.3$ (b) For same thermal state from Bruenn (1985)

Figure 5.2.2: Neutrino opacities for a thermal state adopted from Bruenn (1985) Fig. 37 ($\rho = 10^{11}$ g cm^{-3}, $T = 4.11 \times 10^{11}$ K, $Y_e = 0.3$): solid lines are for neutrinos and dashed lines are for antineutrinos. The neutrino–electron scattering and pair creation and annihilation opacities were computed with the neutrino and antineutrino number densities set to zero, as Bruenn did in Bruenn (1985). The EOS used for `WeakLib` plot in Figure 5.2.2a is SFHo. Figure 5.2.2b is adapted from Bruenn (1985) Fig. 37 with manually colored for comparison. The color on the left and right matches besides magenta on the right for the pair process, while black on the left. Note that the right figure has more detailed categories, which can be combined in the left figure.

et al. (2021). Spark has more than one option for both spatial reconstruction and Riemann solver. It default setting uses fifth-order weighted essentially non-oscillatory (WENO) spatial reconstruction, and the HLLD approximate Riemann solver. We use the default settings for this dissertation.

5.4 Code Interfaces

In this section, we discuss how the interfaces between Flash-X + WeakLib, and Flash-X + thornado, were built.

5.4.1 Flash-X + WeakLib Interface

WeakLib is included in Flash-X as an external library (Flash-X/lib/weaklib). A unit test designed for the Flash-X + WeakLib interface is an adiabatic collapse test using the WeakLib EOS table. This test uses a progenitor profile, such as S15 from Woosley and Weaver (1995), to initialize the radial grid in spherical coordinates, with a reflecting inner boundary and an outflowing outer boundary. The setup syntax, parameter file, progenitor profile, and initialization code are under source/Simulation/SimulationMain/CCSN_WL/. This adiabatic collapse is leveraged from the existing Flash-X unit test using other EOS options for an adiabatic collapse simulation. We confirmed the Flash-X + WeakLib interface by running the adiabatic collapse using WeakLib and other EOS options to shock formation and until shock leaves the domain.

5.4.2 Flash-X + thornado Interface

With the EOS and after the hydrodynamics update made by Flash-X Spark, thermodynamic quantities are ready to be provided to thornado. For thornado to have the fluid density, temperature, electron fraction, specific internal energy, entropy per baryon, pressure and et al., an interface is needed.

`thornado` is included in Flash-X as an external library (`Flash-X/lib/thornado`). The main function of the Flash-X + `thornado` interface is to map data between the `thornado` DG grid and the Flash-X finite volume (FV) grid. Inspired by Dumbser et al. (2014), we consider DG elements as comprising FV subcells. We implement subcell projection and reconstruction to move between DG and FV representations. When the FV variables are represented on a subgrid with the same number of degrees of freedom as the DG representation, we can move between representations without loss of information. For the Flash-X + `thornado` interface, the default setting is even Flash-X cell with first-order DG `thornado` grid ($k = 1$, degree of freedom per dimension $= 2$) so that the total number of degrees of freedom remains the same. See Figure 5.4.1 for an example in two spatial dimensions, $k = 1$. On the subgrid, the representation is given by cell averages, which are used to reconstruct the nodal values on the DG node points.

The `thornado` time stepping module is part of the interface. It feeds the PDARS2 scheme with data that in Flash-X block size and converted to `thornado` manner (grid and unit). In Figure 5.4.2, the standard procedure of how Flash-X calls `thornado` is represented. In general, the transport update requires a smaller time step Δt_T than the hydrodynamics update allows Δt_H. We allow multiple updates from radiation within a hydrodynamics update to gain efficiency.

The unit tests for the Flash-X + `thornado` interface include a streaming sine wave test for advection, a streaming Doppler shift test for observer corrections, a relaxation test for the collision term, and a deleptonization wave test for all the above.

Subcell Reconstruction and Projection

Consider an element $\boldsymbol{K} \subset \mathbb{R}^d$ where the DG representation is denoted $u_h(\boldsymbol{x}, t) \in \mathbb{V}^k$, where $\mathbb{V}^k$ is constructed from the tensor product of one-dimensional polynomials of maximal degree k

$$u_h(\boldsymbol{x}, t) = \sum_{j=1}^{(k+1)^d} u_j(t)\, \Phi_j(\boldsymbol{x}). \tag{5.15}$$

Next, consider dividing the element $\boldsymbol{K}$ into a subgrid S of $(k+1)^d$ nonoverlapping FV cells S_j, $S = \cup_{j=1}^{(k+1)^d} S_j$, so that $K \setminus S = \emptyset$. On the subgrid, the representation is given by piecewise constants (cell averages)

$$v_h(\boldsymbol{x}, t) = \sum_{j=1}^{(k+1)^d} \chi(S_j)\, v_j(t), \tag{5.16}$$

where $v_j(t)$ is the cell average in subgrid cell S_j and the $\chi(S_j)$ is the indicator function on S_j.

FV to DG Representation (Reconstruction) Knowing the cell averages v_j (we suppress time dependence from here on), we reconstruct the DG representation u_h by requiring that

$$\frac{1}{|S_i|}\int_{S_i} u_h(\boldsymbol{x})\, d\boldsymbol{x} = \frac{1}{|S_i|}\int_{S_i} v_h(\boldsymbol{x})\, d\boldsymbol{x} = v_i, \forall\ S_i \in S. \tag{5.17}$$

With the definition in Equation (5.15), this gives

$$R^{-1}\,\boldsymbol{u} = \boldsymbol{v}, \tag{5.18}$$

where $\boldsymbol{u} = (u_1, \ldots, u_{(k+1)^d})^T$, $\boldsymbol{v} = (v_1, \ldots, v_{(k+1)^d})^T$, and the components of the $(k+1)^d \times (k+1)^d$ inverse reconstruction matrix are

$$R^{-1}_{ij} = \frac{1}{|S_i|}\int_{S_i} \Phi_j(\boldsymbol{x})\, d\boldsymbol{x}. \tag{5.19}$$

The reconstruction step amounts to inverting Equation (5.18) to find

$$\boldsymbol{u} = R\,\boldsymbol{v}. \tag{5.20}$$

DG to FV Representation (Projection) Knowing the DG representation $u_h(\boldsymbol{x})$, we can easily compute the cell averages for the finite volume representation

$$v_i = \frac{1}{|S_i|} \int_{S_i} u_h(\boldsymbol{x})\, d\boldsymbol{x} = \frac{1}{|S_i|} \sum_{j=1}^{(k+1)^d} \int_{S_i} \Phi_j(\boldsymbol{x})\, d\boldsymbol{x}\, u_j, \tag{5.21}$$

which can be written as

$$\boldsymbol{v} = P\, \boldsymbol{u}, \tag{5.22}$$

where the components of the $(k+1)^d \times (k+1)^d$ projection matrix P are

$$P_{ij} = \frac{1}{|S_i|} \int_{S_i} \Phi_j(\boldsymbol{x})\, d\boldsymbol{x}. \tag{5.23}$$

From the definitions above, it is obvious that $R\,P = I$; i.e., we do not lose any information when switching between DG and FV representations.

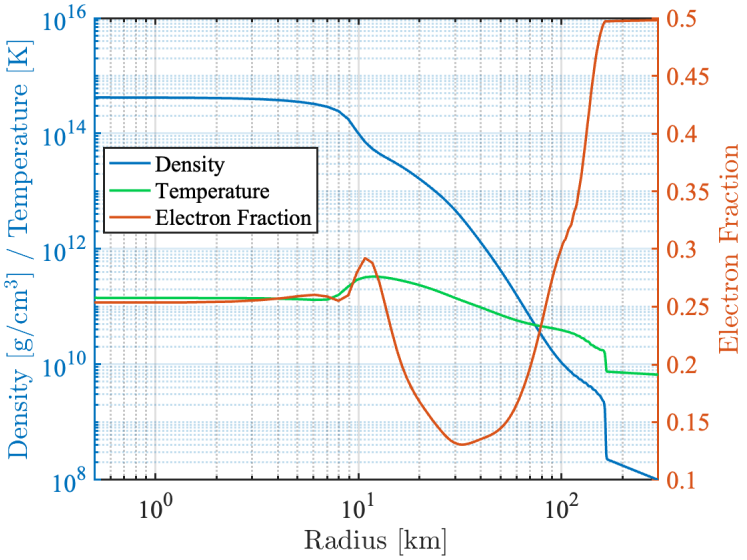

Figure 5.2.3: Thermal state at 100 ms after bounce given by the CHIMERA simulation for S25. This profile is used in `WeakLib` opacity test (Section 5.2.5), the relaxation problem (Section 5.6.1), and the deleptonization wave problem (Section 5.6.3).

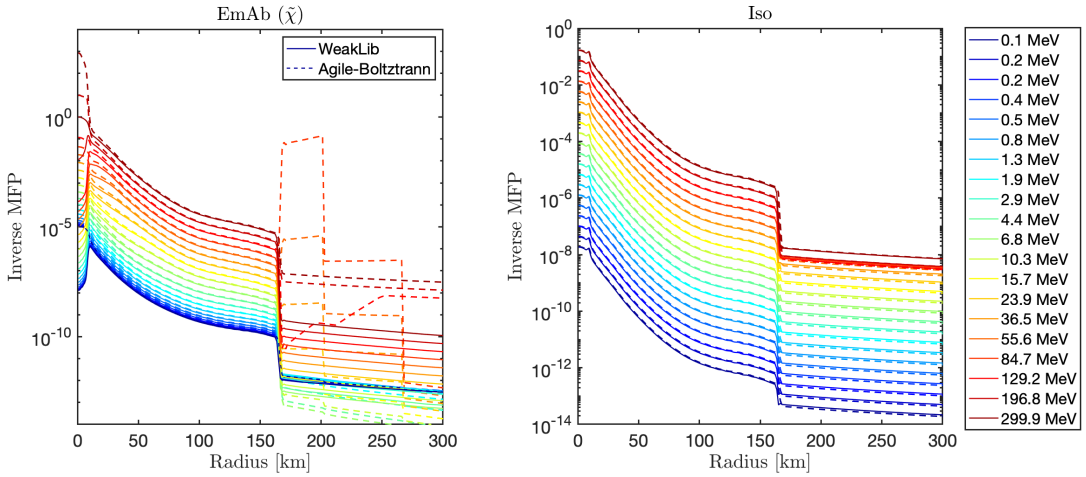

(a) AbEm

(b) Iso

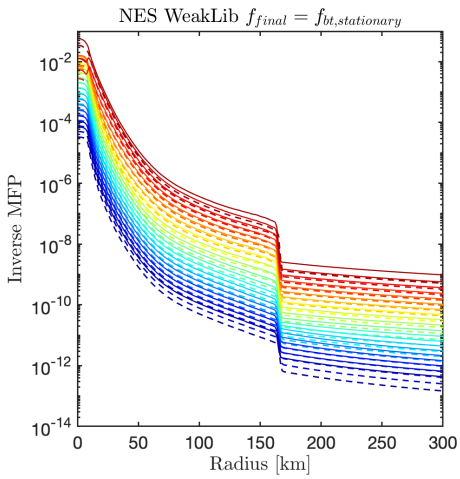

(c) NES

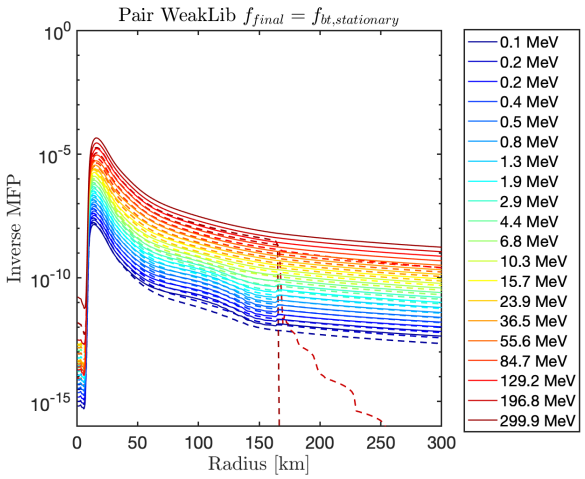

(d) Pair

Figure 5.2.4: Opacity comparison between results obtained by `WeakLib` and `Agile-Boltztran` for Bruenn (1985) electron-neutrino interactions using the LS220 EOS and a 25 $M_\odot$ 100 ms post-bounce profile.

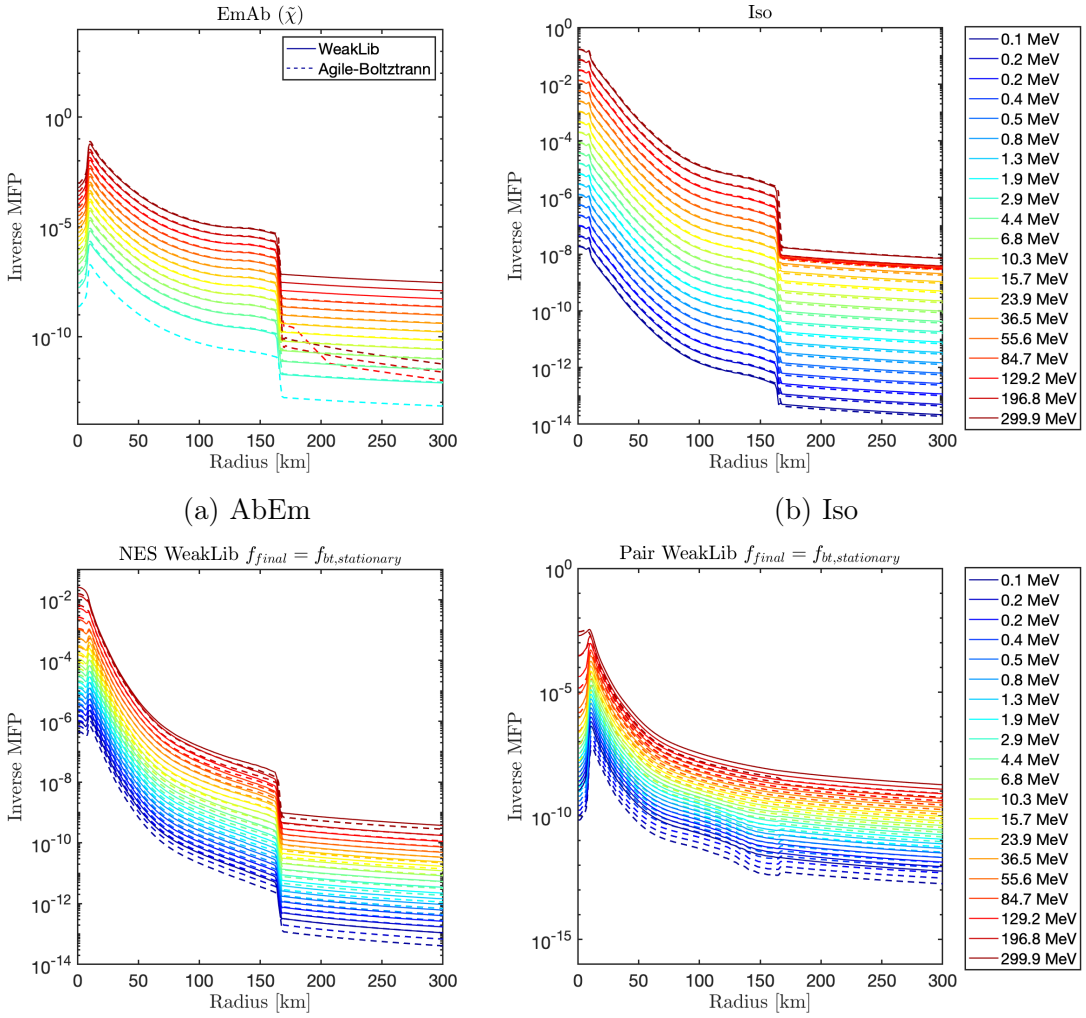

(a) AbEm (b) Iso

(c) NES (d) Pair

Figure 5.2.5: Opacity comparison between results obtained by `WeakLib` and `Agile-Boltztran` for Bruenn (1985) electron-antineutrinos interactions using the LS220 EOS and a 25 $M_\odot$ 100 ms post-bounce profile. Same as Figure 5.2.4 but for electron-antineutrinos.

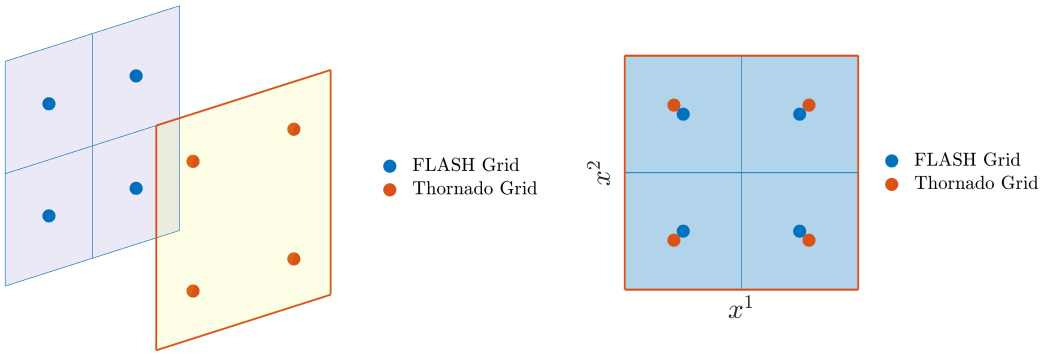

Figure 5.4.1: Using a 2D grid as an example of Flash-X + `thornado` FV-DG mapping. Division of a DG element into a subgrid of FV cells in two spatial dimensions using DG polynomials of maximal degree $k = 1$.

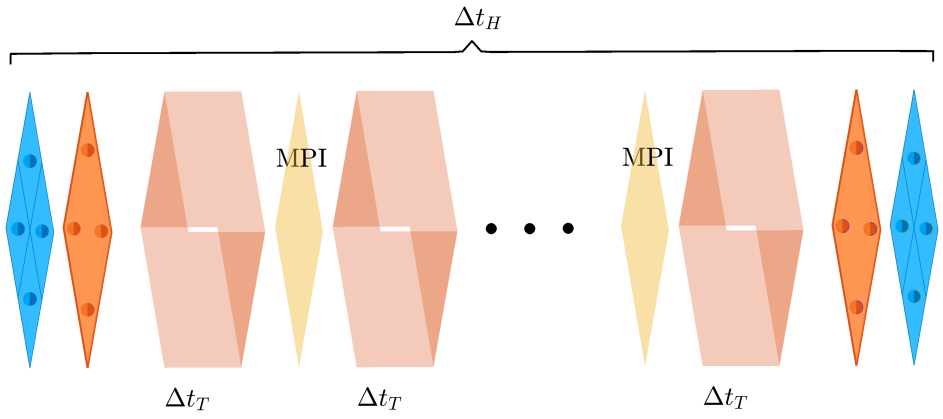

Figure 5.4.2: Flash-X + `thornado` interface procedure. The Flash-X + `thornado` interface is called to map data between Flash-X FV grid and `thornado` DG grid at the beginning and end, as the blue and orange slices indicate. In general, the radiation transport update requires a smaller time step Δt_T than the hydrodynamics time step Δt_H. We allow multiple radiation updates within a hydrodynamics update to gain efficiency. The pink blocks represent the transport updates. Between each transport update, MPI syncs the whole computation domain, as the yellow slices represent.

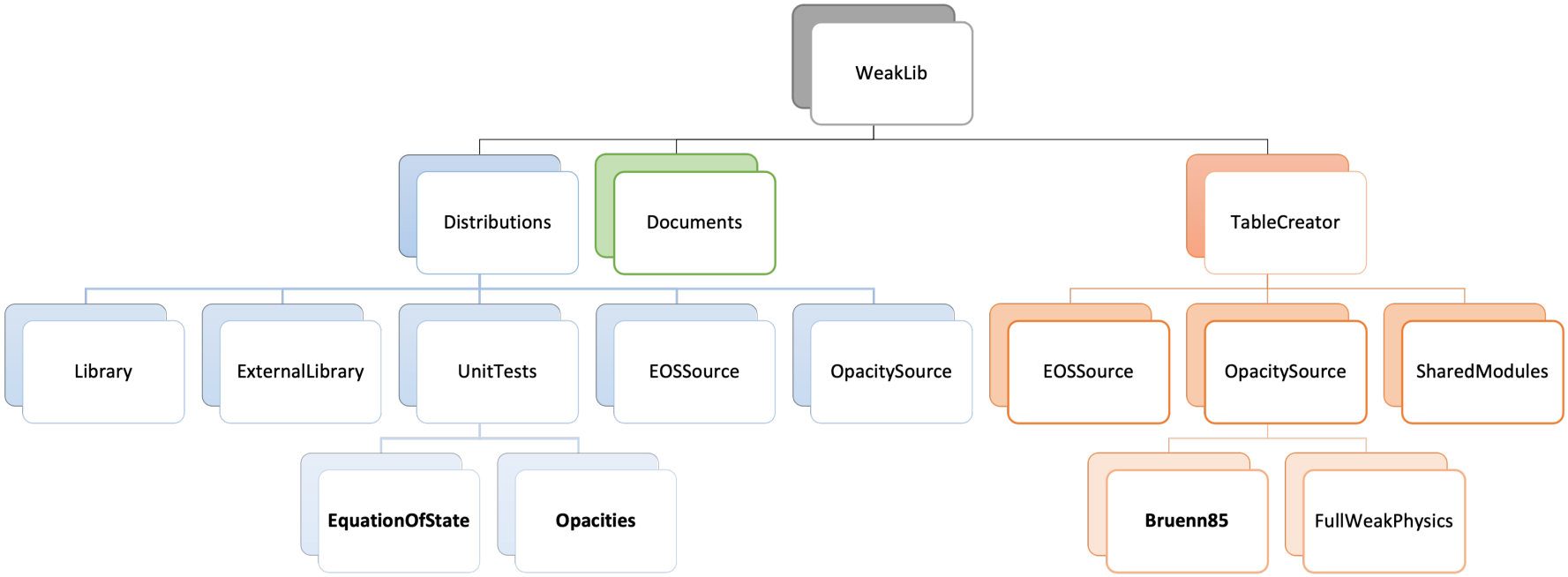

Figure 5.4.3: `WeakLib` module hierarchy. The major modules used in this dissertation are listed in bold.

Table 5.1: Summary of Neutrino Opacities.

Category	Weak Interaction	in Moment Equations	in `WeakLib`	References
Absorption and emission	$\nu_e + n \rightleftarrows e^- + p$ $\bar{\nu}_e + p \rightleftarrows e^+ + n$ $\nu_e + A \rightleftarrows e + A'$	Section 2.4.2 $\tilde{\chi} = (\eta + \chi)$	Section 5.2.4 $\tilde{\chi}(\varepsilon, \rho, T, Y_e)$	Bruenn (1985)
Coherent isoenergetic scattering	$\nu + A \rightarrow \nu + A$ $\nu + N \rightarrow \nu + N$	Section 2.4.2 $-\frac{4\pi\varepsilon^2}{c(2\pi\hbar c)^3}\left[\Phi_{\text{Iso}\,0}(\varepsilon) - \frac{1}{3}\Phi_{\text{Iso}\,1}(\varepsilon)\right]$	Section 5.2.4 $\frac{1}{c(2\pi\hbar c)^3}\Phi_{\text{Iso}}(\varepsilon, l, \rho, T, Y_e)$	Bruenn (1985)
Non-isoenergetic scattering	$\nu + e^- \rightleftarrows \nu + e^-$	Section 2.4.2 $-\frac{4\pi}{c(2\pi\hbar c)^3}\int_0^\infty \Phi^{\text{out}}_{0,\text{NES}}(\varepsilon, \varepsilon')\,\varepsilon'^2 d\varepsilon'$	Section 5.2.4 $\frac{C_l}{c(2\pi\hbar c)^3} C_1 H_l^{\text{I/II}}(\varepsilon', \varepsilon, l, T, \eta)$	Bruenn (1985) Mezzacappa and Bruenn (1993c)
Pair creation and annihilation	$e^- + e^+ \rightleftarrows \nu + \bar{\nu}$	Section 2.4.2 $-\frac{4\pi}{c(2\pi\hbar c)^3}\int_0^\infty \Phi^{p}_{0,\text{Pair}}(\varepsilon, \varepsilon')\,\varepsilon'^2 d\varepsilon'$	Section 5.2.4 $\frac{C_l}{c(2\pi\hbar c)^3} C_2 J_l^{\text{I/II}}(\varepsilon', \varepsilon, l, T, \eta)$	Bruenn (1985)

where $\nu = \nu_{e,\mu,\tau}, \bar{\nu}_{e,\mu,\tau}$, $\nu_{e,\mu,\tau}$ = electron, muon, tau neutrino, $\bar{\nu}$ = antiparticle of particle ν, n = free neutrons, p = free protons, N = free neutrons or protons, A = nuclei, e^- = electrons, e^+ = positrons, and $C_l = \frac{2l+1}{2}$, with l the order of Legendre coefficients, $C_1 = \frac{G^2}{\pi\varepsilon^2\varepsilon'^2}\int_0^{+\infty} dE_e F_e(E_e)\left[1 - F_e(E_e + \varepsilon - \varepsilon')\right]$, $C_2 = \frac{2G^2}{2\pi}\int_0^{\varepsilon+\varepsilon^+} dE_e\left[1 - F_e(E_e)\right]\left[1 - F_{e^+}(\varepsilon + \varepsilon' - E_e)\right]$

5.5 Solver for Neutrino–Matter Coupling

Neutrino–matter coupling solver is the most expensive part of a CCSN simulation, not only because it is called the most, but also because it needs the most information, on the fluid field, the radiation field, and on the weak interactions. The main cost of weak interactions comes from energy-exchanging interactions, such as neutrino-electron scattering and neutrino pair production and annihilation. The interpolations for energy-exchanging interactions increase in $\mathcal{O}(N_\varepsilon^2)$ with energy grid size N_ε, other than the $\mathcal{O}(N_\varepsilon)$ of non-energy-exchanging (single-energy-dependent) interactions. In addition, because neutrino–matter coupling solver updates both the fluid field and the radiation field, any achievement in improving efficiency or accuracy is explicit. We present the development of our neutrino–matter coupling solver in this section.

With the vector of 'collision invariants' which we define as $\mathbf{U}(\boldsymbol{\mathcal{U}}, \boldsymbol{u}) = (\,\rho,\, \mathsf{F}_j,\, \mathsf{E},\, \mathsf{N}\,)^{\mathrm{T}}$, with the total momentum $\mathsf{F}_j = \rho v_j + F_{Ej}$, energy $\mathsf{E} = E_{\mathrm{f}} + E = \rho\epsilon_f + E$, and lepton number $\mathsf{N} = n_{\mathrm{e}} + N$, and using the same notation as in Equation (5.1) and (5.2), we can write the neutrino-matter coupling equations as

$$\partial_t \boldsymbol{\mathcal{U}} = \boldsymbol{\mathcal{C}}(\boldsymbol{\mathcal{U}}, \boldsymbol{u}), \tag{5.24}$$

$$\partial_t \mathbf{U} = 0. \tag{5.25}$$

We solve the above nonlinear equations, together with corresponding equations for the matter, which is updated by enforcing preservation of the collision invariants. The nonlinear system solver we employ is an extension of the nested fixed-point iteration scheme presented in Laiu et al. (2021). Other useful references are Laiu et al. (2020); Endeve et al. (2022a); Endeve et al. (2022b). Given implicit time integration, Equations (5.24) and (5.25) become to solve

$$\boldsymbol{\mathcal{U}}^{n+1} = \boldsymbol{\mathcal{U}}^{n} + \Delta t\, \boldsymbol{\mathcal{C}}(\boldsymbol{\mathcal{U}}^{n+1}, \boldsymbol{u}^{n+1}), \tag{5.26}$$

$$\mathbf{U}(\boldsymbol{\mathcal{U}}^{n+1}, \boldsymbol{u}^{n+1}) = \mathbf{U}(\boldsymbol{\mathcal{U}}^{n}, \boldsymbol{u}^{n}). \tag{5.27}$$

The unknown fluid variables in the collision solve are ρ, v_j, E_f, and Y_e, so that Equation (5.25) gives

$$\rho^{n+1} = \rho^n = \rho, \tag{5.28a}$$

$$\rho v_j^{n+1} + F_{Ej}^{n+1} = \rho v_j^n + F_{Ej}^n, \tag{5.28b}$$

$$\rho \epsilon_f^{n+1} + E^{n+1} = \rho \epsilon_f^n + E^n, \tag{5.28c}$$

$$\rho\, Y_e^{n+1} + N^{n+1} = \rho\, Y_e^n + N^n, \tag{5.28d}$$

with the following quantities dependent on the primitive moments

$$F_{Ej}^{n+1} = F_{Ej}(\boldsymbol{\mathcal{M}}^{n+1}, \boldsymbol{v}^{n+1}), \tag{5.29a}$$

$$E^{n+1} = E(\boldsymbol{\mathcal{M}}^{n+1}, \boldsymbol{v}^{n+1}), \tag{5.29b}$$

$$N^{n+1} = N(\boldsymbol{\mathcal{M}}^{n+1}, \boldsymbol{v}^{n+1}), \tag{5.29c}$$

while the radiation momentum, energy, and lepton number densities depend on the primitive moments and fluid three-velocity. The radiation variables are updated implicitly as

$$\boldsymbol{\mathcal{U}}(\boldsymbol{\mathcal{M}}^{n+1}, \boldsymbol{v}^{n+1}) = \boldsymbol{\mathcal{U}}(\boldsymbol{\mathcal{M}}^{n}, \boldsymbol{v}^{n}) + \Delta t\, \boldsymbol{\mathcal{C}}\big(\boldsymbol{\mathcal{M}}^{n+1}, \rho, T(\epsilon_f^{n+1}), Y_e^{n+1}\big). \tag{5.30}$$

Equations (5.28) and (5.30) can be solved as a fixed-point problem, such that

$$\boldsymbol{\mathcal{M}}^{n+1} = G(\boldsymbol{\mathcal{M}}^{n+1}, \boldsymbol{z}^{n+1}), \tag{5.31}$$

$$\boldsymbol{z}^{n+1} = g(\boldsymbol{\mathcal{M}}^{n+1}, \boldsymbol{z}^{n+1}), \tag{5.32}$$

$$\boldsymbol{z} = (\boldsymbol{v}, \epsilon_f, Y_e), \tag{5.33}$$

where $G(\boldsymbol{\mathcal{M}}, \boldsymbol{z})$ is the operator corresponding to Equation (5.30), $g(\boldsymbol{\mathcal{M}}, \boldsymbol{z})$ is the operator corresponding to Equations (5.28), and we write $\boldsymbol{z} = g(\boldsymbol{\mathcal{M}}, \boldsymbol{z})$, $\boldsymbol{z}$ is a subset of $\boldsymbol{u}$.

5.5.1 Picard iteration

A procedure for generating a sequence of functions that approximate the solution is Picard iteration. Picard iteration applied to Equations (5.31) and (5.32), given the initial guess $\boldsymbol{\mathcal{M}}^0$ and $\boldsymbol{z}^0$, which are from the initial state or the previous step, and iterate

$$\boldsymbol{\mathcal{M}}^{k+1} = G(\boldsymbol{\mathcal{M}}^k, \boldsymbol{z}^k), \tag{5.34}$$

$$\boldsymbol{z}^{k+1} = g(\boldsymbol{\mathcal{M}}^k, \boldsymbol{z}^k), \tag{5.35}$$

for $k = 0, 1, ...$ until a convergent solution is found. The convergence requires operators G and g be contraction maps, i.e.,

$$|\boldsymbol{\mathcal{M}}^{k+1} - \boldsymbol{\mathcal{M}}^k| \leq L_M |\boldsymbol{\mathcal{M}}^k - \boldsymbol{\mathcal{M}}^{k-1}|, \quad L_M \leq 1, \tag{5.36}$$

and

$$|\boldsymbol{z}^{k+1} - \boldsymbol{z}^k| \leq L_z |\boldsymbol{z}^k - \boldsymbol{z}^{k-1}|, \quad L_z \leq 1. \tag{5.37}$$

This is the issue with applying Picard iteration to Equation (5.34) and (5.35) – the convergence is not guaranteed. Besides, the realizability of numerical solutions for primitive moments $\boldsymbol{\mathcal{M}}$ requires choosing the update operator G carefully.

5.5.2 Nested algorithm

A modification to the fixed-point problem given by Equation (5.28) and (5.30) is a nested algorithm. In a nested algorithm, the problem is solved in four steps.

- **Step 1:** Compute opacities using $(\boldsymbol{z}^n, \boldsymbol{\mathcal{M}}^n) = (\boldsymbol{z}^k, \boldsymbol{\mathcal{M}}^k)$ ($k = 0$ for the initial iteration).
- **Step 2:** Find a $\boldsymbol{\mathcal{M}}^*$ that is the limit of $\boldsymbol{\mathcal{M}}^{l+1} = G(\boldsymbol{\mathcal{M}}^l, \boldsymbol{z}^k)$, $l = 0, 1, 2, ...$

- **Step 3:** Find $\boldsymbol{z}^{k+1}$ such that $\boldsymbol{z}^{k+1} = g(\boldsymbol{\mathcal{M}}^*, \boldsymbol{z}^k)$.
- **Step 4:** Check for convergence. If $\boldsymbol{z}^{k+1}$ is not converged, go back to Step 1 with $\boldsymbol{\mathcal{M}}^{k+1}, \boldsymbol{z}^{k+1} = \boldsymbol{\mathcal{M}}^*, \boldsymbol{z}^k$. Otherwise, exit and set $(\boldsymbol{z}^{n+1}, \boldsymbol{\mathcal{M}}^{n+1}) = (\boldsymbol{z}^{k+1}, \boldsymbol{\mathcal{M}}^*)$.

Step 2 for finding $\boldsymbol{\mathcal{M}}^*$ is in an inner loop, while Steps 3 and 4 for $\boldsymbol{z}^{k+1}$ and Step 1 for evaluating the opacities are part of the outer loop. Fixed-point iteration is relatively easy to implement and extend when opacities are added. The nested structure provides additional flexibility to reduce computational costs by reducing expensive opacity evaluations. Fixed-point iteration avoids the Jacobian matrix constructions and dense linear systems, though its convergence rate can be low (Laiu et al., 2021). In `thornado`, Anderson acceleration (Anderson, 1965) is applied separately to the outer and inner loops to accelerate the convergence of the fixed-point method (Laiu et al., 2021). More details about its code implementation, convergence properties, efficiency, comparison with other methods in the context of CCSN simulations can be found in Laiu et al. (2021); Laiu et al. (2022); Endeve et al. (2022b).

5.6 Numerical Test

This section presents a suite of test problems designed to verify the framework of Flash-X + `thornado`. These tests use realistic opacities provided by `WeakLib`.

5.6.1 Relaxation Test

To further examine the collision term, we performed a relaxation to equilibrium test. This test only includes the update from the collision term, and the transport operator is not included. The purpose of this test is to determine if the code can maintain at the theoretical equilibrium state numerically.

We adopt matter profiles for mass density, temperature, and electron fraction obtained with the CHIMERA code using a 25 $M_\odot$ progenitor from Woosley and Heger

(2007) and the Lattimer-Swesty LS220 EOS (Lattimer and Swesty, 1991) (profiles are provided by Stephen Bruenn, private communication). The fluid velocity is set to zero. See Figure 5.2.3 for the fluid state plot. Electron flavor neutrino emission and absorption on nucleons and nuclei, and isoenergetic scattering on nucleons and nuclei, are included in this test. The initial number density of neutrinos is set to be the thermal equilibrium distribution given by the Fermi-Dirac distribution function

$$f_{\rm eq}(\varepsilon) = \frac{1}{e^{(\varepsilon-\mu_{\nu_e})/k_BT}+1}, \tag{5.38}$$

where μ_{ν_e} is the ν_e-neutrino chemical potential. If the system remains in the Fermi-Dirac equilibrium state, the code has computed the correct equilibrium distribution.

Ten energy groups, ranging from 1.0 to 100 MeV, with a spatial element size of 0.625 km, spanning 0 to 300 km are used. We run the test for 1 s. The difference between the final state and the initial state is small, and proportional to the spatial resolution and number of time steps. An comparison between the initial state and the final state is presented in Figure 5.6.1, where the number densities at the initial state are plotted in solid lines, and the number densities at the final state are in dotted lines. Color represents neutrino energy.

The result indicates that Flash-X + `thornado` is able to maintain at the theoretical equilibrium state numerically.

5.6.2 Homogeneous Sphere Problem

To further examine the coupling between the collision term and the advection term in transport, we performed a homogeneous sphere problem. This test was also used to test the Flash-X +`thornado` interface by performing within the `thornado` environment and repeated using Flash-X +`thornado`. A version of this test problem is discussed in Bruenn (1985); Messer (2000); Endeve et al. (2018) and Chu et al. (2019b). It mimics a static ($v = 0$) stellar core of radius R surrounded by a tenuous atmosphere. The idea is to set the absorption opacity and equilibrium distribution

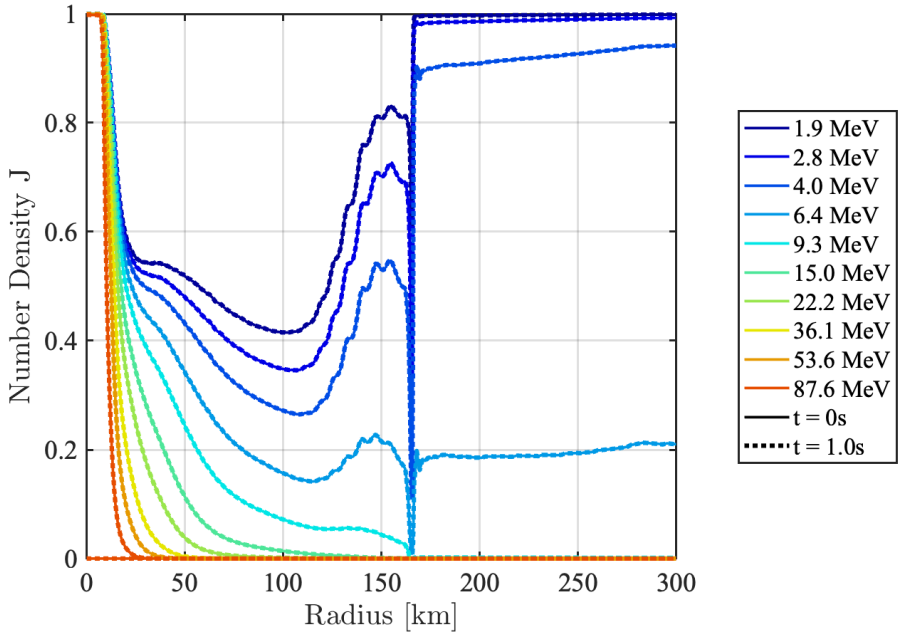

Figure 5.6.1: Result of the number density for the relaxation test. The initial conditions, given by Equation (5.38), are plotted in colored solid lines, and the final state after 1 s evolution is plotted in colored dotted lines. Color represents neutrino energy, as the legend marks. The two line types overlap because the radiation field remains at equilibrium.

function to constant values inside the sphere, and the other opacities to zero. Outside the sphere, the absorption opacity is close to zero. Here we present a spectral version of the test in 1D spherical coordinates. We impose reflecting inner boundary conditions and outflowing outer boundary conditions in space. The two runs, within the `thornado` environment and using Flash-X+`thornado`, are performed, and give the same result to machine accuracy.

The steady state solution of this problem can be obtained by solving the steady state transport equation in spherical symmetry (Smit et al., 2000):

$$f_{\mathrm{A}}(r,\mu) = f_0\left(1 - e^{-\chi_0 s(r,\mu)}\right), \tag{5.39}$$

where f_0 is the equilibrium distribution,

$$s(r,\mu) = \begin{cases} r\mu + Rg(r,\mu) & \text{if } r < R, \quad \mu \in [-1,+1] \\ 2Rg(r,\mu) & \text{if } r \geq R, \quad \mu \in \left[\left(1-(R/r)^2\right)^{1/2}, +1\right] \\ 0 & \text{otherwise,} \end{cases} \tag{5.40}$$

and $g(r,\mu) = \left[1-(r/R)^2\left(1-\mu^2\right)\right]^{1/2}$.

We take the one-dimensional spherical coordinates domain to $D = \{r \in \mathbf{R}^+, \theta \in [0,\pi], \varphi \in [0,2\pi) : r \in [0,500]$ km$, \theta = \frac{\pi}{2}, \varphi = \pi\}$ and $R = 100$ km. The edge of the core is sharp, and we use a geometrical mesh so that the transition from the interior values to the exterior values happens in a $\sim$1 km radial zone. In addition, we impose a slope limiter to improve accuracy. We use 20 geometrically spaced energy groups covering $[1,150]$ MeV, with a zoom of 1.7; i.e.,

$$(\Delta\varepsilon)_{n+1} = 1.7 \times (\Delta\varepsilon)_n. \tag{5.41}$$

(This setting gives convergent luminosity and root-mean-square energy values when computed to the results obtained with 64 geometrically spaced energy groups covering

$[0.1, 300]$ MeV.) The opacities are given by the `WeakLib` Bruenn 1985 tables using SFHo EOS.

Three thermal states for $r \in [0, R]$ km are assumed, as listed in Table 5.2. Model A represents a high-density, hot core. Model B represents a low-density, relatively cold core. Model C represents a low-density core at a temperature intermediate between model A and model B. The corresponding opacities, χ, are plotted versus energy in Figure 5.6.2. The radiation field is initialized using the analytic solution, computed using f_{A} in Equation (5.39). We run the test for t=10 ms till a stationary radiation field is achieved (i.e. until the change in radiation variables is zero).

Figure 5.6.3 compares the difference in the neutrino and antineutrino luminosities between the analytical values and the values given by `thornado` using the CB closure, where we define the radial luminosity as

$$L_r = (4\pi r)^2 \int_{\mathbb{R}^+} \mathcal{H}_r \varepsilon^3 d\varepsilon. \tag{5.42}$$

We see that the performance of `thornado` is problem-dependent, but has some common features. First, `thornado` consistently yields lower luminosities. Second, the maximum relative difference is inside the core. Third, the minimum difference between the analytical and computed results occurs outside the core and is maintained to the edge of the domain. For model A, `thornado` computes approximately 80% less neutrino luminosity inside the core and 4.5% less luminosity outside the core, and 25% less antineutrino luminosity inside the core and 5% less luminosity outside the core. For model B, `thornado` computes 30% less neutrino luminosity inside the core and 2% less luminosity outside the core, and 28% less antineutrino luminosity inside the core and 4% less luminosity outside the core. For model C, `thornado` computes 45% less neutrino luminosity inside the core and 3% less outside the core, and 35% less antineutrino luminosity inside the core and 3% less luminosity outside the core. We will see later how the algebraic closure approximation affects the numerical solutions.

Table 5.2: Thermal states used in the homogeneous sphere tests.

Model A	Model B	Model C
$\rho = 10^{13}$ g cm^{-3}, T = 16 MeV, $Y_e = 0.14$	$\rho = 3 \times 10^{11}$ g cm^{-3}, T = 4 MeV, $Y_e = 0.2$	$\rho = 10^{11}$ g cm^{-3}, T = 8 MeV, $Y_e = 0.15$

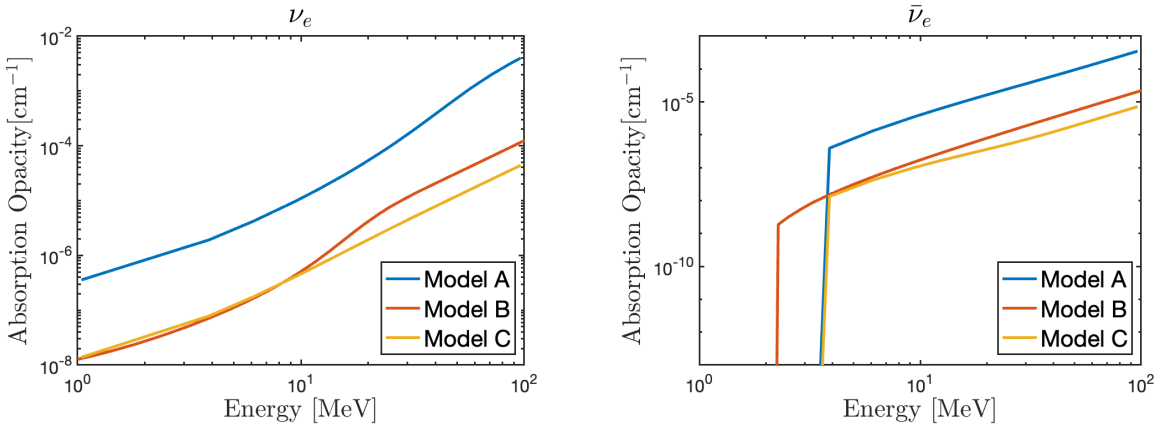

(a) Electron neutrino absorption opacity

(b) Electron antineutrino absorption opacity

Figure 5.6.2: Absorption opacities for the homogeneous sphere test. Color indicates the different thermal state. See Table 5.2 for details of each model.

Figure 5.6.4 shows the root-mean-square (RMS) energies of the emitted neutrinos, defined as

$$\varepsilon_{\mathrm{RMS}} = \sqrt{\langle \varepsilon^2 \rangle} = \sqrt{\frac{\int_{\mathbb{R}+} \mathcal{J} \varepsilon^5 d\varepsilon}{\int_{\mathbb{R}+} \mathcal{J} \varepsilon^3 d\varepsilon}}. \tag{5.43}$$

We see the problem-dependent performance again. However, the agreement with the analytical values is very good, with a maximum difference 0.5%, which is in model B for the antineutrino RMS energy and is maintained to the edge of the domain.

Closure Comparison

The purpose of this section is to compare the results obtained using the different algebraic closures discussed in Section 2.5.2 and to understand how the choice of closure affects the result. Other closure comparison work can be found in Smit et al. (2000); Vaytet et al. (2011); Just et al. (2015); Murchikova et al. (2017); Pan et al. (2019); Richers (2020). Here, we use the abbreviations for difference closures: CB for Cernohorsky and Bludman (1994), MI for Minerbo (1978), KE for Kershaw (1976); Banach and Larecki (2017), and LE for Levermore (1984).

In this work, we focus on the electron-neutrino luminosity and compare the results obtained using different closures, which are presented in Figure 5.6.5. The left panels show the whole domain, and the right panels show a zoom-in at the core center, where the largest difference from the analytic values occur. For model A, the list of closures based on their performance from best to worst is CB, KE, MI, LE. For model B, the list is the same: CB, KE, MI, LE. For model C, the list is CB $\approx$ MI, LE, KE.

The impact different closures have on neutrino luminosity is 15% at the inner region and 4% at the outer region. For example, consider model B, the results for different closures have the maximum difference of 27%(CB) to 42%(LE), and the minimum of 6%(LE) to 2%(CB).

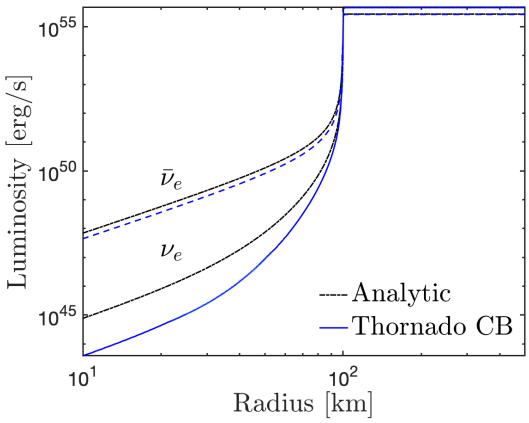

(a) Neutrino luminosity for model A

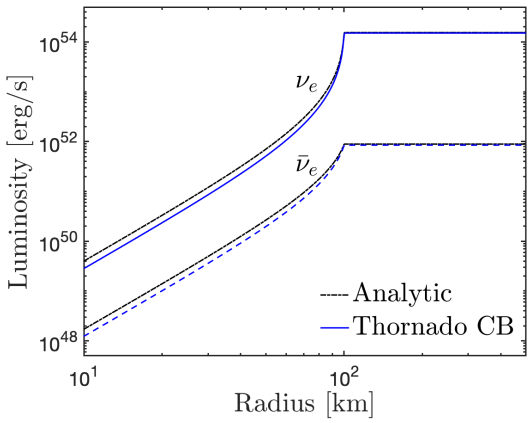

(b) Neutrino luminosity for model B

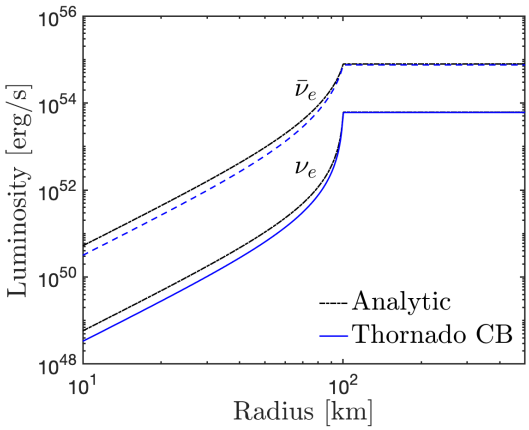

(c) Neutrino luminosity for model C

Figure 5.6.3: Electron neutrino and antineutrino luminosities for the results of the homogeneous sphere problem using `thornado` with CB closure. Results for electron-neutrino are plotted in solid line and dashed lines for electron-antineutrino. Analytic solutions are plotted in black, and numerical solutions given by `thornado` using CB closure are plotted in blue. See Table 5.2 for details of each model.

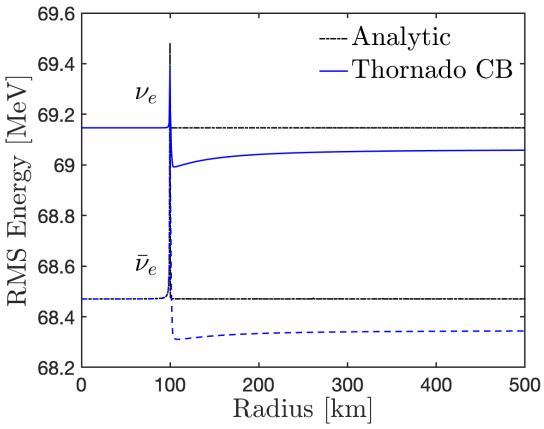

(a) Neutrino RMS energy for model A

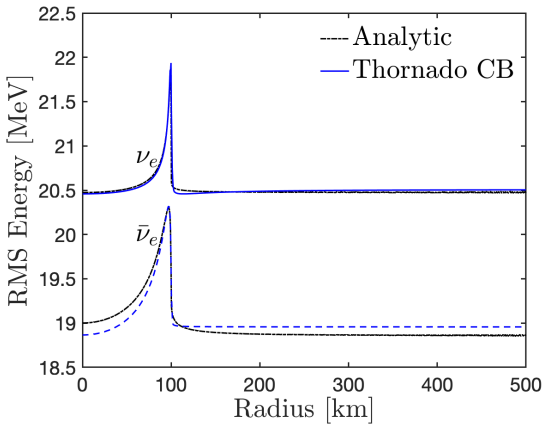

(b) Neutrino RMS energy for model B

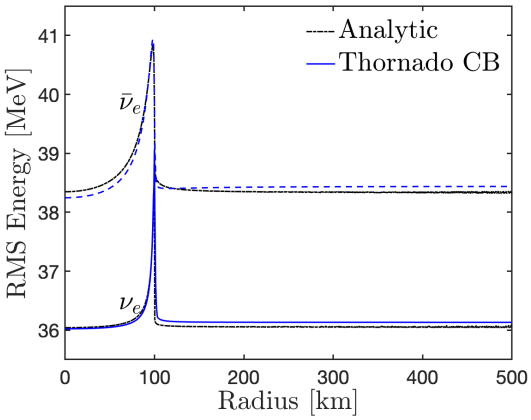

(c) Neutrino RMS energy for model C

Figure 5.6.4: Electron neutrino and antineutrino RMS energy for the homogeneous sphere problem using `thornado` with CB closure. Results for electron-neutrino are plotted in solid line and dashed lines for electron-antineutrino. Analytic solutions are plotted in black, and numerical solutions given by `thornado` using CB closure are plotted in blue. See Table 5.2 for details of each model.

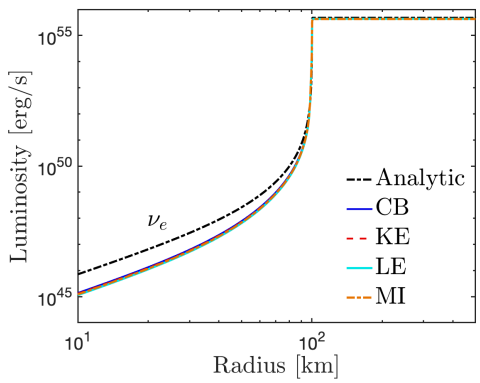

(a) Model A

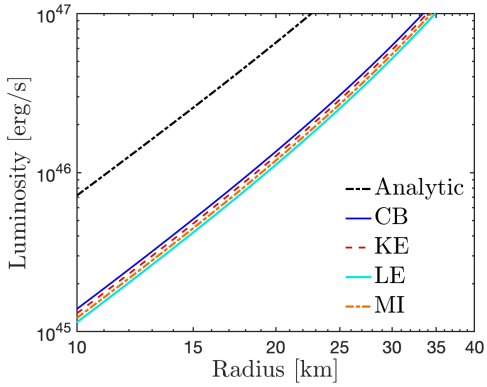

(b) Model A zoom in

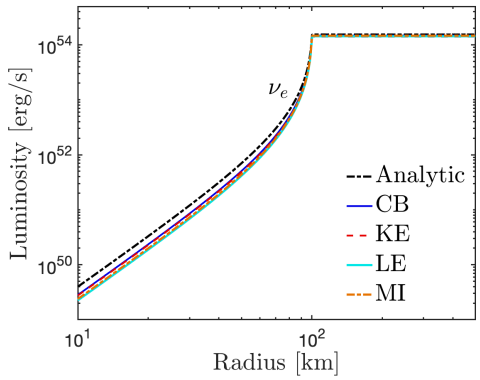

(c) Model B

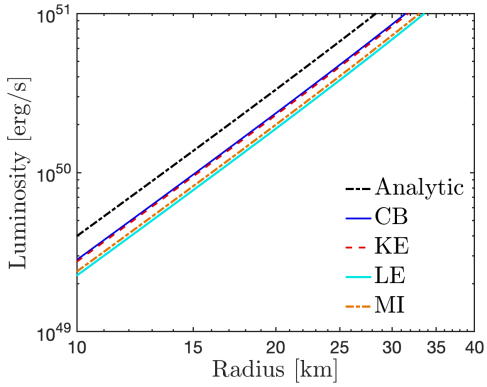

(d) Model B zoom in

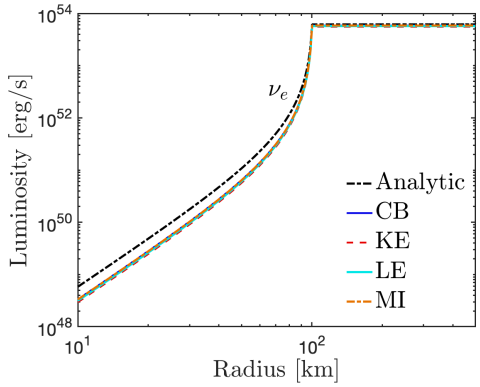

(e) Model C

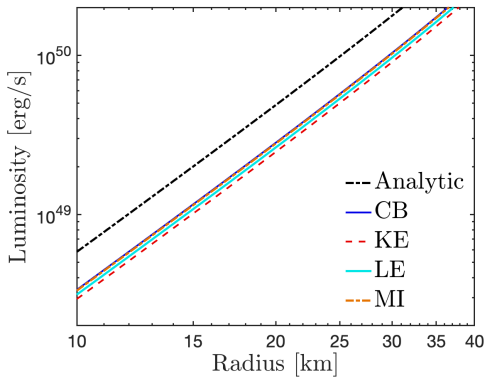

(f) Model C zoom in

Figure 5.6.5: Result for electron-neutrino luminosities from solving the multi-group homogeneous sphere problem with the DG(2)+PDARS method using 144 spatial elements and 20 energy groups. Analytic solutions are plotted in black, and numerical solutions given by `thornado` using different closures are plotted in color.

We can see why closures make this difference by plotting the Eddington factor they predict. Eddington factor is defined as

$$k = \frac{\mathcal{K}}{\mathcal{J}}, \tag{5.44}$$

where $\mathcal{K}$ is the scalar value of the second-order moment $\boldsymbol{\mathcal{K}}$. The analytic values computed using distribution function in Equation (5.39) are plotted in solid line in Figure 5.6.6. The CB closure, which gives the best result in all three models, has a maximum 30% less Eddington factor k around the sphere, which is presented in dash line. A smaller Eddington factor results in advection from the core, since less pressure around the sphere. The core loses more neutrinos at the beginning and reaches a steady state with lower luminosity later. We indeed observed that when the accuracy of the closure method improves, the outcome spontaneously improves. In all three models, the biggest difference between numerical solution and analytic value in k is at the transition region for the low energy group. The biggest challenge for the closure is that it cannot follow the non-monotone behavior at the transition edge, $r = 100$ km. Despite these differences, the CB closure gives correct value at the diffusion limit at the center, and behavior good at streaming limit at the outer region.

5.6.3 Deleptonization Wave Test

The deleptonization wave test has the most sophisticated settings that a CCSN simulation requires. It includes `WeakLib` tables and interpolation, Flash-X `Spark` hydrodynamic, the interfaces between Flash-X and `thornado`, and `thornado`'s $\mathcal{O}(v/c)$ transport. It is designed to investigate the performance of the code in a realistic setting. We adopt the matter profiles for mass density, temperature, and electron fraction obtained using the CHIMERA code in a CCSN simulation for a 25 $M_\odot$ progenitor. See Figure 5.2.3 for the initial condition.

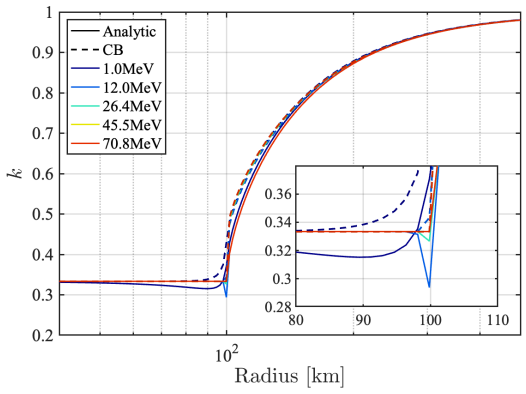

(a) Model A

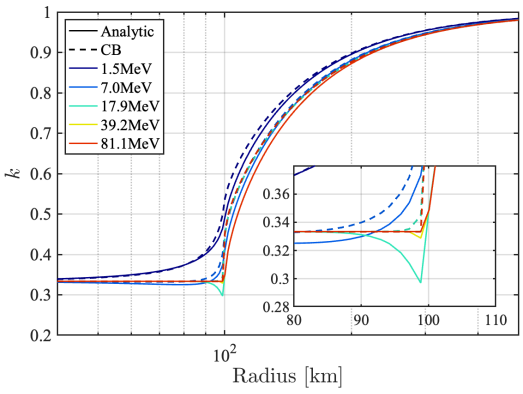

(b) Model B

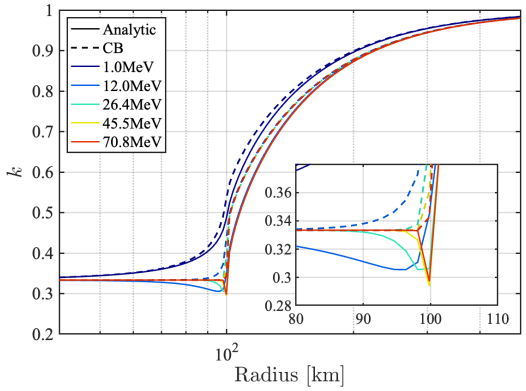

(c) Model C

Figure 5.6.6: Result for Eddington factor in homogeneous sphere problem using `thornado` with CB closure on selected energy groups. The numerical solutions are plotted in dash line. The analytic values computed using distribution function in Equation (5.39) are plotted in solid line. The color indicates the energy group.

We use the density, temperature, and electron fraction from the profile, with zero fluid velocity, to initialize the fluid field, and include the electron-flavor neutrino interactions in Bruenn (1985) to our model. The radiation quantities are also initialized using the CHIMERA radiation profile (provided by Stephen Bruenn, private communication). A plot for the initial radiation filed measured by neutrino RMS energy (Equation (5.43)) and averaged flux factor, i.e.,

$$\bar{\mathcal{H}}_x = \frac{\int_0^\infty \mathcal{J}\varepsilon^3 d\varepsilon}{\int_0^\infty \mathcal{H}_x \varepsilon^3 d\varepsilon}, \tag{5.45}$$

is presented in Figure 5.6.7.

Comparison of Steady States Due to the difference in neutrino transport, the radiation state given by CHIMERA is not necessary to be the stationary state in `thornado` using the two-moment method with different closures. To investigate the difference different transport and the closure method can make, we run a steady state with a stationary ("frozen") fluid field. The closures we considered here include: CB for Cernohorsky and Bludman (1994), BL for Banach and Larecki (2013), MI for Minerbo (1978), KS for Kershaw (1976); Banach and Larecki (2013), and LE for Levermore (1984). For each closure we considered here, we relaxed the radiation field till a steady state was reached. Results for this process are presented in Figure 5.6.8 with the initial (CHIMERA) condition in black, and `thornado` results in color: the results of the CB closure are in blue, red for the BL closure, yellow for the KS closure, purple for the LE closure, and green for the MI closure. The results given by `thornado` using different closures are almost identical in this setting for both neutrino RMS energies and averaged flux factors. `thornado` has lower electron-neutrino and electron-antineutrino RMS energies, and higher electron-neutrino and electron-antineutrino averaged flux factors. These differences are caused by the different CHIMERA's one-moment method and `thornado`'s two-moment method.

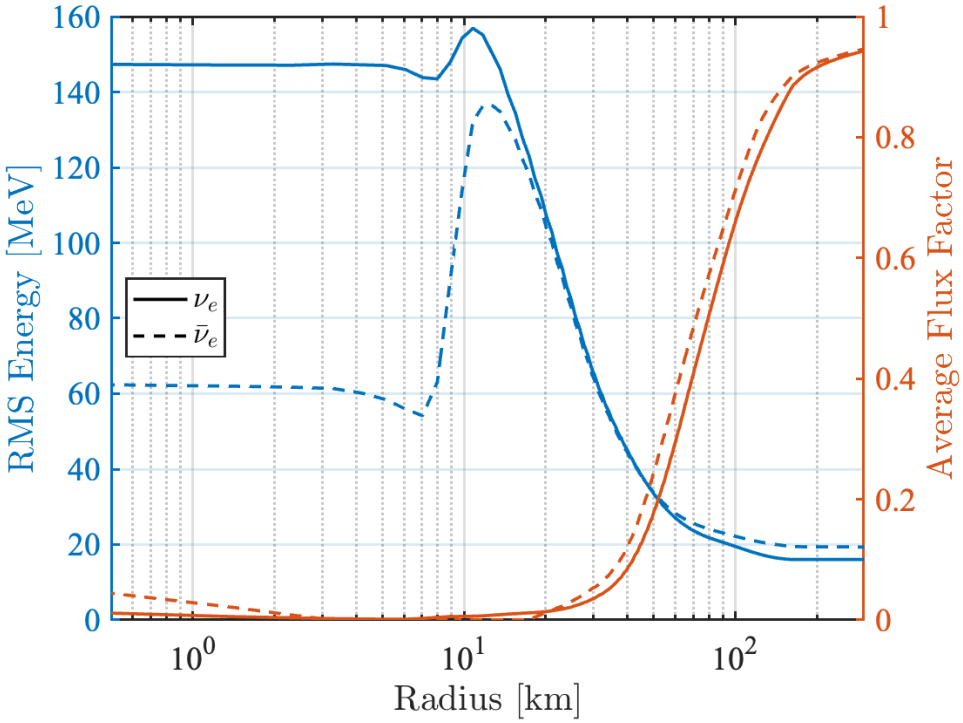

Figure 5.6.7: Initial radiation condition for the deleptonization wave test. The settings for electron-neutrino are plotted in solid lines, and dashed lines for electron-antineutrino. Neutrino RMS energies are plotted in blue based on the left y-axis, and neutrino averaged flux factors are plotted in red based on the right y-axis.

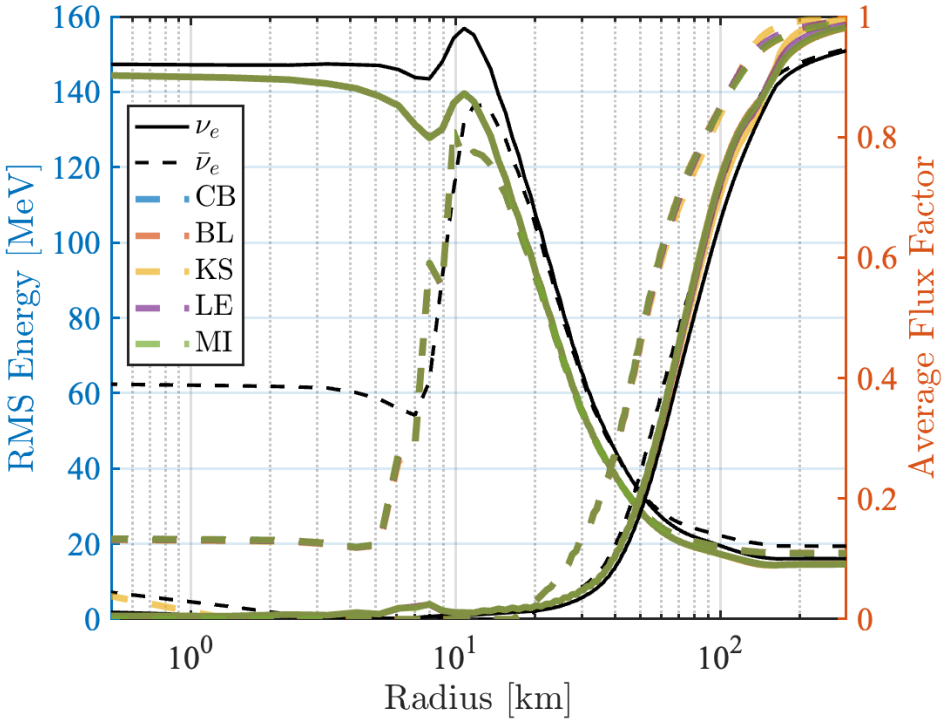

Figure 5.6.8: Steady radiation field with stationary fluid field in deleptonization problem for all closures. The black lines represent the initial (CHIMERA) state, and `thornado` results in color: the results of the CB closure are in blue, red for the BL closure, yellow for the KS closure, purple for the LE closure, and green for the MI closure.

Comparison of Deleptionization with Different Closures The deleptonization test was run for 10 ms from the initial settings, and the result was compared against the initial setting. The evolution of the electron fraction is illustrated in Figure 5.6.9a for the Minerbo closure, and in Figure 5.6.9b for the CB closure. The dynamic of the two evolutions is very close, in both deleptonizing rates and deleptonization over the whole domain. The biggest difference is around 10 km, where the opacities change rapidly (Figures 5.2.4–5.2.5), CB closure leads to more electron loss at transiting to the high opacity region ($4 - 20$ km). Another difference is at the finial state, which is compared to cross all closures in Figures 5.6.10 and 5.6.11. Figures 5.6.10 plots the results obtained using the exact same radiation initial (CHIMERA) states, while Figure 5.6.11 plots the results obtained using the steady state for each closure (as shown in Figure 5.6.8). Overall, the difference in the final state obtained using difference closures is small and only noticeable around the transition region. And the difference between the results obtained using different closures can be slightly affected by the initial condition. Considering the rapid radiation evolution in CCSN simulation, especially around bounce, the difference caused by the closure method is subtle compared to the impact from the transport moment method.

5.7 Conclusion

The development of `WeakLib` is ongoing in order to include more state-of-the-art set of neutrino interactions and nuclear corrections. The work done in `WeakLib` for this dissertation was established the fundamental functions and code framework for the basic neutrino interaction set of Bruenn (1985) and is extensible to a more comprehensive set of weak interactions. The Flash-X–`thornado` interface was tested for accuracy and efficiency, using several numerical tests. Three numerical tests were performed to verify the framework of Flash-X + `thornado`. The relaxation test shows Flash-X + `thornado` is able to arrive and maintain at the theoretical equilibrium

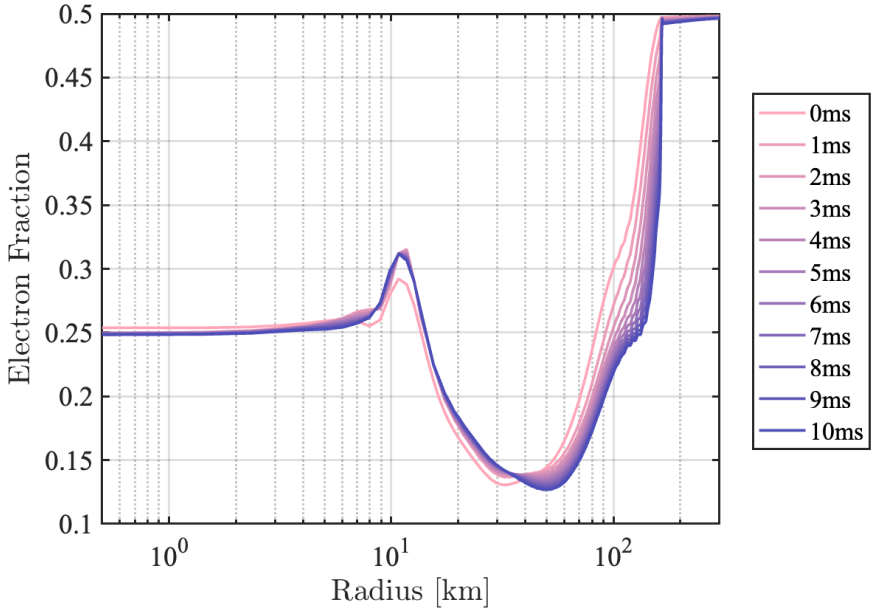

(a) Minerbo Closure

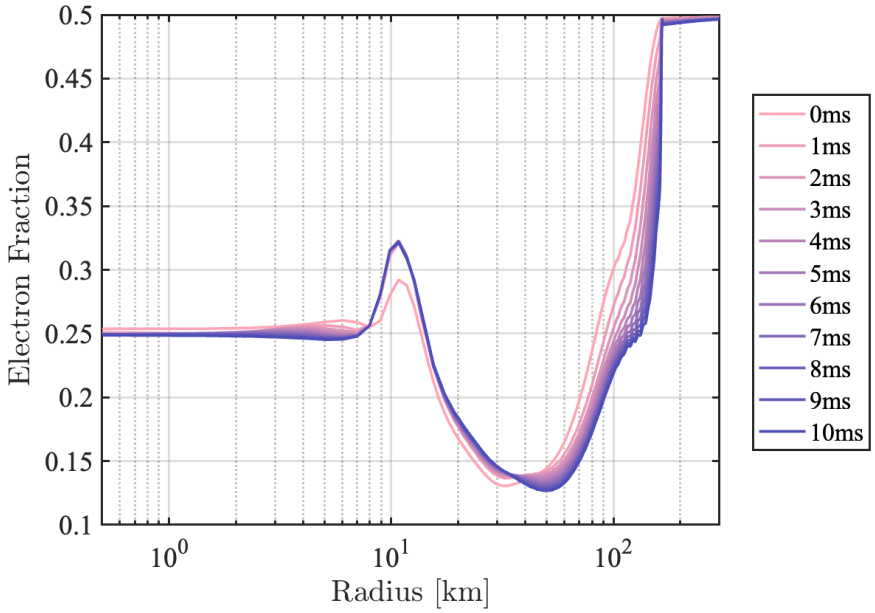

(b) CB Closure

Figure 5.6.9: Electron fraction evolution in deleptonization wave test with different closures for 10 ms duration initiated at the same radiation condition (Figure 5.6.10).

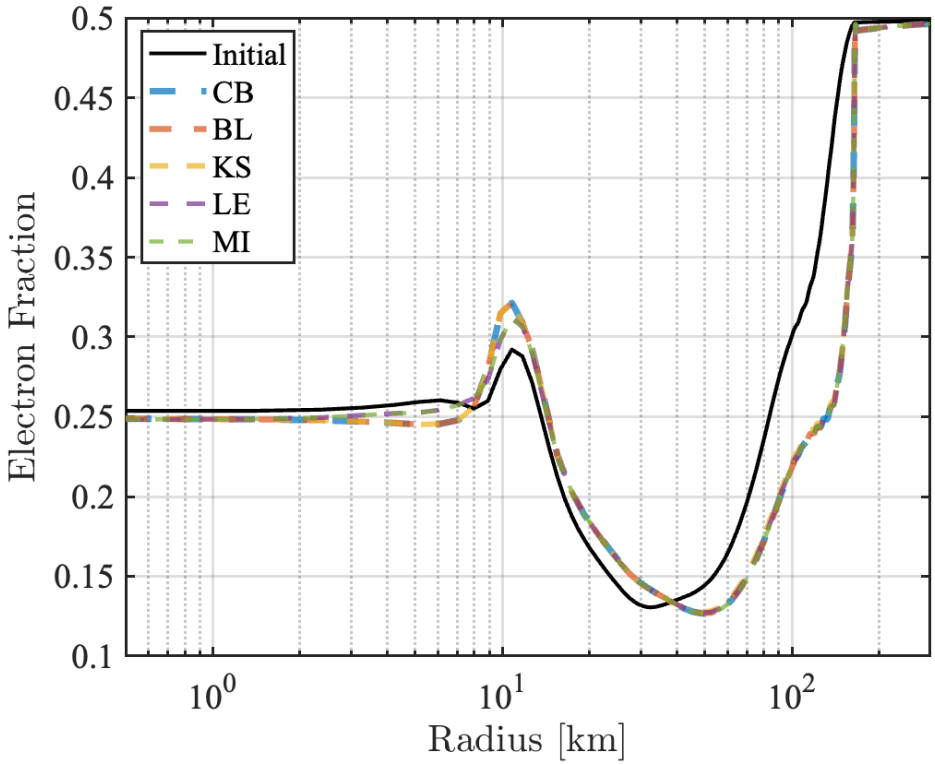

Figure 5.6.10: Comparison of electron fraction profiles in the deleptonization wave test after 10 ms deleptonization obtained with different closures. The initial electron fraction profile is plotted in black, while the results after 10 ms deleptonization are plotted in color. The result for the CB closure is plotted in blue, while red for the BL closure, yellow for the KS closure, purple for the LE closure, and green for the MI closure. Two radiation initial conditions were used. The results for the exact same radiation condition for different closure settings are presented in Figure 5.6.10. The results for using individual steady radiation conditions for each closure setting are presented in Figure 5.6.11.

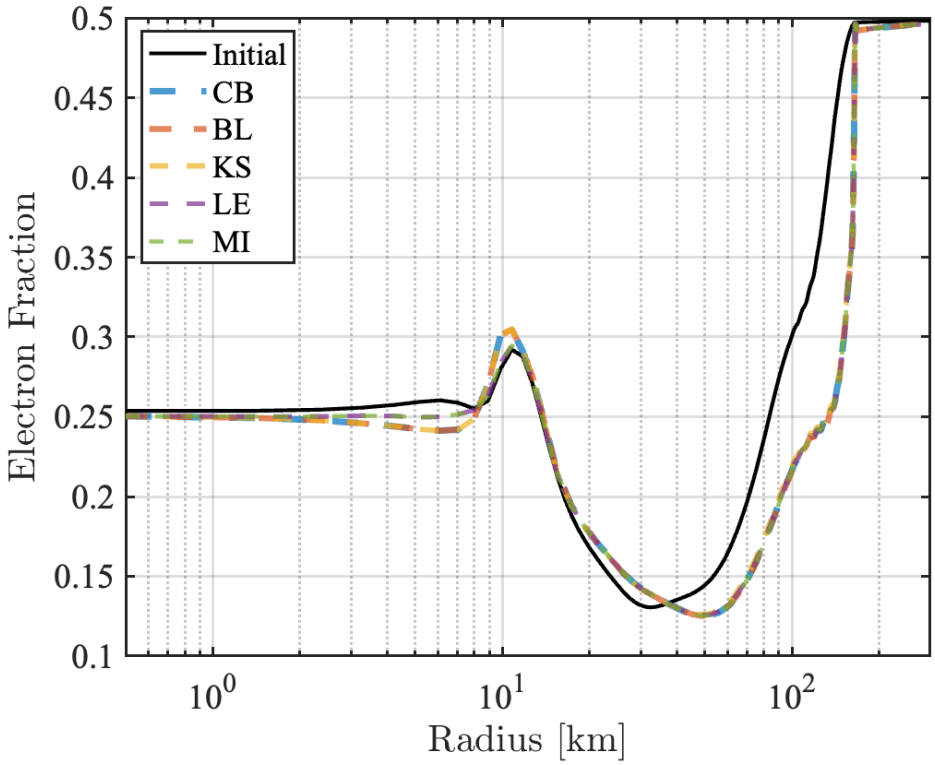

Figure 5.6.11: Comparison of electron fraction profiles in the deleptonization wave test after 10 ms deleptonization obtained with different closures. The initial electron fraction profile is plotted in black, while the results after 10 ms deleptonization are plotted in color. The result for the CB closure is plotted in blue, while red for the BL closure, yellow for the KS closure, purple for the LE closure, and green for the MI closure. Two radiation initial conditions were used. The results for the exact same radiation condition for different closure settings are presented in Figure 5.6.10. The results for using individual steady radiation condition for each closure setting are presented in Figure 5.6.11.

state numerically. The homogeneous sphere problem shows Flash-X + `thornado` is able to simulate a steady radiation with a realistic radiation setting, and has a good agreement with analytic solution. The result of the deleptonization wave test suggests that the numerical implementation for Flash-X + `thornado` has successfully been benchmarked and the code is ready to be used in CCSN simulations.

Chapter 6

CCSN Simulation in Spherical Symmetry: A Comparison with CHIMERA

Supernova codes are complex objects that execute the numerical solution of equations for radiation-hydrodynamics. Their radiation-hydrodynamics are supplemented by equations of state, neutrino transport with multiple sources of opacities, nuclear transmutations, and relativistic gravity. Different numerical techniques each have their own advantages and disadvantages. When simulating a nonlinear system with such uncertainty, it is important to validate code. The study in this chapter is intended to test our neutrino radiation-hydrodynamics implementations and to provide a basis for comparison and verification of Flash-X + `thornado` to be used in the future.

6.1 Introduction

Code verification is an essential step for new code development. For example, Bruenn et al. (2020) performed code comparison (Chapter 9) for comparison between

CHIMERA, AGILE-BOLTZTAN, and PROMETHEUS-VERTEX. For another example, Just et al. (2018) performed code comparison for comparison between AENUS-ALCAR and PROMETHEUS-VERTEX. More publications for CCSN code comparisons can be found in Bruenn (1985); Mezzacappa and Bruenn (1993a,b,c); Yamada et al. (1998); Messer et al. (1998); Burrows et al. (2000); Bruenn et al. (2001); Calder et al. (2002); Rampp and Janka (2002); Liebendörfer et al. (2005); Buras et al. (2006); Ott et al. (2008); Just et al. (2015); Skinner et al. (2016); Richers et al. (2017); O'Connor et al. (2018); Just et al. (2018); Glas et al. (2019); Pan et al. (2019); Bruenn et al. (2020).

This chapter describes a comparison designed to verify the capability of Flash-X + `thornado` to perform supernova simulations. The code we compare with is CHIMERA (Messer et al., 2008; Bruenn et al., 2020), which was developed by the UT-ORNL led CCSN collaboration. It is a CCSN code that incorporates sophisticated neutrino transport, three-dimensional hydrodynamics, realistic neutrino–matter interactions and nuclear, leptonic, and photonic EOS, nuclear reaction network. CHIMERA has been used to study the role of different aspects in CCSN simulation, such as hydrodynamic instabilities, neutrino radiation, and various input physics in the explosion mechanism, as well as compute gravitational radiation (Bruenn et al., 2006, 2009; Yakunin et al., 2010; Bruenn et al., 2013; Yakunin et al., 2015; Lentz et al., 2015; Bruenn et al., 2016; Yakunin et al., 2017; Harris et al., 2017; Messer et al., 2018; O'Connor et al., 2018; Raphael Hix et al., 2019; Mezzacappa et al., 2020b, 2022). CHIMERA comparisons with other codes have been documented in O'Connor et al. (2018) and in Bruenn et al. (2020). We compare Flash-X + `thornado` and CHIMERA in the context of a spherically symmetric CCSN simulation, and carefully control the initial conditions and input physics to ensure a meaningful and informative comparison. We aim to demonstrate the ability of Flash-X + `thornado` to simulate CCSNe by comparing our Flash-X + `thornado` result with that obtained with CHIMERA for a given progenitor, input physics (neutrino opacities and equation of state). To be precise, we compare electron-flavor spectral two-moment neutrino transport in `thornado` and multi-group flux-limited diffusion neutrino transport in

CHIMERA in spherically symmetric. We compare the early evolution of a 9 $M_\odot$ progenitor, including central fluid parameters, shock radius, neutrino luminosities and RMS energies (Equation 5.43) from both codes. Given the diversity of neutrino transport, the resolution, and non-NSE treatment, we find good agreement in many critical quantities, including the thermal states at the core bounce, PNS radius, and RMS energy.

6.2 Initial Models, Codes, and Methodology

6.2.1 Models

For the first code verification and comparison, we perform a CCSN simulation in spherical symmetry (1D), initiated with a low-mass pre-collapse progenitor previously modeled throughout all stages of stellar evolution: a 9 $M_\odot$ progenitor from Sukhbold et al. (2016), denoted as S9. The initial condition is displayed in Figure 7.2.1. Newtonian compressible hydrodynamics and gravity (Flash-X) are coupled with $\mathcal{O}(v/c)$ neutrino transport (`thornado`). The Flash-X hydrodynamics solver is based on a finite-volume implementation, and the gravitational potential is computed using a multipole Possion solver. Electron-type neutrinos and antineutrinos are evolved. The industry-standard SFHo EOS and the "standard" opacity set in Bruenn (1985) are used. Since the initial conditions and input physics are carefully set to be the same, the main difference between the two codes for this comparison will stem from the neutrino transport method used, non-NSE treatment at large radius, and potentially difference in grids, et cetera.

6.2.2 Methodology and Code

Weak Physics The `WeakLib` tables provide the SFHo EOS to both codes and the Bruenn 1985 opacity rates to Flash-X + `thornado`. CHIMERA is an evolving code,

and the results used in this chapter were obtained using its "F-Series" setting, Bruenn 1985 opacities, and including the non-NSE regime in the EOS.

Gravity and Hydrodynamics The hydrodynamics in both codes are Newtonian. We ran Flash-X + `thornado` using `Spark`'s default HLLD approximate Riemann solver with Newtonian monopole gravity. CHIMERA's hydrodynamics were evolved with a Lagrangian-plus-remap version of the Piecewise Parabolic Method (PPMLR) extended to include multi-species advection, multidimensional gravity, neutrino coupling, and with radial grid movement (Bruenn et al., 2020).

Transport Flash-X + `thornado` was run with the $\mathcal{O}(v/c)$ spectral two-moment neutrino transport in `thornado`, which is a higher-order moment method (second-order) than the flux-limited diffusion (first-order) method used in CHIMERA. Both `thornado` and CHIMERA use Eddington factor closure, which is an algebraic closure, to represent higher angular moments and to close their corresponding systems of moment equations.

6.2.3 Detailed Settings

Flash-X + `thornado`: Flash-X + `thornado` used 16 geometrically-spaced, first-order, DG energy elements (giving 32 energy nodes) spanning the range from 0.1 to 300 MeV with the first element width being 2.172 MeV and the last element width being 61.74 MeV. The spatial domain $[0, 3000]$ km is divided into 4096 DG elements, uniformly in radius, giving Δr=0.732 km per element. The mesh is (uniformly) fixed through the simulation.

CHIMERA: CHIMERA used a geometrically spaced energy grid with 20 zone-centered energies from 4–250 MeV, the first cell center at 2.57 MeV, and the last cell center at 251.97 MeV. It was performed using 720 adaptive radial zones. As the simulation progressed past bounce, CHIMERA zones moved with the fluid and were adjusted

to maintain an good resolution – an approximately constant $\Delta r/r$ with limiting the maximum value of $\Delta\rho/\rho$. So that CHIMERA can maintain a good resolution at the surface of the PNS. This setting leads to the spatial domain $[0, 21600]$ km being adaptively meshed with $\Delta r_{\min}$ $\sim$0.07 km during core bounce. (The adaptive mesh will be seen in the plots discussed below.)

6.3 Results

Each simulation produces significant data. We start with a comparison across the different phases of evolution: i.e., pre-bounce, bounce, and post-bounce evolution. We plot the fluid quantities, i.e., the rest-mass density, the electron fraction, and the specific internal energy, along with the fluid radial velocity, entropy per baryon, and temperature, all as a function of both the radius and the enclosed baryon mass. We present selected quantities as functions of time; e.g., the trajectories of the position of the shock, the conditions at the core center, the neutrino luminosities and RMS energies sampled at a fixed 500 km radius, and the net mass accretion rate sampled at a fixed 350 km radius. The key neutrino transport quantities we choose to plot are the neutrino luminosity and RMS energy profiles as measured in the fluid rest frame. In both runs, the physical time is synchronized at bounce ($t_{pb} = 0$). When the central density reaches a local maximum immediately before the shock is formed, we consider the bounce is formed, $t_{pb} = 0$. Instances before core bounce therefore have negative values. The maximum of the infall velocity is used to define shock position.

6.3.1 Infall

In Figure 6.3.1, we plot the evolution of the central entropy per baryon and central electron fraction during infall: the top (bottom) panel shows the evolution of the matter entropy per baryon (electron fraction) in the innermost zone. Before a shock forms ($\rho_c < 4 \times 10^{14}\mathrm{g/cm^3}$), the central entropy rises and the central electron fraction

decreases. The evolution given by the two codes is similar, with a slightly lower value in both central entropy per baryon and central electron fraction for Flash-X + `thornado`. The decline in central electron fraction indicates the core is losing electrons, or deleptonizing or neutronizing. During the evolution, if neutrinos are formed at high densities, which are at or near the center, it is harder for them to escape than if they are formed at lower density. Hence, neutrinos are trapped in the inner stellar core during infall, which leads to a trapped degenerate sea of electron neutrinos. For a short time, the neutrino trapping is complete. Soon after, the neutrinos and electrons establish an equilibrium. Through detailed balance, the electron capture and neutrino absorption rates are related in equilibrium, and the final Y_e becomes a function of the local electron chemical potential, which is assumed by the EOS. That is why the central electron fraction is flatted out at larger density, since the electron chemical potential is insensitive at these times, and EOS, the input physics, and initial conditions define the evolution. Because the same nuclear EOS and initial progenitor were used, the starting values and evolution are close, as expected. We see that trapping occurs almost simultaneously for CHIMERA and Flash-X + `thornado`. A slightly higher entropy per baryon and lower electron fraction in Flash-X + `thornado` was observed compared to CHIMERA. And a "jump" in entropy for densities exceeding 10^{14} g/cm^3 is observed in Flash-X + `thornado`. It happens coincidentally with a temperature jump in the inner-most-core around core bounce. The origin of this anomalous behavior requires further investigation.

The evolution of pre-bounce states at certain central densities during collapse is presented in Figures 6.3.2 and 6.3.3. Excellent agreement between the two codes is observed, with the exception of the entropy per baryon and temperature in the innermost zone. This issue remains unresolved at this time. More investigations are needed to address the cause of this difference. In addition, lower entropy per baryon and specific internal energy, higher pressure was observed near the outer boundary in Flash-X + `thornado`. These differences are in the non-NSE region. CHIMERA determines whether a zone is in NSE based on an empirically-determined expression.

It assumes a linear relationship between the NSE transition temperature $T_{\rm NSE}$ and the density (Equation (7) in Section 3.4 from Bruenn et al. (2020)):

$$T_{\rm NSE}(\rho) = \begin{cases} C_1\rho + C_2 & \text{if } \rho < 2 \times 10^8 \text{ g cm}^{-3} \\ 6.5 \times 10^9 \text{ K} & \text{otherwise,} \end{cases} \tag{6.1}$$

where $C_1 \equiv 5.333$ K g^{-1}cm^3 and $C_2 \equiv 5.433 \times 10^9$ K. Any non-NSE zone for which $T \geq T_{\rm NSE}$ is transitioned to NSE at the beginning of a global time-step. This generally includes the iron core during collapse and moves outward with the shock once it forms. More details can be found in Section 3.4 from Bruenn et al. (2020).

6.3.2 Bounce

In Figures 6.3.4 and 6.3.5, the fluid quantities at core bounce, as functions of radius and enclosed mass, are presented, where CHIMERA results are plotted in black and Flash-X + `thornado` in green. We define the bounce as the moment when the central density reaches the maximum density, and the fluid velocity is about to change the sign behind the shock and form a shock. The agreement between the results of both simulations is excellent at this time: the shock is formed at the same location (velocity plot in Figure 6.3.4); the density profiles are nearly indistinguishable; the entropy per baryon, electron fraction, and specific internal energy have the overall good agreement aside from some local differences. Because of the definition of bounce, and the dramatic change that happens about it, we see differences in the velocity profiles in the inner-most core (upper left plot in Figure 6.3.4). The infall velocities in the outer core agree well. We observe a difference in temperature at the core center (bottom left plot in Figure 6.3.4). A jump in the electron fraction at an enclosed mass of 0.72 M$_\odot$ occurs in the Flash-X + `thornado` simulation, but not in CHIMERA (bottom middle plot in Figure 6.3.4). This jump in the Flash-X + `thornado` simulation appears before core bounce, as can be seen from Figures 6.3.2 and 6.3.3. It is a feature that has evolved during infall by Flash-X + `thornado` but disappears soon after bounce –

it is not seen at 3 ms, as can be seen in Figure 6.3.12. Meanwhile, the entropy per baryon and temperature are coincidentally also higher in Flash-X + `thornado` than in CHIMERA at the jump. More testing is required to determine the causes of this behavior. Another difference, the specific internal energy in the outer core, occurs in the non-NSE region. It is caused by the different EOS treatments in the two codes in this region. Flash-X + `thornado` uses one tabulated SFHo NSE EOS table. CHIMERA treats the NSE and non-NSE region differently. In NSE, CHIMERA uses the SFHo table, as does Flash-X + `thornado`, while in non-NSE, CHIMERA evolves the nuclear composition using the `XNet` thermonuclear reaction network code given the density, temperature and electron fraction. To be more precise, in CHIMERA's non-NES treatment, the thermodynamic state depends on the isotopic composition, density and temperature. Its electron fraction is calculated using $Y_e = \sum_i Z_i Y_i$, where Z_i is the proton number of an isotope, and Y_i is the molar abundance of that isotope. The practical effect of this is that Flash-X + `thornado` assumes the average atomic mass is ~ 60 in the silicon shell, twice the correct value. This results in the number density of nuclei in the silicon shell being half the correct value, impacting the pressure slightly, but the entropy greatly, since the entropy contains a large contribution from the non-degenerated nuclei. Most of these differences are introduced during the last 0.5 ms before bounce. The profiles are in excellent agreement before that.

Again, despite these differences, the overall agreement at core bounce between CHIMERA and Flash-X + `thornado`, as shown in both radius in Figure 6.3.4 and in enclosed mass scale in Figure 6.3.5, is very good.

6.3.3 Comparisons as a Function of Time

Figure 6.3.6-6.3.10 compare the shock trajectories, mass shell trajectories, PNS radius, neutrino RMS energies at 500 km, neutrino luminosities at 500 km, and net mass accretion rates at 350 km computed by the two codes as a function of time from

bounce to 180 ms post-bounce. The luminosity is obtained by computing

$$L_\nu = 4\pi r^2 \frac{2\pi c}{(hc)^3} \int \mathcal{H}\varepsilon^3 d\varepsilon, \tag{6.2}$$

where $\mathcal{H}$ is the number flux. In Figure 6.3.6, the number of each mass shell trajectory indicates the enclosed mass in $M_\odot$, with Flash-X + `thornado` mass shell trajectories plotted in green, and CHIMERA trajectories plotted in black. The solid lines trace the position of the shock for each code. The difference in the shock trajectories is initially not very large, especially for the first 3 ms. (See Figures 6.3.11and 6.3.12 for the snapshot comparison plots at 3 ms.) The biggest difference in the shock trajectories is about 100 ms. (See Figure 6.3.14 for snapshot plots at 100 ms, which will be discussed in detail later.) This sharp increase in the shock trajectory for CHIMERA is due to the passage of the shock into the silicon layer, with its associated drop in density (see Figure 7.2.1 for the density at around 1200 km) and reduction in the inwardly directed ram pressure on the shock. Both the Flash-X + `thornado` and CHIMERA shocks exhibit this change of slope due to the shock passage into the silicon layer at about 100 ms after bounce, but the change is much less dramatic for Flash-X + `thornado`. It should be noted that after 70 ms, the shock exits the region $\rho > 2 \times 10^8 \mathrm{g/cm^3}$, which is covered by the SFHo EOS in both Flash-X + `thornado` and CHIMERA, and enters a region where the EOS is treated differently. (Refer to Equation (6.1) for the CHIMERA NSE/non-NSE EOS transition condition.) When this transition takes effect, it makes the comparisons problematic. The CHIMERA shock trajectory is 25 km above Flash-X + `thornado` when $t = 75$ ms and the transition take effect. Then the difference in shock trajectories increases dramatically, to a maximum 55 km at 100 ms. The divergence is affected by both the NSE/non-NSE EOS transition and shock passage through the progenitor density profile, as we will see in Figure 6.3.10. The divergence also suggests that non-NSE treatment is important.

The PNS radius evolution is plotted in Figure 6.3.7 for both codes. The results are very similar: both PNS radii decrease from around 90 km to around 70 km by 180 ms post-bounce at the same rate, as the core cools down and deleptonizes.

The neutrino RMS energies and luminosities sampled at a fixed radius of 500 km are shown in Figures 6.3.8 and 6.3.9, respectively. The two simulation results are qualitatively similar. One noticeable difference is that Flash-X + `thornado` luminosities and RMS energy exhibit a higher electron-neutrino burst peak and larger electron-neutrino and electron-antineutrino luminosities thereafter, reflecting its more rapid shock retraction. At the burst, `thornado` has the peak in RMS energy around 20 MeV, while CHIMERA has the peak ∼6 ms later, around 15 MeV. The largest deviation in RMS energy after the burst is in electron-antineutrino RMS energy at most 17% around 20 ms. At the burst, `thornado` has the peak around 670 B/s, while CHIMERA has the peak ∼6 ms later, around 373 B/s. The largest deviation in electron-antineutrino luminosity after the burst is at most 50% around 20 ms, while in electron-neutrino luminosity is 30% around 60 ms. These differences result from the difference in neutrino radiation method. CHIMERA one-moment method assumes an isotropic propagation for each neutrino, while `thornado` two-moment method allows the neutrino to be polarized in angular distribution. So that the burst in `thornado` result was observed earlier and stronger than in CHIMERA result at 500 km – a location distant from the major neutrino source. The different radiation methods lead to a late consequence of the deleptonization differences during the neutrino burst.

The net mass accretion rates computed by two codes at a fixed potion of 350 km are present in Figure 6.3.10. The net mass accretion rate is defined as

$$\dot{M}(r) = 4\pi r^2 \rho(r) v(r). \tag{6.3}$$

Again, the two results are close to each other for the first 70 ms. Then a dip happens in the CHIMERA result, followed by Flash-X + `thornado` around 10 ms later. This drop is associated with the drop in density that also affected the shock trajectory.

The shock passes through the EOS switch region in CHIMERA at almost the same time, which enhances the drop in accretion rate over the drop in `thornado` result.

6.3.4 Post-Bounce: 3 ms

The time slice at 3 ms post-bounce captures the launch of the electron neutrino burst. This moment is captured in Figures 6.3.11 and 6.3.12. At this time, the results of both simulations are still similar. With the exception of the difference in the outer core in entropy per baryon and specific internal energy, and the difference at the core in temperature.

6.3.5 Comparisons at 70 ms after Bounce

The time slice at 70 ms post-bounce captures is presented in Figure 6.3.13. The electron fraction profile has a good agreement: two codes have the same feature around 12 km and around PNS surface (70 km). Difference in inner core for Flash-X + `thornado`, higher temperature and higher entropy, are still observed, which is rooted in the earlier difference around bounce (Figures 6.3.4 and 6.3.5). Flash-X + `thornado` has a stronger shock at an inner location compared to the result of CHIMERA. At this time, the shock exists in the region $\rho > 2 \times 10^8 \mathrm{g/cm}^3$, see the density plot at the top central panel, and the temperature is relative low (lower left panel), which is covered by the SFHo EOS in CHIMERA and enters a region where the EOS is treated differently by each code: CHIMERA implements a non-NSE treatment (Equation (6.1)) for the outer layer. And the difference between two codes, in shock trajectory and accretion rate, is exaggerated from now on.

6.3.6 Comparisons at 100 ms after Bounce

The time slice at 100 ms post-bounce captures is presented in Figure 6.3.14. Again, the electron fraction profile has a good agreement: two codes have the same feature around 12 km and around the PNS surface. And Flash-X + `thornado` has more

electron loss at PNS surface ($\approx$ 70 km). The shock trajectory of the two codes has the biggest difference at this moment, and the shock in CHIMERA is about to stall and even move inward. (Figure 6.3.6) This difference, that CHIMERA shock is about to move inward, and Flash-X + `thornado` shock stands, can be explained by the shock velocity difference and density difference behind and ahead of the shock (Figure 6.3.14): Flash-X + `thornado` has a relative larger running pressure. The difference in temperature and entropy at the inner area, and the difference around shock, are the same as those at 70 ms.

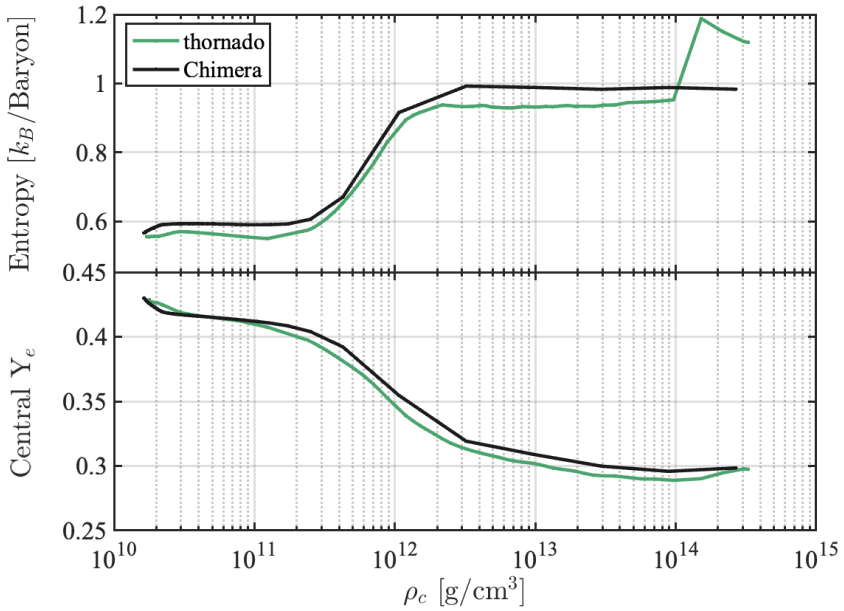

Figure 6.3.1: Comparison with CHIMERA in central entropy per baryon (upper panel) and central electron fraction (bottom panel) for evolution before core collapse. The Flash-X + `thornado` results are plotted in green and marked as 'thornado', while the CHIMERA results are plotted in black and marked as 'Chimera'.

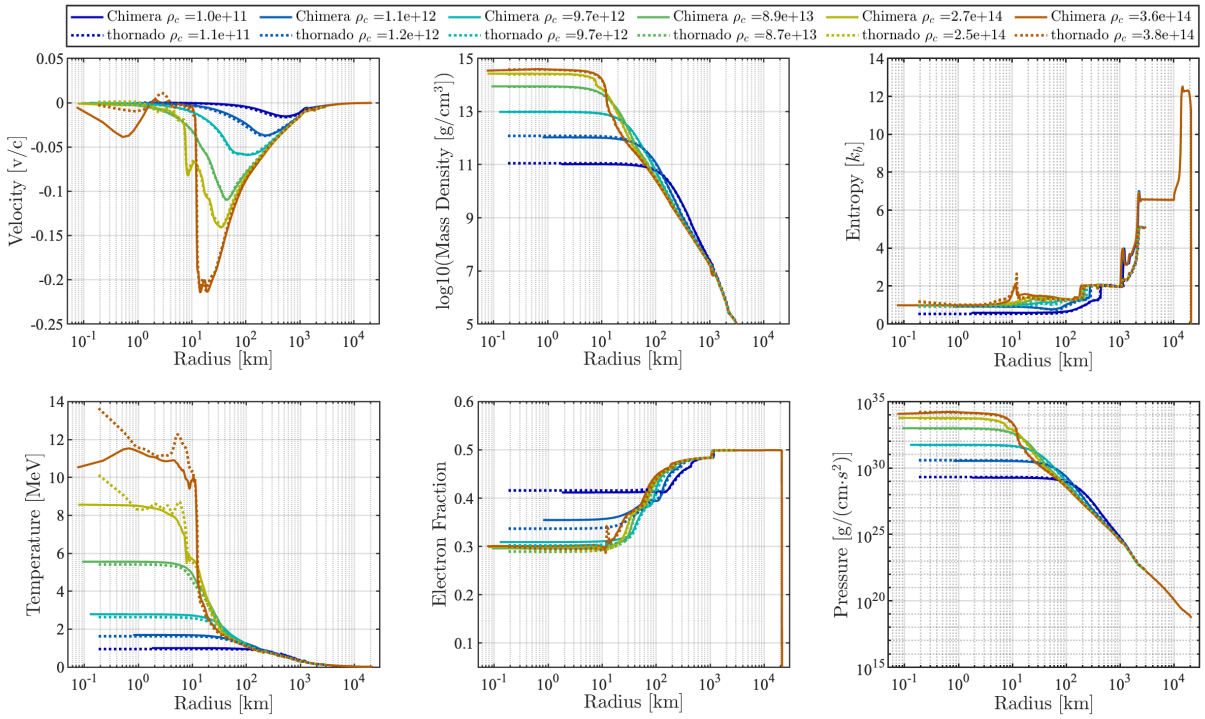

Figure 6.3.2: Comparison with CHIMERA in fluid quantities versus radius at certain snapshots during collapse, as the legend indicates. CHIMERA results are plotted with solid lines, while Flash-X + `thornado` results are plotted with dotted lines. Line color indicates different collapse times, as indicated by the central density.

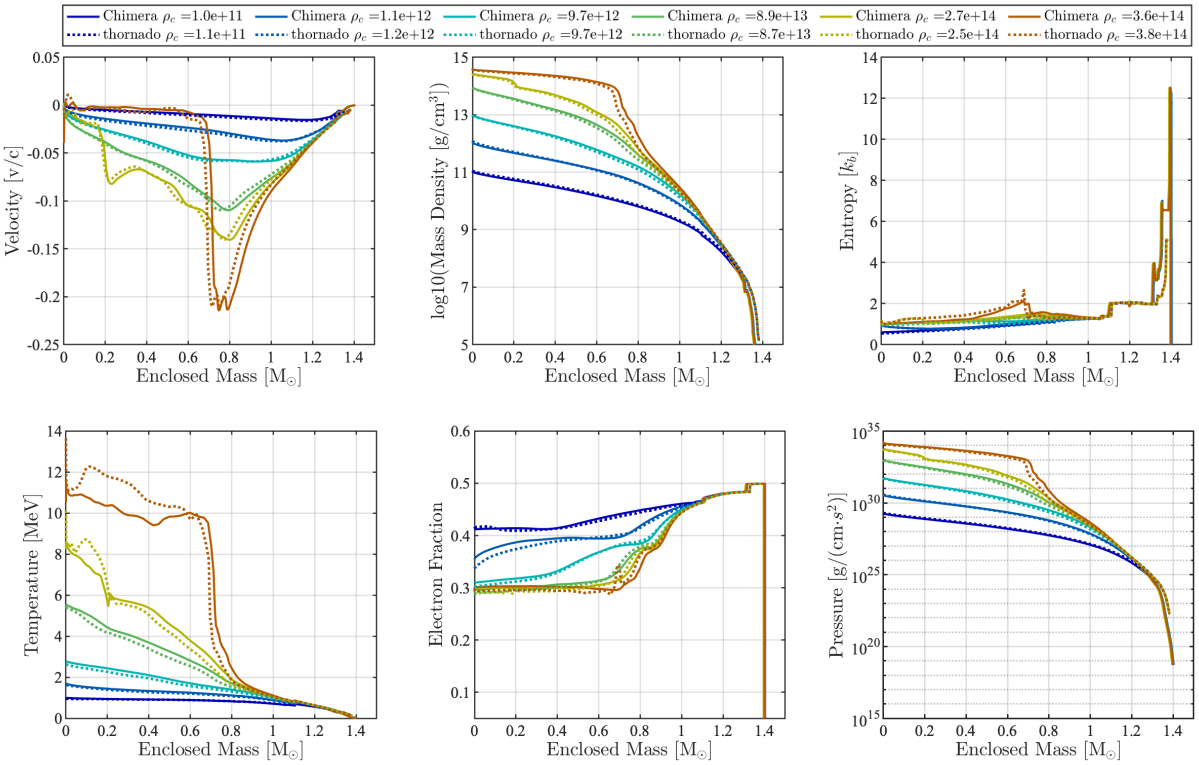

Figure 6.3.3: Comparison with CHIMERA in fluid quantities versus enclosed mass at certain snapshots during collapse, as the legend indicates. CHIMERA results are plotted with solid lines, while Flash-X + `thornado` results are plotted with dotted lines. Line color indicates different collapse times, as indicated by the central density.

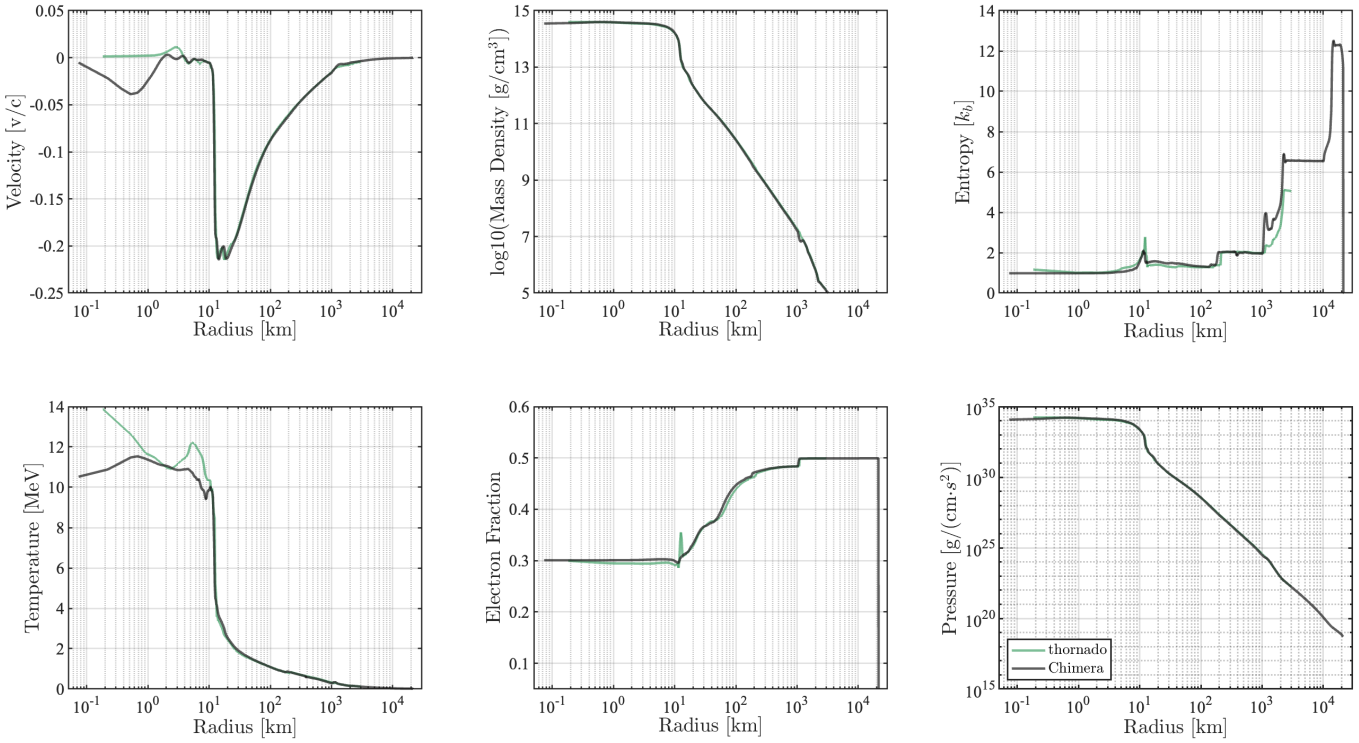

Figure 6.3.4: The fluid quantities – fluid velocity (upper left), density (upper middle), entropy (upper right), temperature (bottom left), electron fraction (bottom middle), and pressure (bottom right) – at core bounce are plotted as functions of radius.

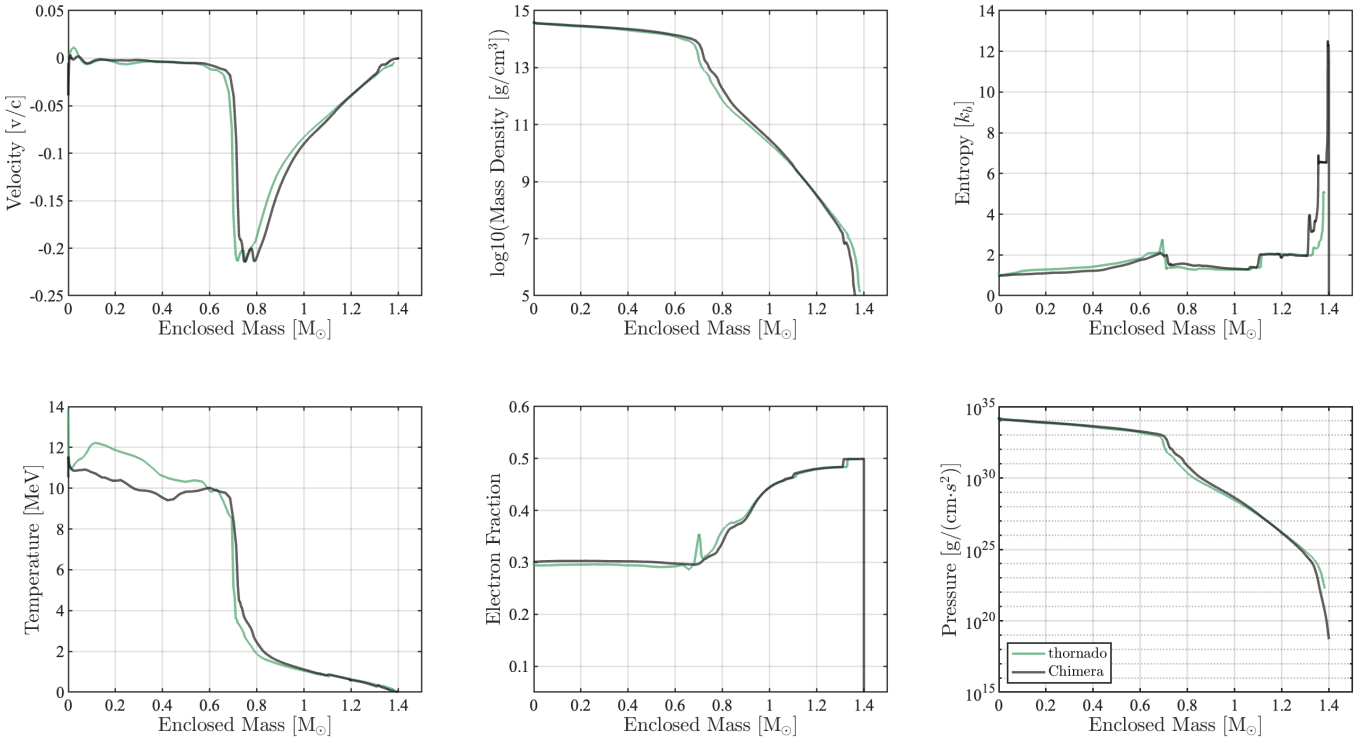

Figure 6.3.5: The fluid quantities – fluid velocity (upper left), density (upper middle), entropy (upper right), temperature (bottom left), electron fraction (bottom middle), and pressure (bottom right) – at core bounce are plotted as functions of enclosed mass.

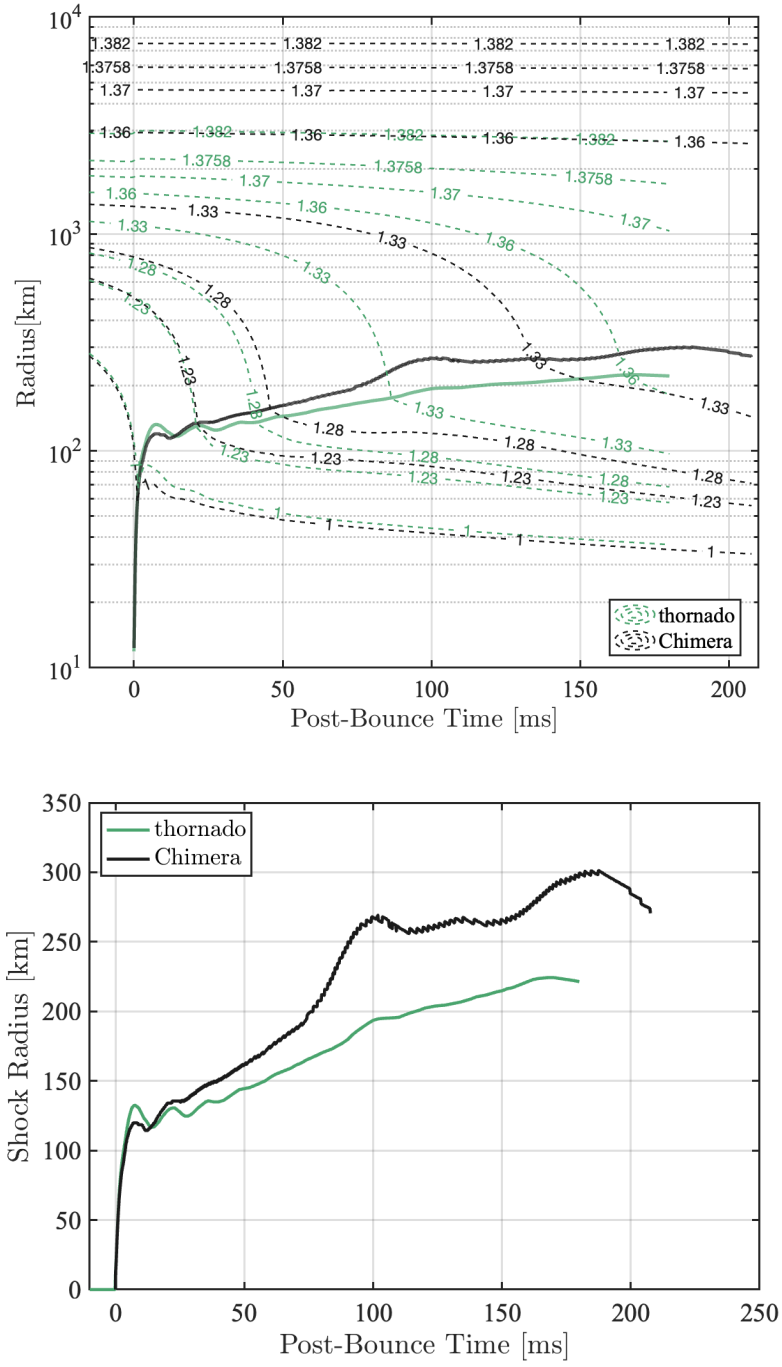

Figure 6.3.6: Comparison of CHIMERA and Flash-X + `thornado` shock radii (both panels) and mass shell trajectories (upper panel) as a function of time after bounce.

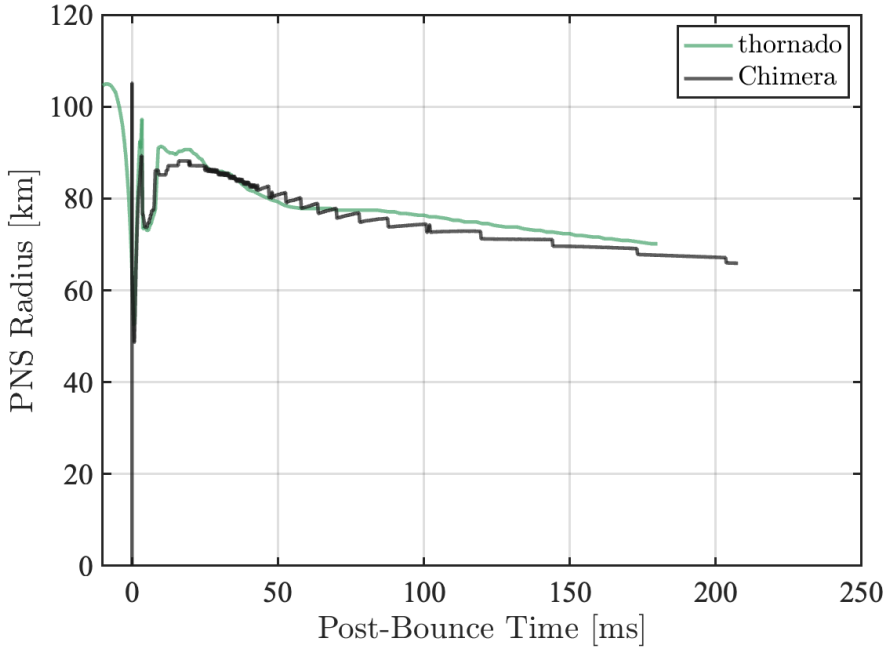

Figure 6.3.7: Comparison of CHIMERA and Flash-X + `thornado` PNS radii as a function of time after bounce.

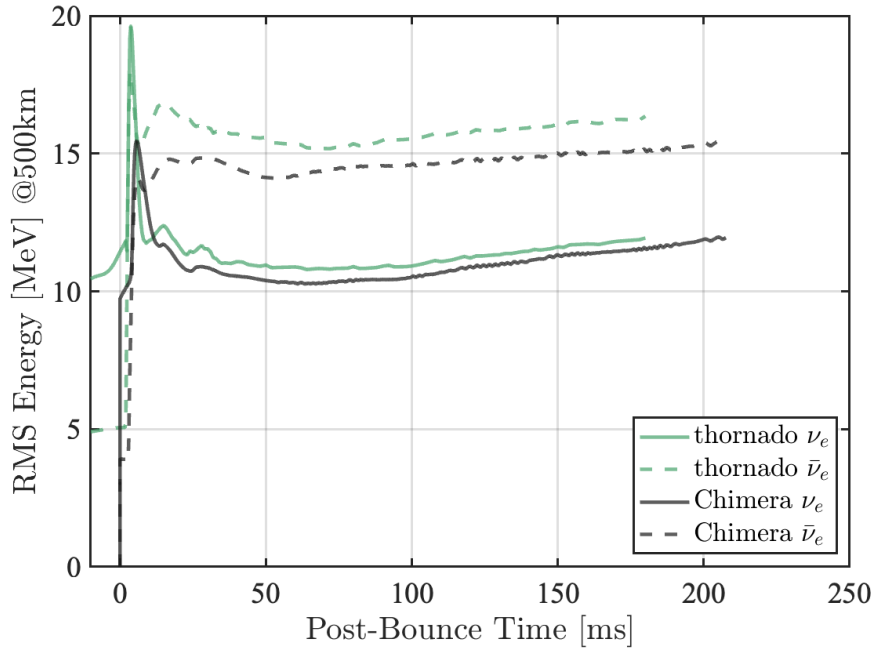

Figure 6.3.8: Comparison of CHIMERA and Flash-X + `thornado` neutrino RMS energies sampled at 500 km as a function of time after bounce. `thornado` has the peak around 20 MeV. CHIMERA has the peak ∼6 ms later, around 15 MeV.

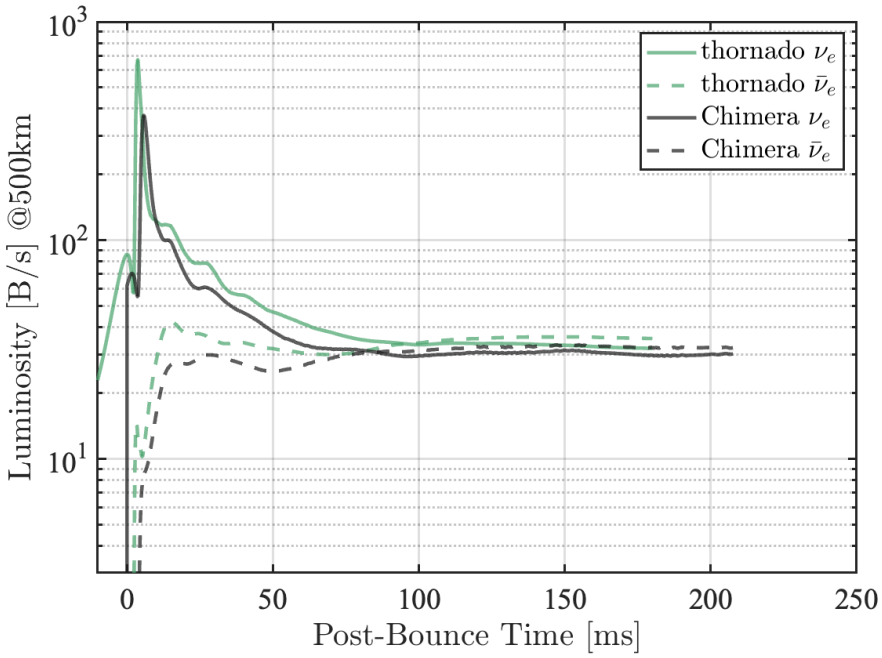

Figure 6.3.9: Comparison of CHIMERA and Flash-X + `thornado` neutrino luminosities sampled at 500 km as a function of time after bounce. `thornado` has the peak around 670 B/s. CHIMERA has the peak ∼6 ms later, around 373 B/s.

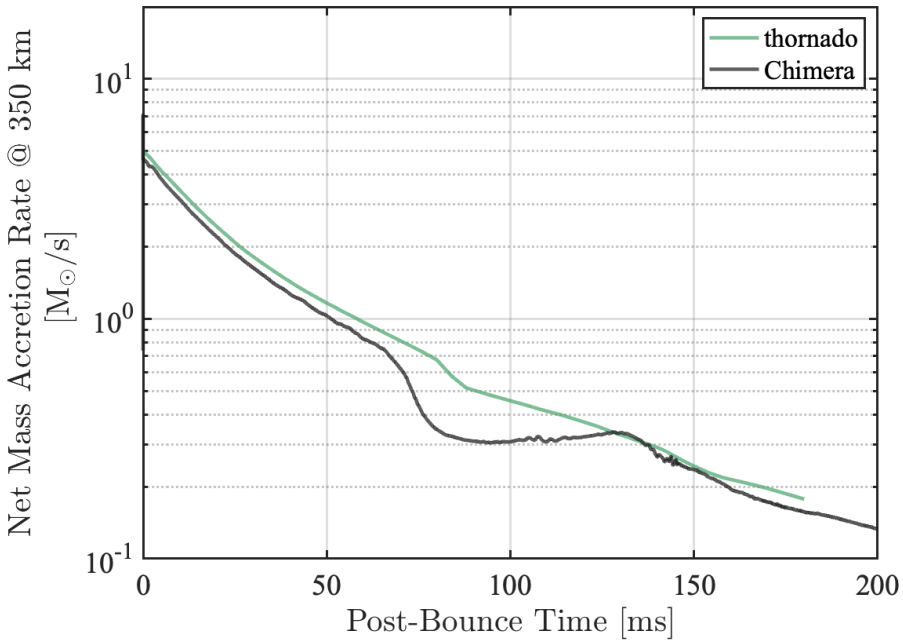

Figure 6.3.10: Comparison with CHIMERA in net mass accretion rate sampled at 350 km as a function of time.

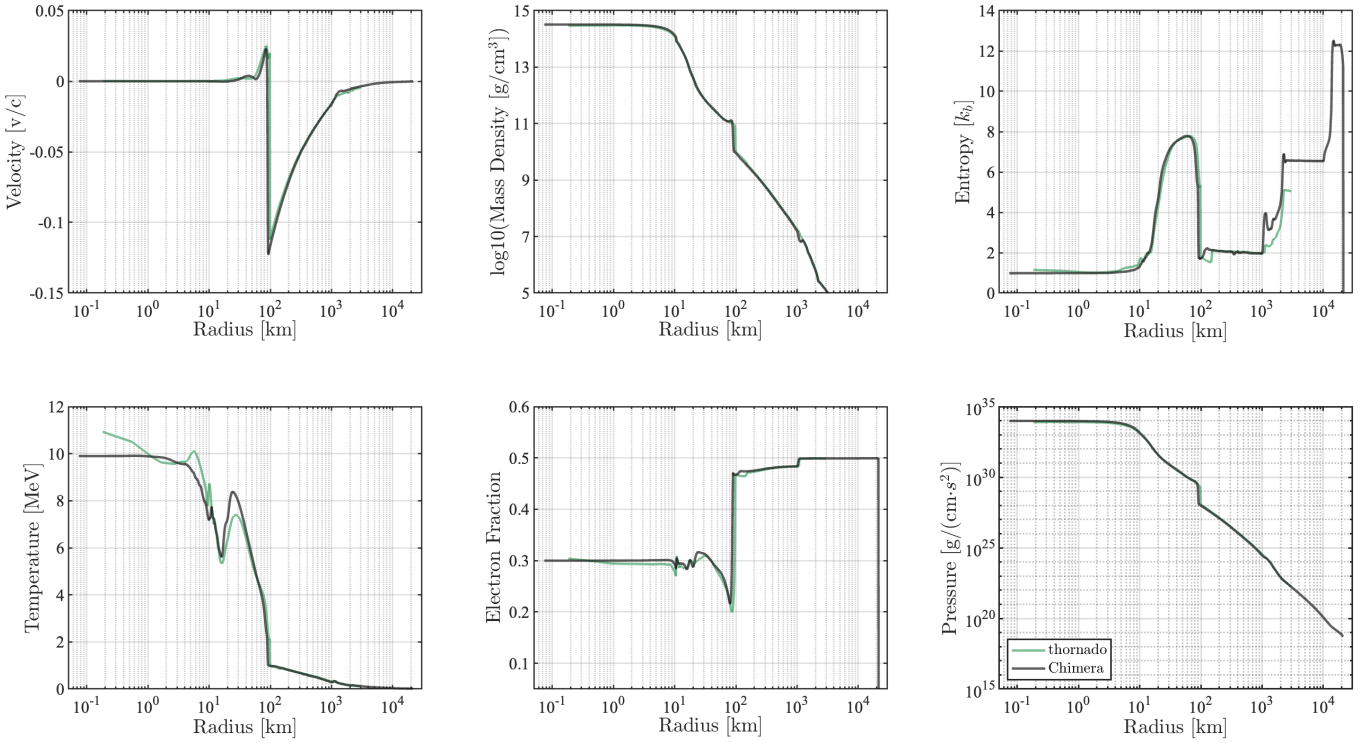

Figure 6.3.11: The fluid quantities – fluid velocity (upper left), density (upper middle), entropy (upper right), temperature (bottom left), electron fraction (bottom middle), and pressure (bottom right) – at 3 ms post-bounce are plotted as functions of radius.

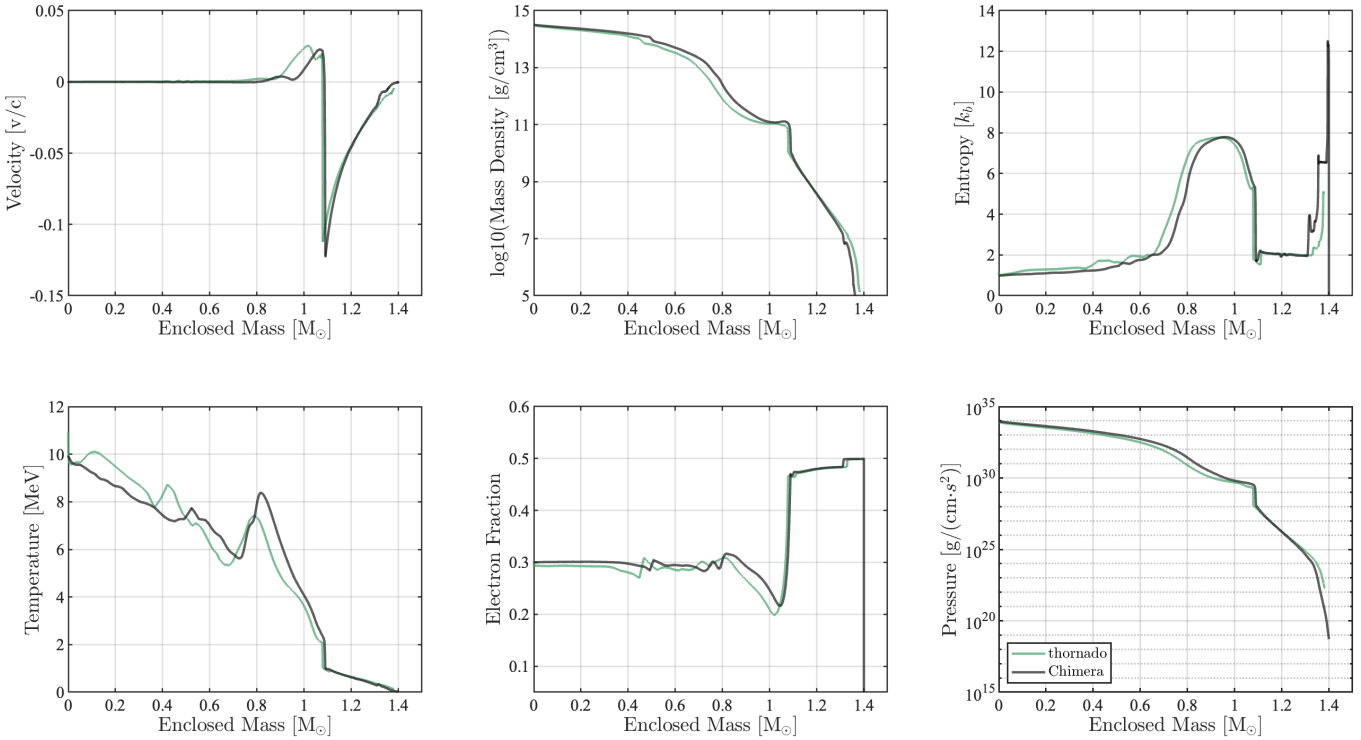

Figure 6.3.12: The fluid quantities – fluid velocity (upper left), density (upper middle), entropy (upper right), temperature (bottom left), electron fraction (bottom middle), and pressure (bottom right) – at 3 ms post-bounce are plotted as functions of enclosed mass.

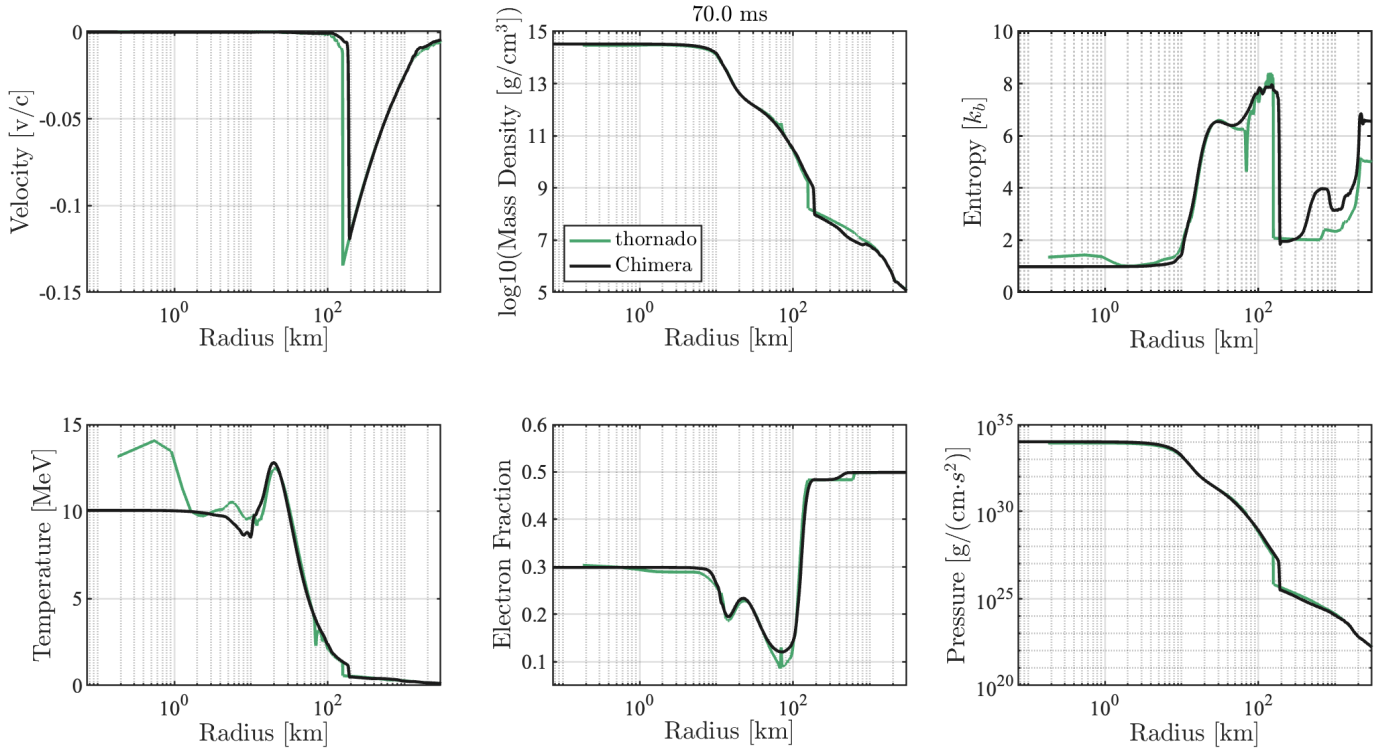

Figure 6.3.13: The fluid quantities – fluid velocity (upper left), density (upper middle), entropy (upper right), temperature (bottom left), electron fraction (bottom middle), and pressure (bottom right) – at 70 ms post-bounce are plotted as functions of radius.

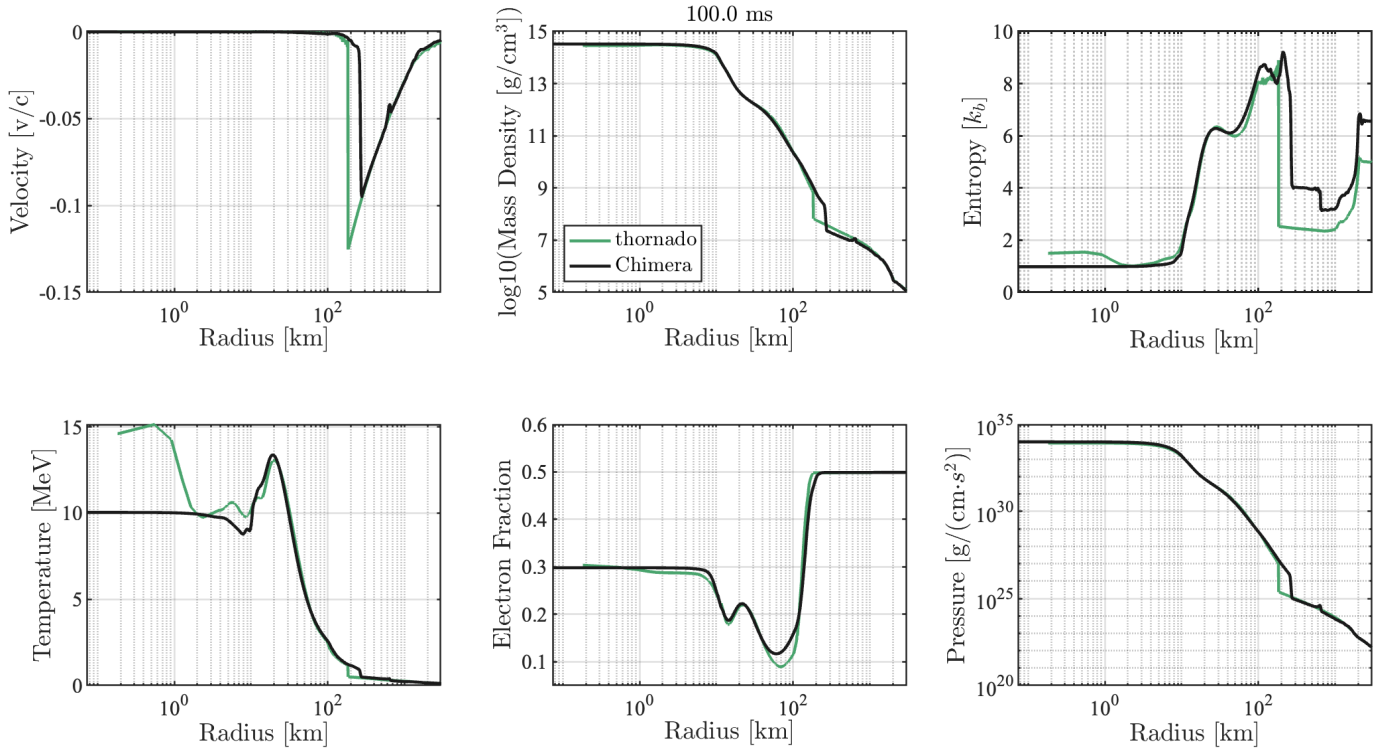

Figure 6.3.14: The fluid quantities – fluid velocity (upper left), density (upper middle), entropy (upper right), temperature (bottom left), electron fraction (bottom middle), and pressure (bottom right) – at 100 ms post-bounce are plotted as functions of radius.

6.4 Summary and Discussion

This comparison study demonstrates the ability of Flash-X + `thornado` to perform CCSN simulations. Most of the results from CHIMERA and Flash-X + `thornado` are in qualitative agreement. The quantitative differences are to be expected, given the different treatments of neutrino transport (one-moment versus two-moment closure), the different numerical methods employed, the different resolutions achieved, and in some respects the different input physics (e.g., the different treatments of non-NSE material). Our results provide a starting point to extend the comparison to higher spatial dimensions, more comprehensive modern weak physics, and general relativity.

Chapter 7

CCSN Simulations in Spherical Symmetry: Low-Mass Progenitors

This chapter describes the simulations of core collapse, bounce, shock propagation and stagnation of the core of a series of low-mass progenitor stars of 9, 10, and 11 $M_\odot$ (S9, S10, S11) from Sukhbold et al. (2016), and in the case of S9 simulations with different physics inputs. All three progenitors are nonrotating, non-perturbed, have Solar metallicity, and have been evolved in 1D. We evolved the progenitors from the onset of collapse with Flash-X + `thornado`.

7.1 Introduction

Only stars more massive than ∼8.0 $M_\odot$ ends as CCSN. And approximately ∼50% of the mass function of massive stars above ∼8.0 $M_\odot$ lies below ∼13.0 $M_\odot$. Therefore, understanding the mechanism and character of explosions in this modest mass range is important. We limit ourselves to Solar-metallicity models and do not consider low-mass progenitor models with 10^{-4} or zero metallicity. All in all, we choose a series of low-mass progenitor stars, S9, S10, and S11 from Sukhbold et al. (2016), which are

also used in Radice et al. (2017); Burrows et al. (2019); Couch et al. (2020); Stockinger et al. (2020).

The material in this chapter is organized as follows. We discuss the evolution common to all of our progenitors using S9 in Section 7.3, the impact of different initial progenitor structure in Section 7.4, comparing the results obtained with S9, S10 and S11, then quantification of how different input physics can affect the core evolution in Section 7.5, including leaving out neutrino interactions and tuning scattering.

7.2 Simulation Setup

Physics The SFHo EOS (Steiner et al., 2010) and Bruenn (1985) opacity rates are provided by `WeakLib` tables. The SFHo EOS is consistent with all known nuclear and astrophysical constraints (Tews et al., 2017), while the Bruenn 1985 opacity set is the minimal set of neutrino interactions considered in core-collapse simulations. Emission and absorption from nuclei and nucleons, isoenergetic scattering on nuclei and nucleons, and neutrino-electron scattering (and pair creation and annihilation processes) are included for electron neutrino and electron antineutrino. The Newtonian hydrodynamics equations with a monopole approximation to gravity is solved by the Flash-X `Spark` module.

Grids and Domain Sixteen geometrically spaced linear DG energy elements (giving 32 energy groups) span the range from 0.1 to 300 MeV, with the first element width being 2.172 MeV and the last element width being 61.74 MeV. We used uniformly mesh spatial grid, with $\Delta r \approx 0.73$ km. The outer spatial boundary for each progenitor is determined by the `WeakLib` EOS table boundary, which has lower bounds of $\sim 1.66\times10^{3}$ g/cm^3 in density, $\sim 1.16\times10^{9}$ K in temperature, $\sim$0.01 in electron fraction, $\sim$-1.39×10^{17} erg/g in internal energy, $\sim 5.10\times10^{21}$ dyn/cm^2 in pressure, and $\sim 1.49\times10^{-3}$ k$_B$ in entropy. To be precise, we used 3000 km with $\Delta r =$

0.73 km for model S9, 3700 km with $\Delta r = 0.72$ km for model S10, and 4000 km with $\Delta r = 0.74$ km for model S11.

In radius, we apply an inner reflecting boundary and a ghost cell with fixed conditions as the outer boundary condition. Although the constant density inflow is not ideal regarding shock revival, the retained outer boundary is a better treatment than "free-flow", which leads to mass flux increasing inflow. (In the "free-flow" outer boundary condition, the material outside the computational domain is treated as having the same speed as the material at the outer boundary. But the material at the outer boundary actually flows quicker than the material further out but the density falls off as well.)

The future development of Flash-X will include more realistic prescriptions for nuclear combustion, which will allow us to run with more than one EOS and keep zones in the original model to the oxygen shell and beyond. After that, we can enlarge the computational domain and evolve the model to later time.

Initial Condition The initial conditions are displayed in Figure 7.2.1 for all three progenitors. They are similar overall, especially for S10 and S11. S9 has a slightly sharper density profile, wider and faster infalling speed, and bigger nucleon rich region. The initial neutrino number density across all energy groups and species is 10^{-20} per phase space, and the initial number flux is zero per phase space.

7.3 Result 1: Standard Evolution – S9

We begin with the core of the 9 $M_\odot$ model, S9, which has a mass of 1.382 $M_\odot$ and a radius of 3000 km. All plots in this section are based on simulation results obtained with Minerbo closure. The S9 model has a 1.32 $M_\odot$ iron core, which is surrounded by a silicon shell of 0.06 $M_\odot$. See Figure 7.2.1 for the initial density, temperature, electron fraction, and velocity versus radius, and Figure 7.3.1 for the initial density, temperature, electron fraction, velocity, A and Z for the SFHo EOS, versus enclosed

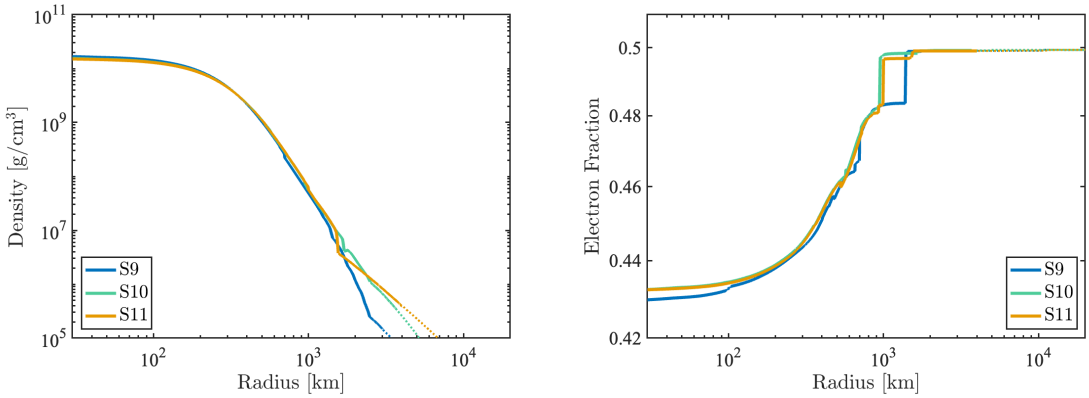

(a) Density profiles in g/cm^3

(b) Electron Fraction

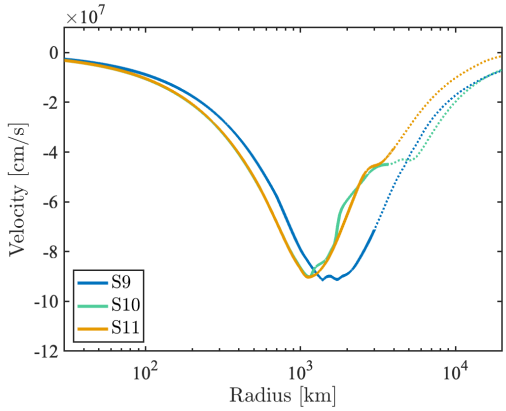

(c) Velocity in cm/s

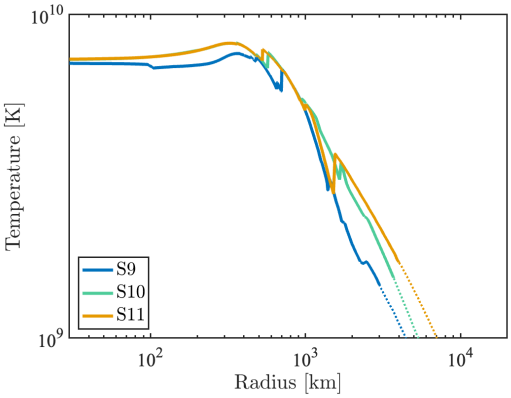

(d) Temperature in K

Figure 7.2.1: Initial conditions for the three low-mass progenitor models from Sukhbold et al. (2016). We used 3000 km with $\Delta r = 0.73$ km for S9, 3700 km with $\Delta r = 0.72$ km for S10, and 4000 km with $\Delta r = 0.74$ km for S11. The solid lines represent the initial condition in the computation domain, while the dotted lines are for the available data from Sukhbold et al. (2016).

mass. We run the simulation until the SFHo EOS is invalid – i.e., where the EOS fails to provide a unique thermal state for each spatial node on the domain.

To obtain a bird's-eye view of the evolution, we present in Figure 7.3.2 the mass shell trajectories, as well as the electron fraction along each trajectory for the duration of the run. The background color of Figure 7.3.2 encodes the electron fraction. The upper red dotted line marks the 1.382 $M_\odot$ shell, which is the total enclosed mass on the computation domain initially. The second upper red dotted line marks the 1.3758 $M_\odot$ shell, which traces the first-order discontinuous point in the initial density profile at 2378 km. The other red dotted lines mark the corresponding mass shells. The black line follows the shock position. Three additional crucial lines are plotted. The red line tracks the proto-neutron star (PNS) radius, which is defined by the density 10^{11} g/cm^3. The dashed black line and the dotted black line track the mean electron-neutrino–sphere and the mean electron-antineutrino–sphere, respectively. The neutrino sphere is the radius at which the neutrino optical depth equals 2/3:

$$\bar{\tau}_x \equiv \int_\infty^r dr'/\lambda_x = 2/3, \tag{7.1}$$

where λ_x is the neutrino-energy-dependent mean free path per species x, $x = \nu_e, \bar{\nu}_e, \nu_\mu, \bar{\nu}_\mu, \nu_\tau, \bar{\nu}_\tau$, i.e., for each x,

$$\bar{\tau} = \frac{\int_\infty^r dr' \int_0^\infty \chi \mathcal{J} \varepsilon^3 d\varepsilon}{\int_0^\infty \mathcal{J} \varepsilon^3 d\varepsilon}, \tag{7.2}$$

where ε is neutrino energy, $\mathcal{J}$ is neutrino number density, χ is neutrino total opacity. In our model, electron-neutrinos and electron-antineutrinos are included, and the corresponding sphere radii are plotted in Figure 7.3.2. As the background color indicates, the outer layer is electron-rich, while the inner layer is relative electron-poor and losing electrons. This deleptonization occurs through electron-neutrino emission during stellar core collapse, and continues via neutrino diffusion after core bounce. The outer layers compress to the core, as the mass shell indicates. The mass shell

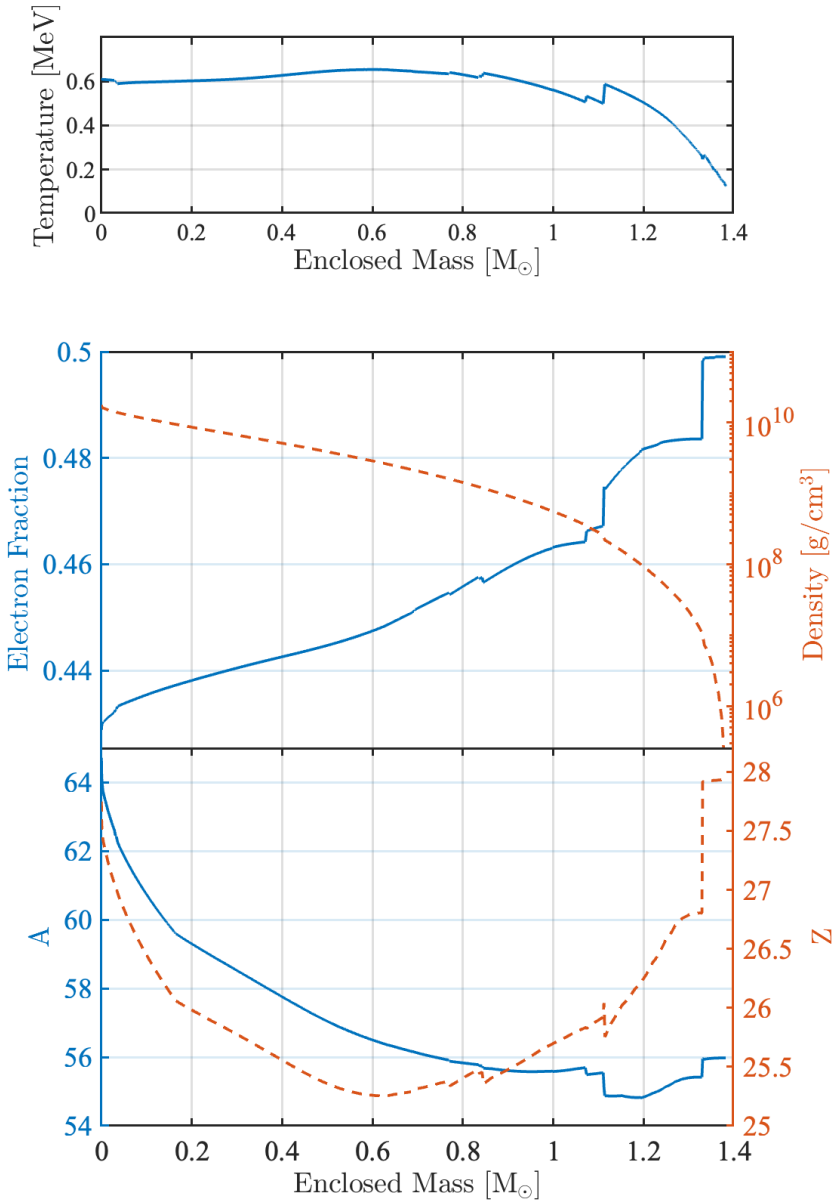

Figure 7.3.1: Initial A and Z profiles for model S9 using the SFHo EOS.

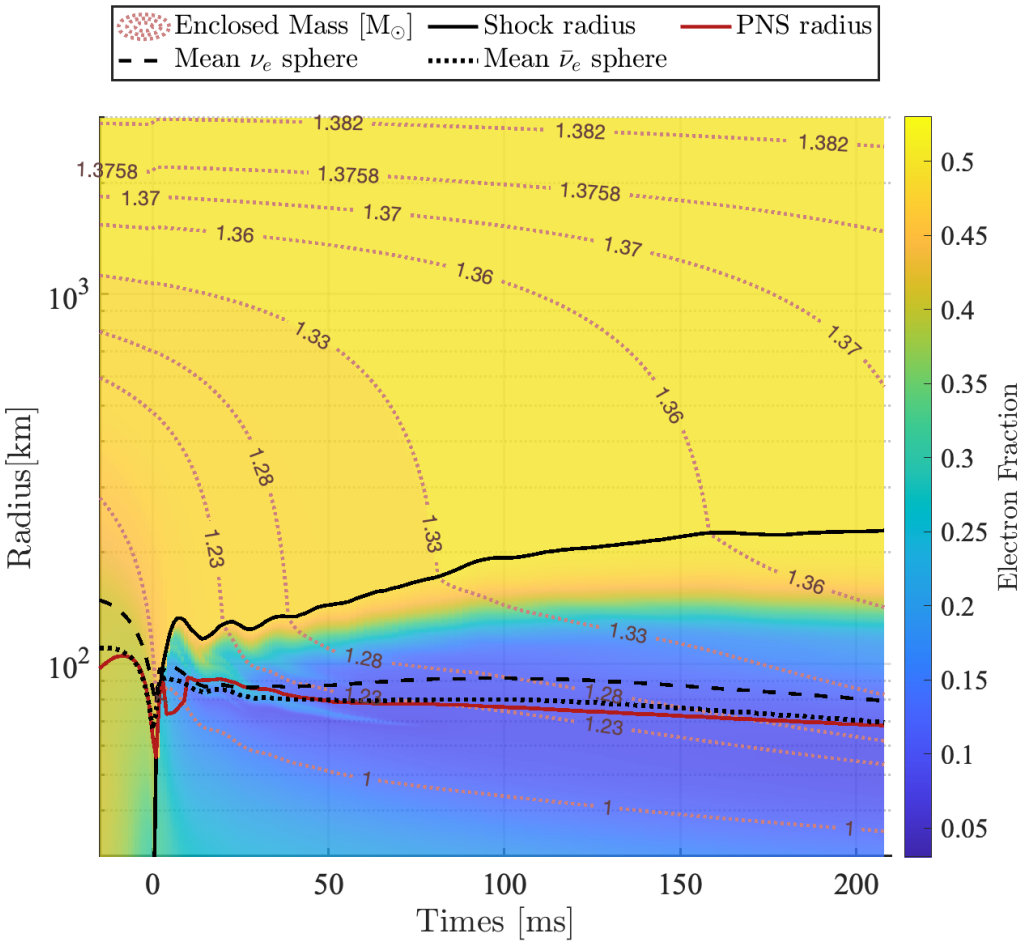

Figure 7.3.2: Radial mass shell trajectories on an electron-fraction color map for model S9. The upper red dotted line tracks the 1.382 $M_\odot$ shell, which is the total enclosed mass on the computational domain initially. The second upper red dotted line tracks the 1.3758 $M_\odot$ shell, which traces the discontinuous point in the initial density profile at 2378 km. And the other red dotted lines track the corresponding mass shells. The black line tracks the shock position. The red line marks the density 10^{11} g/cm^3, which is often used to define proto-neutron star radius. The dashed black line and the dotted black line represent the mean electron-neutrino sphere and the mean electron-antineutrino sphere, respectively. The background color indicates the electron fraction.

trajectories bend as they pass through the shock, and their infall is decelerated. The shock launches at 0.78 $M_\odot$ (≈13 km), propagates to ∼1.15 $M_\odot$ (≈132 km) at 7 ms, and eventually to a radius of 229 km (≈ 1.368 $M_\odot$) at 208 ms. The PNS comprises the hot shocked mantle. As it cools and contracts, it radiates neutrinos of all types from its cold, unshocked inner core. The shock recedes with time, as the PNS cools, which eventually leads to a neutron star or black hole formation. The mean electron-antineutrino–sphere is always below the mean electron-neutrino–sphere. We will give a more detailed discussion later.

In Figure 7.3.3, the evolution of density, entropy, electron fraction, and velocity versus radial position at various central densities during collapse and at later times is displayed. As one can read off of the color bar, the blue-colored lines mark the pre-bounce states. The gray lines indicate the state at core bounce. And the red-colored lines mark the post-bounce states. During collapse, the central density increases from $\mathcal{O}(10^{11}$ g/cm$^3)$ to $\mathcal{O}(10^{14}$ g/cm$^3)$, the central electron fraction decreases from ∼0.4 to ∼0.3, and the inward velocity develops a negative peak with maximum absolute value at ∼0.23 c. Core bounce occurs at a central density of 4.0×10^{14} g/cm^3 and a central electron fraction of 0.31, and a shock forms. As shown in Figure 7.3.3d by the red lines, positive velocity for outflowing matter is exhibited behind the shock. The location of shock formation is evident in all four plots. As one can see, each of these quantities has a sharp discontinuity at 13 km (gray lines). We can see both from Figure 7.3.2 and from Figure 7.3.3c, the pre- and post-bounce deleptonization due to electron-neutrino emission. The discontinuity in velocity in Figure 7.3.3d, which is the location of shock, is traced by the shock radius in Figure 7.3.2. After shock breakout at the electron-neutrino sphere, at around 7 ms, the shock (at ∼132 km) has been transformed into an accretion shock. Figure 7.3.3d shows that the velocity right behind the shock becomes negative at this time. This transition corresponds to the first peak, at around 7 ms, in the shock radius in Figure 7.3.2. A deep trough in electron fraction directly behind the shock, shown in Figure 7.3.3c, also formed due to the electron-neutrino burst. As the simulation continues, this trough grows

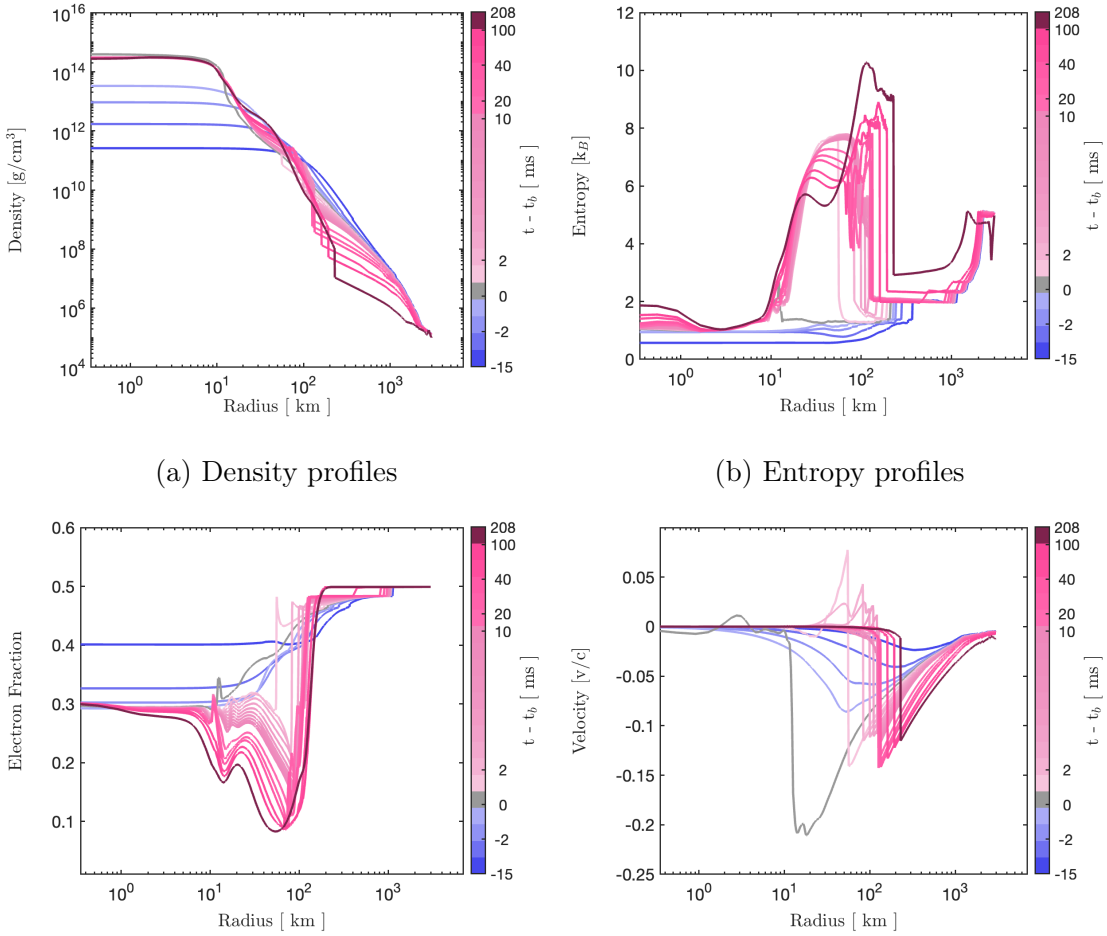

(a) Density profiles

(b) Entropy profiles

(c) Electron fraction profiles

(d) Velocity profiles

Figure 7.3.3: Evolution of model S9. The lines with the same color show the core properties at the same moment indicated by the color bar. The blue-colored lines mark the pre-bounce states. The gray lines indicate the state at core bounce. And the red-colored lines mark the post-bounce states.

deeper. Then it reaches a minimum electron fraction of 0.0828 by the last time slice at 208 ms. Meanwhile, after the shock initially stalls, the post-shock velocities steadily become more negative. The shock continues to move out due to accretion through it. As shown in both Figure 7.3.2 and Figure 7.3.3d, the shock has a maximum radius of ∼229 km at 208 ms for S9 which tends to increase as time passes. The high entropy stays well below the shock, and expands during the time, as Figure 7.3.3b shows.

Figure 7.3.4 is plotted to present the evolution of entropy during the simulation. The lines in the figure are the same as those in Figure 7.3.2 with the background color encodes the entropy per baryon. One can read that the high entropy region below the shock (red area), which is the gain region, expands as time goes. The gain region is collection energy when the simulation ends.

To trace the evolution at the core center, we plot Figure 7.3.5. The top/bottom panels show the evolution of the matter entropy/lepton number fraction in the innermost zone. The left panels show entropy and lepton number fraction versus central density for pre-bounce evolution. The right panels show the post-bounce evolution versus post-bounce time. The evolution of these three properties is determined by the implementation of the nuclear EOS and the progenitor. We presented a detailed comparison for this evolution using the same EOS and progenitor with CHIMERA's result in Chapter 6. We can read that before trapping, the entropy rises and the electron fraction decreases due to the emission of electron neutrinos. And after the onset of neutrino trapping, the matter entropy and the electron fraction remain relatively constant.

The RMS energies (Equation(5.43)) and the neutrino luminosity (Equation (6.2)) sampled at a fixed radius 500 km as a function of time after bounce are presented in Figure 7.3.6 and Figure 7.3.7, respectively. When the shock propagates outward, it encounters the electron-antineutrino sphere, and then the electron-neutrino sphere at ∼1 ms after bounce. The mean electron-antineutrino sphere is always below the mean electron-neutrino sphere because electron-antineutrinos have weaker interactions with matter. The electron antineutrinos escape from a deeper core region with higher

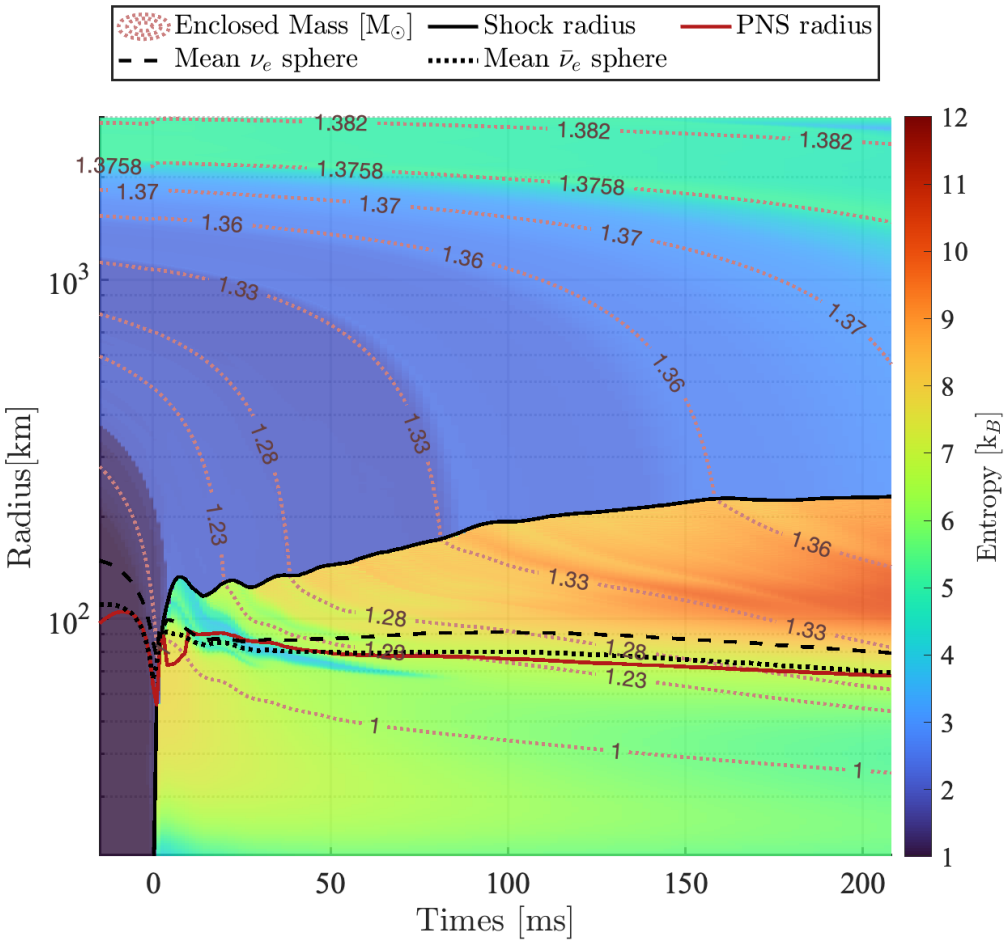

Figure 7.3.4: Radial mass shell trajectories superimposed on an entropy color map for model S9. The lines are defined as in Figure 7.3.2: the red dotted lines track the corresponding mass shells; the black line tracks the shock position; the red line marks PNS radius; the dashed black line and the dotted black line represent the mean electron-neutrino sphere and the mean electron-antineutrino sphere, respectively.

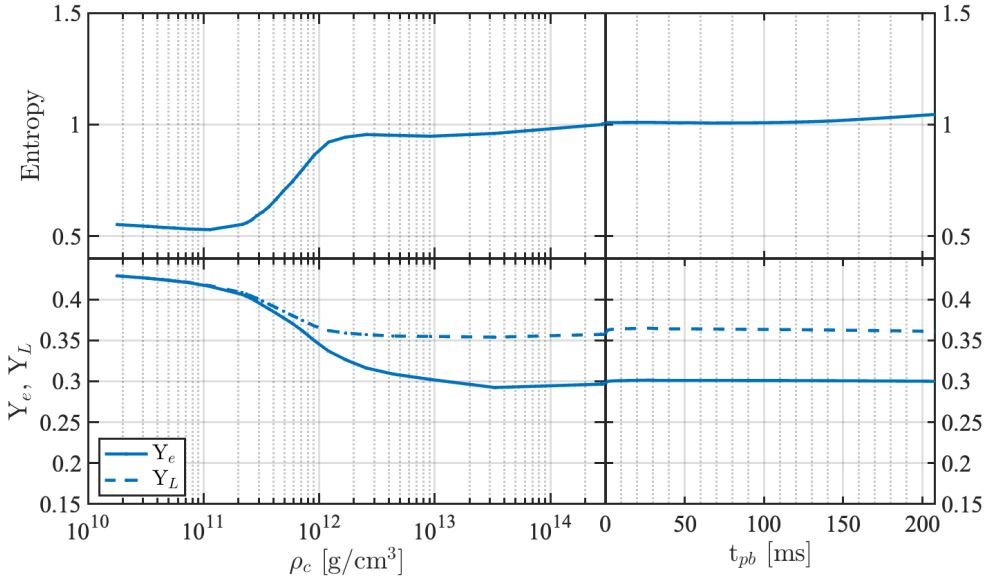

Figure 7.3.5: The evolution of central entropy and lepton number for model S9. In the left (right) panels are the pre-bounce (post-bounce) values of the central entropy (top) and electron fraction (Y_e) and total lepton fraction ($Y_L = Y_e + Y_\nu$) (bottom). The pre-bounce evolution is plotted versus the central density, while the post-bounce evolution is plotted versus time.

temperature, which results in higher RMS energy. Because the PNS contracts with time, the neutrino sphere temperatures increase, increasing the RMS energies. When the shock passes the electron-neutrino sphere, the electron-neutrino luminosity increases markedly as the electron-neutrinos produced by electron capture on protons escape, producing a peak in the luminosity plot. The increase of electron-antineutrino luminosity is slower than in electron-neutrino luminosity due to the degeneracy of the electrons. It is because a large electron chemical potential implies a large negative positron chemical potential. The production of electron-antineutrinos through positron absorption is suppressed. The production of electron-antineutrinos through the pair processes is also suppressed by a large chemical potential of electron-neutrinos.

The neutrino burst can be viewed more clearly in Figures 7.3.8 and 7.3.9, in which a color map for electron-neutrino luminosity and a color map for electron-antineutrino luminosity are plotted, respectively. The red band is the luminosity peak. The white dotted line along the luminosity peak is the reference line for propagation outward at light speed. The burst is generated when the shock passes through the electron-neutrino sphere. A tremendous number of neutrinos are generated around the PNS surface due to neutrino emission from the nucleons, and are released after the shock passes the trapping region. Both electron-neutrino and electron-antineutrino are generated and released, and leave the hot PNS mantle have electron and positron. Electron-antineutrinos have a deeper trapping radius – electron-antineutrino–sphere. The degeneracy of the electrons causes the increase in the electron-antineutrino luminosity to be slower than the increase in the electron-neutrino luminosity. The electron degeneracy is lifted in the hot shocked mantle of the PNS.

Figure 7.3.10 shows the net neutrino heating rate due to emission and absorption of electron-neutrinos and electron-antineutrinos. The net neutrino heating rate is computed using

$$\frac{d\epsilon}{dt} = -\frac{\sum_s \int_{\mathbb{R}+} \chi_s (f_{eq,s} - D_s)\varepsilon^3 d\varepsilon}{4\pi\rho}, \tag{7.3}$$

where ρ is the matter density, $\sum_s$ is a sum over all species s (which is ν_e and $\bar{\nu}_e$ in here), $f_{eq,s}$ is the equilibrium distribution of the species s, and D_s is the specie s number density in the Lagrangian frame,

$$D_s = \frac{1}{4\pi} \int_{\mathbb{S}^2} f_s d\omega. \tag{7.4}$$

The heating region is marked in red, while the cooling region is in blue. Behind the shock, the matter cools for the first 60 ms. Meanwhile, the gain region is steadily expanding in radius, as consistent with the expanding region of high entropy seen in Figure 7.3.3b and Figure 7.3.4. After 100 ms post bounce, the matter behind the shock is consistently heated. Outside the shocked region, the neutrinos stream freely, and the matter has a low cooling rate.

7.4 Result 2: Impact of Different Progenitors

To understand how the core evolution differs with progenitor mass, we ran simulations using two other low-mass progenitors, S10 and S11. All the progenitors have evolved to the point of core-collapse, as defined by the moment when their radial infall velocity has reached 1000 km/s. All results presented in this section are obtained using the same input physics as in the previous section, except for the initial progenitor.

Figure 7.2.1 provides the collection of initial condition. S9 is at the lower end of the mass function and has a steeper mass density profile with radius above 1000 km than S10 and S11. All three progenitors have a unique structure in density: the S9 density profile has the most apparent slope change around 2500 km with enclosed mass around 1.376 $M_\odot$, while the slope change for S10 occurs at 1700 km and 1.437 $M_\odot$, and the slope change for S11 occurs at 1550 km and 1.423 $M_\odot$. In the S10 progenitor profile, there is a small density inversion, which would be Rayleigh-Taylor unstable, and is not expected to be present in nature (Radice et al., 2017). The initial condition of model S9 also differs from S10 and S11 by temperature, electron fraction and velocity.

Model S9 is cooler than models S10 and S11, and has less electron fraction at inner most regions, and larger nucleon rich (electron fraction lower than 0.5) regions. Model S9 also has a slightly larger velocity peak standing at the larger radius. Model S10 and S11 are relatively similar. The difference in electron fraction between the S10 and S11 throughout the iron core is less than 0.005. The temperature and velocity structure of S10 and S11 are similar. The difference between model S10 and S11 is most noticeable around 2000 km, where model S11 has a slight bigger drop in density, a bigger increase in electron fraction, and a bigger discontinuous in temperature.

A first glance of the results is presented in Figure 7.4.1, where the shock radii for all three models versus post-bounce time are presented: blue line for S9, green line for S10, and yellow line for S11. Same as observed in other work (Radice et al., 2017), none of the progenitors exploded in 1D simulations. All three models have "waves" within the first 50 ms. Within this time window, shock of model S9 pushed relatively farther than that for S10 and S11, and S10 and S11 had almost identical shock trajectories. Later than that, the shock speed of model S9 was accelerated around 82 ms after bounce. The shock for model S10 and S11 had almost the same shock radii till to 108 ms. Then the shock of S11 accelerates and reached 250 km at 126 ms. The shock of S10 accelerates last, around 140 ms. The analysis of the accretion rate can provide insight into the reason for the different evolution.

In Figure 7.4.2, the net mass accretion rates (defined by Equation (6.3)) sampled at a fixed radius 500 km for the three models are plotted. Each of them has a step in the accretion rate: 72 ms for S9, 140 ms for S10, and 100 ms for S11. The sequential order is the same as the “acceleration” order observed in the shock trajectory plot, Figure 7.4.1. These steps are corresponded to the changes in each initial density profile, see Figure 7.2.1a. The sudden growth of the accretion rate of model S10 around 140 ms is due to the small density inversion present in the initial density profile. A steep drop in the accretion rate at early times, when the neutrino luminosities are still large, is required for a successful explosion in 1D. Apparently, none of these accretion rates dropped quickly enough.

The evolution of entropy is presented in Figure 7.4.3 for model S10, Figure 7.4.4 for S11, same as Figure 7.3.4 for model S9. One can clearly see that the high entropy bands followed each "weak explosion" behind the shock, such as around 150 ms for S10. And the high entropy area emergent later expanded with time. We will see this heating region growth again in the net heating rates. The different mass shell, as the red dotted lines mark in the figures, is a direct consequence of the initial density profile difference. Same as in Figure 7.3.4, the PNS radii and neutrino sphere radii are also plotted in Figures 7.4.3 and 7.4.4. The location and behavior of the changes of these three lines for each model are similar, which play a main role in determining radiation properties. These similarities indicate similar PNSs and envelopes around the PNSs, and lead to similar radiation properties, as we will see below.

Though the dynamics below 500 km, a radius the shock never reaches in these simulations, are different for different progenitors, the radiation properties at 500 km have relatively similar behavior. The neutrino luminosity and neutrino RMS energy sampled at a fixed 500 km radius are plotted in Figure 7.4.5 and 7.4.6, respectively, for the three models considered here. And a snapshot of neutrino luminosity at 150 ms post-bounce versus radius is plotted in Figure 7.4.7. The results for model S9 is colored blue, while green for S10 and yellow for S11. The radiation properties – RMS energy and luminosity – of the three models are relatively similar in terms of the fluid properties. This is because neutrinos are mainly generated around the PNS surface, which among the three low-mass models has similar properties and size, as we mentioned earlier in Figures 7.3.4, 7.4.3, and 7.4.4. Because of the accelerated contraction rate of the PNS, all RMS energies increase. Despite the similarity in the RMS energy and luminosity evolution at a fixed 500 km radius, a difference in luminosity at 150 ms versus radius is observed, Figure 7.4.7. The luminosity of the three models diverges outside the PNS radii. S10 had the highest luminosity at 150 ms around the shock, because its shock was pushing outwards at fastest speed, Figure 7.4.1.

Net heating rates (defined in Equation (7.3)) for the three models considered here are also plotted: Figure 7.3.10 for S9, Figure 7.4.8 for S10, and Figure 7.4.9 for S11. Red region is heating and blue region is cooling. They have the same cooling to heating transition behind shock and same heating region expansion between the shock and gain radius (the while band separating blue cooling region and red heating region) before the shock receded.

7.5 Result 3: Impacts of Neutrino-Matter Interaction Set – S9

The results presented in this section are the result of numerical experiments with the spherically symmetric neutrino radiation hydrodynamics code Flash-X + `thornado` to examine the effects of altering the neutrino–matter interactions. The first set compares the results obtained with reduced neutrino opacities versus our fiducial set of opacities. The second set examines the sensitivity of spherically symmetric CCSN simulation to variations in the treatment of isoenergetic scattering. All results presented in this section use S9 progenitor as initial conditions.

7.5.1 Set 1: Reduced Neutrino Opacities

The first set of neutrino opacities we considered here contains three settings that vary the fidelity of opacities. Setting A, electron-neutrino and electron-antineutrino emission, absorption and iso-energetic scattering on nucleon and nuclei are included, labeled as 'EmAb + Iso'. Setting B adds neutrino-electron scattering to setting A, and is labeled 'EmAb + Iso + NES'. Setting C further adds neutrino pair production and annihilation, and is labeled as 'EmAb + Iso + NES + Pair'. All else, including closure, physical domain, resolution, and limiters, is the same as in Section 7.3. Setting B corresponds to the opacities used in Sections 7.3 and 7.4.

In Figure 7.5.1, the evolution of central entropy, electron fraction and lepton fraction is plotted, with setting A in cyan lines, setting B in blue lines, and setting C in yellow lines. Like Figure 7.3.5, the left panels show entropy and lepton number fraction versus central density for pre-bounce evolution, and the right panels show the post-bounce evolution versus post-bounce time. While the setting B and setting C models have similar evolution, the result of setting A is separated from them. Setting A, which omitted NES, has less central entropy pre-bounce, higher entropy around and post-bounce, and more electron in the PNS. This occurs because NES is the key neutrino–matter interaction at bounce for neutrino trapping. Without NES, neutrinos escape more quickly, and are less likely to be captured by neutrons at core, leading to less deleptonization. It demonstrates, as we mentioned earlier, that the evolution of central properties is determined by the implementation of the nuclear EOS and neutrino interactions.

The shock trajectories for all three settings versus post-bounce time are presented in Figure 7.5.2, with setting A marked by a dotted cyan line, setting B in dashed blue line, and setting C in yellow solid line. The results of setting A are very different from the results of setting B and setting C, which are almost identical. It demonstrates the importance of including neutrino-electron scattering (NES) in a CCSN simulation, since NES dramatically impacts the dynamics.

The neutrino luminosity and neutrino RMS energy sampled at a fixed 500 km radius are plotted in Figure 7.5.3 and 7.5.4, respectively, for the three opacity settings. The results of setting A are marked by dotted cyan lines, while setting B are dashed blue lines, and setting C are yellow solid lines. Setting A had the highest luminosity and RMS energy, in both electron-neutrino and electron-antineutrino, at pulse and during later evolution. Setting B had the second high luminosity and RMS energy at neutrino pulse. Setting B has similar luminosity and RMS energy during later evolution to setting C. The difference between setting A, setting B and setting C tends to decrease as time passes, when the PNS is relatively steady.

A snapshot of properties comparison for the three opacity settings at bounce is presented in Figure 7.5.5 for density, temperature, electron fraction, entropy, pressure and velocity versus enclosed mass. The result of setting A is marked by a dotted cyan line, while setting B in blue lines, and setting C in yellow lines. A excellent agreement between setting B and setting C is observed. The result of setting A had shock at the outer area, with a slight stronger shock and higher electron fraction at the center core. Other than that, the features in the fluid properties between the three settings are the same.

The evolution of electron fraction with the mass shell trajectories for setting A is presented in Figure 7.5.6 to compare with the result of setting B, which is presented in Figure 7.3.2. (Setting C had almost identical history as setting B, and is omitted here.) The first difference is the deleptonization behind the shock around the bounce. Because setting A had stronger shock and less "obstacle" ahead of the shock, due to omission of NES, its shock "over-shoot" is larger and had more deleptonization up to 200 km around 10 ms as the background color marks. In addition, because of the "over-shot" shock, the mass shells, specifically 1.23 $M_{\odot}$ and 1.28 $M_{\odot}$, crossed the shock radius sooner.

Figure 7.5.7 shows the net neutrino heating rate due to emission and absorption of electron neutrinos and antineutrinos for setting A, comparable to Figure 7.3.10 for setting B. Because of the absence of NES, the matter that ahead of shock was more transparent to the neutrino and had less heating/cooling rate. Setting A also had a larger and consistent heating region behind the shock compared to setting B. Therefore, NES plays an important role in the dynamics at bounce and during the late time evolution. NES is essential to be included in a CCSN simulation.

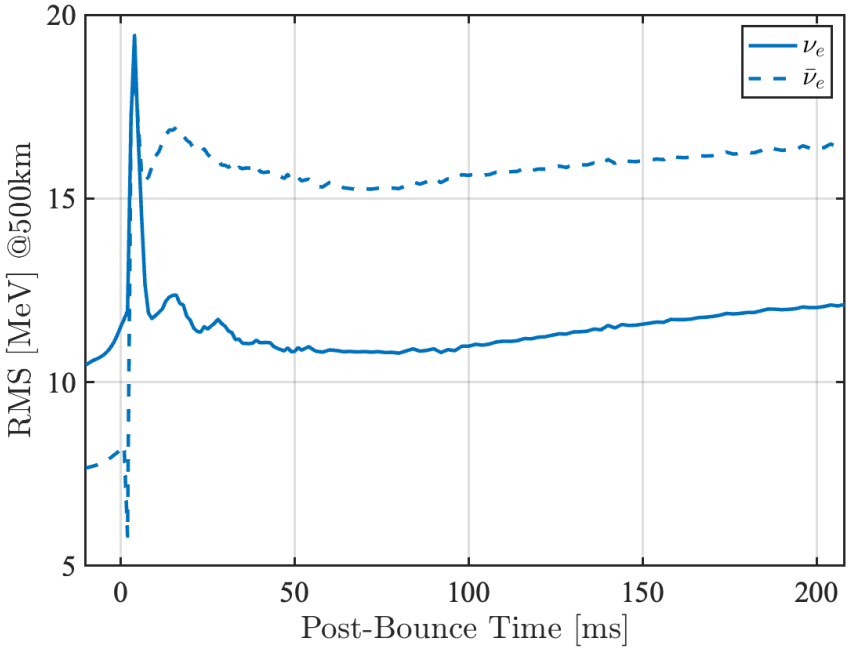

Figure 7.3.6: Neutrino RMS energies at 500 km as a function of time since the onset of collapse for model S9. Solid line marks result for electron-neutrinos and dashed line for electron-antineutrinos.

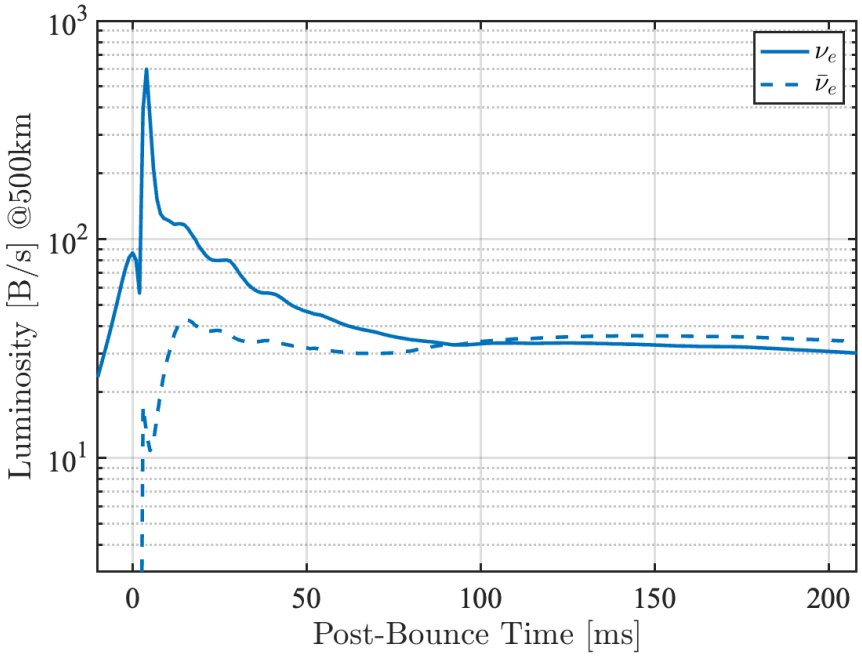

Figure 7.3.7: Neutrino luminosities at 500 km as a function of time since the onset of collapse for model S9. Solid line marks result for electron-neutrinos and dashed line for electron-antineutrinos.

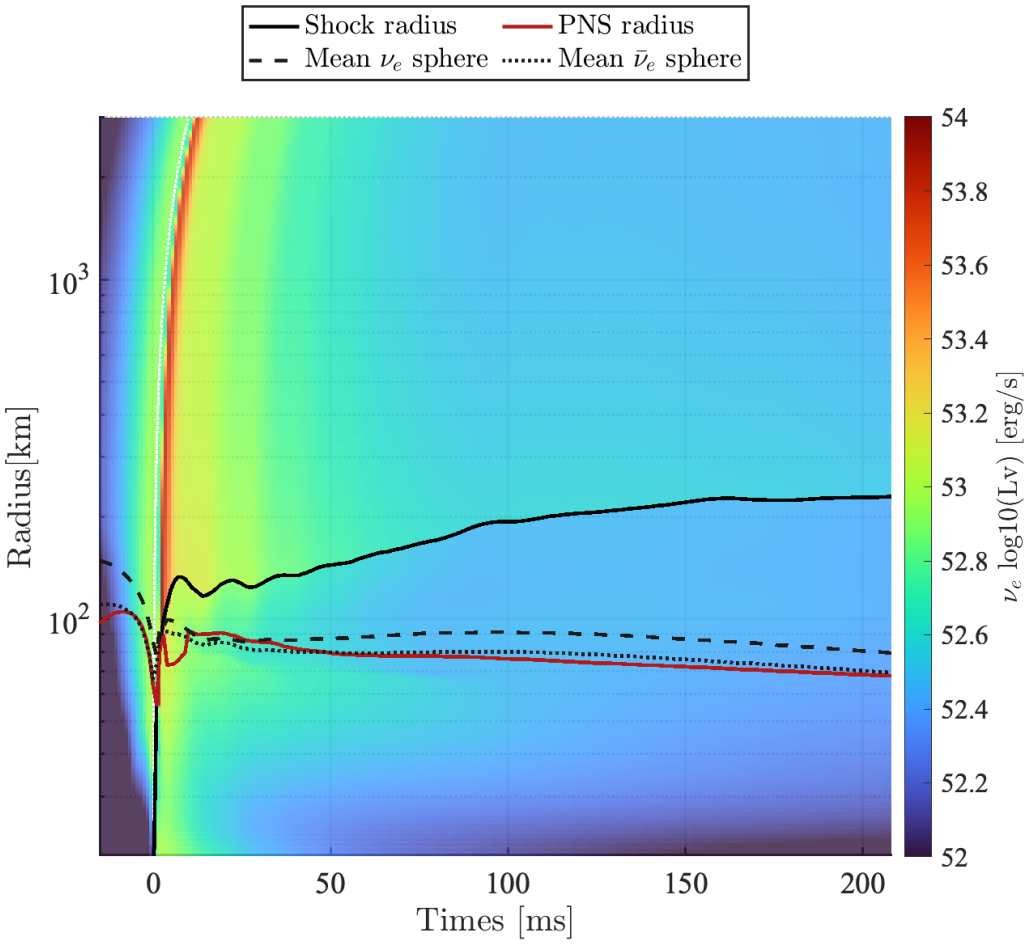

Figure 7.3.8: Electron-neutrino luminosity evolution map for model S9. The white dotted line along the luminosity peak (red band) is the reference line for propagation outward at light speed. The other lines are defined the same way as in previous plots. The background is colored based on the neutrino luminosity, as the color bar indicates.

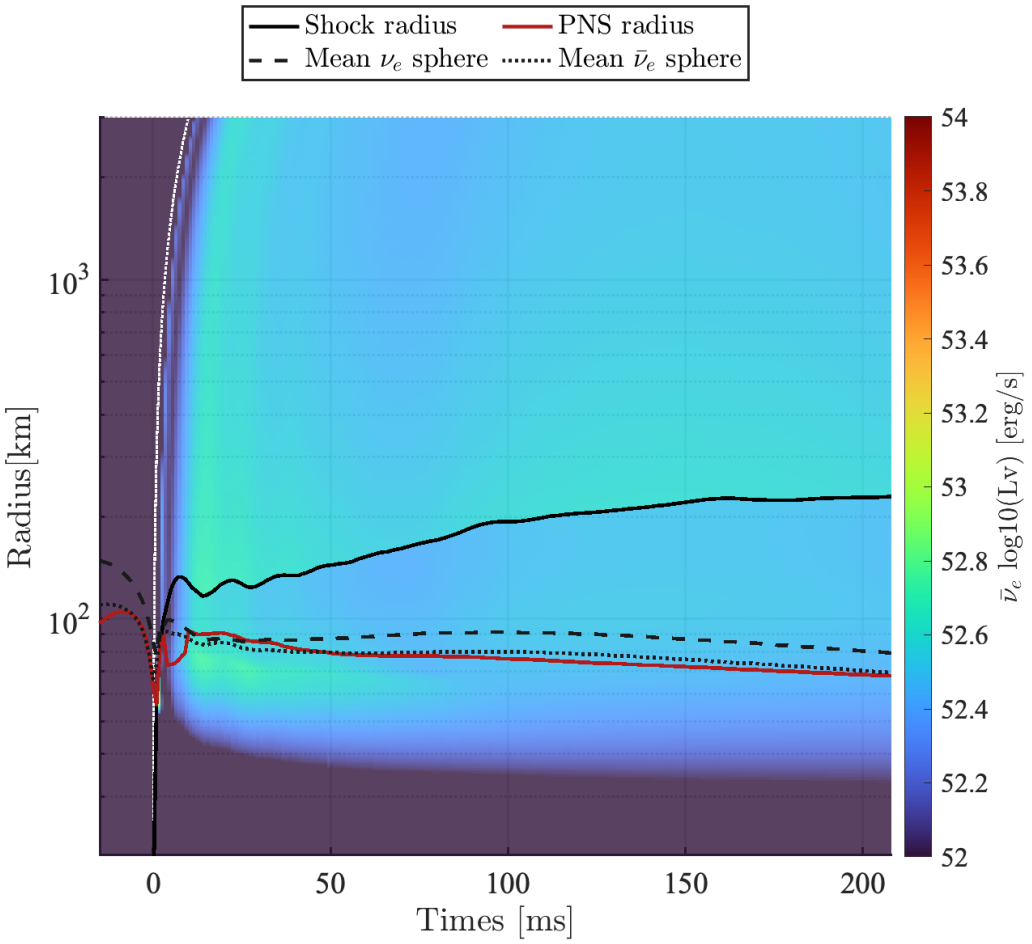

Figure 7.3.9: Electron-antineutrino luminosity evolution map for model S9. The while dotted line is the reference line for propagation outward at light speed. The other lines are as defined in the previous plots. The background is colored based on the neutrino luminosity, as the color bar indicates.

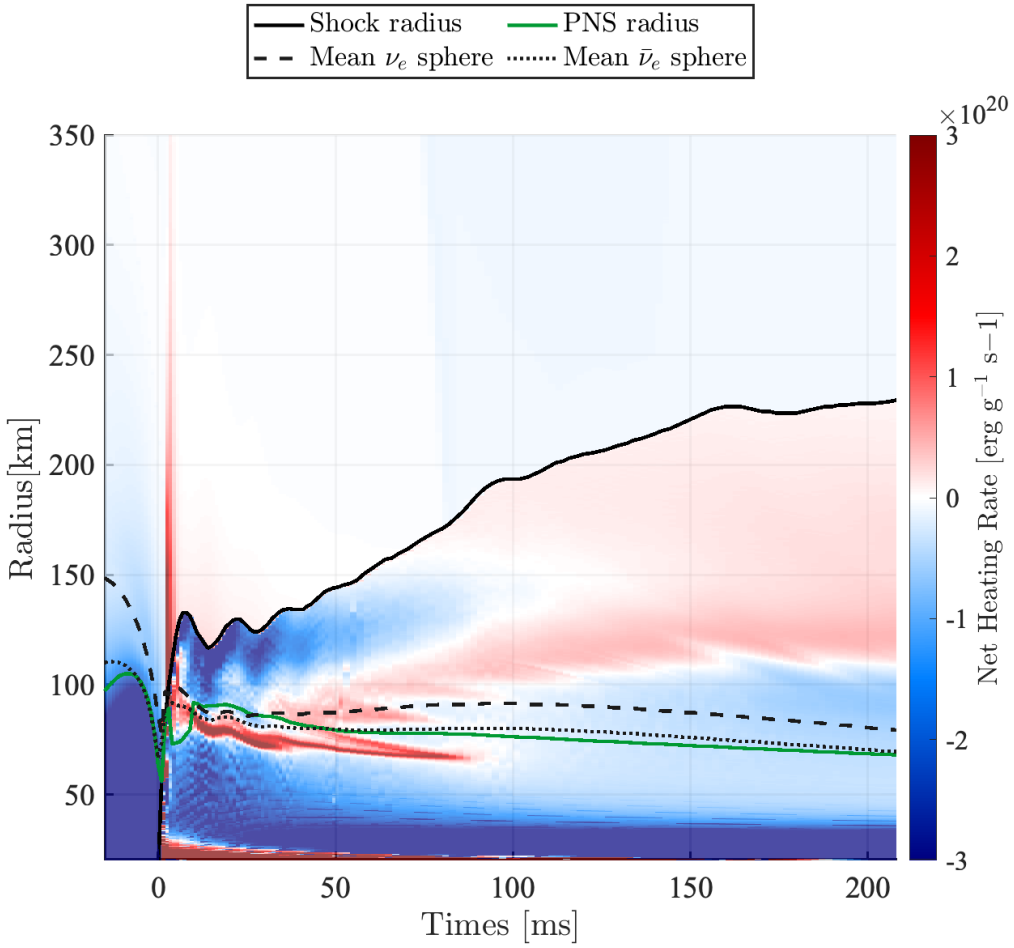

Figure 7.3.10: Net heating rates from emission and absorption of electron-neutrinos and electron-antineutrinos, and neutrino–electron scattering at various post-bounce times for model S9. The black line tracks the shock position. The green line marks the density 10^{11} g/cm^3, which is often used to define proto-neutron star radius. The dashed black line and the dotted black line represent the mean electron-neutrino sphere and the mean electron-antineutrino–sphere, respectively.

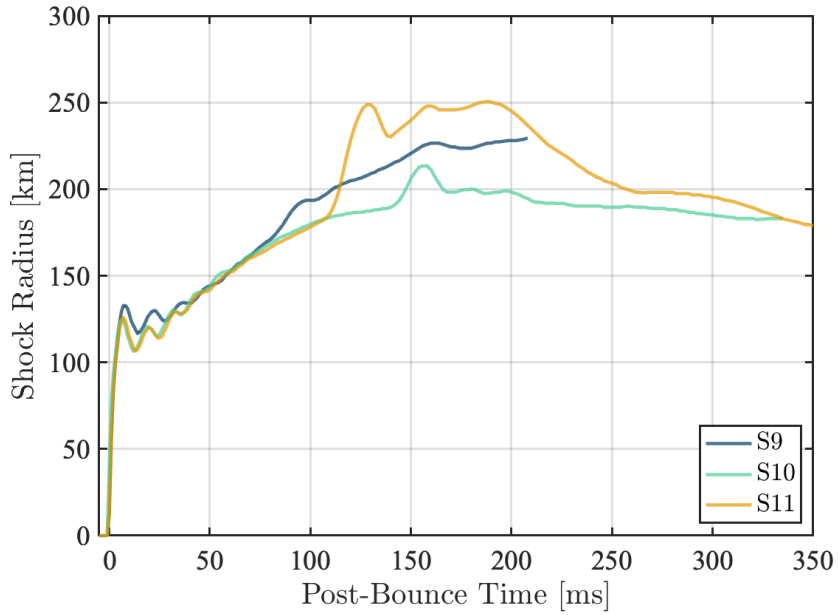

Figure 7.4.1: Shock radii for all three models considered here versus post-bounce time. Blue line marks result for S9, while green line for S10, and yellow line for S11.

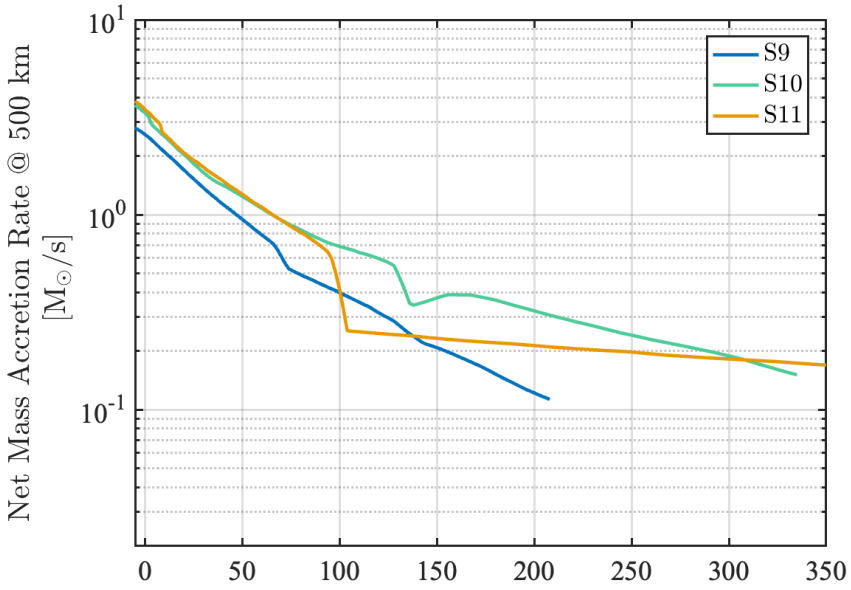

Figure 7.4.2: Accretion rates for three models considered here. Blue line marks result for S9, while green line for S10, and yellow line for S11.

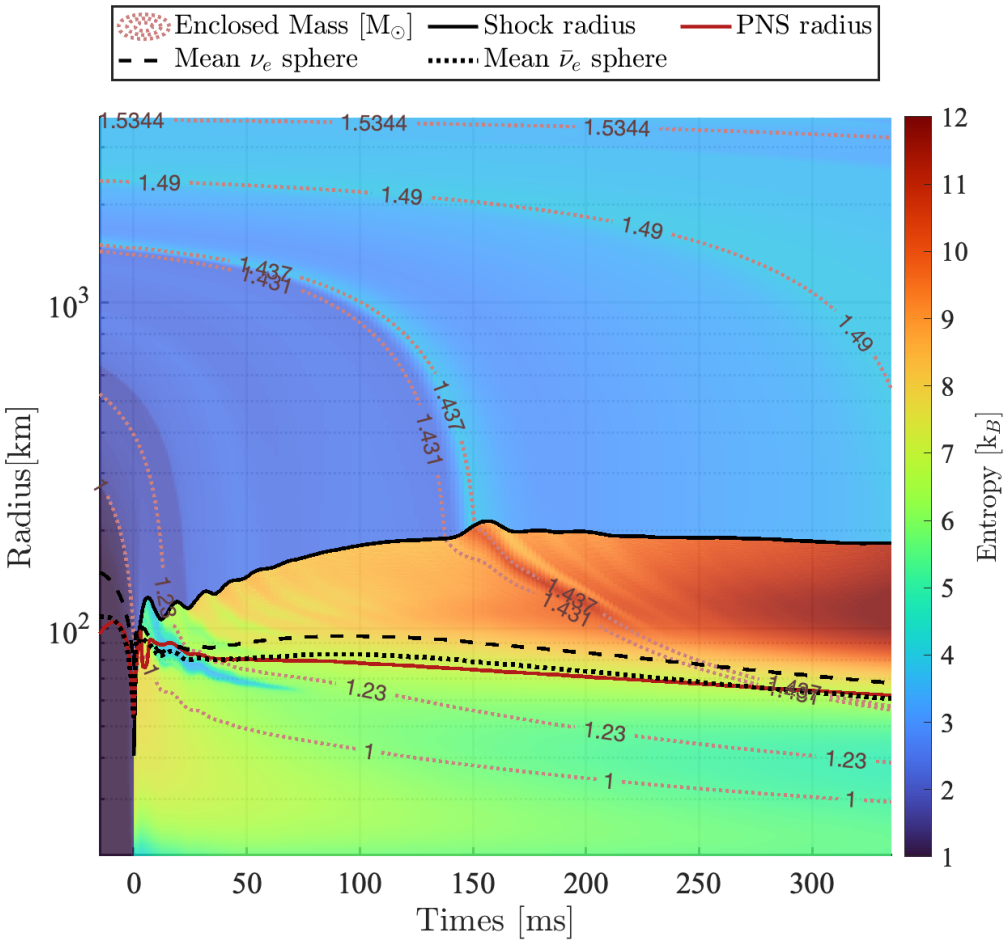

Figure 7.4.3: Radial mass shell trajectories superimposed on color maps of entropy for model S10. The red dotted lines track the corresponding mass shells. The black line tracks the shock position. The red line marks the PNS radius. The dashed black line and the dotted black line represent the mean electron-neutrino sphere and the mean electron-antineutrino sphere, respectively.

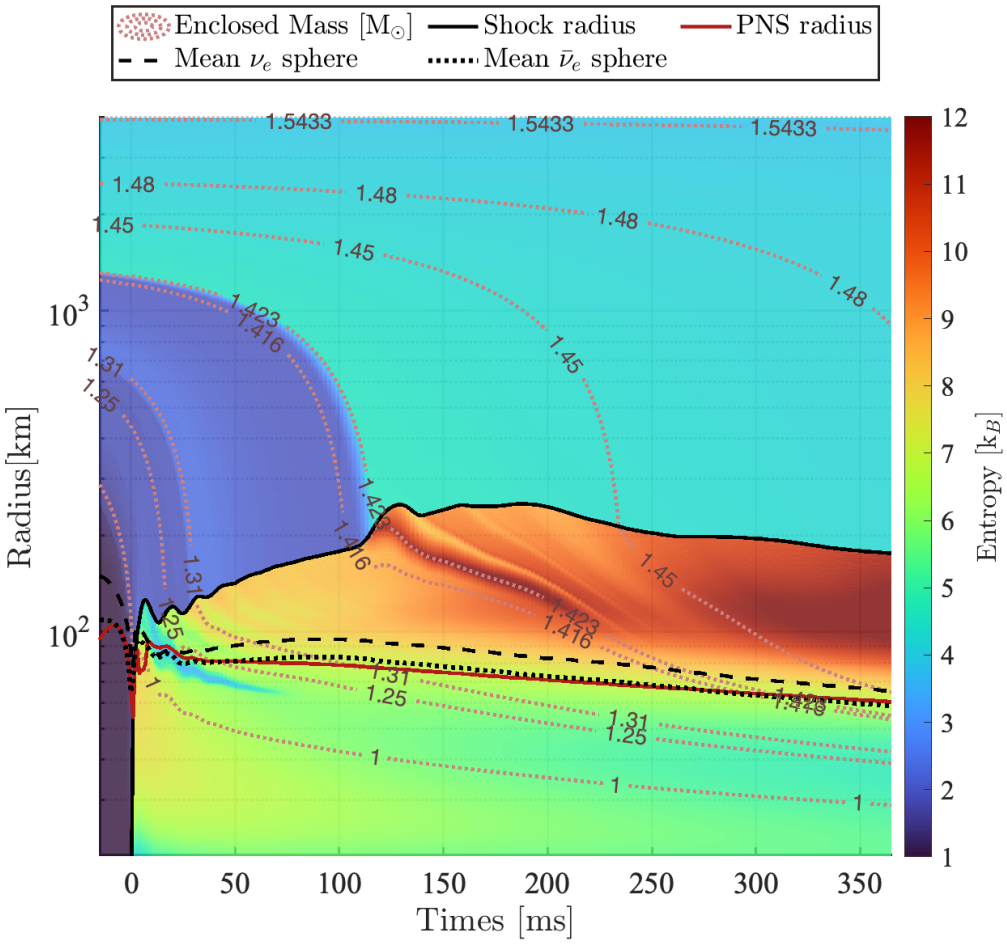

Figure 7.4.4: Radial mass shell trajectories superimposed on color maps of entropy for S11. The red dotted lines track the corresponding mass shells. The black line tracks the shock position. The red line marks the PNS radius. The dashed black line and the dotted black line represent the mean electron-neutrino sphere and the mean electron-antineutrino sphere, respectively.

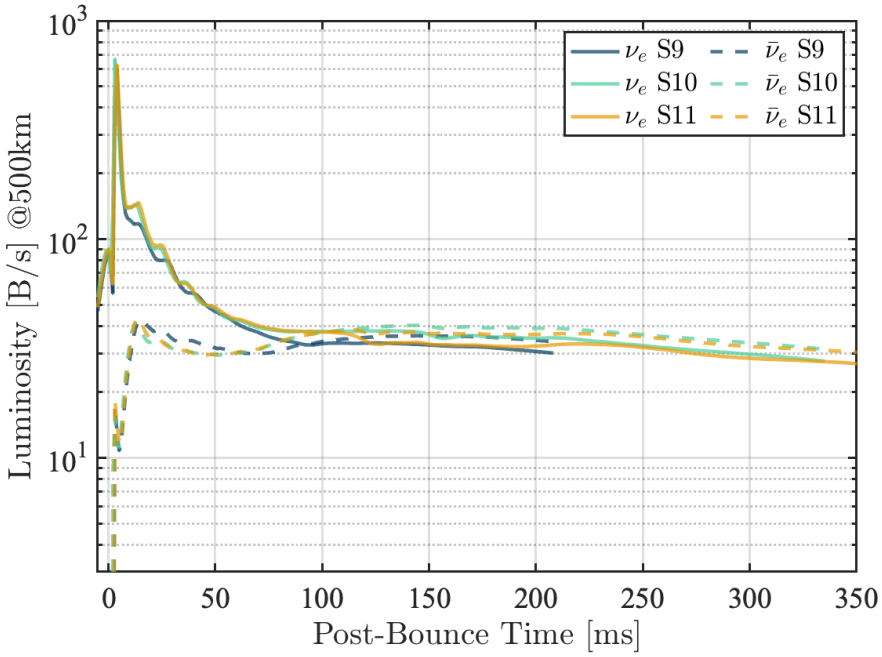

Figure 7.4.5: Comparison of neutrino luminosity versus post-bounce time for all three models considered here. Solid lines mark results for electron-neutrino and dashed lines for electron-antineutrino. Blue lines mark result for S9, while green lines for S10, and yellow lines for S11. At neutrino pulse, model S10 has the strongest peak in both electron-neutrino luminosity and electron-antineutrino luminosity, then S11 and S9, with the largest relative difference $\sim$10%.

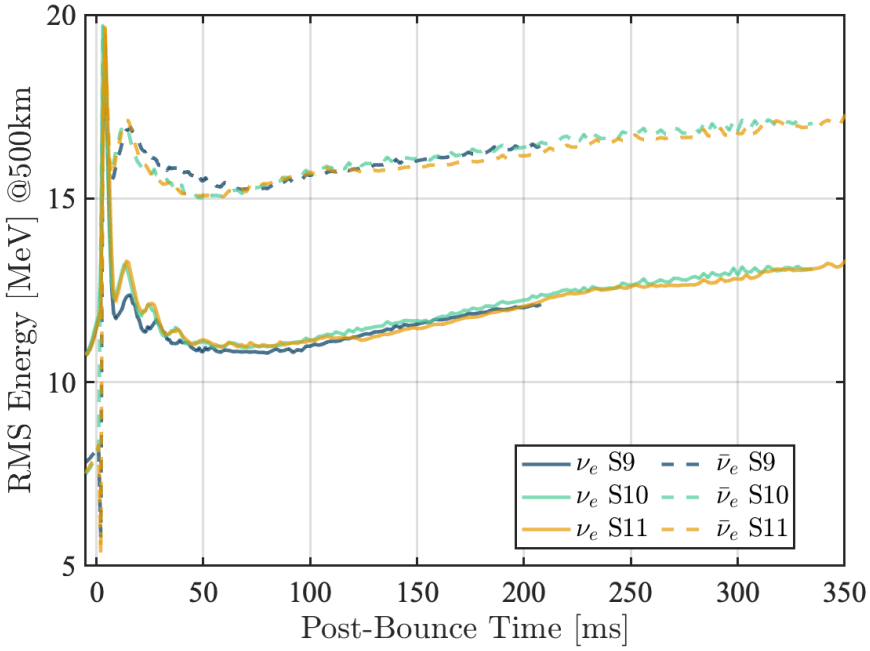

Figure 7.4.6: Comparison of neutrino RMS energy versus post-bounce time for all three models considered here. Solid lines mark results for electron-neutrino and dashed lines for electron-antineutrino. Blue lines mark result for S9, while green lines for S10, and yellow lines for S11. At neutrino pulse, model S10 has the strongest peak in both electron-neutrino RMS energy and electron-antineutrino RMS energy, then S11 and S9,with the largest relative difference $\sim$2%.

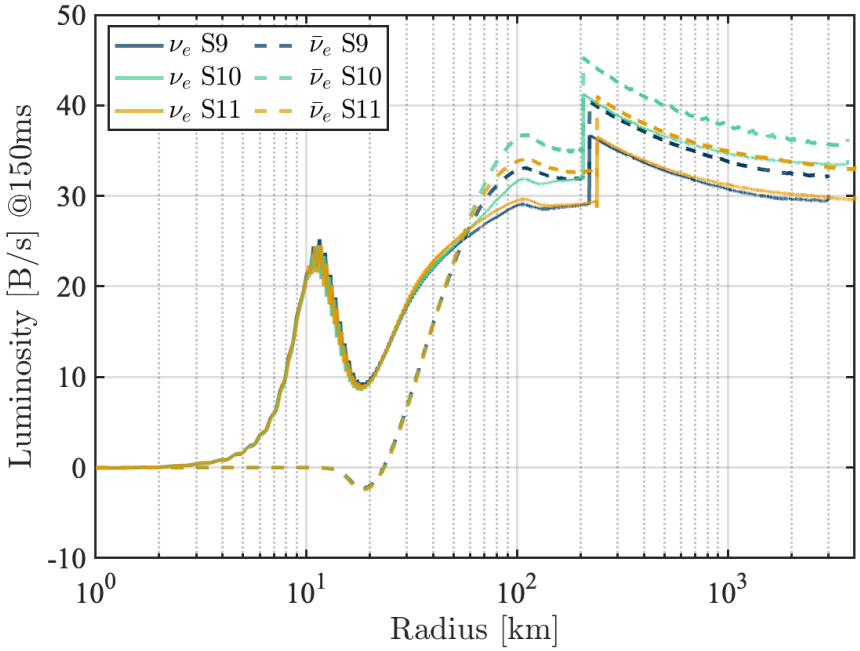

Figure 7.4.7: Comparison of neutrino luminosity at 150 ms post-bounce as a function of radius for all three models considered here. Solid lines mark results for electron-neutrino and dashed lines for electron-antineutrino. Blue lines mark result for S9, while green lines for S10, and yellow lines for S11.

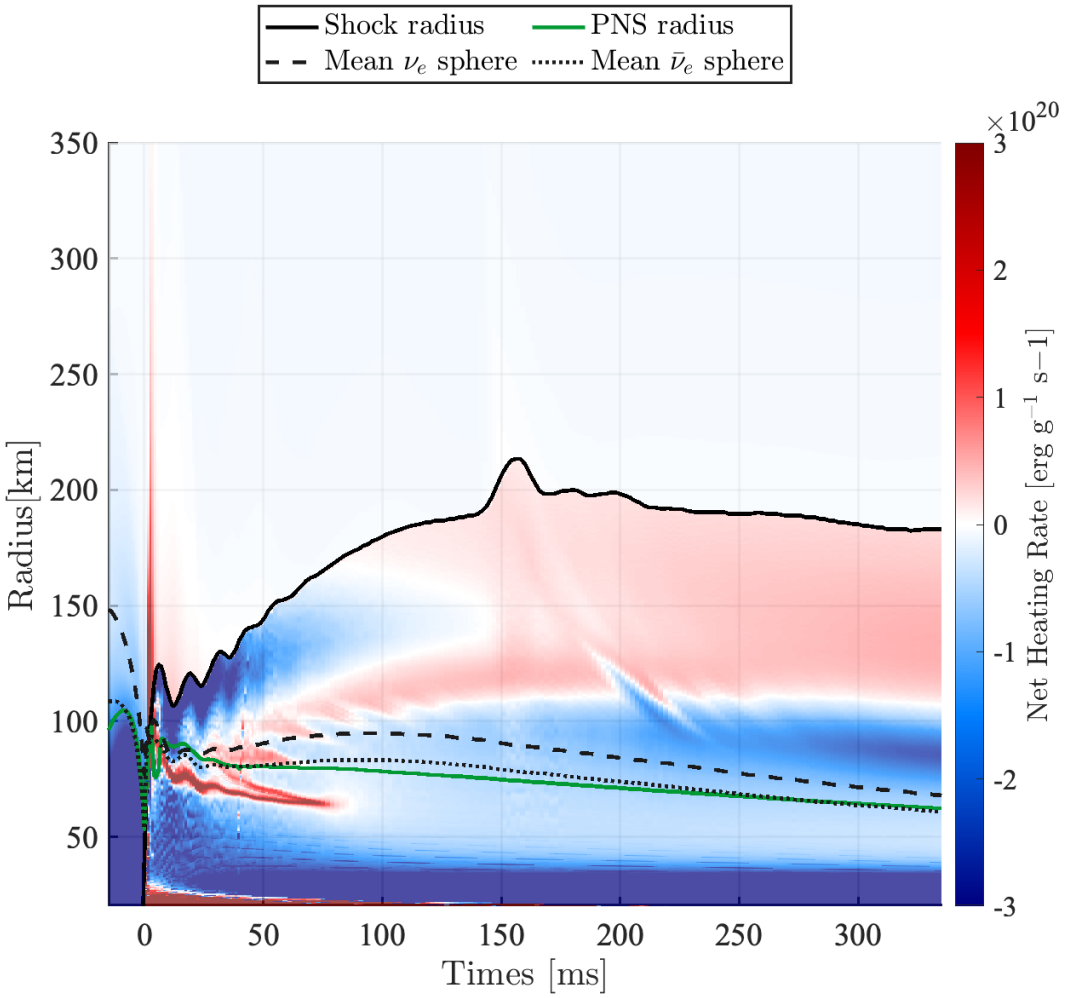

Figure 7.4.8: Net heating rates for model S10 as a function of radius and time. The black line tracks the shock position. The green line marks the PNS radius. The dashed black line and the dotted black line represent the mean electron-neutrino sphere and the mean electron-antineutrino sphere, respectively.

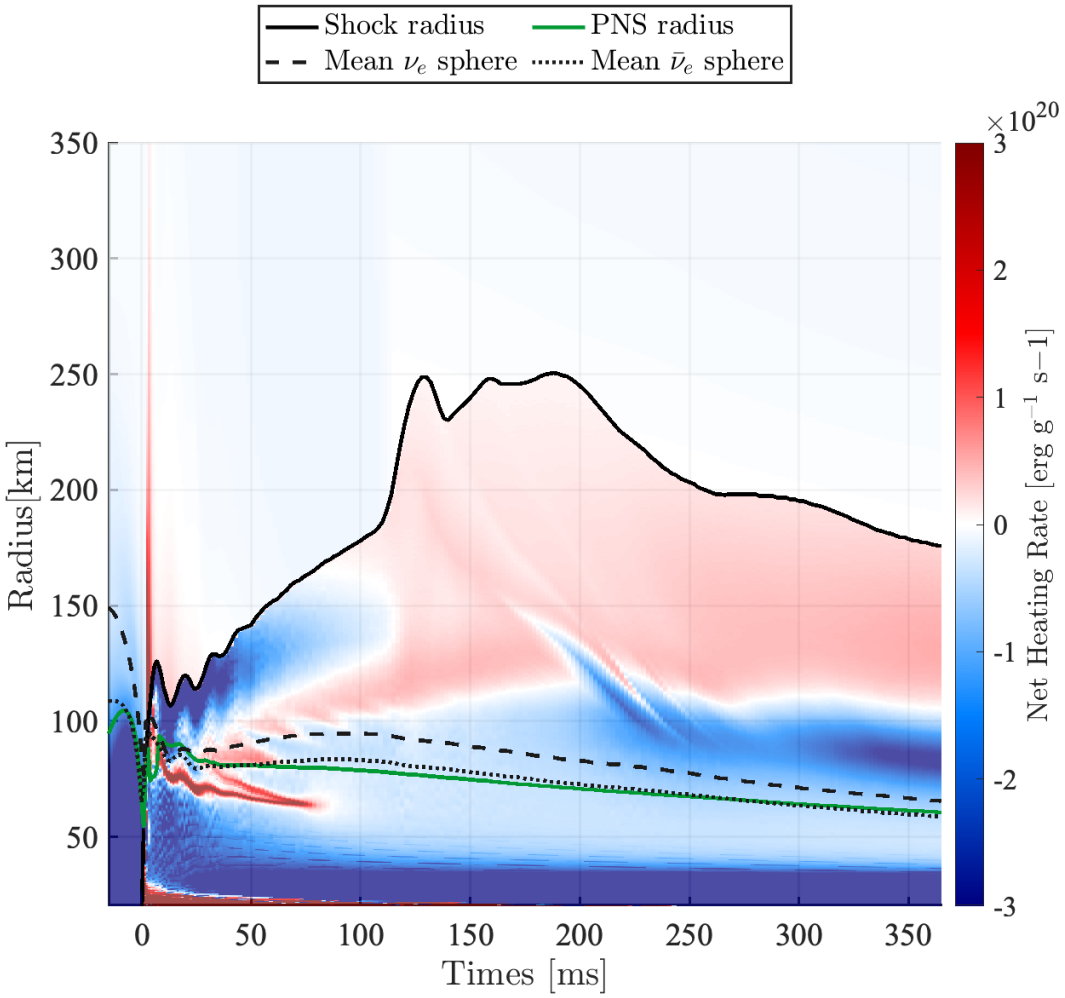

Figure 7.4.9: Net heating rates for model S11 as a function of radius and time. The black line tracks the shock position. The green line marks the PNS radius. The dashed black line and the dotted black line represent the mean electron-neutrino sphere and the mean electron-antineutrino sphere, respectively.

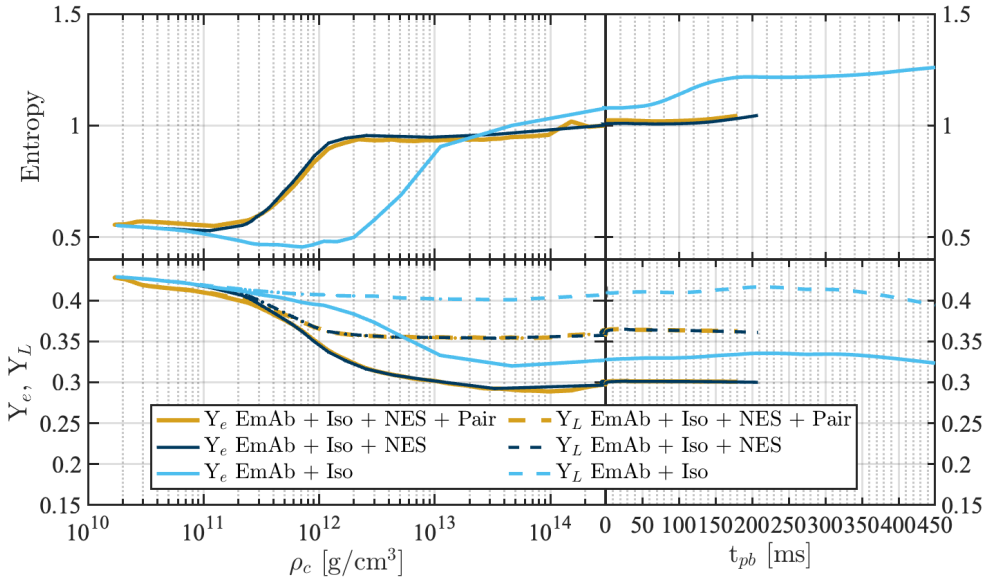

Figure 7.5.1: The evolution of central entropy and lepton number in reduced opacity comparison for model S9. In the left (right) panels are the pre-bounce (post-bounce) values of the central entropy (top) and electron fraction (Y_e) and total lepton fraction ($Y_L = Y_e + Y_\nu$) (bottom). The pre-bounce evolution is plotted versus the central density, while the post-bounce evolution is plotted versus time. Cyan lines mark result for setting A, labeled "EmAb + Iso". Blue lines mark result for setting B, labeled "EmAb + Iso + NES". And yellow lines mark result for setting C, labeled "EmAb + Iso + Pair".

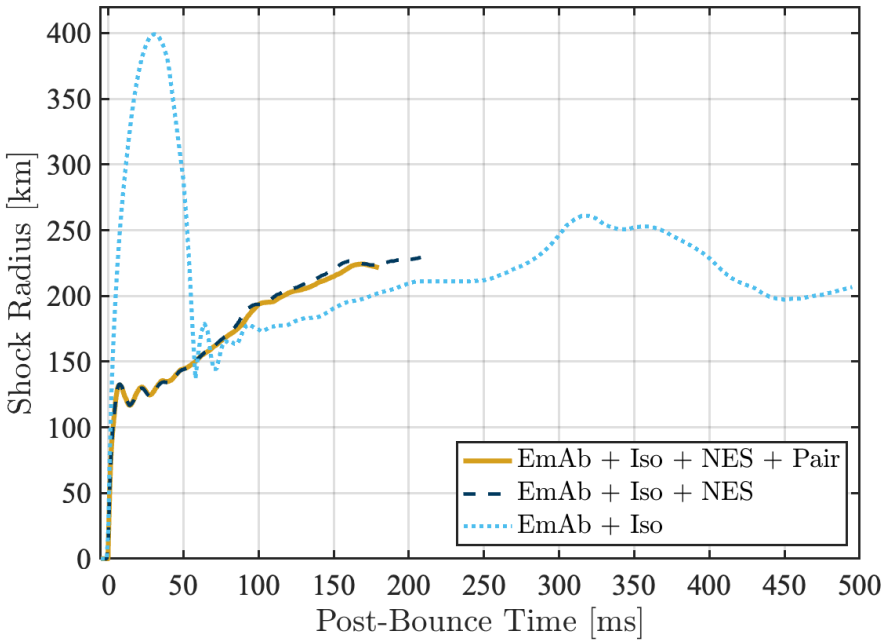

Figure 7.5.2: Shock radii for all three opacity settings considered here versus post-bounce time. Cyan lines mark result for setting A, labeled "EmAb + Iso". Blue lines mark result for setting B, labeled "EmAb + Iso + NES". And yellow lines mark result for setting C, labeled "EmAb + Iso + Pair".

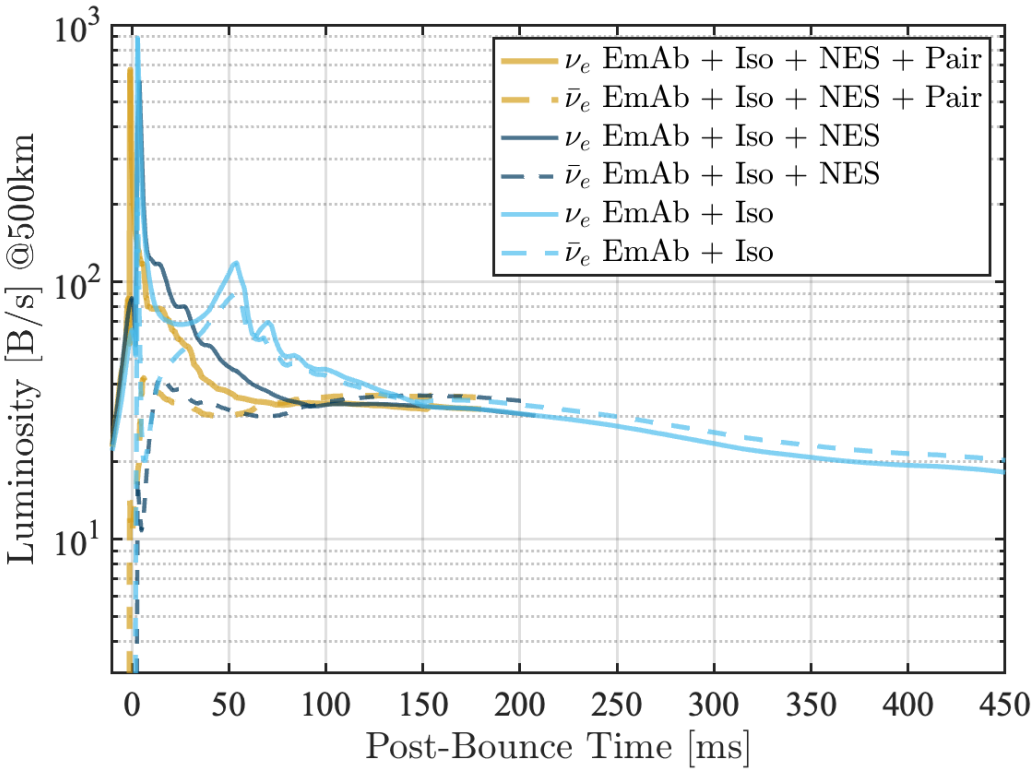

Figure 7.5.3: Comparison of luminosity across simulations with different opacity sets, for the S9 model. Solid lines mark results for electron-neutrino and dashed lines for electron-antineutrino. Cyan lines mark result for setting A, labeled "EmAb + Iso". Blue lines mark result for setting B, labeled "EmAb + Iso + NES". And yellow lines mark result for setting C, labeled "EmAb + Iso + Pair". At neutrino pulse, setting A has the strongest peak in both electron-neutrino luminosity and electron-antineutrino luminosity, then setting C and setting B, with the relative difference between setting A and setting B be $\sim$50%.

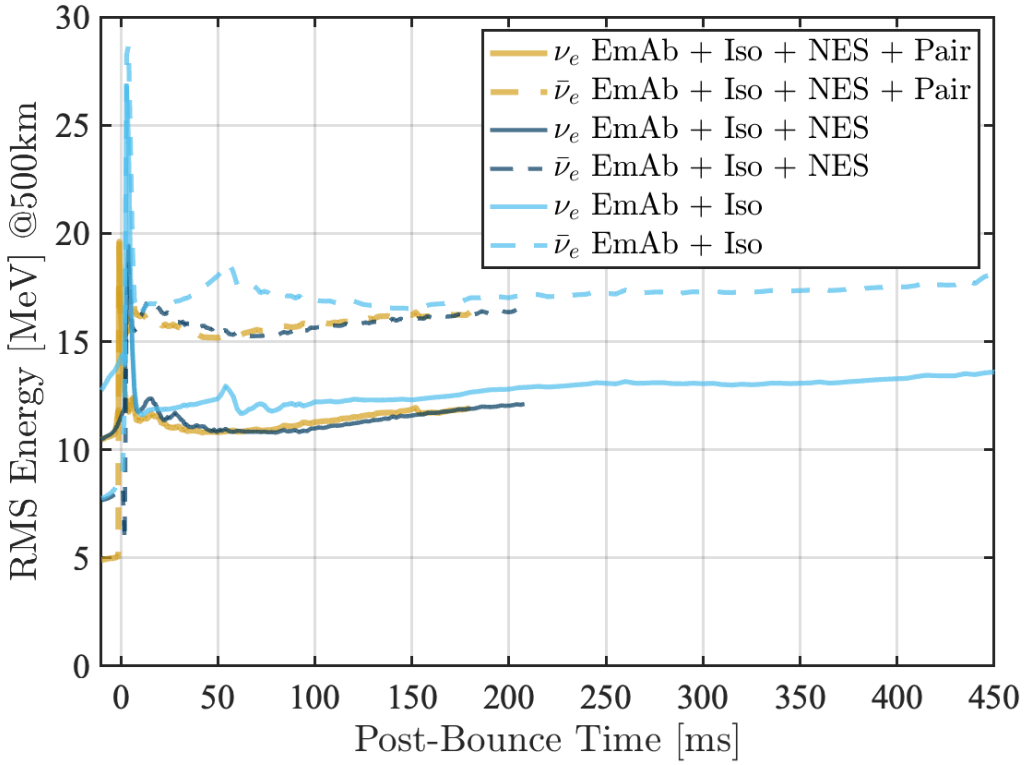

Figure 7.5.4: Comparison of RMS energy across simulations with different opacity sets, for the S9 model. Solid lines mark results for electron-neutrino and dashed lines for electron-antineutrino. Cyan lines mark result for setting A, labeled "EmAb + Iso". Blue lines mark result for setting B, labeled "EmAb + Iso + NES". And yellow lines mark result for setting C, labeled "EmAb + Iso + Pair". At neutrino pulse, setting A has the strongest peak in both electron-neutrino luminosity and electron-antineutrino luminosity, then setting C and setting B, with the largest relative difference $\sim 40\%$. Electron-antineutrino has higher RMS energy than electron-neutrino in result for setting A, while electron-neutrino has higher RMS energy for setting B and setting C.

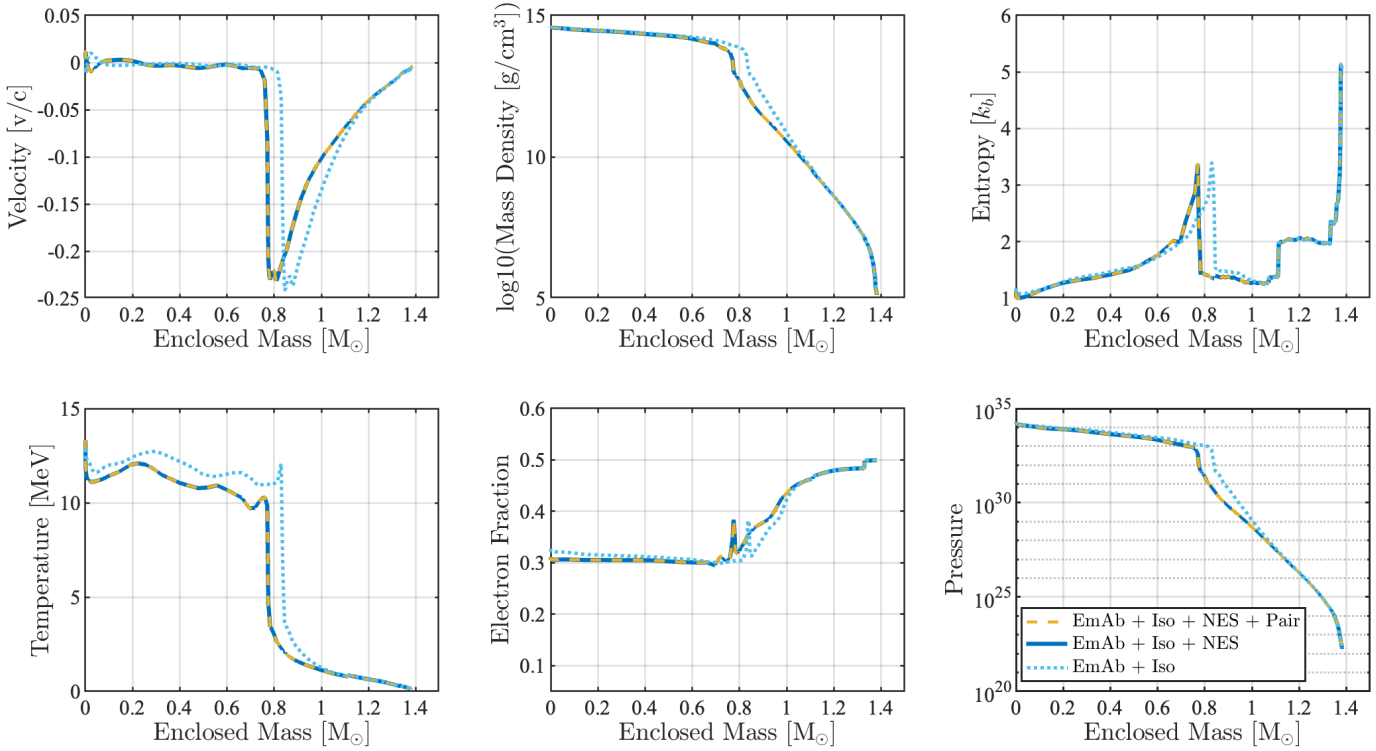

Figure 7.5.5: Plots of velocity, density, entropy, temperature, electron fraction, and pressure at core bounce across three models with different input physics. Cyan lines mark result for setting A, labeled "EmAb + Iso". Blue lines mark result for setting B, labeled "EmAb + Iso + NES". And yellow lines mark result for setting C, labeled "EmAb + Iso + Pair".

7.5.2 Set 2: Sensitivity to Variations in Isoenergetic Scattering

In this section, we focus on investigating the sensitivity of the model to variations in the isoenergetic scattering cross section. This study was inspired by Melson et al. (2015a), where they showed that introducing a factor (moderate strangeness-dependent contribution) in the axial-vector coupling constant could cause an non-exploding model to explode. The modification is in the direction of current experimental results and reduces the neutral-current scattering opacity of neutrons (Melson et al., 2015a). In Melson et al. (2015a), this change increased luminosities and mean energies of all neutrino species, and strengthened the neutrino-energy deposition in the heating layer.

We chose the S9 progenitor to perform this test, because S9 has the steepest density profile among three progenitors, a characteristic conducive to explosion. All else, including closure, physical domain, resolution, and limiters, is the same as in Section 7.3.

Following Horowitz (2002); Langanke and Martinez-Pinedo (2003); Melson et al. (2015a), the axial-vector coupling constants, c_a, with a strange-quark contribution to the nucleon spin can be expressed as

$$c_a = \frac{1}{2}\left(\pm g_a - g_a^s\right), \tag{7.5}$$

where the plus sign is for νp scattering, and the minus sign is for νn scattering. The cross section for isoenergetic scatting is

$$\sigma_0^{\mathrm{t}} = \int_{4\pi} d\Omega \frac{d\sigma_0}{d\Omega}(1-\cos\theta) = \frac{2G_{\mathrm{F}}^2\varepsilon^2}{3\pi}\left(c_{\mathrm{v}}^2 + 5c_{\mathrm{a}}^2\right), \tag{7.6}$$

where G_F is Fermi's constant. With negative g_a^s, the cross section increases for νp-scattering and decreases for νn-scattering. We define the cross section change ratio

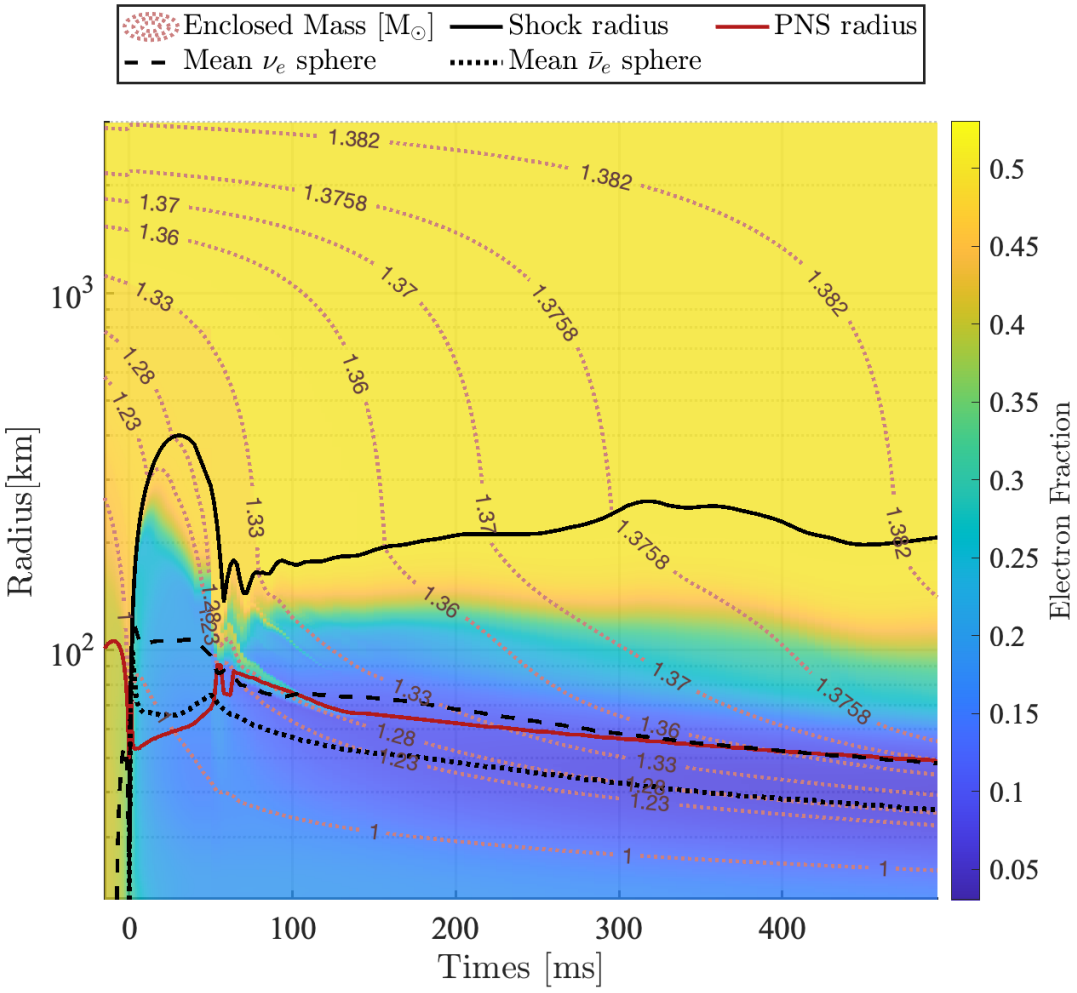

Figure 7.5.6: Electron fraction evolution map for reduced opacity comparison for model S9 using setting A. Same as in Figure 7.3.2 for setting B, the red dotted lines track the corresponding mass shells. The black line tracks the shock position. The red line marks PNS radius. The dashed black line and the dotted black line represent the mean electron-neutrino sphere and the mean electron-antineutrino sphere, respectively.

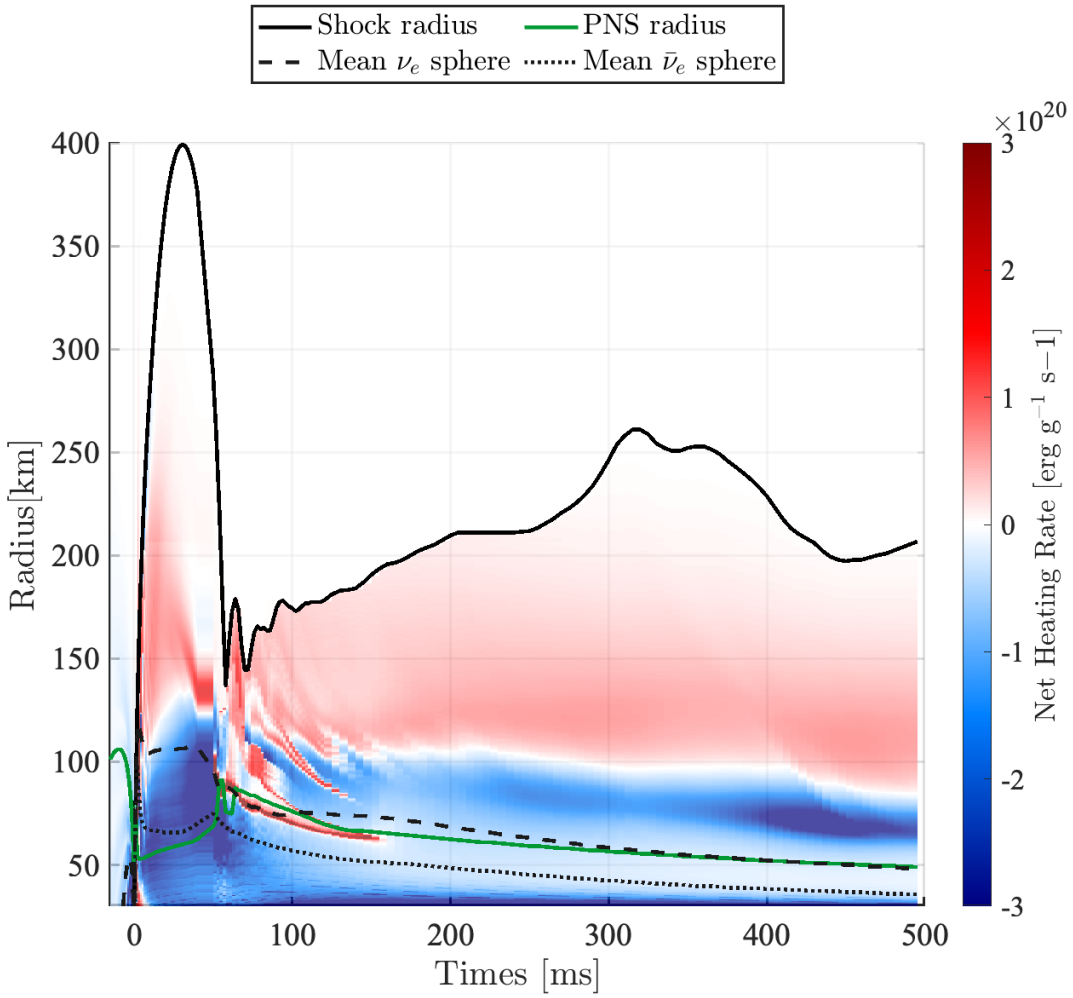

Figure 7.5.7: Net heating rates in reduced opacity comparison for model S9 using setting A. Same as in Figure 7.3.10 for setting B, the black line tracks the shock position. The green line marks PNS radius. The dashed black line and the dotted black line represent the mean electron-neutrino sphere and the mean electron-antineutrino sphere, respectively.

as

$$\text{The cross section change ratio} = \frac{\sigma_0^{t\prime}}{\sigma_0^{t}} = \frac{\left(c_v^2 + \frac{5}{4}\left(\pm g_a - g_a^s\right)^2\right)}{\left(c_v^2 + \frac{5}{4}g_a^2\right)}, \tag{7.7}$$

with $+g_a$ for νp scattering and $-g_a$ for νn scattering. And in Figure 7.5.8, the cross section change ratio versus g_a^s with $g_a = 1.21$ is plotted, from which one can read that $g_a^s = -0.2$

The shock radii obtained with various g_a^s values are plotted in Figure 7.5.9. In Melson et al. (2015a), they found, for a $20M_\odot$ progenitor, adding $g_a^s = -0.2$ to the axial-vector coupling constant $g_a \approx 1.26$ can turn an unsuccessful three-dimensional explosion model into a successful explosion model. We adopted their setting, $g_a^s = -0.2$, as well as some other settings, in our one-dimensional models, all using the S9 progenitor. Here $g_a^s = 0.0, -0.2, -0.4$, and -1.0, corresponding to that νn decreasing ratio (defined by Equation (7.7) with $-g_a$) be 1.0(no change), $\sim$0.73, $\sim$0.51, and $\sim$0.15, respectively, as shown in Figure 7.5.8. Figure 7.5.9 shows that none of our simulations exploded by the end of the simulation. Neither different g_a^s led to different shock behavior, since all shock trajectories were overlapped.

Besides the shock trajectories, the radiation properties – neutrino luminosities and RMS energies – sampled at a fixed 500 km radius versus post bounce time are also plotted, in Figure 7.5.10 and Figure 7.5.11, respectively. Same as seen in shock trajectory (Figure 7.5.9), the simulations with different g_a^s yield the same radiation properties, in both neutrino luminosities and neutrino RMS energies. In conclusion, our one-dimensional model is not sensitive to differences in g_a^s in both shock radius and radiation field quantities. It can be understood by relating with the result in the previous section, Section 7.5.1, that NES plays a more crucial role than iso-energetic scattering in our models.

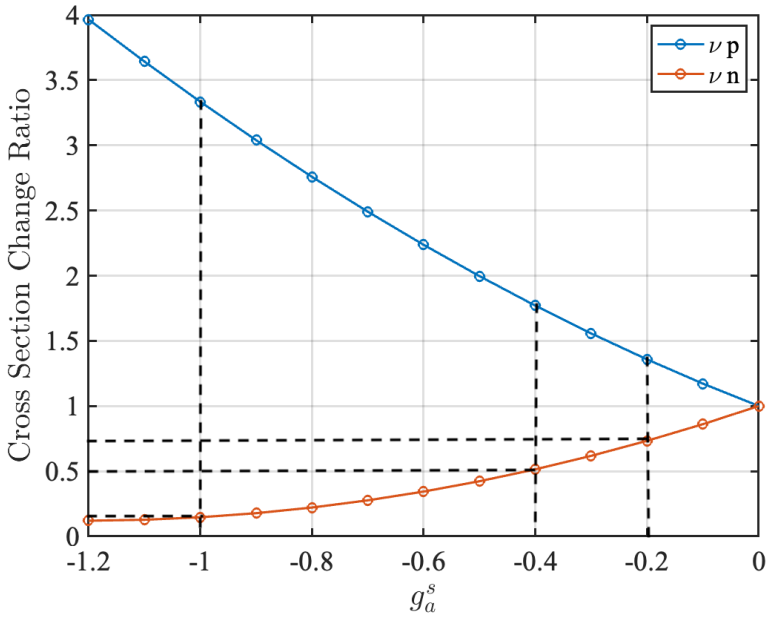

Figure 7.5.8: Following the definition in Melson et al. (2015b), plots the ratio change in the total transport cross section Equation (7.6) versus g_a^s with $g_a = 1.21$. Blue line marks the change in νp cross section, and red line for νn cross section. $g_a^s = 0.0, -0.2, -0.4$, and -1.0, corresponding to that νn decreasing ratio (defined by Equation (7.7) with $-g_a$) be 1.0(no change), $\sim$0.73, $\sim$0.51, and $\sim$0.15, respectively.

7.6 Summary and Discussion

We presented a series of CCSN simulations in spherical symmetry obtained using Flash-X + `thornado`. Starting with the simulation using a 9 solar mass progenitor, we discussed the 1D CCSN simulation results in detail, with discussion of the infall, bounce, and post-bounce evolution, and of critical fluid and radiation quantities as a function of time, as well as the physics involved. Then we compared the simulation results obtained using three different progenitors – S9, S10, and S11. Not surprisingly, we found that the progenitor structure can affect the evolution, but none of the three models exploded by the end of our runs. And the 1D supernova models for the S9, S10 and S11 progenitors do not behave monotonically. Others observe similar results: Radice et al. (2017) used the same three progenitors and came to the same conclusions. However, S9, S10 and S11 models do explode in 3D using FORNAX (Burrows et al., 2019). This is evidence that CCSNe need to be simulated in multi-dimensions. After the progenitor comparison, we presented two sets of simulations with different neutrino–matter interactions using S9. The results demonstrate the importance of including a comprehensive set of neutrino–matter interactions in CCSN simulations.

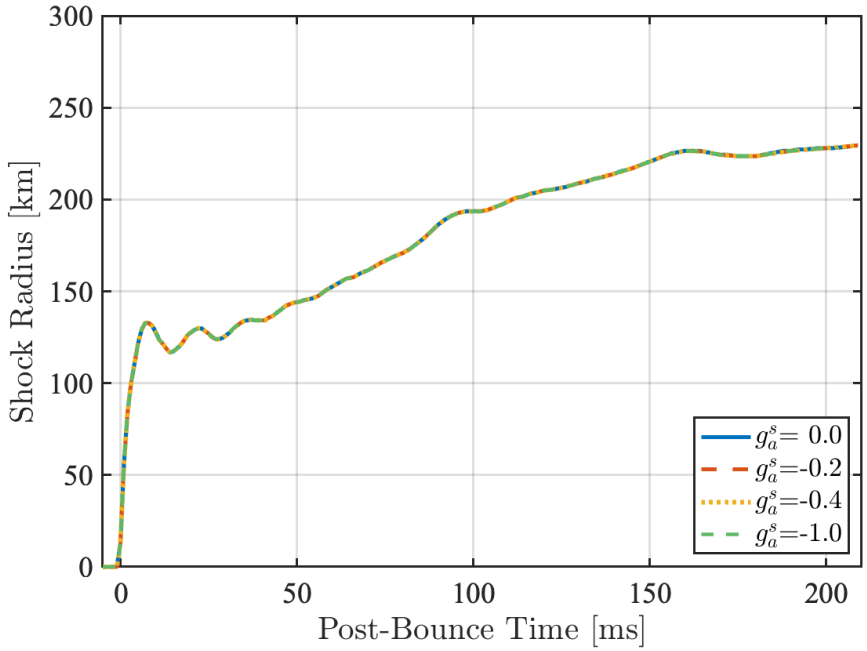

Figure 7.5.9: Comparison isoenergetic scattering opacity simulations in shock radii for model S9, with different g_a^s and $g_a = 1.21$. The blue line marks the result for $g_a^s = 0.0$, red for -0.2, yellow for -0.4, and green for -1.0.

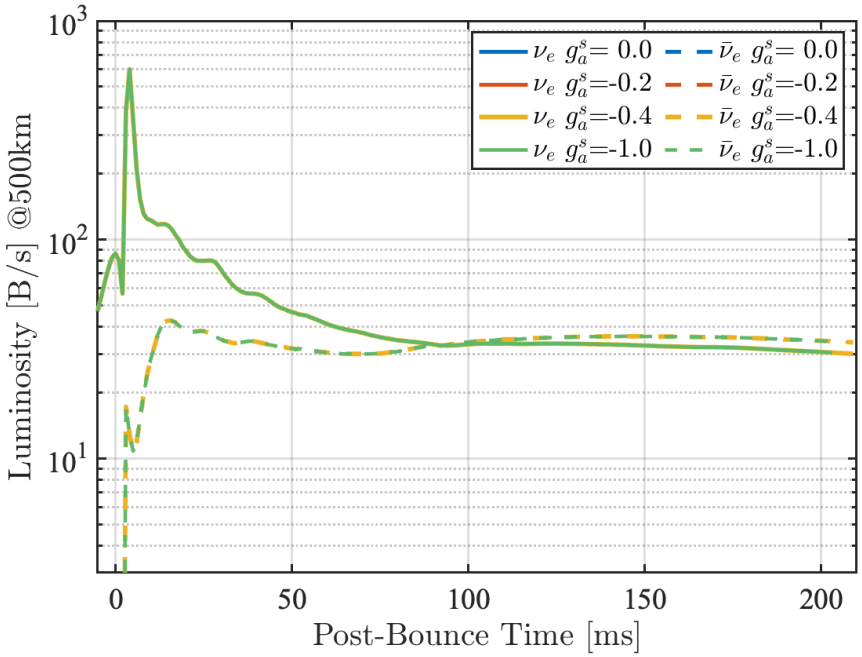

Figure 7.5.10: Comparison isoenergetic scattering opacity simulations in luminosity for model S9, with different g_a^s and $g_a = 1.21$. The solid lines mark the result for electron-neutrino, and the dashed lines for electron-antineutrino. The blue line marks the result for $g_a^s = 0.0$, red for -0.2, yellow for -0.4, and green for -1.0.

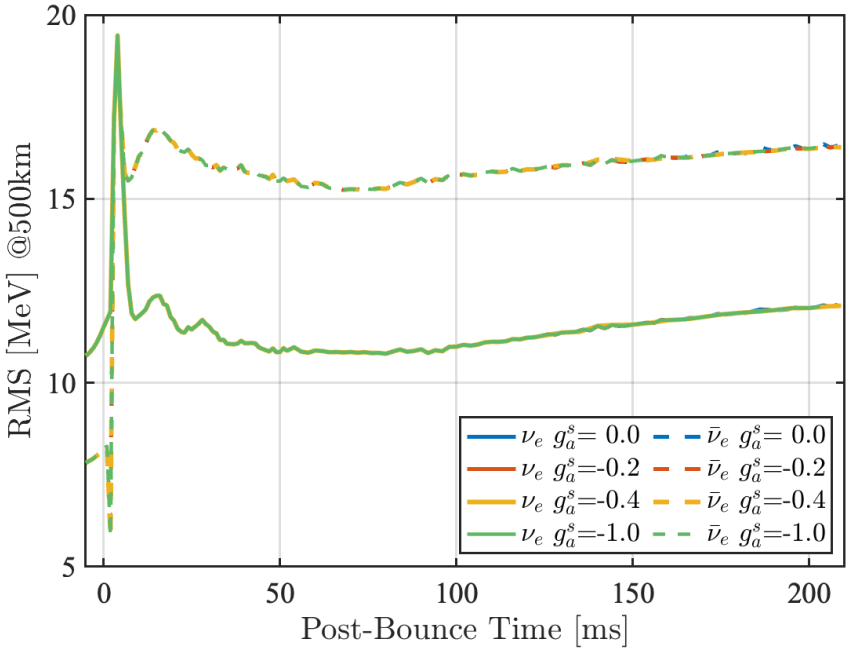

Figure 7.5.11: Comparison isoenergetic scattering opacity simulations in RMS energy for model S9, with different g_a^s and $g_a = 1.21$. The solid lines mark the result for electron-neutrino, and the dashed lines for electron-antineutrino. The blue line marks the result for $g_a^s = 0.0$, red for -0.2, yellow for -0.4, and green for -1.0.

Chapter 8

Summary, Conclusions and Outlook

This chapter concludes this dissertation by summarizing the key research findings in relation to our research aims — developing a next-generation, state-of-the-art neutrino kinetics simulation capability for the CCSN community. It discusses the value and contribution of this dissertation, reviews the limitations of the study, and proposes opportunities for future research. The context is presented in the above order.

8.1 Summary and Conclusions

The primary focus of this dissertation is to develop a next-generation, state-of-the-art neutrino kinetics (transport) capability in the combined core-collapse supernova simulation frameworks Flash-X + `thornado`. Flash-X is a composable software system that delivers a flexible, high-performance platform and can be used to simulate physical phenomena in several scientific domains. `thornado` is a framework/toolkit that aims to provide numerical solution methods with applications to relativistic astrophysical systems, such as core-collapse supernova. `thornado` transport is a next-generation, state-of-the-art neutrino kinetics capability based on two-moment neutrino transport and discontinuous Galerkin methods. A detailed description of the equations solved by `thornado` transport in the Newtonian gravity, $\mathcal{O}(v/c)$ limit was presented in Chapter 2, as well as the weak physics included and the closure

method used. We also clearly explained the importance of preserving realizability, the conservation of lepton number, and the conservation of four-momentum (momentum and energy). Our effort to develop numerical methods for two-moment neutrino transport satisfying these requirements was presented in Chapter 3 for $\mathcal{O}(1)$ transport and Chapter 4 for $\mathcal{O}(v/c)$ transport. We started with the relatively simple $\mathcal{O}(1)$ two-moment neutrino transport, designed the PDARS IMEX schemes with a realizability-enforcing limiter, and tested the methods with several numerical tests for their accuracy, efficiency, realizability-preserving properties, and adherence to the diffusion limit. Then, we enhanced the numerical method by upgrading the model from $\mathcal{O}(1)$ to $\mathcal{O}(v/c)$, no gravity in the transport equations, and added a comprehensive set of neutrino–matter interaction terms. We explained the difficulty of preserving realizability with special relativity correction terms added, proposed a modified numerical method with positivity-preserving limiter, and used the limiters in code verification tests and scientific simulations. The $\mathcal{O}(v/c)$ two-moment neutrino transport was tested in pure transport problems – numerical tests with updates from transport only. Then we presented the Flash-X + `thornado` numerical implementation in Chapter 5, including `WeakLib` for tabulated opacity rates and table interpolation, the interface for Flash-X + `thornado` coupling, and the iteration method for the nonlinear solver for the collision term. `WeakLib` code validation and the Flash-X + `thornado` framework validation were also presented. The incorporated framework was tested in realistic settings. These tests include: (a), the relaxation test for maintaining the theoretical equilibrium state, (b), the homogeneous sphere problem for static radiation and the difference the closure method can make, and (c), the deleptonization wave test for the coupling of the frameworks. In Chapter 6, the ability of Flash-X + `thornado` to perform CCSN simulation is demonstrated by performing a detailed comparison of CCSN simulation results obtained with Flash-X + `thornado` and CHIMERA, a well-known CCSN simulation code, for the S9 progenitor and assuming spherical symmetry, including only electron-type neutrinos and antineutrinos using the industry-standard SFHo EOS and neutrino-matter

interactions from Bruenn (1985). Good agreement was observed in both the fluid variables and the radiation variables during core collapse, at core bounce, and after core bounce. After verifying the capability of Flash-X + `thornado`to perform core collapse supernova simulations under the assumptions made, we performed a series of CCSN simulations under the same assumptions with low-mass progenitors from Sukhbold et al. (2016) and presented our results in Chapter 7. The collapse, bounce, and late-time evolution of three different progenitors — S9, S10, and S11 — have been simulated. The dynamics and neutrino observables for all three models are similar. The S9, S10, and S11 progenitor models do not result in an explosion during the first 250 ms, 320 ms, and 350 ms after core bounce, respectively. We not only detailed the evolution of the core in these three cases, but also discussed the impact different progenitors and weak physics have on the evolution.

8.2 Contributions

The author's contributions include

1. Enabled neutrino opacity in `WeakLib`.
2. Helped understand the importance of realizability of moment and developed realizability-preserving DG IMEX scheme for two-moment neutrino transport.
3. Built, helped optimize, and tested Flash-X + `thornado`.
4. Made a code comparison between Flash-X + `thornado` and CHIMERA.
5. Made a serial of 1D CCSN simulations using Flash-X + `thornado` on Oak Ridge Leadership Computing Facility (OLCF) – Summit supercomputer.

8.3 Outlook

While the development of `thornado` transport documented here is a significant step forward for reasons discussed, realistic CCSN simulations will require the following:

1. `thornado` transport must include heavy-flavor neutrino species.

2. `WeakLib` must be extended beyond the interaction rates from Bruenn (1985) to include state-of-the-art weak physics, such as that discussed in Hannestad and Raffelt (1998); Thompson et al. (2000, 2003); Rampp and Janka (2002); Horowitz (2002); Hix et al. (2003); Buras et al. (2006); O'Connor (2015); Horowitz et al. (2017).

3. `thornado` transport must be general relativistic.

4. The Flash-X + `thornado` interface must be developed to enable mesh refinement and GPU acceleration.

5. A 3D CCSN simulation is demanded.

Development of `thornado`, as well as Flash-X, continues to include new features and other enhancements will be reported in the future.

Bibliography

An open catalog for supernova data. Accessed: 2019-02-19. 3

E. Abdikamalov, S. Gossan, A. M. DeMaio, and C. D. Ott. Measuring the angular momentum distribution in core-collapse supernova progenitors with gravitational waves. *Physical Review D*, 90(4):044001, 2014. 3

M. L. Adams. Discontinuous finite element transport solutions in thick diffusive problems. *Nuclear science and engineering*, 137(3):298–333, 2001. 10, 54

D. G. Anderson. Iterative procedures for nonlinear integral equations. *Journal of the ACM (JACM)*, 12(4):547–560, 1965. 118

J. Anderson and E. Spiegel. The moment method in relativistic radiative transfer. *The Astrophysical Journal*, 171:127, 1972. 22

D. Arnett and W. D. Arnett. *Supernovae and nucleosynthesis: An investigation of the history of matter, from the Big Bang to the present*, volume 7. Princeton University Press, 1996. 2

U. Ascher, S. Ruuth, and R. Spiteri. Implicit-explicit Runge-Kutta methods for time-dependent partial differential equations. *Applied Numerical Mathematics*, 25: 151–167, 1997. 58

Z. Banach and W. Larecki. Spectral maximum entropy hydrodynamics of fermionic radiation: a three-moment system for one-dimensional flows. *Nonlinearity*, 26(6): 1667, 2013. 37, 130

Z. Banach and W. Larecki. Kershaw-type transport equations for fermionic radiation. *Zeitschrift für angewandte Mathematik und Physik*, 68(4):100, 2017. 37, 42, 43, 124

F. Bassi, N. Franchina, A. Ghidoni, and S. Rebay. A numerical investigation of a spectral-type nodal collocation discontinuous galerkin approximation of the euler and navier–stokes equations. *International Journal for Numerical Methods in Fluids*, 71(10):1322–1339, 2013. 10

T. W. Baumgarte and S. L. Shapiro. Numerical integration of einstein's field equations. *Physical Review D*, 59(2):024007, 1998. 5

R. Bollig, H.-T. Janka, A. Lohs, G. Martínez-Pinedo, C. J. Horowitz, and T. Melson. Muon creation in supernova matter facilitates neutrino-driven explosions. *Physical Review Letters*, 119(24):242702, 2017. 27

S. Bruenn and A. Mezzacappa. Ion screening effects and stellar collapse. *Physical Review D*, 56(12):7529, 1997. 6

S. Bruenn, K. De Nisco, and A. Mezzacappa. General relativistic effects in the core collapse supernova mechanism. *The Astrophysical Journal*, 560(1):326, 2001. 27, 139

S. Bruenn, A. Mezzacappa, W. Hix, J. Blondin, P. Marronetti, O. Messer, C. Dirk, and S. Yoshida. 2d and 3d core-collapse supernovae simulation results obtained with the chimera code. In *Journal of Physics: Conference Series*, volume 180, page 012018. IOP Publishing, 2009. 139

S. W. Bruenn. Stellar core collapse - numerical model and infall epoch. *APJS*, 58: 771–841, Aug 1985. doi: 10.1086/191056. vii, 4, 5, 6, 9, 27, 28, 71, 80, 95, 98, 99, 100, 101, 102, 103, 104, 110, 111, 114, 119, 130, 133, 139, 140, 164, 211, 212

S. W. Bruenn, J. R. Buchler, and W. R. Yueh. Neutrino transport in supernova models: A multigroup, flux limited diffusion scheme. *Astrophysics and Space Science*, 59(2):261–284, 1978. 22

S. W. Bruenn, C. Dirk, A. Mezzacappa, J. Hayes, J. Blondin, W. Hix, and O. Messer. Modeling core collapse supernovae in 2 and 3 dimensions with spectral neutrino transport. In *Journal of Physics: Conference Series*, volume 46, page 054. IOP Publishing, 2006. 139

S. W. Bruenn, A. Mezzacappa, W. R. Hix, E. J. Lentz, O. B. Messer, E. J. Lingerfelt, J. M. Blondin, E. Endeve, P. Marronetti, and K. N. Yakunin. Axisymmetric ab initio core-collapse supernova simulations of 12-25 solar-mass stars. *The Astrophysical Journal Letters*, 767(1):L6, 2013. 4, 139

S. W. Bruenn, E. J. Lentz, W. R. Hix, A. Mezzacappa, J. A. Harris, O. B. Messer, E. Endeve, J. M. Blondin, M. A. Chertkow, E. J. Lingerfelt, et al. The development of explosions in axisymmetric ab initio core-collapse supernova simulations of 12–25 stars. *The Astrophysical Journal*, 818(2):123, 2016. 4, 139

S. W. Bruenn, J. M. Blondin, W. R. Hix, E. J. Lentz, O. B. Messer, A. Mezzacappa, E. Endeve, J. A. Harris, P. Marronetti, R. D. Budiardja, et al. Chimera: a massively parallel code for core-collapse supernova simulations. *The Astrophysical Journal Supplement Series*, 248(1):11, 2020. viii, 4, 138, 139, 141, 144

R. Buras, H.-T. Janka, M. T. Keil, G. G. Raffelt, and M. Rampp. Electron neutrino pair annihilation: A new source for muon and tau neutrinos in supernovae. *The Astrophysical Journal*, 587(1):320, 2003. 5, 27

R. Buras, M. Rampp, H.-T. Janka, and K. Kifonidis. Two-dimensional hydrodynamic core-collapse supernova simulations with spectral neutrino transport-i. numerical method and results for a 15 m $\odot$ star. *Astronomy & Astrophysics*, 447(3):1049–1092, 2006. 4, 5, 6, 139, 212

A. Burrows and R. Sawyer. Effects of correlations on neutrino opacities in nuclear matter. *Physical Review C*, 58(1):554, 1998. 5, 27

A. Burrows and D. Vartanyan. Core-collapse supernova explosion theory. *Nature*, 589 (7840):29–39, 2021. 3, 4

A. Burrows, T. Young, P. Pinto, R. Eastman, and T. A. Thompson. A new algorithm for supernova neutrino transport and some applications. *The Astrophysical Journal*, 539(2):865, 2000. 139

A. Burrows, S. Reddy, and T. A. Thompson. Neutrino opacities in nuclear matter. *Nuclear Physics A*, 777:356–394, 2006. 7

A. Burrows, D. Vartanyan, J. C. Dolence, M. A. Skinner, and D. Radice. Crucial physical dependencies of the core-collapse supernova mechanism. *Space Science Reviews*, 214(1):1–22, 2018. 27

A. Burrows, D. Radice, and D. Vartanyan. Three-dimensional supernova explosion simulations of 9-, 10-, 11-, 12-, and 13-solar mass stars. *Monthly Notices of the Royal Astronomical Society*, 485(3):3153–3168, 2019. 3, 164, 205

A. C. Calder, B. Fryxell, T. Plewa, R. Rosner, L. Dursi, V. Weirs, T. Dupont, H. Robey, J. Kane, B. Remington, et al. On validating an astrophysical simulation code. *The Astrophysical Journal Supplement Series*, 143(1):201, 2002. 139

C. Y. Cardall and A. Mezzacappa. Conservative formulations of general relativistic kinetic theory. *Physical Review D*, 68(2):023006, 2003. 12, 19, 20

C. Y. Cardall, E. Endeve, and A. Mezzacappa. Conservative 3+ 1 general relativistic boltzmann equation. *Physical Review D*, 88(2):023011, 2013. 12, 19, 24, 80

D. Cavaglieri and T. Bewley. Low-storage implicit/explicit Runge–Kutta schemes for the simulation of stiff high-dimensional ODE systems. *Journal of Computational Physics*, 286:172 – 193, 2015. ISSN 0021-9991. 68, 72

J. Cernohorsky and S. A. Bludman. Maximum entropy distribution and closure for bose-einstein and Fermi-Dirac radiation transport. *Astrophysical Journal*, 433(1): 450 – 455, 1994. 40, 41, 48, 124, 130

J. Cernohorsky and C. G. Van Weert. Relativistic two-moment neutrino transport. *The Astrophysical Journal*, 398:190–202, 1992. 22

A. Chertock, S. Cui, A. Kurganov, and T. Wu. Steady state and sign preserving semi-implicit runge–kutta methods for odes with stiff damping term. *SIAM Journal on Numerical Analysis*, 53(4):2008–2029, 2015. 61

R. Chu, E. Endeve, C. D. Hauck, and . A. Mezzacappa. Realizability-Preserving DG-IMEX Method for the Two-Moment Model of Fermion Transport. *Journal of Computational Physics*, 389:62–93, July 2019a. ISSN 00219991. 7, 11, 35, 36, 38, 46, 50, 51, 55, 60, 61, 63, 64, 65, 67, 68, 69, 84

R. Chu, E. Endeve, C. D. Hauck, A. Mezzacappa, and B. Messer. thornado-transport: IMEX schemes for two-moment neutrino transport respecting Fermi-Dirac statistics. *Journal of Physics: Conference Series*, 1225(1):012013, June 2019b. 11, 51, 62, 64, 67, 68, 75, 76, 77, 78, 84, 119

B. Cockburn and C.-W. Shu. The runge–kutta discontinuous galerkin method for conservation laws v: multidimensional systems. *Journal of Computational Physics*, 141(2):199–224, 1998. 73

B. Cockburn and C.-W. Shu. Runge-Kutta Discontinuous Galerkin Methods for Convection-Dominated Problems. *Journal of Scientific Computing*, 16:173–261, 2001. 10, 53, 54

P. Colella and P. R. Woodward. The piecewise parabolic method (ppm) for gas-dynamical simulations. *Journal of computational physics*, 54(1):174–201, 1984. 5, 6

M. S. Coleman, A. Burrows, and C. J. White. The physical effects of progenitor rotation: Comparing two long-duration 3d core-collapse supernova simulations. *arXiv preprint arXiv:2111.00022*, 2021. 3

S. A. Colgate and R. H. White. The hydrodynamic behavior of supernovae explosions. *The astrophysical journal*, 143:626, 1966. 4

S. M. Couch, M. L. Warren, and E. P. O'Connor. Simulating turbulence-aided neutrino-driven core-collapse supernova explosions in one dimension. *The Astrophysical Journal*, 890(2):127, 2020. 164

S. M. Couch, J. Carlson, M. Pajkos, B. W. O'Shea, A. Dubey, and T. Klosterman. Towards performance portability in the spark astrophysical magnetohydrodynamics solver in the flash-x simulation framework. *Parallel Computing*, 108:102830, 2021. 7, 11, 18, 102

G. Dimarco and L. Pareschi. Asymptotic preserving implicit-explicit runge–kutta methods for nonlinear kinetic equations. *SIAM Journal on Numerical Analysis*, 51 (2):1064–1087, 2013. 58

H. Dimmelmeier, J. A. Font, and E. Müller. Relativistic simulations of rotational core collapse i. methods, initial models, and code tests. *Astronomy & Astrophysics*, 388(3):917–935, 2002. 4, 5

H. Dimmelmeier, J. Novak, J. A. Font, J. M. Ibáñez, and E. Müller. Combining spectral and shock-capturing methods: A new numerical approach for 3d relativistic core collapse simulations. *Physical Review D*, 71(6):064023, 2005. 4, 5

A. Dubey, K. Antypas, M. K. Ganapathy, L. B. Reid, K. Riley, D. Sheeler, A. Siegel, and K. Weide. Extensible component-based architecture for flash, a massively parallel, multiphysics simulation code. *Parallel Computing*, 35(10-11):512–522, 2009. 4, 7

A. Dubey, K. Weide, J. O'Neal, A. Dhruv, S. Couch, J. A. Harris, T. Klosterman, R. Jain, J. Rudi, B. Messer, M. Pajkos, J. Carlson, R. Chu, M. Wahib, S. Chawdhary, P. M. Ricker, D. Lee, K. Antypas, K. M. Riley, C. Daley, M. Ganapathy, F. X. Timmes, D. M. Townsley, M. Vanella, J. Bachan, P. M. Rich, S. Kumar, E. Endeve, W. R. Hix, A. Mezzacappa, and T. Papatheodore. Flash-x: A multiphysics simulation software instrument. *SoftwareX*, 19:101168, 2022. ISSN 2352-7110. doi: https://doi.org/10.1016/j.softx.2022.101168. URL https://www.sciencedirect.com/science/article/pii/S2352711022001030. 4, 7, 102

M. Dumbser, O. Zanotti, R. Loubère, and S. Diot. A posteriori subcell limiting of the discontinuous galerkin finite element method for hyperbolic conservation laws. *Journal of Computational Physics*, 278:47–75, 2014. 106

E. Endeve, C. D. Hauck, Y. Xing, and A. Mezzacappa. Bound-preserving discontinuous galerkin methods for conservative phase space advection in curvilinear coordinates. *Journal of Computational Physics*, 287:151–183, 2015. 10, 54

E. Endeve, R. Chu, A. Mezzacappa, I. Messer, et al. Towards a discontinuous galerkin method for the multi-group two-moment model of neutrino transport. Technical report, Oak Ridge National Lab.(ORNL), Oak Ridge, TN (United States), 2018. 119

E. Endeve, P. Laiu, Z. Elledge, and A. Mezzacappa. DG-IMEX method for a two-moment model for radiation transport in the $\mathcal{O}(v/c)$ limit. *Journal of Computational Physics, in prep.*, 2022a. 7, 22, 55, 115

E. Endeve et al. thornado-transport: neutrino radiation hydrodynamics with discontinuous galerkin methods. *in prep.*, 2022b. 7, 22, 25, 26, 55, 83, 115, 118

T. Fischer, G. Guo, G. Martínez-Pinedo, M. Liebendörfer, and A. Mezzacappa. Muonization of supernova matter. *Physical Review D*, 102(12):123001, 2020. 96

F. Foucart, E. O'Connor, L. Roberts, M. D. Duez, R. Haas, L. E. Kidder, C. D. Ott, H. P. Pfeiffer, M. A. Scheel, and B. Szilagyi. Post-merger evolution of a neutron star-black hole binary with neutrino transport. *Physical Review D*, 91(12):124021, 2015. 2, 39

F. Foucart, E. O'Connor, L. Roberts, L. E. Kidder, H. P. Pfeiffer, and M. A. Scheel. Impact of an improved neutrino energy estimate on outflows in neutron star merger simulations. *Physical Review D*, 94(12):123016, 2016. 2

B. Fryxell, E. Müller, and D. Arnett. Computation of multi-dimensional flows with non-uniform composition. In *Nuclear Astrophysics*, 1989. 5

B. Fryxell, K. Olsen, P. Ricker, F. Timmes, M. Zingale, D. Lamb, P. MacNeice, R. Rosner, J. Truran, and H. Tufo. Flash: An adaptive mesh hydrodynamics code for modeling astrophysical thermonuclear flashes. *The Astrophysical Journal Supplement Series*, 131:273–334, November 2000. 4, 7

R. Glas, O. Just, H.-T. Janka, and M. Obergaulinger. Three-dimensional core-collapse supernova simulations with multidimensional neutrino transport compared to the ray-by-ray-plus approximation. *The Astrophysical Journal*, 873(1):45, 2019. 139

E. Gottlieb, C.-W. Shu, and E. Tadmor. Strong Stability-Preserving High-Order Time Discretization Methods. *SIAM Review*, 43:89–112, 2001. 68, 70

J.-L. Guermond and G. Kanschat. Asymptotic analysis of upwind discontinuous galerkin approximation of the radiative transport equation in the diffusive limit. *SIAM Journal on Numerical Analysis*, 48(1):53–78, 2010. 10, 54

S. Hannestad and G. Raffelt. Supernova neutrino opacity from nucleon-nucleon bremsstrahlung and related processes. *The Astrophysical Journal*, 507(1):339, 1998. 5, 6, 27, 96, 212

R. S. Hansen, M. Lindner, and O. Scholer. Timing the neutrino signal of a galactic supernova. *arXiv preprint arXiv:1904.11461*, 2019. 3

J. A. Harris, W. R. Hix, M. A. Chertkow, C. Lee, E. J. Lentz, and O. B. Messer. Implications for post-processing nucleosynthesis of core-collapse supernova models with lagrangian particles. *The Astrophysical Journal*, 843(1):2, 2017. 139

J. A. Harris, R. Chu, S. M. Couch, A. Dubey, E. Endeve, A. Georgiadou, R. Jain, D. Kasen, M. P. Laiu, O. B. Messer, et al. Exascale models of stellar explosions: Quintessential multi-physics simulation. *The International Journal of High Performance Computing Applications*, page 10943420211027937, 2021. 4, 7, 11

A. Heger, S. Woosley, and H. Spruit. Presupernova evolution of differentially rotating massive stars including magnetic fields. *The Astrophysical Journal*, 626(1):350, 2005. 3

J. S. Hesthaven and T. Warburton. *Nodal discontinuous Galerkin methods: Algorithms, analysis and applications*. Springer, 2008. 10, 54

K. Hirata, T. Kajita, M. Koshiba, M. Nakahata, Y. Oyama, N. Sato, A. Suzuki, M. Takita, Y. Totsuka, T. Kifune, et al. Observation of a neutrino burst from the supernova sn1987a. *Physical Review Letters*, 58(14):1490, 1987. 2

W. Hix, O. Messer, A. Mezzacappa, M. Liebendörfer, J. Sampaio, K. Langanke, D. Dean, and G. Martínez-Pinedo. Consequences of nuclear electron capture in core collapse supernovae. *Physical Review Letters*, 91(20):201102, 2003. 6, 27, 212

W. R. Hix and F.-K. Thielemann. Computational methods for nucleosynthesis and nuclear energy generation. *Journal of Computational and Applied Mathematics*, 109(1-2):321–351, 1999. 6, 7

C. Horowitz. Neutrino trapping in a supernova and the screening of weak neutral currents. *Physical Review D*, 55(8):4577, 1997. 6

C. Horowitz. Weak magnetism for antineutrinos in supernovae. *Physical Review D*, 65(4):043001, 2002. 7, 200, 212

C. Horowitz, O. Caballero, Z. Lin, E. O'Connor, and A. Schwenk. Neutrino-nucleon scattering in supernova matter from the virial expansion. *Physical Review C*, 95 (2):025801, 2017. 7, 212

J. Hu, R. Shu, and X. Zhang. Asymptotic-preserving and positivity-preserving implicit-explicit schemes for the stiff BGK equation. *SIAM Journal on Numerical Analysis*, 56(2):942–973, 2018. 59, 61, 68

N. Itoh, R. Asahara, N. Tomizawa, S. Wanajo, and S. Nozawa. Ion-ion correlation effect on the neutrino-nucleus scattering in supernova cores. *The Astrophysical Journal*, 611(2):1041, 2004. 5

H.-T. Janka, R. Dgani, and L. J. van den Horn. Fermion angular distribution and maximum entropy Eddington factors. *Astronomy & Astrophysics*, 265:345–354, 1992. 39

H.-T. Janka, T. Melson, and A. Summa. Physics of core-collapse supernovae in three dimensions: a sneak preview. *Annual Review of Nuclear and Particle Science*, 66: 341–375, 2016. 3

S. Jin and C. Levermore. Numerical Schemes for Hyperbolic Conservation Laws with Stiff Relaxation Terms. *Journal of Computational Physics*, 126:942–973, 1996. 60

O. Just, M. Obergaulinger, and H.-T. Janka. A new multidimensional, energy-dependent two-moment transport code for neutrino-hydrodynamics. *Monthly Notices of the Royal Astronomical Society*, 453(4):3386–3413, 2015. 4, 39, 47, 49, 52, 86, 90, 124, 139

O. Just, R. Bollig, H.-T. Janka, M. Obergaulinger, R. Glas, and S. Nagataki. Core-collapse supernova simulations in one and two dimensions: comparison of codes and approximations. *Monthly Notices of the Royal Astronomical Society*, 481(4): 4786–4814, 2018. 27, 139

D. Kershaw. Flux limiting nature's own way — a new method for numerical solution of the transport equation. Technical Report UCRL-78378, Lawrence Livermore Laboratory, 1976. 37, 42, 44, 124, 130

D. Khaitan. Supernova neutrino detection in lz. *Journal of Instrumentation*, 13(02): C02024, 2018. 3

A. Klöckner, T. Warburton, J. Bridge, and J. S. Hesthaven. Nodal discontinuous galerkin methods on graphics processors. *Journal of Computational Physics*, 228 (21):7863–7882, 2009. 10, 54

K. Kotake, T. Takiwaki, T. Fischer, K. Nakamura, and G. Martínez-Pinedo. Impact of neutrino opacities on core-collapse supernova simulations. *The Astrophysical Journal*, 853(2):170, 2018. 27

M. R. Krumholz. The big problems in star formation: the star formation rate, stellar clustering, and the initial mass function. *Physics Reports*, 539(2):49–134, 2014. 2

T. Kuroda and H. Umeda. Three-dimensional magnetohydrodynamical simulations of gravitational collapse of a 15 solar mass star. *The Astrophysical Journal Supplement Series*, 191(2):439, 2010. 5

T. Kuroda, K. Kotake, and T. Takiwaki. Fully general relativistic simulations of core-collapse supernovae with an approximate neutrino transport. *The Astrophysical Journal*, 755(1):11, 2012. 4

T. Kuroda, T. Takiwaki, and K. Kotake. A new multi-energy neutrino radiation-hydrodynamics code in full general relativity and its application to the gravitational collapse of massive stars. *The Astrophysical Journal Supplement Series*, 222(2):20, 2016. 3, 4, 52

T. Kuroda, K. Kotake, K. Hayama, and T. Takiwaki. Correlated signatures of gravitational-wave and neutrino emission in three-dimensional general-relativistic core-collapse supernova simulations. *The Astrophysical Journal*, 851(1):62, 2017. 3

M. P. Laiu, J. A. Harris, R. Chu, and E. Endeve. thornado-transport: Anderson- and gpu-accelerated nonlinear solvers for neutrino-matter coupling1. In *Journal of Physics: Conference Series*, volume 1623, page 012013. IOP Publishing, 2020. 11, 115

M. P. Laiu, E. Endeve, R. Chu, J. A. Harris, and O. B. Messer. A dg-imex method for two-moment neutrino transport: Nonlinear solvers for neutrino–matter coupling. *The Astrophysical Journal Supplement Series*, 253(2):52, 2021. 7, 11, 55, 115, 118

M. P. Laiu et al. *in prep.*, 2022. 7, 84, 118

R. Landfield. *Sensitivity of Neutrino-Driven Core-Collapse Supernova Models to the Microphysical Equation of State*. PhD thesis, University of Tennessee, Knoxville, December 2018. 8, 95, 97

K. Langanke. K. langanke, g. martínez-pinedo, b. müller, h.-th. janka, a. marek, wr hix, a. juodagalvis, and jm sampaio. *Phys. Rev. Lett.*, 100:011101, 2008. 5

K. Langanke and G. Martinez-Pinedo. Nuclear weak-interaction processes in stars. *Reviews of Modern Physics*, 75(3):819, 2003. 200

K. Langanke, G. Martinez-Pinedo, J. Sampaio, D. Dean, W. Hix, O. Messer, A. Mezzacappa, M. Liebendörfer, H.-T. Janka, and M. Rampp. Electron capture rates on nuclei and implications for stellar core collapse. *Physical Review Letters*, 90(24):241102, 2003. 5, 6, 27

W. Larecki and Z. Banach. Entropic Derivation of the Spectral Eddington Factors. *JQSRT*, 112:2486–2506, 2011. 37, 40, 41, 44

E. W. Larsen, J. E. Morel, and W. F. Miller Jr. Asymptotic solutions of numerical transport problems in optically thick, diffusive regimes. *Journal of Computational Physics*, 69(2):283–324, 1987. 54

J. M. Lattimer and F. D. Swesty. A generalized equation of state for hot, dense matter. *Nuclear Physics A*, 535(2):331–376, 1991. 97, 102, 119

E. J. Lentz, A. Mezzacappa, O. B. Messer, M. Liebendörfer, W. R. Hix, and S. W. Bruenn. On the requirements for realistic modeling of neutrino transport in simulations of core-collapse supernovae. *The Astrophysical Journal*, 747(1):73, 2012. 27

E. J. Lentz, S. W. Bruenn, W. R. Hix, A. Mezzacappa, O. B. Messer, E. Endeve, J. M. Blondin, J. A. Harris, P. Marronetti, and K. N. Yakunin. Three-dimensional core-collapse supernova simulated using a 15 solar mass progenitor. *The Astrophysical Journal Letters*, 807(2):L31, 2015. 4, 139

C. D. Levermore. Relating Eddington factors to flux limiters. *JQSRT*, 31:149–160, 1984. 6, 37, 38, 44, 124, 130

M. Liebendörfer, M. Rampp, H.-T. Janka, and A. Mezzacappa. Supernova simulations with boltzmann neutrino transport: A comparison of methods. *The Astrophysical Journal*, 620(2):840, 2005. 139

X.-D. Liu and S. Osher. Nonoscillatory high order accurate self-similar maximum principle satisfying shock capturing schemes i. *SIAM Journal on Numerical Analysis*, 33(2):760–779, 1996. 66

P. MacNeice, K. M. Olson, C. Mobarry, R. De Fainchtein, and C. Packer. Paramesh: A parallel adaptive mesh refinement community toolkit. *Computer physics communications*, 126(3):330–354, 2000. 7

A. Marek, H.-T. Janka, R. Buras, M. Liebendörfer, and M. Rampp. On ion-ion correlation effects during stellar core collapse. *Astronomy & astrophysics*, 443(1): 201–210, 2005. 5

R. McClarren, T. Evans, R. Lowrie, and J. Densmore. Semi-implicit time integration for PN thermal radiative transfer. *Journal of Computational Physics*, 227(16): 7561–7586, 2008. ISSN 0021-9991. 68, 69, 72

T. Melson, H.-T. Janka, R. Bollig, F. Hanke, A. Marek, and B. Müller. Neutrino-driven explosion of a 20 solar-mass star in three dimensions enabled by strange-quark contributions to neutrino–nucleon scattering. *The Astrophysical Journal Letters*, 808(2):L42, 2015a. 200, 203

T. Melson, H.-T. Janka, and A. Marek. Neutrino-driven supernova of a low-mass iron-core progenitor boosted by three-dimensional turbulent convection. *The Astrophysical Journal Letters*, 801(2):L24, 2015b. 27, 204

O. Messer, A. Mezzacappa, S. Bruenn, and M. Guidry. A comparison of boltzmann and multigroup flux-limited diffusion neutrino transport during the postbounce shock reheating phase in core-collapse supernovae. *The Astrophysical Journal*, 507 (1):353, 1998. 139

O. Messer, S. Bruenn, J. Blondin, W. Hix, and A. Mezzacappa. Multidimensional, multiphysics simulations of core—collapse supernovae. In *Journal of Physics: Conference Series*, volume 125, page 012010. IOP Publishing, 2008. 139

O. Messer, J. A. Harris, W. R. Hix, E. J. Lentz, S. Bruenn, and A. Mezzacappa. Multi-dimensional simulations of core-collapse supernova explosions with chimera. In *AIP Conference Proceedings*, volume 1947, page 020017. AIP Publishing LLC, 2018. 139

O. E. Messer. *Questing for the grail: Spherically symmetric supernova simulations with boltzmann neutrino transport*. PhD thesis, University of Tennessee, Knoxville, 2000. 71, 119

A. Mezzacappa and S. W. Bruenn. Type ii supernovae and boltzmann neutrino transport-the infall phase. *The Astrophysical Journal*, 405:637–668, 1993a. 139

A. Mezzacappa and S. W. Bruenn. A numerical method for solving the neutrino boltzmann equation coupled to spherically symmetric stellar core collapse. *The Astrophysical Journal*, 405:669–684, 1993b. 139

A. Mezzacappa and S. W. Bruenn. Stellar core collapse-a boltzmann treatment of neutrino-electron scattering. *The Astrophysical Journal*, 410:740–760, 1993c. 6, 100, 114, 139

A. Mezzacappa, E. Endeve, O. B. Messer, and S. W. Bruenn. Physical, numerical, and computational challenges of modeling neutrino transport in core-collapse supernovae. *Living Reviews in Computational Astrophysics*, 6(1):1–174, 2020a. 3, 8, 9, 12, 25, 27

A. Mezzacappa, P. Marronetti, R. E. Landfield, E. J. Lentz, K. N. Yakunin, S. W. Bruenn, W. R. Hix, O. B. Messer, E. Endeve, J. M. Blondin, et al. Gravitational-wave signal of a core-collapse supernova explosion of a 15 solar mass star. *Physical Review D*, 102(2):023027, 2020b. 139

A. Mezzacappa, P. Marronetti, R. E. Landfield, E. J. Lentz, W. R. Hix, J. A. Harris, S. W. Bruenn, J. M. Blondin, O. Messer, J. Casanova, et al. Core collapse supernova gravitational wave emission for progenitors of 9.6, 15, and 25 solar masses. *arXiv preprint arXiv:2208.10643*, 2022. 139

D. Mihalas and B. Mihalas. Foundations of radiation hydrodynamics oxford university press, 1984. 18

G. N. Minerbo. Maximum entropy Eddington factors. *JQSRT*, 20:541–545, 1978. 5, 42, 124, 130

P. Mösta, S. Richers, C. D. Ott, R. Haas, A. L. Piro, K. Boydstun, E. Abdikamalov, C. Reisswig, and E. Schnetter. Magnetorotational core-collapse supernovae in three dimensions. *The Astrophysical Journal Letters*, 785(2):L29, 2014. 3

P. Mösta, C. D. Ott, D. Radice, L. F. Roberts, E. Schnetter, and R. Haas. A large-scale dynamo and magnetoturbulence in rapidly rotating core-collapse supernovae. *Nature*, 528(7582):376–379, 2015. 3

B. Müller. The status of multi-dimensional core-collapse supernova models. *Publications of the Astronomical Society of Australia*, 33, 2016. 3

B. Müller. Neutrino Emission as Diagnostics of Core-Collapse Supernovae. pages 1–26, apr 2019. 3

B. Müller. Hydrodynamics of core-collapse supernovae and their progenitors. *Living Reviews in Computational Astrophysics*, 6(1):1–104, 2020. 3

B. Müller and H.-T. Janka. Non-radial instabilities and progenitor asphericities in core-collapse supernovae. *Monthly Notices of the Royal Astronomical Society*, 448 (3):2141–2174, 2015. 4

B. Müller, H.-T. Janka, and H. Dimmelmeier. A new multi-dimensional general relativistic neutrino hydrodynamic code for core-collapse supernovae. i. method and code tests in spherical symmetry. *The Astrophysical Journal Supplement Series*, 189(1):104, 2010. 4, 5, 52

B. Müller, H.-T. Janka, and A. Marek. A new multi-dimensional general relativistic neutrino hydrodynamics code for core-collapse supernovae. ii. relativistic explosion models of core-collapse supernovae. *The Astrophysical Journal*, 756(1):84, 2012. 27

E. M. Murchikova, E. Abdikamalov, and T. Urbatsch. Analytic closures for M1 neutrino transport. *MNRAS*, 469:1725–1737, 2017. 39, 42, 124

M. Obergaulinger. PhD thesis, Technische Universit at Munchen, 2008. 4, 5

E. O'Connor and S. Couch. Two Dimensional Core-Collapse Supernova Explosions Aided by General Relativity with Multidimensional Neutrino Transport. *The*

Astrophysical Journal, 854(1):63, 2015. ISSN 1538-4357. doi: 10.3847/1538-4357/aaa893. 52

C. D. Ott, A. Burrows, L. Dessart, and E. Livne. Two-dimensional multiangle, multigroup neutrino radiation-hydrodynamic simulations of postbounce supernova cores. *The Astrophysical Journal*, 685(2):1069, 2008. 139

C. D. Ott, C. Reisswig, E. Schnetter, E. O'Connor, U. Sperhake, F. Loeffler, P. Diener, E. Abdikamalov, I. Hawke, and A. Burrows. Dynamics and gravitational wave signature of collapsar formation. *Physical Review Letters*, 106(16):161103, 2011. 3

C. D. Ott, L. F. Roberts, A. da Silva Schneider, J. M. Fedrow, R. Haas, and E. Schnetter. The progenitor dependence of core-collapse supernovae from three-dimensional simulations with progenitor models of 12–40 solar mass. *The Astrophysical Journal Letters*, 855(1):L3, 2018. 3

F. Özel, D. Psaltis, R. Narayan, and J. E. McClintock. The black hole mass distribution in the galaxy. *The Astrophysical Journal*, 725(2):1918, 2010. 2

F. Özel, D. Psaltis, R. Narayan, and A. S. Villarreal. On the mass distribution and birth masses of neutron stars. *The Astrophysical Journal*, 757(1):55, 2012. 2

E. O'Connor. An open-source neutrino radiation hydrodynamics code for core-collapse supernovae. *The Astrophysical Journal Supplement Series*, 219(2):24, 2015. 212

E. O'Connor, R. Bollig, A. Burrows, S. Couch, T. Fischer, H.-T. Janka, K. Kotake, E. J. Lentz, M. Liebendörfer, O. B. Messer, et al. Global comparison of core-collapse supernova simulations in spherical symmetry. *Journal of Physics G: Nuclear and Particle Physics*, 45(10):104001, 2018. 139

E. P. O'Connor and S. M. Couch. Two-dimensional core-collapse supernova explosions aided by general relativity with multidimensional neutrino transport. *The Astrophysical Journal*, 854(1):63, 2018. 86, 87

E. P. O'Connor and S. M. Couch. Exploring fundamentally three-dimensional phenomena in high-fidelity simulations of core-collapse supernovae. *The Astrophysical Journal*, 865(2):81, 2018. 3, 4

K.-C. Pan, C. Mattes, E. P. O'Connor, S. M. Couch, A. Perego, and A. Arcones. The impact of different neutrino transport methods on multidimensional core-collapse supernova simulations. *Journal of Physics G: Nuclear and Particle Physics*, 46(1): 014001, 2019. 124, 139

L. Pareschi and G. Russo. Implicit-Explicit Runge-Kutta Schemes and Application to Hyperbolic Systems with Relaxation. *Journal of Scientific Computing*, 25:129–155, 2005. 57, 58, 68, 71, 72

D. Pochik, B. L. Barker, E. Endeve, J. Buffaloe, S. J. Dunham, N. Roberts, and A. Mezzacappa. thornado-hydro: a discontinuous galerkin method for supernova hydrodynamics with nuclear equations of state. *The Astrophysical Journal Supplement Series*, 253(1):21, 2021. 8, 55

G. C. Pomraning. *The equations of radiation hydrodynamics*. Courier Corporation, 2005. 19

J. A. Pons, J. M. Ibáñez, and J. A. Miralles. Hyperbolic character of the angular moment equations of radiative transfer and numerical methods. *MNRAS*, 317: 550–562, 2000. 39

J. Powell, M. Szczepanczyk, and I. S. Heng. Inferring the core-collapse supernova explosion mechanism with three-dimensional gravitational-wave simulations. *Physical Review D*, 96(12):123013, 2017. 3

D. Radice and L. Rezzolla. Discontinuous galerkin methods for general-relativistic hydrodynamics: Formulation and application to spherically symmetric spacetimes. *Physical Review D*, 84(2):024010, 2011. 10, 54

D. Radice, E. Abdikamalov, L. Rezzolla, and C. D. Ott. A new spherical harmonics scheme for multi-dimensional radiation transport I. Static matter configurations. *Journal of Computational Physics*, 242:648–669, 2013. 10, 54, 69

D. Radice, A. Burrows, D. Vartanyan, M. A. Skinner, and J. C. Dolence. Electron-capture and low-mass iron-core-collapse supernovae: new neutrino-radiation-hydrodynamics simulations. *The Astrophysical Journal*, 850(1):43, 2017. 164, 176, 177, 205

D. Radice, V. Morozova, A. Burrows, D. Vartanyan, and H. Nagakura. Characterizing the gravitational wave signal from core-collapse supernovae. *The Astrophysical Journal Letters*, 876(1):L9, 2019. 3

M. Rampp and H.-T. Janka. Radiation hydrodynamics with neutrinos-variable eddington factor method for core-collapse supernova simulations. *Astronomy & Astrophysics*, 396(1):361–392, 2002. 4, 5, 6, 139, 212

W. Raphael Hix, J. Austin Harris, E. J. Lentz, S. Bruenn, O. Bronson Messer, and A. Mezzacappa. Learning about nucleosynthesis from multi-dimensional simulations of core-collapse supernovae. In *Nuclei in the Cosmos XV*, pages 115–120. Springer, 2019. 139

S. Reddy, M. Prakash, and J. M. Lattimer. Neutrino interactions in hot and dense matter. *Physical Review D*, 58(1):013009, 1998. 6, 27

S. Reddy, M. Prakash, J. M. Lattimer, and J. A. Pons. Effects of strong and electromagnetic correlations on neutrino interactions in dense matter. *Physical Review C*, 59(5):2888, 1999. 7

W. H. Reed and T. Hill. Triangular mesh methods for the neutron transport equation. Technical report, Los Alamos Scientific Lab., N. Mex.(USA), 1973. 10, 54

L. Rezzolla and O. Zanotti. *Relativistic hydrodynamics*. Oxford University Press, 2013. 14

S. Richers. Rank-3 moment closures in general relativistic neutrino transport. *Physical Review D*, 102(8):083017, 2020. 48, 124

S. Richers, H. Nagakura, C. D. Ott, J. Dolence, K. Sumiyoshi, and S. Yamada. A detailed comparison of multidimensional boltzmann neutrino transport methods in core-collapse supernovae. *The Astrophysical Journal*, 847(2):133, 2017. 139

L. F. Roberts, C. D. Ott, R. Haas, E. P. O'Connor, P. Diener, and E. Schnetter. General-Relativistic Three-Dimensional Multi-group Neutrino Radiation-Hydrodynamics Simulations of Core-Collapse Supernovae. *Astrophysical Journal*, 831:98, 2016. 39, 52

K. Schaal, A. Bauer, P. Chandrashekar, R. Pakmor, C. Klingenberg, and V. Springel. Astrophysical hydrodynamics with a high-order discontinuous galerkin scheme and adaptive mesh refinement. *Monthly Notices of the Royal Astronomical Society*, 453 (4):4278–4300, 2015. 10, 54

K. Scholberg. Supernova neutrino detection. *Annual Review of Nuclear and Particle Science*, 62:81–103, 2012. 3

M. Shibata and T. Nakamura. Evolution of three-dimensional gravitational waves: Harmonic slicing case. *Physical Review D*, 52(10):5428, 1995. 5

M. Shibata, K. Kiuchi, Y.-i. Sekiguchi, and Y. Suwa. Truncated moment formalism for radiation hydrodynamics in numerical relativity. *Progress of Theoretical Physics*, 125(6):1255–1287, 2011. 6, 80

J. Shohat and J. Tamarkin. *The Problem of Moments*. Mathematical Surveys and Monographs. American Mathematical Society, 1943. 37, 44

C.-W. Shu. High order weno and dg methods for time-dependent convection-dominated pdes: A brief survey of several recent developments. *Journal of Computational Physics*, 316:598–613, 2016. 10

C.-W. Shu and S. Osher. Efficient Implementation of Essentially Non-oscillatory Shock-Capturing Schemes. *Journal of Computational Physics*, 77:439–471, 1988. 63

M. A. Skinner and E. C. Ostriker. A Two-moment Radiation Hydrodynamics Module in Athena Using a Time-explicit Godunov Method. *Astrophysical Journal Supplement Series*, 206:21, 2013. 69, 86

M. A. Skinner, A. Burrows, and J. C. Dolence. Should one use the ray-by-ray approximation in core-collapse supernova simulations? *The Astrophysical Journal*, 831(1):81, 2016. 139

M. A. Skinner, J. C. Dolence, A. Burrows, D. Radice, and D. Vartanyan. Fornax: a flexible code for multiphysics astrophysical simulations. *The Astrophysical Journal Supplement Series*, 241(1):7, 2019. 4, 6, 52

J. Smit, L. Van den Horn, and S. Bludman. Closure in flux-limited neutrino diffusion and two-moment transport. *Astronomy and Astrophysics*, 356:559–569, 2000. 39, 121, 124

A. W. Steiner, J. M. Lattimer, and E. F. Brown. The equation of state from observed masses and radii of neutron stars. *The Astrophysical Journal*, 722(1):33, 2010. 71, 97, 164

G. Stockinger, H.-T. Janka, D. Kresse, T. Melson, T. Ertl, M. Gabler, A. Gessner, A. Wongwathanarat, A. Tolstov, S. Leung, et al. Three-dimensional models of core-collapse supernovae from low-mass progenitors with implications for crab. *Monthly Notices of the Royal Astronomical Society*, 496(2):2039–2084, 2020. 164

T. Sukhbold, T. Ertl, S. Woosley, J. M. Brown, and H.-T. Janka. Core-collapse supernovae from 9 to 120 solar masses based on neutrino-powered explosions. *The Astrophysical Journal*, 821(1):38, 2016. viii, 140, 163, 166, 211

S. A. Teukolsky. Formulation of discontinuous galerkin methods for relativistic astrophysics. *Journal of Computational Physics*, 312:333–356, 2016. 10, 54

I. Tews, J. M. Lattimer, A. Ohnishi, and E. E. Kolomeitsev. Symmetry parameter constraints from a lower bound on neutron-matter energy. *The Astrophysical Journal*, 848(2):105, 2017. 164

T. A. Thompson, A. Burrows, and J. E. Horvath. μ and τ neutrino thermalization and production in supernovae: Processes and time scales. *Physical Review C*, 62 (3):035802, 2000. 7, 212

T. A. Thompson, A. Burrows, and P. A. Pinto. Shock breakout in core-collapse supernovae and its neutrino signature. *The Astrophysical Journal*, 592(1):434, 2003. 7, 212

K. S. Thorne. Relativistic radiative transfer: moment formalisms. *Monthly Notices of the Royal Astronomical Society*, 194(2):439–473, 1981. 22

N. Vaytet, E. Audit, B. Dubroca, and F. Delahaye. A numerical model for multigroup radiation hydrodynamics. *Journal of Quantitative Spectroscopy and Radiative Transfer*, 112(8):1323–1335, 2011. 6, 49, 90, 124

J. R. Wilson, R. Couch, S. Cochran, J. Le Blanc, and Z. Barkat. Neutrino flow and the collapse of stellar coresfn1. *Annals of the New York Academy of Sciences*, 262 (1):54–64, 1975. 22

S. Woosley and A. Heger. Nucleosynthesis and remnants in massive stars of solar metallicity. *Physics Reports*, 442(1-6):269–283, 2007. 102, 118

S. Woosley and T. A. Weaver. The evolution and explosion of massive stars. ii. explosive hydrodynamics and nucleosynthesis. *The Astrophysical Journal Supplement Series*, 101(181-235), 1995. doi: 10.1086/192237. 105

S. E. Woosley, A. Heger, and T. A. Weaver. The evolution and explosion of massive stars. *Reviews of modern physics*, 74(4):1015, 2002. 2

K. Wu and H. Tang. Physical-constraint-preserving central discontinuous galerkin methods for special relativistic hydrodynamics with a general equation of state. *The Astrophysical Journal Supplement Series*, 228(1):3, 2016. 10, 54

K. N. Yakunin, P. Marronetti, A. Mezzacappa, S. W. Bruenn, C.-T. Lee, M. A. Chertkow, W. R. Hix, J. M. Blondin, E. J. Lentz, O. B. Messer, et al. Gravitational waves from core collapse supernovae. *Classical and Quantum Gravity*, 27(19): 194005, 2010. 139

K. N. Yakunin, A. Mezzacappa, P. Marronetti, S. Yoshida, S. W. Bruenn, W. R. Hix, E. J. Lentz, O. B. Messer, J. A. Harris, E. Endeve, et al. Gravitational wave signatures of ab initio two-dimensional core collapse supernova explosion models for 12–25 solar mass stars. *Physical Review D*, 92(8):084040, 2015. 3, 139

K. N. Yakunin, A. Mezzacappa, P. Marronetti, E. J. Lentz, S. W. Bruenn, W. R. Hix, O. Messer, E. Endeve, J. M. Blondin, and J. A. Harris. The gravitational wave signal of a core collapse supernova explosion of a 15 solar mass star. *arXiv preprint arXiv:1701.07325*, 2017. 139

S. Yamada, H.-T. Janka, and H. Suzuki. Neutrino transport in type ii supernovae: Boltzmann solver vs. monte carlo method. *Arxiv preprint astro-ph/9809009*, 1998. 139

W. Yueh and J. Buchler. Neutrino transport in supernova models-sn method. *The Astrophysical Journal*, 217:565–577, 1977. 22

W. Zhang, A. Almgren, V. Beckner, J. Bell, J. Blaschke, C. Chan, M. Day, B. Friesen, K. Gott, D. Graves, et al. Amrex: a framework for block-structured adaptive mesh refinement. *Journal of Open Source Software*, 4(37):1370–1370, 2019. 7

X. Zhang and C.-W. Shu. On positivity-preserving high order discontinuous galerkin schemes for compressible euler equations on rectangular meshes. *Journal of Computational Physics*, 229(23):8918–8934, 2010. 66

Alphabetical Index

Vita

Ran Chu was born and raised in China. She received her B.A. in physics from South China University of Technology in 2013. She received her master's degree in nuclear physics in 2016 from University of Tennessee, Knoxville. By the end of this program, she has lived in Knoxville for 9 years, 1/3 of her life.